

# **Wave Propagation and Scour Failure of Coastal Structures due to Tsunamis**

**Adewale Olusola Abimbola**

**A thesis submitted in partial fulfilment of the requirements of the  
University of East London for the degree of Doctor of Philosophy**

**September 2018**

## Abstract

The extensive research on the influence of sea dike geometry on tsunami-induced scour indicates the necessity for a suitable model that can forecast the scour depth behind coastal structures and thus minimize the damaging effect of a high category tsunami occurrence. Current attempts to study this phenomenon have not gained worldwide acceptance and have been limited to unproven analytical methods, and either laboratory or numerical methods. These indicate the need for a verifiable predictive expression that links both the sediment characteristics and coastal defence geometry.

A comprehensive laboratory experiment was conducted to better understand the propagation mechanism of tsunami waves around four varying dikes sizes; two of which were modelled after dikes in Iwanuma and Soma cities in Japan that were affected by the 2011 Great Eastern Japan Earthquake and Tsunami. This investigation contributed to the understanding of the influence of dike dimensions on the flow variables. Afterwards, the mechanism of the induced local scour at the landward region was studied in detail because of the destructive impact it could have on the stability of the structures. These led to the development of a predictive scour model, from which a tsunami-induced scour resilient structure can be proposed. Also, using the particle size analysis, the median grain size and permeability properties of the sediment grain were determined and used to form the boundary condition of the expression.

The two-dimensional CFD analyses of the wave propagation and associated induced scour were investigated using ANSYS Fluent software package and sedFoam-2.0 solver respectively, and the results validated against the laboratory data showed good agreement. The Reynolds-Averaged Navier-Stokes (RANS) modelling approach with Realizable  $k-\epsilon$  turbulence model and scalable wall function for wall modelling were employed for the wave flow, while turbulence-averaged Eulerian two-phase flow equations with the kinetic theory of granular flows for intergranular stress models and a  $k-\epsilon$  turbulence model were used for the numerical implementation of the sediment scour.

Title page	i
Abstract	ii
Table of Contents	iii
List of Figures	vii
List of Tables	xiii
Nomenclature	xv
Abbreviations	xxi
Acknowledgements	xxiii
Dedication	xxiv
1 Introduction	1
1.1 Background of the Study	3
1.2 Aim and Objectives of the Study	4
1.3 The Scope of the Study	5
1.4 Outline of Thesis	5
2 Literature Review	7
2.1 Introduction	7
2.2 Water Wave Mechanics	7
2.3 Background of Tsunami studies	10
2.3.1 Tsunami	10
2.3.2 Experimental studies	11
2.3.3 Numerical studies	13
2.4 Flooding and Tsunami Mitigation Measures for Resilient Coastal Dike in Japan	14
2.5 Early History and Development of Numerical Simulation	19
2.6 Computational Fluid Dynamics Theory	21
2.6.1 Navier-Stokes equations	22
2.6.2 Reynolds-Averaged Navier-Stokes equations	23
2.6.3 $k - \epsilon$ turbulence model	27

2.6.3.1	Standard k - $\epsilon$ model	27
2.6.3.2	Realizable k - $\epsilon$ model	29
2.6.4	The Volume of fluid method	30
2.6.5	Near-wall modelling	31
2.6.6	Wall functions	31
2.6.6.1	Standard wall functions	33
2.6.6.2	Scalable wall functions	35
2.7	Sediment Transport Mechanisms	35
2.7.1	Modes of sediment transport	35
2.7.2	Sediment transport modelling	36
2.7.2.1	Empirical bed load transport equations	39
2.7.2.2	Two-phase equation by Cheng and Hsu (2014)	44
2.7.2.3	Sediment transport model by Zhang and Shi (2016)	46
2.8	Summary	47
3	Tsunami Wave Propagation over Sea Dikes	48
3.1	Introduction	48
3.2	Laboratory Experiments	50
3.3	Tsunami Wave Flow over Sea Dike	54
3.3.1	Velocity distributions	54
3.3.2	The configuration of a pressure analog input measurement	60
3.3.3	Total tsunami wave pressure	61
3.3.3.1	Model A	62
3.3.3.2	Model B	62
3.3.3.3	Model C	63
3.3.3.4	Model D	63
3.3.4	Overflowing Wave pressure	68
3.4	Conclusions	70

4	Tsunami Induced Scour Profile on Erodeable Boundaries	72
	4.1 Introduction	72
	4.2 Experimental Work	74
	4.3 Scour Profile Characteristics	78
	4.4 Scour Occurrence Validation with Shields parameter	84
	4.5 Representative Scour Depth Predictive Model	87
	4.6 Proposed Sea Dike Section to Resist Landward Toe Scour	92
	4.7 Conclusions	94
5	Numerical Simulation of Tsunami Waves	96
	5.1 Introduction	96
	5.2 Numerical Investigation of Dam Break Flow – Two-phase Flow	99
	5.2.1 Geometric setup and mesh generation	99
	5.2.2 ANSYS Fluent setup	102
	5.2.3 Total tsunami wave pressure	108
	5.2.3.1 Model A	108
	5.2.3.2 Model B	109
	5.2.3.3 Model C	109
	5.2.3.4 Model D	110
	5.2.4 Velocity distributions at the landward region	119
	5.2.5 Comparison between the numerical simulation and laboratory experiment	128
	5.3 Numerical Methodology of Dam Break Flow - Comparison using ANSYS Fluent	129
	5.3.1 Introduction	129
	5.3.2 Computational setup	131
	5.3.3 Results and discussion	132
	5.4 Conclusions	134
6	Numerical Simulation of Tsunami-induced Sediment Scour	136
	6.1 Introduction	136
	6.2 SedFoam-2.0 Model- Two-phase Flow Solver	139
	6.2.1 The governing equations	139
	6.2.2 Turbulence modelling	140

6.2.3	Kinetic theory model	140
6.2.4	Model setup, initial and boundary conditions and mesh generation	141
6.2.4.1	Logarithmic velocity distribution	145
6.2.4.2	The shear stress at bottom-wall	145
6.2.5	Solution procedure	150
6.3	Scour Profile Characteristics	152
6.4	Comparison between the Numerical Simulation and Laboratory Experiment	160
6.5	Conclusions	162
7	Conclusions and recommendations	163
7.1	Conclusions	163
7.2	Recommendations	167
	References	169
	Bibliography	184
	Appendices	186

## List of Figures

Figure 1.1. Examples of damages caused by the 2011 Great Eastern Japan Earthquake and Tsunami (Jayaratne et al., 2013).	2
Figure 1.2. Representation of the predictive model parameters.	4
Figure 2.1. Characteristics of linear water wave.	9
Figure 2.2. Phases of the evolution of a typical seismic generated tsunami from source to shore (Rossetto et al., 2011).	13
Figure 2.3. Parts of a dike (Japan International Cooperation Agency, 2010).	15
Figure 2.4. Evolution of official Japanese design guidelines following the 2011 Great Eastern Japan Earthquake (Raby et al., 2015).	17
Figure 2.5. Integration of trees with coastal dike (Torii, 2014).	17
Figure 2.6. Proposed resilient structure for coastal dike (Kato et al., 2012).	19
Figure 2.7. Variation of a velocity component, $u$ , in turbulent flow (Cengel and Cimbala, 2014).	23
Figure 2.8. Near-wall cell (Craft, 2011).	32
Figure 2.9. Subdivisions of the near-wall region (Salim and Cheah, 2009).	33
Figure 2.10. The near-wall nodes (Launder and Spalding, 1974).	33
Figure 2.11. Bed load and suspended load (Julien, 2010).	36
Figure 2.12. Initiation of motion according to Shields (Van Rijn, 1984).	40
Figure 2.13. Bed-load motion at equilibrium (Chanson, 1999).	43
Figure 3.1 Front view of hydraulic flume channel.	51
Figure 3.2. The layout of hydraulic flume (Not to scale).	51
Figure 3.3. Location of pressure sensors.	52
Figure 3.4. Sea dike model geometry.	54

Figure 3.5. Section classification of the hydraulic flume.	56
Figure 3.6. Velocity distribution in the hydraulic flume.	58
Figure 3.7. Total wave pressure distribution in Model A under various hydraulic conditions.	64
Figure 3.8. Total wave pressure distribution in Model B under various hydraulic conditions.	65
Figure 3.9. Total wave pressure distribution in Model C under various hydraulic conditions.	66
Figure 3.10. Total wave pressure distribution in Model D under various hydraulic conditions.	67
Figure 3.11. The relationship between overflowing wave pressure and flow quantities from experimental (Exp.) studies.	68
Figure 4.1. Schematic sketch of the experimental set-up at UEL.	74
Figure 4.2. Front view of the representation of experimental set-up.	75
Figure 4.3. Grain size distribution curve.	75
Figure 4.4. Point gauge (manually operated) for measuring scour profile.	77
Figure 4.5. Snapshot of model C scour experiments.	78
Figure 4.6. Non-dimensional scour profiles of sea dike models (Models A, B, C, and D).	80
Figure 4.7. Scour development profile (Models A, B, C, and D).	83
Figure 4.8. The non-dimensional relationship between the average horizontal location of maximum scour depth and angle of seaward slope.	83
Figure 4.9. The non-dimensional relationship between the average horizontal location of maximum scour depth and angle of landward slope.	84
Figure 4.10. The Shields parameter as a function of the dimensionless diameter (Miedema, 2008).	85



Figure 4.11. A comparison between the Hjulstrom curve and the shields curve (Miedema, 2008).	86
Figure 4.12. Mathematical modelling construction steps (Giordano et al., 2009).	87
Figure 4.13. The relationship between relative scour depth and maximum overflowing wave pressure.	89
Figure 4.14. Design recommendation for a resilient coastal dike structure to mitigate the landward toe scour.	93
Figure 5.1. ANSYS Workbench project tab.	100
Figure 5.2. Geometry generation using DesignModeler.	100
Figure 5.3. Mesh generation using meshing application.	101
Figure 5.4. Different parts for boundary condition set up in Fluent.	101
Figure 5.5. Quality metrics of mesh.	102
Figure 5.6. Multiphase model set-up.	103
Figure 5.7. The solution method for setting up physics of flow.	106
Figure 5.8. The volume fraction of the phases during flow over the sea dike model.	107
Figure 5.9. The volume fraction of the phases after flow over the sea dike model.	107
Figure 5.10. Solution procedure flowchart in ANSYS Workbench 18.1.	108
Figure 5.11. Total wave pressure distribution in Model A under various hydraulic conditions.	112
Figure 5.12. Total wave pressure distribution in Model B under various hydraulic conditions.	114
Figure 5.13. Total wave pressure distribution in Model C under various hydraulic conditions.	116

Figure 5.14. Total wave pressure distribution in Model D under various hydraulic conditions.	118
Figure 5.15. maximum scour velocity comparison between numerical and laboratory data.	119
Figure 5.16. Velocity distribution behind Model A under various hydraulic conditions.	121
Figure 5.17. Velocity distribution behind Model B under various hydraulic conditions.	123
Figure 5.18. Velocity distribution behind Model C under various hydraulic conditions.	125
Figure 5.19. Velocity distribution behind Model D under various hydraulic conditions.	127
Figure 5.20. The relationship between overflowing wave pressure and flow quantities from experimental (Exp.) and numerical (Num.) simulation.	128
Figure 5.21. A side view of hydraulic flume with locations of water level measuring positions (left) and a front view showing the locations of pressure sensors at the impact wall downstream the dam (right). Dimensions in millimetres(Lobovsky et al., 2014).	130
Figure 5.22. Different zones for boundary condition setup in Fluent (Zone 1: Free surface, Zone 2: Inlet, Zone 3: Right wall, Zone 4: Bottom wall, Zone 5: Left wall).	131
Figure 5.23. H = 300 mm; free surface flow at 183 and 263 ms.	132
Figure 5.24. Free surface profile and upstream wave at the instant of complete dam gate removal. H = 300 mm (left), H = 600 mm (right).	133
Figure 5.25. Numerical simulation value of dynamic pressure at sensors 1 – 4 (s1 - s4).	133
Figure 5.26. H = 300 mm; numerical and experimental comparison of impact event pressure from four pressure sensors.	134
Figure 6.1. Transport properties.	142

Figure 6.2. Fine grid size (Block 0 cell size is the sediment region, and Block 1 cell size is the water region).	143
Figure 6.3. Schematics of the landward region (refer to the boundary and zone columns in Table 6.1).	144
Figure 6.4 Shear stress distribution at bottom-wall (Zone 2) of Model A under various hydraulic conditions.	146
Figure 6.5 Shear stress distribution at bottom-wall (Zone 2) of Model B under various hydraulic conditions.	147
Figure 6.6. Shear stress distribution at bottom-wall (Zone 2) of Model C under various hydraulic conditions.	148
Figure 6.7. Shear stress distribution at bottom-wall (Zone 2) of Model D under various hydraulic conditions.	149
Figure 6.8. Using logarithmic velocity distribution to link two CFD tools for tsunami-induced scour process.	150
Figure 6.9. Solution procedure flowchart in sedFoam-2.0 (Adapted from Cheng and Hsu, 2014; Chauchat et al. 2017).	151
Figure 6.10. Coarse grid size (Block 0 cell size is the sediment region, and Block 1 cell size is the water region).	153
Figure 6.11. Stability of sediment concentration calculation at 4 s by using a fine grid size.	153
Figure 6.12. Instability of sediment concentration calculation at 0.5 s by using a coarse grid size.	154
Figure 6.13. Scour profile of Model A under various hydraulic conditions.	156
Figure 6.14. Scour profile of Model B under various hydraulic conditions.	157
Figure 6.15. Scour profile of Model C under various hydraulic conditions.	158
Figure 6.16. Scour profile of Model D under various hydraulic conditions.	159

Figure 6.17. The relationship between relative scour depth and impact overflowing wave pressure.

160

## List of Tables

Table 2.1. Wave classification (Anderson & Frigaard, 2008).	9
Table 2.2. Crest width of a dike (Japan International Cooperation Agency, 2010).	15
Table 2.3. Minimum required freeboard (Japan International Cooperation Agency, 2010).	16
Table 2.4. RANS turbulence model description (ANSYS, 2006).	26
Table 2.5. RANS turbulence model behaviour and usage (ANSYS, 2006).	27
Table 2.6. Comparison of Sediment transport model (Hanna, 2014).	37
Table 2.7. Empirical and semi-empirical correlations of bed load transport (Chanson, 1999).	42
Table 2.8. Bed-load transport rate calculations (Chanson, 1999).	44
Table 3.1. Hydraulic conditions used in experiments.	52
Table 3.2. Coastal dike model geometry.	53
Table 3.3: Bore velocity readings for model dikes (Models A, B, C, and D).	58
Table 3.4. Average Error of the observed data from the overflowing wave pressure model.	69
Table 4.1. Root mean square error of the field survey data compared with the scour predictive model.	90
Table 4.2. Root mean square error of the experimental data compared with the scour predictive model.	91
Table 4.3. What-If analysis for maximum scour depth $D_s$ – the variation of landward slope $\theta_2$ , inundation depth $h$ , and dike height $H_{d2}$ .	93
Table 5.1 Physical properties of the Eulerian phases.	104
Table 5.2 Boundary conditions for geometry parts in Fluent.	105

Table 5.3. Comparison of numerical and experimental average Errors of the observed data from the overflowing wave pressure model.	129
Table 5.4. Boundary conditions for geometry parts in Fluent.	131
Table 6.1. Summary of boundary condition in the 2D sediment scour experimental configuration: zG = zeroGradient, fV = fixedValue, dM = directionMixed, fFP = FixedFluxPressure and hp = hydrostatic pressure.	144
Table 6.2. Root mean square error of the numerical data compared with the scour predictive model.	161

## Nomenclature

### Roman Symbols

$a$	Speed of sound
$a$	Wave amplitude
$A$	Area of the cross section
$C$	Correction factor
$C$	Wave celerity
$C_c$	Coefficient of curvature
$C_u$	Uniformity coefficient
$C'$	Chézy-coefficient related to surface or grain roughness of the sediment bed
$C_s$	Mean sediment concentration
$c_{1\varepsilon}, c_{2\varepsilon}, c_{3\varepsilon}$	Empirical coefficients in the $k$ - $\varepsilon$ Model
$c_{4\varepsilon}, S_{US}$	Empirical coefficients in the $k$ - $\varepsilon$ Model
dM	directionMixed
$D$	Water depth
$D_s$	Representative/maximum scour depth
$D_{10}$	Diameter just larger than the diameters of 10% of the soil grain
$D_{50}$	Average sediment size
$D_{60}$	Diameter just larger than the diameters of 60% of the soil grain
$D_{90}$	Diameter just larger than the diameters of 90% of the soil grain
$D_*$	Dimensionless grain diameter/Bonneville parameter
$D/Dt$	Substantial derivative in Cartesian coordinates
$E$	Average error
$E$	Empirical constant; the function of wall roughness
$f$	Body force
$f_i$	External force that drives the flow
fFP	FixedFluxPressure
fV	fixedValue
$g_i$	Gravitational vector component in the $i$ th direction
$g$	Gravitational acceleration
$h$	Inundation height.
$h_b$	Flow depth

$h_d$	Downstream water depth
$h_o$	Initial bed depth
$h_p$	Hydrostatic pressure
$h_u$	Upstream water depth
$H_{d2}$	Height of structure measured on the landward side
$i$	Unit vector along the x-axis
$I$	Turbulent intensity
$j$	Unit vector along the y-axis
$J_{int}$	Fluid-particle interaction term
$k$	Unit vector along the z-axis
$K$	Coefficient of soil permeability
$K$	Drag parameter
$k$	Turbulent kinetic energy
$k_p$	Turbulence kinetic energy at the near-wall node $P$
$k_s$	Nikuradse roughness length/equivalent roughness of the bed
$K_w$	Angular wave number
$L$	Wavelength
$L_m$	Model length
$L_{ms}$	Horizontal location of representative/maximum scour depth
$L_p$	Prototype length
$L_R$	Length ratio between prototype and model
$L_s$	Scour length
$M_i^{fs}/M_i^{sf}$	Interphase momentum transfer term between sediment and fluid phase
$M_t$	Turbulent Mach number
$\dot{m}_{pq}$	mass transfer from phase p to q
$\dot{m}_{qp}$	mass transfer from phase q to p
$n$	Porosity
$N$	Total number of data
$N_x$	Grid length in the x-direction
$N_y$	Grid length in the y-direction
$N_z$	Grid length in the z-direction
$P$	Wetted parameter
$P_b$	Buoyancy effect



$P_m$	Model wave pressure
$P_{om}$	Maximum Overflowing Pressure
$P_p$	Prototype wave pressure
$p^a$	Particle pressure
$\hat{p}^a$	Particle normal stress
$p^f$	Fluid pressure
$P_k$	Production of $k$
$p^s$	Particle pressure
P1	Pressure sensor one
P2	Pressure sensor two
P3	Pressure sensor three
P4	Pressure sensor four
P5	Pressure sensor five
$Pr_t$	Prandtl number
$q^*$	Dimensionless bed flux
$q_b$	Bed-load transport
$q_{bi}$	Bed load sediment transport rate at $i$ direction
$q_j$	Granular temperature flux
$q_0/q_s$	Bed-load transport rate per unit width
Re	Reynolds number
$R^2$	Coefficient of determinant
$R_b$	Hydraulic radius
$R_d$	Relative density
s	Specific gravity
S	Modulus of the mean rate-of-strain tensor
$S_{ij}$	Strain rate tensor
$S_{\alpha q}$	Source term
$S^s_{ij}$	Deviatoric part of strain rate tensor for sediment phase
$S_{US}$	Inverse of Schmidt number
t	Time
$t_{mf}$	Turbulent drag parameter
T	Transport stage parameter
$T$	Wave period

$T_m$	model time
$T_p$	Prototype time
$T_{ij}$	Total shear stress/ Reynolds stress tensor
$T_w$	Bottom wall shear stress
$u$	Velocity in the $x$ -direction
$U_p$	Mean velocity of the fluid at the near-wall node $P$
$\bar{u}$	Steady/mean velocity term
$u'$	Fluctuating velocity term
$u'_*$	Bed shear velocity related to grains
$u_i^f/u_i^b$	$i$ velocity component of the fluid phase
$u_i^s/u_i^a$	$i$ velocity component of the sediment phase
$u_*$	Shear velocity
$u_{*,cr}$	Shields critical bed shear velocity
$U^*$	Dimensionless velocity
$U_{cr}$	Critical average velocity above the bed
$v$	Velocity in the $y$ -direction
$V$	Velocity component
$\nu^b$	Fluid viscosity
$V_m$	Maximum velocity over the crest measured at the landward region
$V_p$	Prototype velocity
$V_s$	Average sediment velocity in the bed load layer
$\nu_t^b$	Turbulent viscosity
$w$	Velocity in the $z$ -direction
$x$	Streamwise direction
$\hat{X}$	Dimensionless maximum overflowing wave pressure
$y$	Spanwise direction
$Y_i$	Observed data
$y_p$	Distance from point $P$ to the wall
$Y_M$	Dilation dissipation
$\hat{Y}$	Model data
$y^+/y^*$	Dimensionless distance from the wall
$z$	Vertical direction
$zG$	zeroGradient

$z_o$  Constant of integration in the rough wall log-law

## Greek Symbols

$\alpha$	Angle of slope of the bed
$\alpha$	Particle volumetric concentration
$\alpha_i$	Dimensionless initial downstream water depth
$\beta$	Fluid volumetric concentration
$\beta$	Thermal expansion coefficient
$\Gamma$	Energy dissipation rate due to an inelastic collision
$\Delta x$	Grid length in the x-direction
$\Delta y$	Grid length in the y-direction
$\Delta z$	Grid length in the z-direction
$\delta_s$	Average saltation height measured perpendicular to the bed
$\delta_{ij}$	Kronecker delta
$\partial$	Partial derivative
$\varepsilon$	Turbulent dissipation
$\eta$	Water surface elevation
$\theta_2$	Angle of landward slope of the coastal dike
$\theta/\tau^*$	Dimensionless shear stress/Shields parameter
$\theta_{cr}/\tau^*_c$	Critical Shields parameter
$\theta_{cro}$	Critical shields number at the horizontal bed
$\theta_f/\varphi$	Angle of repose of the sediment
$l$	Turbulent length scale
$\kappa$	Von Kármán constant
$\lambda$	Scour fitted coefficient
$\lambda_f$	Friction coefficient
$\mu$	Dynamic viscosity of a fluid
$\mu_t$	Turbulent eddy viscosity
$\mu^{sf}$	Frictional viscosity
$\nu/\nu^b$	Kinematic viscosity
$\rho$	Density of water
$\rho^f/\rho^b$	Density of fluid phase
$\rho^s/\rho^a$	Density of sediment phase

$\rho_s$	Density of sediment
$\tau$	Viscous stress
$\tau_i$	Shear stress at $i$ direction
$\tau_{ij}^b$	Fluid shear stress
$\tau_{ij}^s/\tau_{ij}^a$	Particle stress
$\tau_0$	Bed shear stress
$\tau_w$	Shear stress on the wall
$\phi$	Sediment volumetric concentration
$\overline{\Omega_{ij}}$	Mean rate-of-rotation tensor observed in a rotating reference frame
$\Omega$	Computational domain
$\omega$	Angular frequency
$\omega$	Specific rate of dissipation
$\omega_k$	Angular velocity

### Other Symbols

$\Theta$	Granular temperature
$\nabla$	Vector operator in the Cartesian coordinates
$\nabla^2$	Laplacian operator in Cartesian coordinate
$\overline{(\ )}$	Spatial filtering

## Abbreviations

1D	One-dimensional
IDV	One-dimensional Vertical
2-D	Two Dimensional
3-D	Three Dimensional
CFD	Computational Fluid Dynamics
COMCOT	Cornell Multi-grid Coupled Tsunami Model
DAQ	Data Acquisition
DART	Deep-ocean Assessment and Reporting of Tsunamis
DBW	Dam Break Wave
DNS	Direct Numerical Simulation
FDM	Finite Difference Method
FEM	Finite Element Method
FPS	Frame Per Seconds
FVM	Finite Volume Method
GUI	Graphical User Interface
LBM	Lattice Boltzmann Method
LES	Large Eddy Simulation
MAC	Marker-and-Cell
MANIAC	Mathematical and Numerical Integrator and Computer
MWL	Mean Water Level
MOST	Method of Splitting Tsunami
MRS	Mean Reynolds-Stress Closure
MTE	Mean Turbulent Energy
MVF	Mean-Velocity Field Closure
MWL	Mean Water Level
NOAA	National Oceanic and Atmospheric Administration
NCTR	NOAA Center for Tsunami Research
NI	National Instrument
PISO	Pressure-Implicit with Splitting of Operators
PIV	Particle Image Velocimetry
PLIC	Piecewise Linear Interface Calculation
PMEL	Pacific Marine Environmental Laboratory

PTV	Particle Tracking Velocimetry
RANS	Reynolds-Averaged Navier-Stokes
RMSE	Root Mean Square Error
RNG	Re-Normalisation Group
SGS	Subgrid Scale
SIFT	Short-term Inundation Forecasting for Tsunamis
SLIC	Simple Line Interface Calculation
SPH	Smoothed Particle Hydrodynamics
SST	Shear Stress Transport
SW	Well-graded sandy soil
SWL	Still Water Level
TDMS	Technical Data Management Streaming
TIME	Tsunami Inundation Modelling Exchange
UDF	User-Defined Function
USCS	Unified Soil Classification System
VI	Virtual Instrument
VOF	Volume of Fluid

## **Acknowledgements**

My most profound appreciation to my Director of Studies, Dr Ravindra Jayaratne, and supervisor, Dr Ali Abbas, for their continuous support and guidance. I am deeply indebted to Dr Ravindra Jayaratne, for his patience, valuable insight and direction. He always inspired me to approach problems from a new perspective when stagnated. I am much inspired by his attitude to novelty and high quality of research. He provided work reference for me when needed and the opportunity to lecture within the University for three years. I would like to thank Dr Ali Abbas for his valuable suggestions which improved the approach to my methodology and interpretation of results.

My sincere gratitude for the huge input of Mr Neil Goodin and Mr Joe Kennedy, the senior technicians, who helped set up and provided training for the operations of the laboratory equipment and the fabrication of the models employed in the study. Also, I am grateful to Cheryl Wheeler for her computing help in setting up the required software for this project. I am thankful to Mrs Avinder Bhinder, Ms Charlotte Forbes and Mr Richard Bottoms for their administrative assistance during my study.

Dr Awan Nas Ruqiyabi made research methods a passion for doctoral students, not just a class or subject to teach. Her broad knowledge and guidance were helpful during the early period of my work. The lectures provided me the skills to adequately plan for the timely completion of my programme.

I owe thanks to Dr Laszlo Konozy and Dr Zeeshan Rana at Cranfield University for their advice on multiphase flow and turbulence modelling. I am grateful to Dr Martin Marriott, Dr John Walsh and Dr Darion Grant for their contributions during the annual monitoring reviews. My gratitude to Prof Hassan Abdalla for the approval of my continuous professional development training, which helped broaden my knowledge of Computational Fluid Dynamics.

My acknowledgement will not be complete without the unwavering support and sacrifice of my extended family. My lovely wife and son deserve appreciation for being my backbone during this study. I would not have accomplished this research without their understanding and love.

## Dedication

To my wife; *Olori mi*, Adenike, for her unwavering love and support to make this voyage a reality, without her endurance and continual encouragement, this work could not have been completed.

To my son; the beginning of my strength, Oluwadamilare, for the warmth, smile, and joy he brings to my heart; his face continually reminding me of the sacrifice I must make for his future.

To my parents and siblings for their continuous prayers, and support. Always bringing love so close, so familiar yet so sweet.

To Jesus Christ, The Author and Perfecter of my faith and destiny.



# Chapter 1

## Introduction

The giant strides that have been made recently in the study of a tsunami have been due to efforts to understand the complex phenomenon and mitigate the huge damages resulting from the event. These have led to the inclusion of the safety factors in building codes to cater for forces generated by tsunami bores, determination of tsunami impact overflowing pressure over coastal structures, development of different numerical models to comprehend the phenomenon and construction of various hard and soft engineering methods that are being employed to alleviate tsunami impact. Despite these, tsunami-induced scour around coastal structures, which caused the most significant damage in the 2011 Great Eastern Japan Earthquake and Tsunami (Fig. 1.1), has not been meticulously investigated while studies have only been limited to the investigation of scour processes around vertical cylinders and breakwaters, understanding of tsunami flow and the general failure patterns associated with coastal structures.

The surveys of the coastal defences and their environments carried out after the March 11 tsunami showed that the structures might have been designed for a storm surge incidence and a lower level tsunami category. Minimal to extensive damages of the structures were observed at many locations, including the formation of artificial pools in the landward region. Initial observations also revealed that local scour greatly influenced the damage to the landward slope.





Figure 1.1. Examples of damages caused by the 2011 Great Eastern Japan Earthquake and Tsunami (Jayaratne et al., 2013).

The aftermath of the catastrophic damages showed the need for improved structurally resilient coastal defences to a high-level tsunami phenomenon, as comprehensive understanding scour mechanism and associated instability to coastal structures are not yet adequately understood. The high cost of protecting the long stretch of foundation necessitates the study of scour depth and length to assess the risk of such failure (Karim and Ali, 2000). The study of the characteristics of scour holes development behind coastal defences can improve the understanding of their structural stability.

In the past, the primary approach to studying tsunami flows was experimental, and the turbulence in the surf zone is still one of the most challenging natural problems to any researcher in hydrodynamics or fluid mechanics, but with the development of more advanced measuring technology and more advanced numerical models, this hydrodynamics can now be studied in much more detail (Thao, 2007). Mikami et al. (2014) employed Large Eddy Simulation (LES) model in their numerical experiments to study the hydraulic characteristics of overflowing tsunamis around coastal dikes (velocity and pressure fields) and concluded that the structural survival of a coastal dike could depend on a milder landward slope and the construction of obstructions like secondary dikes and coastal forests.

The present research work focuses on carrying out laboratory experiments to analyse tsunami wave propagation, and tsunami-induced scour failure of coastal structures.

The results are then compared with the scour depth model predicted by Jayaratne et al. (2014). Also, a Reynolds-Averaged Navier-Stokes (RANS) turbulence model and a two-phase sediment transport model are employed to validate the laboratory findings numerically.

In this chapter, comprehensive background of the research, the aim and objectives of the study are provided. After that, the scope of the study is described, and the outline of the thesis presented.

## 1.1 Background of the Study

Kato et al. (2012) performed hydraulic model experiments and an extensive field survey along the coastlines of Amori and Chioba prefectures in Japan after the 2011 Tohoku tsunami and concluded that scouring at the leeward toe of the dikes was the dominant failure pattern. The experiment estimated that 49.2% of the eight failure patterns studied was because of scouring at the landward toe. It was against this backdrop that Abimbola (2013) and Jayaratne et al. (2014) employed mathematical modelling technique to develop a scour predictive model for a quasi-steady tsunami flow (Eq. 1 & Fig. 1.2) at University of East London. The model is based on results of field investigation carried out in Miyagi and Fukushima Prefectures of Japan, the maximum wave pressure formula developed by Mizutani and Imamura (2002 cited by Kato et al., 2007), and tsunami velocity model developed by Matsutomi et al. (2010). It applies to sediments with the coefficient of permeability (m/s),  $K$ , between  $10^{-4}$  and  $10^{-3}$ .

$$\frac{D_S}{H_{d2}} = \lambda \left( \exp\left(-\frac{\sqrt{H_{d2}}}{2\lambda\sqrt{h}\sin\theta_2}\right)^4 \right) \quad \left. \vphantom{\frac{D_S}{H_{d2}}} \right\} \quad h > 0 \quad (1)$$

where,  $D_S$  is the representative scour depth (m),  $\lambda$  is the scour coefficient (0.85),  $H_{d2}$  is the height of structure measured in leeward side (m),  $\theta_2$  is the angle of landward slope of coastal dike, and  $h$  is the inundation height (m).

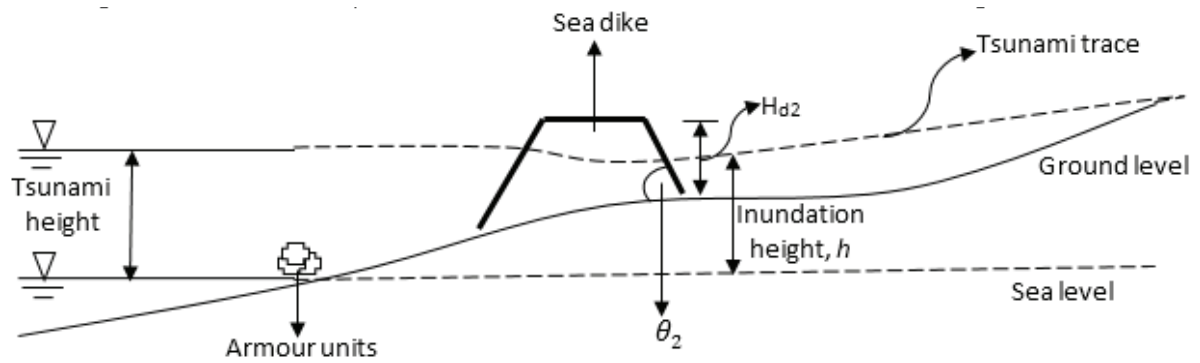


Figure 1.2. Representation of the Predictive Model Parameters.

## 1.2 Aim and Objectives of the Study

The primary aim of this research is to perform extensive small-scale laboratory experiments and numerical simulation to elucidate further the scour failure of coastal dikes due to tsunami wave attack. To meet the general aim of this research project, the study will focus on the following objectives:

- To develop a comprehensive experimental programme to study tsunami flow hydrodynamics and its associated hydro-sedimentary characteristics, to assess the extent of scour failure of coastal defences.
- To implement numerical methods to validate the experimental studies of tsunami propagation and tsunami-induced scour failure at the landward region of a coastal dike.
- To employ both laboratory and numerical data to improve the theoretical scour predictive model developed by Abimbola (2013).
- To use sediment transport theory to support evidence of the laboratory and numerical studies of tsunami-induced scour at the landward toe of the coastal dike.
- To propose viable resilient coastal defence structure to minimize structural damage for future Level 1 and 2 tsunami events (Shibayama et al., 2013).

### **1.3 The Scope of the Study**

The above discussion reveals the need to investigate tsunami wave flow and its induced scour, either by experimental studies or numerical simulations. Thus, this study attempts to improve understanding of these processes.

Experimental works are employed to study tsunami propagation and scour over four sea dikes models, of which two were modelled after some of the prototypes that were substantially damaged in Iwanuma and Soma cities of Japan by the 2011 Great East Japan Earthquake and Tsunami (Jayaratne et al., 2013). The hydrodynamic study was carried out by adopting a two-phase flow model in Ansys Fluent 18.0 to simultaneously solve the flow in both air and water phases. Flow variable results were then adapted into a two-phase flow solver; SedFoam- 2.0, to study the scour process. The experimental and numerical simulations were carried out to validate tsunami field results and results from existing tsunami studies.

### **1.4 Outline of Thesis**

The seven parts of this thesis begin with the introduction in Chapter 1. The other chapters are organised as follows:

Chapter 2 highlights the literature review of the study. The different classifications of water waves are presented, and this leads to the background studies of tsunami waves, including the past occurrences of the phenomenon and its damaging effects on humans and environment. Different recent experimental and numerical studies are detailed to reveal development in tsunami studies. An initial introduction to early history and development of numerical simulation is also included. Important descriptions of the basic theory of Computational Fluid Dynamics (CFD) and sediment transport mechanism that relate to this study.

Experimental studies and results of tsunami flow characteristics are presented in Chapter 3. The procedures for determining the velocities over the sea dikes and the configuration of a pressure analog input measurement are shown. The various pressure distributions over the four model sea dikes are discussed. Detailed analyses about the influence of model geometry, comparison to other tsunami wave studies and statistical comparison are presented.

In Chapter 4, the experimental studies of tsunami-induced scour profile on erodible boundaries are presented. Scour profiles characteristics derived from measurements are shown, including the validation of the possibility of scouring occurrence using Shields parameter. The steps for the derivation of the representative scour depth predictive model were shown, and the section for a coastal dike capable of resisting landward toe scour was proposed.

In Chapter 5, the RANS study of two-dimensional tsunami waves is discussed, and numerical validation of experimental study of tsunami wave propagation is presented. The boundary conditions, computational domain, and the solution procedure are also described. The various pressure distributions over the four model sea dikes are presented, and detailed analyses are carried out with appropriate conclusions provided.

Chapter 6 provides a numerical validation of experimental studies of tsunami-induced scour behind the sea dike models. The solver set-up, boundary conditions, computational domain, and the solution procedure are also described. The computer simulation results of the scour process for the two-phase flow as performed in SedFoam- 2.0 are presented.

In Chapter 7, the main findings and conclusions are summarised, while future work is discussed.

## Chapter 2

### Literature Review

#### 2.1 Introduction

The damaging impact of tsunami wave and the importance of a comprehensive understanding of the flow characteristics to help mitigate its detrimental human and socio-economic effect have been briefly discussed in the previous chapter. Over the years coastal engineers have devoted huge effort and capital in the design of robust structures against different wave classification. However, the initial literature review revealed that only very few studies had been conducted about proposing resilient structures against tsunami-induced scour in the leeward region of coastal structures. Early studies have primarily used physical models and mathematical models to understand the behaviour of several wave characteristics. The advent of faster computers in recent years have accelerated the development of turbulence and sediment transport models, to understand the fluctuating characteristics of turbulent flows and kinematic interaction between sediment particles.

In this review, aspect relating to water wave mechanics and background of experimental and numerical tsunami studies are discussed. The flooding and tsunami prevention measures for resilient coastal dike in Japan, early history and development of numerical simulation, basic Computational Fluid Dynamics (CFD) theories, and sediment transport mechanism as they pertain to the methodologies used in further chapters of this research are presented.

#### 2.2 Water Wave Mechanics

Isaac Newton first attempted the theory of water waves in the seventeenth century, and he deduced an inverse relationship between the frequency of deep-water waves and the square root of wavelength (Craik, 2004). Water waves are commonly understood within the phenomenon of ripples formed on the surface of a body of water because of disturbance caused by stones, winds, raindrops, or by the stir of a ship. It is also called gravity waves because its unsteady free surface flow is subjected to gravitational forces (Mader, 2004).

The complexity and various water wave motions make its classification difficult. According to Mader (2004), oscillatory and translatory waves are the two kinds of water waves based on the transportation of fluid. In translatory waves, transport of fluid occurs in the direction of wave travel, while mass movement of fluid is absent in oscillatory waves. Some examples of a translatory wave include waves generated by the breaking of a dam, tidal bore or moving hydraulic jump, flood waves in rivers and solitary waves. An oscillatory wave can be progressive or standing. The harmonic wave which is defined by a sine or cosine curve is the simplest case of a progressive wave. A standing wave can be considered as the superposition of two waves of the same amplitude and period, but travelling in opposite directions.

Waves can also be grouped based on their frequency and method of generation (Andersen and Frigaard, 2007). The phenomenon presented in the first group (Table 2.1) is characterised by changes in Mean Water Level (MWL) and not commonly referred to as waves.

Wave is also classified based on the depth of the water. Physical observation of water wave reveals that its particles disappear with depth. Particles get more agitated as they approach the shore than in the open sea. This classification is based on the ratio of wave depth,  $D$ , to wavelength,  $L$ . A wave is classified as a deep-water wave or short wave if  $\frac{D}{L} > 0.5$ , intermediate water waves if  $0.05 < \frac{D}{L} < 0.5$ , and shallow-water wave or long wave if  $\frac{D}{L} < 0.05$ .

Figure 2.1 shows the characteristics of a linear wave, where  $L = \frac{gT^2}{2\pi}$  is the wavelength,  $H$  is the wave height,  $a = \frac{H}{2}$  is the wave amplitude,  $D$  is the water depth referenced from the horizontal bed,  $\eta$  is the water surface elevation. Other important parameters are the wave celerity,  $C = \frac{L}{T}$ , angular wave number,  $K_w = \frac{2\pi}{L}$ , and angular frequency,  $\omega = \frac{2\pi}{T}$ , where  $T$  is the wave period.



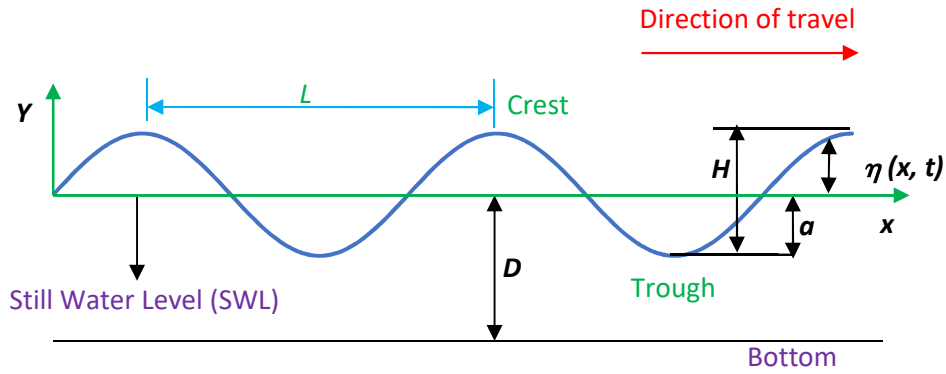


Figure 2.1: Characteristics of linear water wave.

Table 2.1. Wave classification (Andersen and Frigaard, 2007).

Phenomenon	Origin	Period
Surges.	Atmospheric pressure and wind.	1 - 30 days.
Tides.	Gravity forces from the moon and the sun.	Approximately 12 and 24 hours.
Barometric wave.	Air pressure.	1 - 20 hours.
Tsunami.	Earthquake, submarine landslide or submerged volcano.	5 - 60 minutes.
Seiches (Water level fluctuations in bays and harbour basins).	Resonance of long period wave components.	1 - 30 minutes.
Surf boat, mean water level fluctuations at the coast.	Wave groups.	0.5 - 5 minutes.
Swells.	Wave generated by a storm some distance away.	less than 40 seconds.
Wind generated waves.	Wind shear on the water surface.	less than 25 seconds.

It is known that water propagates as its particle moves in an oscillatory action, and the type of action depends on the depth of water. They move in a circular orbit in deep water, elliptical orbit in intermediate water and shallow water (Jayaratne, 2012). According to Kinsman (1965), for an oscillation to occur, there must be an equilibrium state, a disturbing force to disturb the equilibrium and a restoring force to re-establish the equilibrium. He further opined that gravity, surface tension, and Coriolis force are the three principal restoring forces associated with water wave propagation.

This subject of water wave classification would be needed as we focus more on tsunami wave in the following section.

## **2.3 Background of Tsunami Studies**

### **2.3.1 Tsunami**

'Tidal wave' and 'seismic wave' are two old imprecise terms that were generally referred to as tsunami because of the inaccurate understanding of its generation mechanisms. The former suggests the influence of movement of planetary bodies, while the latter only restricts its cause to an earthquake. Tsunami is a wave train generated by a vertical displacement of the water column. It is now acknowledged that this displacement can be generated by an earthquake, volcanic activity, meteorite impact, or landslide. The present study shall be limited to tsunami induced by seismic activity.

The National Oceanic and Atmospheric Administration, NOAA, on their website ([http://www.ngdc.noaa.gov/hazard/tsu\\_db.shtml](http://www.ngdc.noaa.gov/hazard/tsu_db.shtml)), provides details of tsunami events that date back to 2000 B.C in the Global Historical Tsunami Database. Recent tsunami occurrences; 2004 Indian Ocean Tsunami, 2010 and 2015 Chile Tsunami, 2011 Japan Tsunami, and 2013 Solomon Island Tsunami have led to the significant advances made theoretically, experimentally and in numerical studies to better understand the characteristics of tsunami.

Tsunami, like other waves, has a wavelength, wave height, amplitude, period and velocity. It is regarded as a shallow water wave because the wavelength is much longer than the water depth. Its wavelength is usually greater than 100 kilometres, and it depends on the depth of water,  $D$ , and wave period,  $T$ . It is expressed as  $L = T\sqrt{gD}$ . It can have variable wave height and amplitude that depends on water depth. A

tsunami can have a period in the range of five minutes to two hours as opposed to wind-generated waves of five to thirty seconds period. As a shallow water wave, its speed, acceleration due to gravity and water depth relationship,  $C = \sqrt{gd}$ , reveal that tsunami speed will reduce on approach to shore. The high speed coupled with low amplitude make tsunami virtually undetected by human eyes in the deep ocean. A tsunami can travel great distance because the rate at which it loses its energy is inversely related to its wavelength. Since a tsunami has a very large wavelength, it will lose little energy as it propagates. A tsunami will travel at high speeds with little loss of energy in very deep water because the change of total energy of a tsunami is constant.

According to Dias and Dutykh (2006), 'the life of tsunami is usually divided into three phases: the generation (tsunami source), the propagation and the inundation.' The most critical phase, inundation phase, which is associated with large amplitude change of the wave, depends significantly on the bottom bathymetry and the coastline type. The structural and human damages are mainly because of the inundation. The 2004 Indian Ocean Tsunami caused nearly 230,000 deaths and \$10 billion in damage, the 2010 Chile Tsunami resulted in over 156 deaths, \$30 billion damage, 2011 Japan Tsunami caused \$220 billion and over 17,000 deaths, and the 2013 Solomon Island Tsunami caused 10 deaths, 14 injuries, with damage and destruction of more than 700 houses (NOAA, 2014).

### 2.3.2 Experimental Studies

In many hydraulic experimentations, solitary waves have been used as an approximate wave type for tsunami representation, but Rossetto et al., (2011) used a new approach of wave generation to recreate seismic generated tsunami waves in a laboratory. This new concept makes use of a wave generator capable of recreating scaled tsunami waves. The wave generator can be used to reproduce solitary waves and N-waves with large wavelength.

A theoretical solitary wave is described by Miles (1980 cited by Rossetto et al., 2011) as:

$$\eta(x, t) = a \left( \operatorname{sech} \left( x - \frac{ct}{L} \right) \right)^2 \quad (2.1)$$

where,  $\eta$  is the surface elevation (m),  $x$  is the horizontal coordinate,  $t$  is time (s),  $a$  is the wave amplitude (m),  $C$  is the wave celerity (m/s),  $L$  is the wavelength (m), and  $\text{sech}$  is the hyperbolic secant function that defines the exponential behaviour of the wave in space and time.

Using a constant mass density, Le roux (2009) constructed a velocity-pressure; non-homogeneous Euler-like, model to discuss the formation of a tsunami wave. According to Mikami and Shibayama (2013), three types of method are used to generate a tsunami-like flow in a wave flume or numerical model - using a solitary wave, dam break method and a pump flow method. The 2011 Tohoku Earthquake and Tsunami gave rise to the widespread use of the pump flow method because of the ease of creating a prolonged overtopping flow, which the solitary wave method does not offer.

Mizutani and Imamura (2001) discovered that four types of wave pressure are generated by a tsunami wave force acting on a coastal structure: dynamic, sustained, impact standing and overflowing. The hydraulic experiments revealed that the impact standing and overflowing pressures generated the largest wave forces and should be given significant consideration when designing a coastal structure. They observed that the collision between reflected and incident waves generated the impact standing wave pressure, while the wave impact on the back of the structure generated the overflowing wave pressure. The overflowing pressure formulas generated by the study was confirmed by Kato et al. (2007) in their large-scale experiment to evaluate tsunami wave force on coastal dike by taking into consideration the effects of wave transformation and dike slope.

The devastating impact of leading bore during tsunami propagation had necessitated both experimental and numerical study into the inundation phase of the propagation (Fig. 2.2). Rueben et al. (2010) performed the optical measurements of a tsunami inundation through an urban waterfront in a laboratory wave basin. The physical model was designed to study the initial inundation zone along an urban waterfront and the effect of macro-roughness on the bore speed.

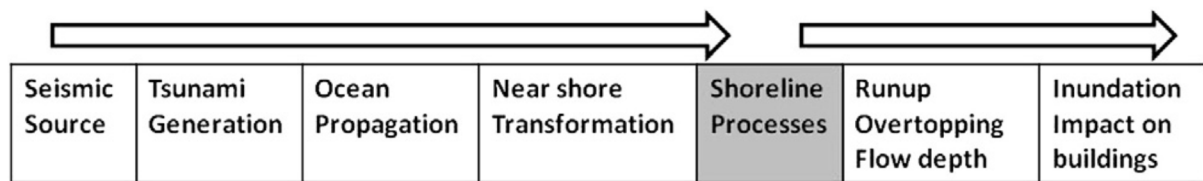


Figure 2.2. Phases of the evolution of a typical seismic generated tsunami from source to shore (Rossetto et al., 2011).

### 2.3.3 Numerical Studies.

COMCOT (Cornell Multi-grid Coupled Tsunami Model) offers the possibility of simultaneously calculating tsunami inundation and tsunami propagation in deep oceans. A nested grid system is adapted to balance its efficiency and accuracy. In this system, a modified leap-frog finite difference method is used to solve the linear or nonlinear shallow water equations (Li et al., 2012; Wang, 2009; Wijetunge, 2009).

TUNAMI-N2 model is based on the TUNAMI-N1 numerical code developed by Dr. Fumihiko Imamura of Tohoku University for the 1995 Tsunami Inundation Modelling Exchange (TIME) project. It was used to study tsunami propagation and its coastal amplification with different initial conditions. It was implemented to simulate tsunami propagation and run-up in Pacific, Atlantic and Indian Oceans, with emphasis around the Japanese, Caribbean, Russian and Mediterranean seas (Yalciner et al., 2004). It uses leap-frog finite difference scheme to discretize a set of nonlinear shallow water equations. A detailed description can be found in Imamura et al. (2006).

The TUNAMI-N2-NUS, a developed version of TUNAMI-N2 model, was developed by Dao and Tkalich (2007) for operational forecasting. It considers phenomena: sea bottom friction, dispersion, spherical curvature, astronomical tide and Coriolis force, which could affect tsunami dynamics.

The MOST (Method of Splitting Tsunami) model developed by Titov of Pacific Marine Environmental Laboratory (PMEL) and Synolakis of University of Southern California is used at the NOAA Centre for Tsunami Research (NCTR) and is capable of simulating three processes of tsunami evolution: earthquake, transoceanic propagation, and inundation of dry land (NOAA Centre for Tsunami Research, 2014). This is the model currently used in the operational tool called SIFT, Short-term Inundation Forecasting for Tsunamis. The NCTR developed this tool for real-time forecasting of actual tsunamis. It involves the gathering of information needed for

tsunami modelling from several observatory systems – seismic network, Deep-ocean Assessment and Reporting of Tsunamis (DART) and coastal tide gauges – to provide inundation forecast; tsunami arrival time and amplitudes and tsunami impact at specific coastal areas during an event (Titov et al., 2001). According to Gica et al. (2007), the system is more than an operational tool as it can also be used for hazard assessment studies by generating and studying different tsunami scenarios.

## **2.4 Flooding and Tsunami Mitigation Measures for Resilient Coastal Dike in Japan**

Dike is usually reconstructed natural ridge or artificial wall built along the banks of stream, river, lake or other bodies of water, primarily for regulation of water levels or flood prevention. Sea dike, also known as embankment, dike or levee, provides socioeconomic and environmental benefits. The benefits include:

- Protection of hinterland or coastal zones to generate revenue from tourism.
- Prevention of high damage cost as a result flooding caused by sea level rise.
- It can be restored quickly if damaged by flood, earthquake, tsunami or other disasters.
- Protection against high water pressure, wind current and storm surges to minimize adverse impacts.
- Its durability suggests that it can last for thousands of years if maintained adequately.
- It can be improved easily if the scale of flood control plan is to be increased.

These benefits are achievable because of the structural design of sea dike components. The high density helps resist high water pressure, sloping sides help reduce wave impact, and in some instances, the crest heights help prevent excessive wave overtopping.

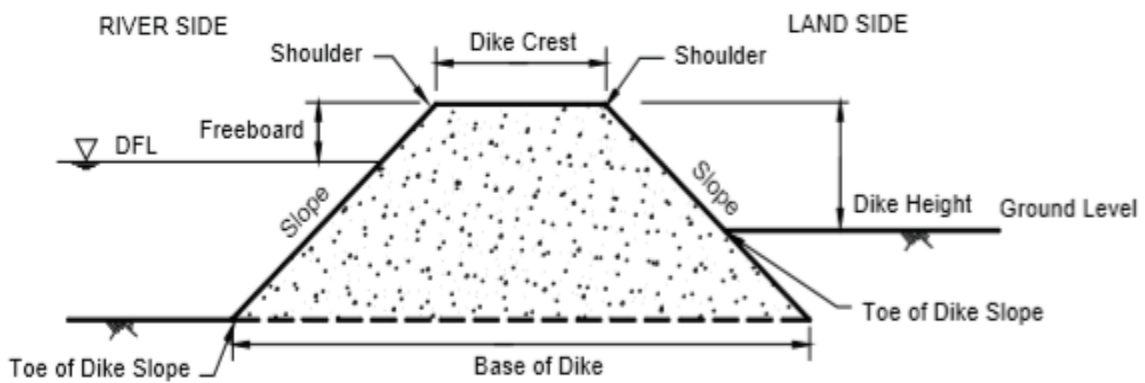


Figure 2.3. Parts of a dike (Japan International Cooperation Agency, 2010).

According to Japan International Cooperation Agency (2010), the technical standards and guidelines for sea dike include:

- The crest width of the dike shall be based on the design flood discharge in Table 2.2 and should be designed for multi-purpose use, such as for patrolling during floods and in the execution of emergency flood prevention works.

Table 2.2. Crest width of a dike (Japan International Cooperation Agency, 2010).

Design flood discharge, Q (m <sup>3</sup> /sec)	Crest Width (m)
Less than 500	3
500 and up to 2,000	4
2,000 and up to 5,000	5
5,000 and up to 10,000	6
10,000 and over	7

- The slope of the dike should be at least lesser than 2:1. However, it could be steeper than 2:1 when a revetment covers the surface of the dike. When the crest height from riverbed is higher than 6 m, the slope of the dike shall be gentler than 3:1. A slope of 4:1 is usually used for a dike consisting of sand and shall be protected by providing at least 300 mm thick cover of sod.

- A berm width of at least 3 m shall be provided along the slope for stability, repair and maintenance purposes if the dike height is more than 5 m.
- Freeboard is the margin from the design flood level up to the elevation of the dike crest. It is designed based on the design flood discharge which shall not be less than the value given in Table 2.3.

Table 2.3. Minimum required freeboard (Japan International Cooperation Agency, 2010).

<b>Design flood discharge Q (m<sup>3</sup>/s)</b>	<b>Freeboard (m)</b>
Less than 200	0.6
200 and up to 500	0.8
500 and up to 2,000	1.0
2,000 and up to 5,000	1.2
5,000 and up to 10,000	1.5
10,000 and over	2.0

Raby et al. (2015) reported about the revisions that have been made to the technical standards, manuals and design guidelines of coastal structures in Japan. These revisions followed the 2011 Great Eastern Japan Earthquake from various site surveying activities, laboratory and numerical studies of failed coastal structures conducted by researchers. Figure 2.4 shows the evolution of these documents following the 2011 event.



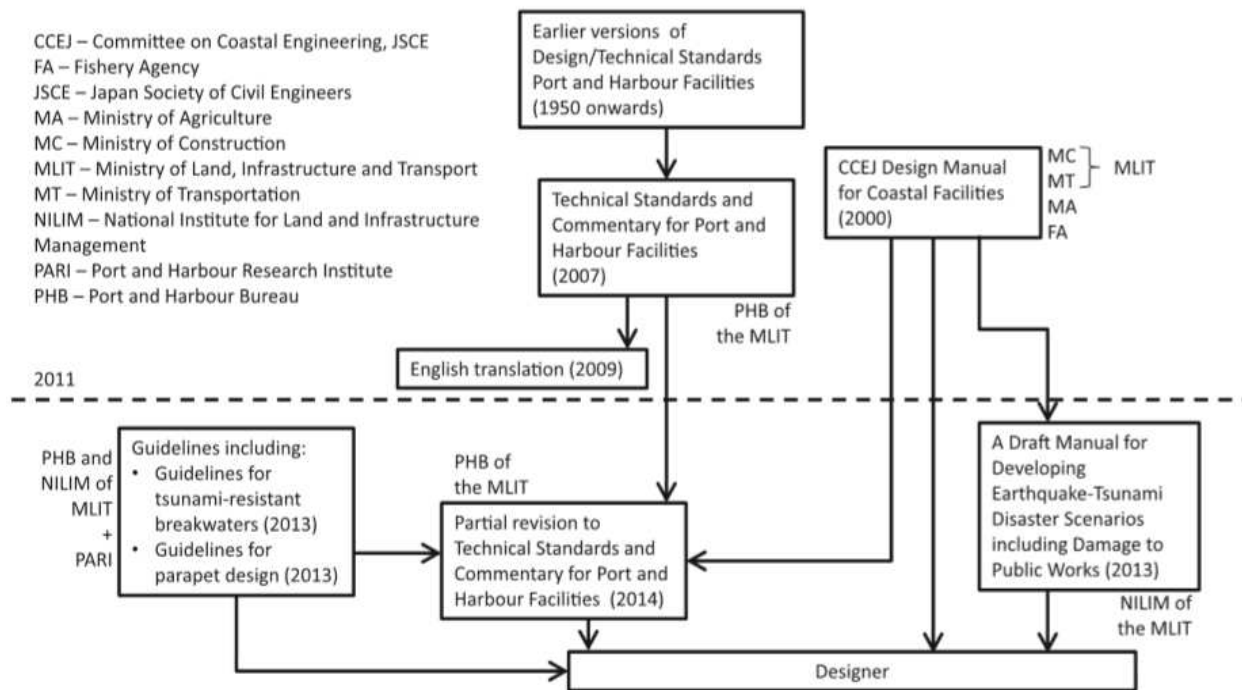


Figure 2.4. Evolution of official Japanese design guidelines following the 2011 Great Eastern Japan Earthquake (Raby et al., 2015).

In 2013, the Coastal Management Review Committee released proposals for coastal management. These were to update the 1999 Seacoast Law, by including lessons from the 2011 Great Eastern Japan Earthquake and the gradual deterioration of coastal protection infrastructure (Suwa and Watanabe, 2014). A disaster mitigation measure of integrating green embankment with resilient coastal dikes was proposed, to reduce inland flood heights and delay wave overtopping for safe evacuation (Fig. 2.5). This system can be sustained for a thousand year through maintenance of the structural measure.

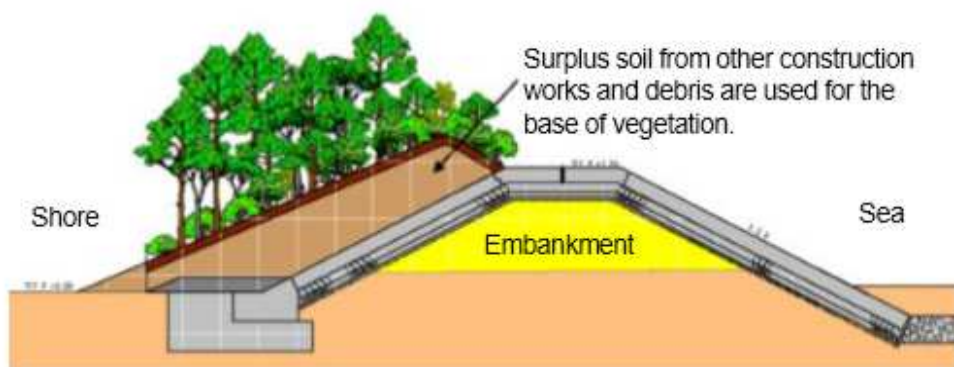


Figure 2.5. Integration of trees with coastal dike (Torii, 2014).

Two levels of a tsunami were established following the 2011 Great Eastern Japan Earthquake. Level 1 tsunami is more frequent with a return period of several decades to few hundred years and has lower inundation height between 7 and 10 m. Level 2 is less frequent with a return period of several hundred years to a few thousand years and has inundation height greater than 10 m. The countermeasures for Level 1 tsunami focus on hard or structural measures such as coastal dikes and breakwaters, while countermeasures for Level 2 focus on soft or non-structural measures such as tsunami evacuation systems. In 2011 the 'Law for Development of Tsunami Disaster Prevention Regions' was established, and it combines the hard and soft measures for the tsunami disaster prevention (Torii, 2014).

Water penetration into a coastal dike and tsunami wave overtopping result in increased saturation of the main body and scouring on the landward side. The 2011 report by the Expert Examination Committee of Central Disaster Prevention Council following the Tohoku Earthquake and Tsunami presents the scour prevention by using back bottom slope protection works and prevention of washout by securing member thickness of back slope covering works as some of the structural measures for a tsunami resilient coastal dike (Suwa, Kato and Hatogai, 2013).

Hydraulic model experiments were conducted by the River Department of National Institute for Land and Infrastructure Management, in conjunction with the Coast Division of Water and Disaster Management Bureau and Tohoku Regional Bureau to reflect changes needed to improve the structural design. Extracts of the results of the study were published by Kato et al. (2012) and Figure 2.6 reveals some of the main observations from the experiments. The use of soil stabilisation technique and foundation work to secure the flat ground of landward bottom slope to keep the scour away from the main body of the dike. The unevenness of the landward slope should be avoided to reduce the effect of hydrodynamic force and destabilisation effect. Also, the use of a single covering block for the crown and landward slope should be avoided to prevent the uplift and destabilisation effects of the negative pressure.

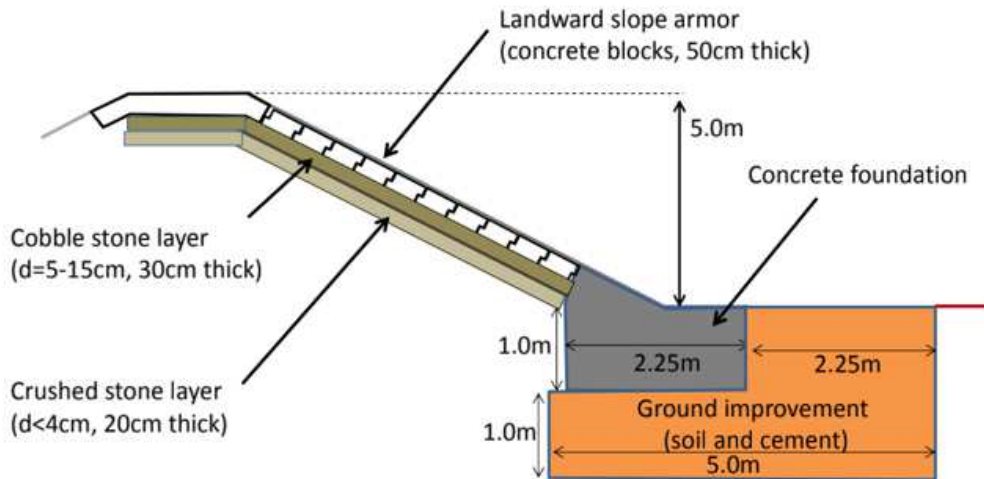


Figure 2.6. Proposed resilient structure for coastal dike (Kato et al., 2012).

## 2.5 Early History and Development of Numerical Simulation

The advent of the computer MANIAC I, the Mathematical and Numerical Integrator and Computer, on March 15, 1952, at Los Alamos, heralded the significant development of numerical simulation to complement theoretical approaches (Viot, 2016). Lilly (1967) defined simulation as the ‘direct numerical time integration of hydrodynamic equations as initial value-boundary problems.’ Fromm and Harlow (1963) employed a high-speed computer for the numerical simulation of a non-linear equation of incompressible flow motion to study the development of vortex street behind a plate. The range of the Reynolds-number, between 15 and 6000, was significantly higher than the 40 to 100 Reynolds-number employed by Hirota and Miyakoda (1964) to investigate a 2-D non-steady flow around a circular cylinder. About this time, numerical simulation was being successfully applied in the fields of meteorology and aerodynamics.

Joseph Smagorinsky, the first director of National Oceanic and Atmospheric Administration (NOAA), first proposed large eddy simulation, LES, for dynamic study of atmospheric flow (Smagorinsky, 1963). Two-dimensional transport properties were popularly considered, and turbulence was not given enough detail, or it was at best treated by non-detailed approximations to simplify the numerical simulation problem. At the time, the numerical resolution of all relevant scales for large Reynolds number was thought impossible and the application of averaging operator to the governing transport equations to filter out the subgrid scale (SGS) motions was employed by

many meteorologists for 2-D atmospheric flows and was met with much success (Smagorinsky, Manabe and Halloway 1965; Mintz 1965).

Lilly (1967) described two models that considered the effects of 3-D transport of turbulence in a 2-D model which he thought would be useful with coarser spatial resolution. He suggested the possibility of only simulating the important effects of the third dimension and the effects of molecular viscosity and diffusion on real fluid without computing motions on all scales. He further opined that the general assumption that the small scales motions are unimportant in quasi 2-D flows is inaccurate because kinetic energy in these motions may interact with those of large scales in diverse ways. He thereby concluded that integration over a 3-D region with sufficient resolution must be employed in the simulation of turbulent flows to include both large and small scales. Williams (1968) described a method of numerically integrating the Navier-Stokes equation, in cylindrical polar co-ordinates form, for the study of 3-D incompressible thermal convection. A description of how to neutralise the computational instability of convection terms, time differencing, diffusion terms, boundary conditions and truncation errors associated with the finite difference forms of the Navier-Stokes equations were examined. Sakamoto and Matsuo (1979) employed both LES (called Deardoff's model) and two-equation model to predict 3-D isothermal flow in a ventilated room and compared results to experimental outputs. The difference between both models in the prediction of the distribution of mean velocity, which is the first requirement in many practical predictions of air flow in a confined space, is not so large and so they favoured the latter model because it gave solutions in shorter computer time.

The application of LES to other engineering related flows became more pronounced in the 1970s. Deardoff (1970) described a 3-D numerical model for the study of turbulent flow at large Reynolds numbers within a channel and proposed ways to improve the reliability and accuracy of the model. One of such ways is to modestly increase the numerical resolution and size of the region being modelled, which will be dependent on the computational speed of the computer. Reynolds (1974) computed turbulent flows by employing Mean Turbulent Energy (MTE) Closure, Mean Reynolds-Stress (MRS) Closure, and Mean-Velocity Field (MVF) Closure which assumes that turbulence adjusts to the changing average conditions and that a universal relationship exists between turbulent stresses and average strain rates. Schumann (1975)

employed the finite difference schemes and the subgrid scale (SGS) motion model to simulate high Reynolds number turbulent flows of incompressible fluids to obtain detailed space and time velocity and pressure components. Shih et al. (1995) developed an improved  $k-\epsilon$  eddy viscosity model for different complex turbulent flows.

There are increased numbers of published articles on numerical simulation using varied turbulence models in Journals and conference papers. The various turbulence models research groups and availability of CFD software packages to perform numerical studies have all contributed to its development and applicability.

## **2.6 Computational Fluid Dynamics (CFD) Theory**

Experimental and theoretical developments have been the major approaches in the field of fluid dynamics since the 17<sup>th</sup> century. The limitations of both developments to completely interpret and understand complex real-life scenarios necessitated the development of computational fluid dynamics. It is the third balancing approach of the trinity of study. The CFD has application in the manufacturing, automobile and aerospace industries to improve understanding of physical flow processes for better design and enhanced performance of different mechanical parts. It offers various advantages: low cost against expensive set up of physical experiments, fast speed of information execution and generation of large results at a single instance, simulate ideal and complex scenarios that cannot be physically examined in a laboratory. The reliance on physical models for validation and presence of numerical errors are some of the limitations of CFD.

Computational fluid dynamics, CFD, is the combination of computers and numerical techniques to solve fluid flow problems. The governing principles of fluid flow; Newton's second law of motion, conservation of mass and energy, are mathematically presented in integral or partial differential equations. These are then discretised using numerical methods to algebraic forms, which are then solved to obtain the quantitative space-time flow field values.

The generic discretisation schemes are finite difference method (FDM), finite volume method (FVM) and finite element method (FEM). The application software employed in this study uses the FVM. The domain would be discretized into cells on which the finite volume method would be employed to transform governing equations of fluid flow into algebraic forms which are then solved to derive the flow field variables. This

method is based on the approximation of integral form of conservation laws for small control volumes that are defined by computer-generated mesh. The governing equations are integrated on each control volumes to construct algebraic equations for unknown discrete dependent flow variables.

### 2.6.1 Navier-Stokes Equations

The Navier-stokes equations are nonlinear partial differential equations. A solution to these equations is called a velocity field of the flow field, as it describes the velocity of the fluid at given point in space and time. The continuity equation describes the mass conservation.

The continuity equation,

$$\frac{\partial \rho}{\partial t} + \nabla \cdot (\rho V) = 0 \quad (2.2)$$

Momentum equations (the Navier-Stokes equations),

X component,

$$\frac{\partial(\rho u)}{\partial t} + \nabla \cdot (\rho u V) = -\frac{\partial \rho}{\partial x} + \frac{\partial \tau_{xx}}{\partial x} + \frac{\partial \tau_{yx}}{\partial y} + \frac{\partial \tau_{zx}}{\partial z} + \rho f_x \quad (2.3)$$

Y component,

$$\frac{\partial(\rho v)}{\partial t} + \nabla \cdot (\rho v V) = -\frac{\partial \rho}{\partial y} + \frac{\partial \tau_{xy}}{\partial x} + \frac{\partial \tau_{yy}}{\partial y} + \frac{\partial \tau_{zy}}{\partial z} + \rho f_y \quad (2.4)$$

Z component,

$$\frac{\partial(\rho w)}{\partial t} + \nabla \cdot (\rho w V) = -\frac{\partial \rho}{\partial z} + \frac{\partial \tau_{xz}}{\partial x} + \frac{\partial \tau_{yz}}{\partial y} + \frac{\partial \tau_{zz}}{\partial z} + \rho f_z \quad (2.5)$$

The variables  $f$  denotes the body forces on the fluid element;  $t$  time;  $\rho$  the density; velocity component  $V = u \mathbf{i} + v \mathbf{j} + w \mathbf{k}$ , where  $\mathbf{i}$ ,  $\mathbf{j}$  and  $\mathbf{k}$  are unit vectors along the  $x$ ,  $y$  and  $z$ -axes respectively;  $\tau$  is the viscous stresses;  $\nabla \equiv \mathbf{i} \partial/\partial x + \mathbf{j} \partial/\partial y + \mathbf{k} \partial/\partial z$  is the vector operator in the Cartesian coordinates.

The governing equations above (2.2 to 2.5) change for incompressible flows where the density is almost constant ( $\frac{\partial \rho}{\partial t} = 0$ ). These can be represented as follows:

Continuity equation,

$$\nabla \cdot V = 0 \quad (2.6)$$

Momentum equations (the Navier-Stokes equations),

x component,

$$\rho \frac{Du}{Dt} = -\frac{\partial \rho}{\partial x} + \mu \nabla^2 u + \rho f_x \quad (2.7)$$

y component,

$$\rho \frac{Dv}{Dt} = - \frac{\partial p}{\partial y} + \mu \nabla^2 v + \rho f_y \quad (2.8)$$

z component,

$$\rho \frac{Dw}{Dt} = - \frac{\partial p}{\partial z} + \mu \nabla^2 w + \rho f_z \quad (2.9)$$

$D/Dt \equiv \partial/\partial t + u \partial/\partial x + v \partial/\partial y + w \partial/\partial z$  the substantial derivative in Cartesian coordinates;  $\nabla^2 \equiv \partial^2/\partial x^2 + \partial^2/\partial y^2 + \partial^2/\partial z^2$  is the Laplacian operator in Cartesian coordinate; the dynamic viscosity  $\mu$  has been treated as a constant in obtaining the components of the momentum equations (2.7 to 2.9).

### 2.6.2 Reynolds-Averaged Navier-Stokes Equations

The idea was first proposed by Reynolds (1895). Time-averaging the continuity, and Navier-Stokes equations can derive the equations for average turbulent flow. The instantaneous value of a variable is decomposed into the steady and fluctuating components. Using Figure 2.7, the instantaneous velocity component,  $u$ , is decomposed into a steady term,  $\bar{u}$ , and a fluctuating term,  $u'$ .

$$u = \bar{u} + u' \quad (2.10)$$

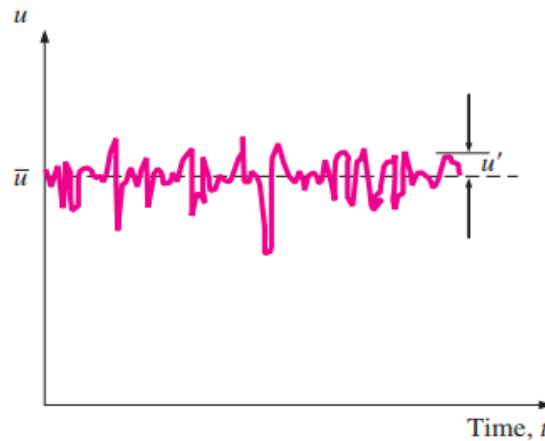


Figure 2.7. Variation of a velocity component,  $u$ , in turbulent flow (Cengel and Cimbala, 2014).

The time-averaged value of the steady component velocity,  $\bar{u}$ , is defined by;

$$\bar{u} = \bar{u} = \lim_{T \rightarrow \infty} \frac{1}{T} \int_{t_0}^{t_0+T} u dt \quad (2.11)$$

The time-averaged value of the fluctuating component,  $u'$ , are defined to be zero;  $\overline{u'} = 0$

Time-averaging the continuity equation (2.6) gives;

$$\overline{\frac{\partial \bar{u}}{\partial x} + \frac{\partial u'}{\partial x} + \frac{\partial \bar{v}}{\partial y} + \frac{\partial v'}{\partial y} + \frac{\partial \bar{w}}{\partial z} + \frac{\partial w'}{\partial z}} = 0 \quad (2.12)$$

$$\frac{\partial \bar{u}}{\partial x} + \frac{\partial \bar{v}}{\partial y} + \frac{\partial \bar{w}}{\partial z} = 0 \quad (2.13)$$

Time-averaging the x-component of the Navier-Stokes equation (2.7)

$$\begin{aligned} & \overline{\rho \left\{ \frac{\partial(\bar{u} + u')}{\partial t} + \frac{\partial(\bar{u} + u')^2}{\partial x} + \frac{\partial(\bar{u} + u')(\bar{v} + v')}{\partial y} + \frac{\partial(\bar{u} + u')(\bar{w} + w')}{\partial z} \right\}} \\ & = -\overline{\frac{\partial(\bar{p} + p')}{\partial x}} + \mu \left\{ \frac{\partial^2(\bar{u} + u')}{\partial x^2} + \frac{\partial^2(\bar{u} + u')}{\partial y^2} + \frac{\partial^2(\bar{u} + u')}{\partial z^2} \right\} + \rho f_x \end{aligned} \quad (2.14)$$

$$\begin{aligned} & \rho \left\{ \frac{\partial \bar{u}}{\partial t} + \frac{\partial \bar{u}\bar{u}}{\partial x} + \frac{\partial \bar{u}'u'}{\partial x} + \frac{\partial \bar{u}\bar{v}}{\partial y} + \frac{\partial \bar{u}'v'}{\partial y} + \frac{\partial \bar{u}'w'}{\partial z} + \frac{\partial \bar{u}\bar{w}}{\partial z} \right\} \\ & = -\frac{\partial \bar{p}}{\partial x} + \mu \left\{ \frac{\partial^2 \bar{u}}{\partial x^2} + \frac{\partial^2 \bar{u}}{\partial y^2} + \frac{\partial^2 \bar{u}}{\partial z^2} \right\} + \rho f_x \end{aligned} \quad (2.15)$$

$\rho f_x$  is not subject to turbulent fluctuation.

x component:

$$\rho \left\{ \frac{\partial \bar{u}}{\partial t} + \bar{u} \frac{\partial \bar{u}}{\partial x} + \bar{v} \frac{\partial \bar{u}}{\partial y} + \bar{w} \frac{\partial \bar{u}}{\partial z} \right\} = -\frac{\partial \bar{p}}{\partial x} + \rho f_x + \mu \nabla^2 \bar{u} - \rho \left\{ \frac{\partial \bar{u}'u'}{\partial x} + \frac{\partial \bar{u}'v'}{\partial y} + \frac{\partial \bar{u}'w'}{\partial z} \right\} \quad (2.16)$$

y component;

$$\rho \left\{ \frac{\partial \bar{v}}{\partial t} + \bar{u} \frac{\partial \bar{v}}{\partial x} + \bar{v} \frac{\partial \bar{v}}{\partial y} + \bar{w} \frac{\partial \bar{v}}{\partial z} \right\} = -\frac{\partial \bar{p}}{\partial y} + \rho f_y + \mu \nabla^2 \bar{v} - \rho \left\{ \frac{\partial \bar{u}'v'}{\partial x} + \frac{\partial \bar{v}'v'}{\partial y} + \frac{\partial \bar{v}'w'}{\partial z} \right\} \quad (2.17)$$

z component;

$$\rho \left\{ \frac{\partial \bar{w}}{\partial t} + \bar{u} \frac{\partial \bar{w}}{\partial x} + \bar{v} \frac{\partial \bar{w}}{\partial y} + \bar{w} \frac{\partial \bar{w}}{\partial z} \right\} = -\frac{\partial \bar{p}}{\partial z} + \rho f_z + \mu \nabla^2 \bar{w} - \rho \left\{ \frac{\partial \bar{u}'w'}{\partial x} + \frac{\partial \bar{v}'w'}{\partial y} + \frac{\partial \bar{w}'w'}{\partial z} \right\} \quad (2.18)$$

Or in Tensor notation:



$$\rho \frac{D\bar{u}_i}{Dt} = -\frac{\partial \bar{p}}{\partial x_i} + \rho f_i + \mu \nabla^2 \bar{u}_i - \rho \left\{ \frac{\partial \overline{u_i' u_j'}}{\partial x_j} \right\} \quad (2.19)$$

$$\rho \frac{D\bar{u}_i}{Dt} = -\frac{\partial \bar{p}}{\partial x_i} + \rho f_i + \mu \frac{\partial}{\partial x_j} \left\{ \frac{\partial \bar{u}_i}{\partial x_j} \right\} - \rho \frac{\partial}{\partial x_j} \left\{ \overline{u_i' u_j'} \right\} \quad (2.20)$$

$$\rho \frac{D\bar{u}_i}{Dt} = -\frac{\partial \bar{p}}{\partial x_i} + \rho f_i + \frac{\partial}{\partial x_j} \left\{ \mu \frac{\partial \bar{u}_i}{\partial x_j} - \rho \overline{u_i' u_j'} \right\} \quad (2.21)$$

where,  $\mu \frac{\partial \bar{u}_i}{\partial x_j} - \rho \overline{u_i' u_j'}$  is the total shear stress,  $T_{ij}$ .

$-\rho \overline{u_i' u_j'}$  is termed the Reynolds stress and its approximation or solution is needed for the closure of the equation.

The eddy viscosity principle by Boussinesq (1877) is still the basis of many turbulence models (Tables 2.4 and 2.5) and leads equation (2.21) to;

$$\rho \frac{D\bar{u}_i}{Dt} = -\frac{\partial \bar{p}}{\partial x_i} + \rho f_i + \frac{\partial}{\partial x_j} T_{ij}. \quad (2.22)$$

where,  $T_{ij} = \mu \frac{\partial \bar{u}_i}{\partial x_j} + \rho \left\{ \mu_t \left( \frac{\partial \bar{u}_i}{\partial x_j} + \frac{\partial \bar{u}_j}{\partial x_i} \right) - \frac{2}{3} k \delta_{ij} \right\}$ ;

$-\rho \overline{u_i' u_j'} = \rho \left\{ \mu_t \left( \frac{\partial \bar{u}_i}{\partial x_j} + \frac{\partial \bar{u}_j}{\partial x_i} \right) - \frac{2}{3} k \delta_{ij} \right\}$  and,  $-\overline{u_i' u_j'} \equiv 2\mu_t S_{ij} - \frac{2}{3} k \delta_{ij}$

where,  $\mu_t$  is the turbulent eddy viscosity; a proportionality factor that depends on the degree of turbulence, and the Kronecker delta,  $\delta_{ij}$ , ensures the validity of equation for normal tension. The turbulent kinetic energy  $k$  is defined by:

$$k = \frac{1}{2} (\overline{u^2} + \overline{v^2} + \overline{w^2}) \quad (2.23)$$

Table 2.4. RANS turbulence model description (ANSYS, 2006).

Model	Description
<b>Spalart – Allmaras</b>	A single transport equation model solving directly for a modified turbulent viscosity. Designed specifically for aerospace applications involving wall-bounded flows on a fine near-wall mesh. FLUENT's implementation allows the use of coarser meshes. Option to include strain rate in k production term improves predictions of vortical flows.
<b>Standard k-ε</b>	The baseline two-transport-equation model solving for k and ε. This is the default k-ε model. Coefficients are empirically derived; valid for fully turbulent flows only. Options to account for viscous heating, buoyancy, and compressibility are shared with other k-ε models.
<b>RNG k-ε</b>	A variant of the standard k-ε model. Equations and coefficients are analytically derived. Significant changes in the ε equation improves the ability to model highly strained flows. Additional options aid in predicting swirling and low Reynolds number flows.
<b>Realizable k-ε</b>	A variant of the standard k-ε model. Its "realizability" stems from changes that allow certain mathematical constraints to be obeyed which ultimately improves the performance of this model.
<b>Standard k-ω</b>	A two-transport-equation model solving for k and ω, the specific dissipation rate ( $\epsilon / k$ ) based on Wilcox (1998). This is the default k-ω model. Demonstrates superior performance for wall-bounded and low Reynolds number flows. Shows potential for predicting transition. Options account for transitional, free shear, and compressible flows.
<b>SST k-ω</b>	A variant of the standard k-ω model. Combines the original Wilcox model for use near walls and the standard k-ε model away from walls using a blending function. Also limits turbulent viscosity to guarantee that $\tau_T \sim k$ . The transition and shearing options are borrowed from standard k-ω. No option to include compressibility.
<b>Reynolds Stress</b>	Reynolds stresses are solved directly using transport equations, avoiding isotropic viscosity assumption of other models. Use for highly swirling flows. Quadratic pressure-strain option improves performance for many basic shear flows.

Table 2.5. RANS turbulence model behaviour and usage (ANSYS, 2006).

Model	Behavior and Usage
<b>Spalart-Allmaras</b>	Economical for large meshes. Performs poorly for 3D flows, free shear flows, flows with strong separation. Suitable for mildly complex (quasi-2D) external/internal flows and boundary layer flows under pressure gradient (e.g. airfoils, wings, airplane fuselages, missiles, ship hulls).
<b>Standard <math>k-\epsilon</math></b>	Robust. Widely used despite the known limitations of the model. Performs poorly for complex flows involving severe pressure gradient, separation, strong streamline curvature. Suitable for initial iterations, initial screening of alternative designs, and parametric studies.
<b>RNG <math>k-\epsilon</math></b>	Suitable for complex shear flows involving rapid strain, moderate swirl, vortices, and locally transitional flows (e.g. boundary layer separation, massive separation, and vortex shedding behind bluff bodies, stall in wide-angle diffusers, room ventilation).
<b>Realizable <math>k-\epsilon</math></b>	Offers largely the same benefits and has similar applications as RNG. Possibly more accurate and easier to converge than RNG.
<b>Standard <math>k-\omega</math></b>	Superior performance for wall-bounded boundary layer, free shear, and low Reynolds number flows. Suitable for complex boundary layer flows under adverse pressure gradient and separation (external aerodynamics and turbomachinery). Can be used for transitional flows (though tends to predict early transition). Separation is typically predicted to be excessive and early.
<b>SST <math>k-\omega</math></b>	Offers similar benefits as standard $k-\omega$ . Dependency on wall distance makes this less suitable for free shear flows.
<b>Reynolds Stress</b>	Physically the most sound RANS model. Avoids isotropic eddy viscosity assumption. More CPU time and memory required. Tougher to converge due to close coupling of equations. Suitable for complex 3D flows with strong streamline curvature, strong swirl/rotation (e.g. curved duct, rotating flow passages, swirl combustors with very large inlet swirl, cyclones).

### 2.6.3 $k-\epsilon$ Turbulence Model

The  $k-\epsilon$  turbulence model is a two-equation model which is based on the Boussinesq eddy viscosity assumption that proportionality exists between Reynolds stress tensor,  $T_{ij}$ , and mean strain rate tensor,  $S_{ij}$ . This assumption permits the introduction of scalar quantities like the turbulent kinetic energy,  $k$ , and turbulent dissipation,  $\epsilon$ , and to relate these to intuitive quantities like turbulence length scale,  $l$ , and turbulence intensity,  $I$ . There are many formulations of  $k-\epsilon$  models, however only standard and realisable models are discussed herein because of their employment in this study.

#### 2.6.3.1 Standard $k-\epsilon$ Model

This is a semi-empirical model proposed by Launder and Spalding (1972) for fully turbulent flow. It is based on two transport equations for the turbulent kinetic energy,  $k$ , and turbulent dissipation,  $\epsilon$ . The transport equation for turbulent kinetic energy is derived from the exact equation while the transport equation for the turbulent

dissipation,  $\varepsilon$ , is limited in its mathematical accuracy. It falls under the classical turbulence modelling techniques and has extensive use for many practical industrial flow and heat transfer problems.

Turbulent kinetic energy,  $k$

$$\frac{\partial}{\partial t}(\rho k) + \frac{\partial}{\partial x_i}(\rho k u_i) = \frac{\partial}{\partial x_j} \left[ \left( \mu + \frac{\mu_t}{\sigma_k} \right) \frac{\partial k}{\partial x_j} \right] + p_k + p_b - \rho \varepsilon - Y_M + S_k \quad (2.24)$$

Turbulent dissipation,  $\varepsilon$

$$\frac{\partial}{\partial t}(\rho \varepsilon) + \frac{\partial}{\partial x_i}(\rho \varepsilon u_i) = \frac{\partial}{\partial x_j} \left[ \left( \mu + \frac{\mu_t}{\sigma_\varepsilon} \right) \frac{\partial \varepsilon}{\partial x_j} \right] + c_{1\varepsilon} \frac{\varepsilon}{k} (P_k + c_{3\varepsilon} P_b) - c_{2\varepsilon} \rho \frac{\varepsilon^2}{k} + S_\varepsilon \quad (2.25)$$

Dilatation dissipation  $Y_M$

This term describes the effect of compressibility on turbulence for high-Mach-number flows. It is ignored in modelling of incompressible fluid flows.

$$Y_M = 2\rho \varepsilon M_t^2 \quad (2.26)$$

The turbulent Mach number,  $M_t = \sqrt{\frac{k}{a^2}}$ , where the speed of sound,  $a \equiv \sqrt{\gamma R T}$  ( $R$  is the gas constant =  $2.87 \times 10^6 \text{ cm}^2\text{s}^{-2}\text{K}^{-1}$ ,  $T$  is the temperature and  $\gamma$  is the heat capacity ratio)

Turbulent eddy viscosity,  $\mu_t$

$$\mu_t = \rho c_\mu \frac{k^2}{\varepsilon} \quad (2.27)$$

Production of  $k$ ,  $P_k$

$$P_k = -\overline{\rho u_i' u_j'} \frac{\partial u_j}{\partial x_i} = \mu_t S^2 \quad (2.28)$$

where, the Modulus of the mean rate-of-strain tensor,  $S \equiv \sqrt{2S_{ij}S_{ij}}$ .

Buoyancy effect  $P_b$

$$P_b = \beta g_i \frac{\mu_t}{\text{Pr}_t} \frac{\partial T}{\partial x_i} \quad (2.29)$$

Prandtl number  $Pr_t$  has a default value of 0.85,  $g_i$  is the gravitational vector component in the  $i$ th direction, and thermal expansion coefficient,  $\beta$ , is defined as  $\beta = \frac{1}{\rho} \left( \frac{\partial \rho}{\partial T} \right)_p$

$$c_{1\varepsilon} = 1.44, c_{2\varepsilon} = 1.92, c_{3\varepsilon} = -0.33, c_\mu = 0.09, \sigma_\varepsilon = 1.3, \sigma_k = 1.0$$

### 2.6.3.2 Realizable $k$ - $\varepsilon$ Model

This is a major development on the standard  $k$ - $\varepsilon$  model by Shih et al. (1995) as it presents a new formulation for the turbulent viscosity and the dissipation rate,  $\varepsilon$ , transport equation derived from a precise equation of the mean-square vorticity fluctuation.

Turbulent kinetic energy  $k$ ,

$$\frac{\partial}{\partial t}(\rho k) + \frac{\partial}{\partial x_j}(\rho k u_j) = \frac{\partial}{\partial x_j} \left[ \left( \mu + \frac{\mu_t}{\sigma_k} \right) \frac{\partial k}{\partial x_j} \right] + \rho k + \rho b - \rho \varepsilon - Y_M + S_k \quad (2.30)$$

Turbulent dissipation  $\varepsilon$

$$\frac{\partial}{\partial t}(\rho \varepsilon) + \frac{\partial}{\partial x_j}(\rho \varepsilon u_j) = \frac{\partial}{\partial x_j} \left[ \left( \mu + \frac{\mu_t}{\sigma_\varepsilon} \right) \frac{\partial \varepsilon}{\partial x_j} \right] + \rho c_{1\varepsilon} S \varepsilon - \rho c_2 \frac{\varepsilon^2}{k + \sqrt{\nu \varepsilon}} + c_{1\varepsilon} \frac{\varepsilon}{k} c_{3\varepsilon} P_b + S_\varepsilon \quad (2.31)$$

where,  $c_1 = \max \left[ 0.43, \frac{\eta}{\eta + 5} \right]$ ,  $\eta = S \frac{k}{\varepsilon}$ ,  $S = \sqrt{2 S_{ij} S_{ij}}$

In these equations,  $P_k$ ,  $P_b$ , and  $Y_M$  are calculated as shown in the standard  $k$ - $\varepsilon$  model above.

Turbulent eddy viscosity,  $\mu_t = \rho c_\mu \frac{k^2}{\varepsilon}$ , Where,  $c_\mu = \frac{1}{A_0 + A_s \frac{k U^*}{\varepsilon}}$ ,

$$U^* \equiv \sqrt{S_{ij} S_{ij} + \tilde{\Omega}_{ij} \tilde{\Omega}_{ij}}, \quad \tilde{\Omega}_{ij} = \Omega_{ij} - 2 \varepsilon_{ijk} \omega_k, \quad \Omega_{ij} = \overline{\Omega_{ij}} - \varepsilon_{ijk} \omega_k$$

$\overline{\Omega_{ij}}$  is the mean rate-of-rotation tensor observed in a rotating reference frame with angular velocity,  $\omega_k$ .

By default,  $-2 \varepsilon_{ijk} \omega_k$  is not included in FLUENT in the calculation of  $\tilde{\Omega}_{ij}$ .

$$A_0 = 4.04, A_s = \sqrt{6} \cos \phi$$

$$\phi = \frac{1}{3} \cos^{-1} (\sqrt{6}W), W = \frac{S_{ij}S_{jk}S_{ki}}{\tilde{S}^3}, \tilde{S} = \sqrt{S_{ij}S_{ij}}, S_{ij} = \frac{1}{2} \left( \frac{\partial u_j}{\partial x_i} + \frac{\partial u_i}{\partial x_j} \right)$$

$$c_{1\varepsilon} = 1.44, c_{2\varepsilon} = 1.9, \sigma_\varepsilon = 1.2, \sigma_k = 1.0$$

#### 2.6.4 Volume of Fluid (VOF) Method

The volume of fluid (VOF) is a numerical modelling technique used for free surface (i.e., the boundary or interface between immiscible fluids, for example, air and water) tracking. This technique was based on the Marker-and-Cell, MAC, method developed by Harlow and Welch (1965) to discretise function of time-dependent viscous incompressible fluid flow. The earliest reference to the current VOF method was by Noh and Woodward (1976) in which they developed the Simple Line Interface Calculation, SLIC, method to account for the difficulty of geometrical approximations to fluid interfaces in a multifluid Eulerian flow. It was majorly accepted as a better numerical technique over the MAC method because of the low computational storage requirement. The commercial CFD Code employed in this study, ANSYS Fluent, employs the VOF with Piecewise Linear Interface Calculation, PLIC, method. The PLIC method was developed by Youngs (1982) to address the limitation in the interface description when the technique of distorting the Lagrangian mesh is applied for a fluid flow problem.

In ANSYS (2009), the flow variables and properties are shared by the phases (different fluids) within the domain. In each control volume, the volume fractions of all phases equal to one. For instance, three conditions are possible if the  $q^{\text{th}}$  fluid's volume fraction in the cell is denoted as  $\alpha_q$ .

- $\alpha_q = 0$ : The cell is empty (of the  $q^{\text{th}}$  fluid)
- $\alpha_q = 1$ : The cell is full (of the  $q^{\text{th}}$  fluid)
- $0 < \alpha_q < 1$ : The cell contains the interface between the  $q^{\text{th}}$  fluid and one or more other fluids.

The interface tracking between the phases is achieved by solving the continuity equation for the volume fraction of one (or more) of the phases either through implicit or explicit time discretization schemes. The form of the volume fraction equation for the  $q^{\text{th}}$  phase is:

$$\frac{1}{\rho_q} \left[ \frac{\partial}{\partial t} (\alpha_q \rho_q) + \nabla \cdot (\alpha_q \rho_q \vec{v}_q) \right] = S_{\alpha_q} + \sum_{p=1}^n (\dot{m}_{pq} - \dot{m}_{qp}) \quad (2.32)$$

where,  $\dot{m}_{qp}$  is the mass transfer from phase q to p,  $\dot{m}_{pq}$  is mass transfer from phase p to q,  $S_{\alpha_q}$  is the source term with the default value of zero. A constant or user-defined mass source can be applied to each phase.

The volume fraction equation will not solve the specified primary phase. Its volume fraction will be computed using:

$$\sum_{q=1}^n (\alpha_q) = 1 \quad (2.33)$$

### 2.6.5 Near Wall Modelling

The near-wall region poses difficult numerical and modelling challenges in turbulent flows because of the viscous effect. In this region, the mean flow properties; velocity, temperature, turbulence properties, undergo their strongest abrupt changes. These effects could be numerically mitigated by using very fine grids and low-Reynold-number model, but these can be computationally expensive for 3-D models and could introduce slow convergence, hence the need to use wall functions where the viscous layer is not resolved like in the low-Reynold-number modelling, but flow behaviour in the region is accounted for by the introduction of approximations (Craft, 2011).

### 2.6.6 Wall Functions

In turbulent flows, the near-wall region is significantly thinner, hence the need for a finer grid to provide accurate resolution of flow quantities. The need to bypass the large computational requirement caused by using very fine mesh in this region, especially in 3-D problems, necessitated the development of the wall function approach.

In this approach, the numerical resolution of the near-wall region is avoided by employing approximate analytical expressions for the mean velocity distribution across this region.

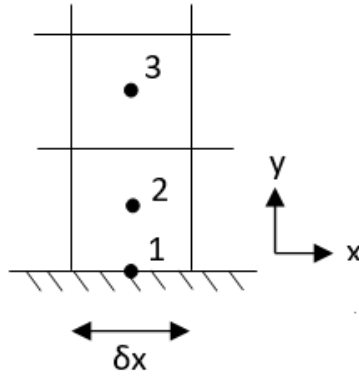


Figure 2.8. Near-wall cell (Craft, 2011).

In a local equilibrium turbulent flow, with  $l = \kappa y$ , the velocity in the turbulent region satisfies the log-law:

$$U^+ = \frac{1}{\kappa} \log (E y^+) \quad (2.34)$$

where,  $\kappa = 0.41$ ,  $E = 9$ ,  $U^+ = \frac{U}{\sqrt{\frac{\tau_w}{\rho}}}$  and  $y^+ = \frac{y \sqrt{\frac{\tau_w}{\rho}}}{\nu}$

Rearranging:

$$\tau_w = \rho \left\{ \frac{\kappa U_2}{\log \frac{E y_2 \sqrt{\frac{\tau_w}{\rho}}}{\nu}} \right\}^2 \quad (2.35)$$

Equation (2.35) above gives an expression for the estimation of wall shear stress,  $\tau_w$ , in terms of the velocity at the near-wall node (node 2) (Fig. 2.8). This near-wall node should now be in the turbulent region (Non-dimensional wall-distance,  $y^+ > 30$ ) where the gradients are less steep than in the viscous region (Fig. 2.9).



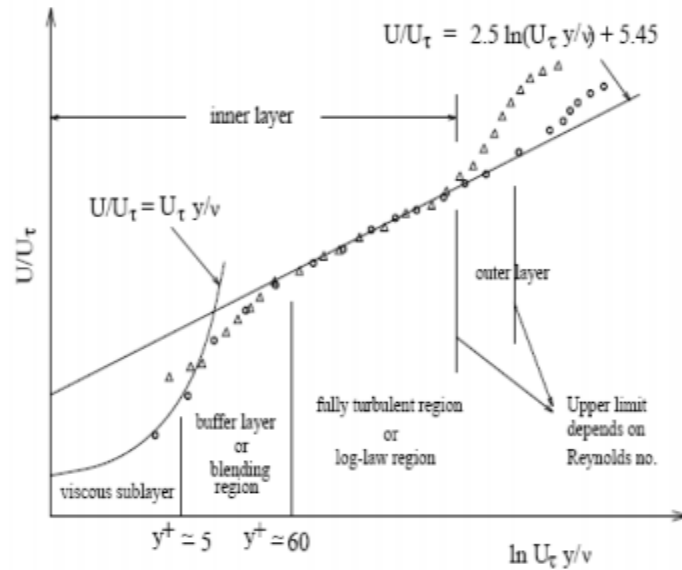


Figure 2.9. Subdivisions of the near-wall region (Salim and Cheah, 2009).

### 2.6.6.1 Standard Wall Functions

This wall function is based on the work of Launder and Spalding (1974) and used in various industrial flows and commercial CFD software.

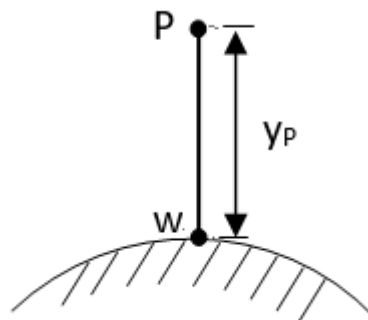


Figure 2.10. The near-wall nodes (Launder and Spalding, 1974).

### Momentum

The fluxes of momentum obey the law-of-the-wall for average velocity:

$$U^* = \frac{1}{\kappa} \log(E y^*) \quad (2.36)$$

where, dimensionless velocity,  $U^* = \frac{U_p C_\mu^{1/4} k_p^{1/2}}{\tau_w / \rho}$  and dimensionless distance from the

wall,  $y^* = \frac{\rho C_\mu^{1/4} k_p^{1/2} y_p}{\mu}$ .

$\kappa$  = von Kármán constant (=0.4187)

$E$  = empirical constant; the function of wall roughness (=9.793)

$U_p$  = mean velocity of the fluid at the near-wall node  $P$

$k_p$  = turbulence kinetic energy at the near-wall node  $P$

$y_p$  = distance from point  $P$  to the wall (Fig. 2.10)

$\mu$  = dynamic viscosity of the fluid

$\tau_w$  = shear stress on the wall in the direction of the velocity  $U_p$

The law-of-the-wall for average velocity is known to be valid for  $30 < y^* < 300$ . In ANSYS FLUENT, the logarithmic law is used when  $y^* > 11.25$ , but laminar stress-strain ( $U^* = y^*$ ) relationship is employed when  $y^* < 11.25$ .

## Turbulence

In the  $k - \varepsilon$  models, the wall boundary conditions can be obtained from the  $k$  equation by solving in the whole domain including the wall-adjacent cells. The boundary condition for turbulent kinetic energy,  $k$  imposed at the wall is:

$$\frac{\partial k}{\partial n} = 0 \quad (2.37)$$

where,  $n$  is the local coordinate normal to the wall.

The production of kinetic energy,  $P_k$ , and its dissipation rate,  $\varepsilon$ , are computed on the assumption that both are equal in the wall-adjacent control volume.

The production of kinetic energy,  $P_k$ , is based on the logarithmic law and is computed from:

$$P_k \approx \tau_w \frac{\partial U}{\partial y} = \tau_w \frac{\tau_w}{\kappa \rho k_p^{1/2} y_p} \quad (2.38)$$

Turbulent kinetic energy dissipation rate,  $\varepsilon$  is computed from:

$$\varepsilon_p = \frac{C_\mu^{3/4} k_p^{3/2}}{\kappa y_p} \quad (2.39)$$

The  $\varepsilon$  equation is not solved at the wall-adjacent cells.

### 2.6.6.2 Scalable Wall Functions

In ANSYS (2016), this approach ensures the usage of the logarithmic law together with the standard wall functions approach by introducing a limiter in the dimensionless distance from the wall,  $y^*$  calculations such that:

$$y^*_{\text{lim}} = \text{MAX}(y^*, y^* \text{ limit}) \quad (2.40)$$

where,  $y^* \text{ limit} = 11.225$

## 2.7 Sediment Transport Mechanisms

The research study on sediment motion by Shields (1936) was a major contribution to understanding sediment transportation. The Shields diagram, his key finding, represents the variation of threshold Shields parameter with shear Reynolds number corresponding to the threshold of sediment entrainment; condition for the initiation of sediment transport.

Grain movement can be induced by both lift and drag forces which must be greater than the gravitational forces and frictional forces that hold the particle together. According to Dey (1999), lift force can be induced by the dynamic pressure difference resulting from maximum velocity gradient, velocity fluctuations acting in the vertical direction, and Magnus effect generated by the rotating motion of particles. The drag force is the frictional force induced by the fluid flow over exposed sediment grain surface, and it depends on the flow velocity, the exposed cross-sectional area impacted by the flow and the surface roughness of the sediment particle.

### 2.7.1 Modes of Sediment Transport

There are various modes of sediment transport and attempts to differentiate these components have been challenging. Komar (1980) opined that sediment transport in rivers is a combination of bed load, suspension load, and wash load. He detailed past research studies performed to differentiate between the modes by relating the cut-off sediment grain size to known river flow variable like velocity, discharge or stress. Francis (1973) observed and described three spinning modes of sediment transport in heavy solid grains – rolling, saltating and suspension. Low and smooth trajectories are

followed by the grain in the saltation mode, while longer, higher and irregular path are travelled in the suspension mode. Julien (2010) only limited the different classification of the mode of transport into bed load and suspended load (Fig. 2.11), while Hicken (2010) shows the separation into the dissolved load, suspended load, intermittent suspension (saltation) load, wash load, and bed load. Bed load is the grain that moves through the water, fully supported by the bed and with the frequent collision with other grains. The bed does not support suspension load but the turbulence of the water.

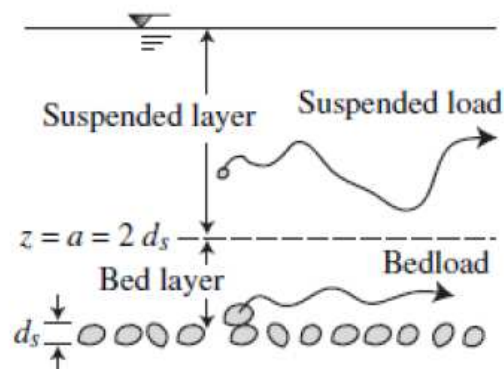


Figure 2.11. Bed load and suspended load (Julien, 2010).

### 2.7.2 Sediment Transport Modelling

Modelling of sediment transport mechanisms is usually based on one-dimensional, two-dimensional and three-dimensional series of governing equations. The mechanisms are based on numerical models and experimental models. The advent of powerful computers in the 20<sup>th</sup> century has spurred increased research in the numerical study of sediment transport and has led to the development of free and commercial sediment models (Table 2.6).

Table 2.6. Comparison of Sediment transport model (Hanna, 2014).

Dimensions	Governing Equations	Model Name	Advantages	Disadvantages
1D	St. Venant Equations	CCHE1D	<ul style="list-style-type: none"> <li>Steady and unsteady flow.</li> <li>Multiple channel bed layers.</li> <li>Non-equilibrium approach.</li> </ul>	<ul style="list-style-type: none"> <li>No water quality analysis.</li> </ul>
		HEC-RAS	<ul style="list-style-type: none"> <li>Steady and unsteady flow.</li> <li>Water quality and temperature modelling included.</li> <li>Accounts for structures.</li> <li>Mixed flow regime profiles.</li> </ul>	<ul style="list-style-type: none"> <li>Not an event-based model.</li> <li>Channel geometry not updated on erosion or deposition.</li> <li>No calculations conducted at specific locations.</li> </ul>
		SAM	<ul style="list-style-type: none"> <li>Calculates slope stability.</li> <li>Represents system as an average (increases simplicity).</li> </ul>	<ul style="list-style-type: none"> <li>Assumes steep banks are vertical (have no influence).</li> <li>Represents system as an average (less accurate).</li> </ul>
		CCHE2D	<ul style="list-style-type: none"> <li>Cohesive and non-cohesive soils.</li> <li>Wetting and drying of domain.</li> <li>Three non-equilibrium approaches to choose from.</li> </ul>	<ul style="list-style-type: none"> <li>Width-averaged flow not accounted for.</li> </ul>

2D	2D Momentum Equation	SED2D	<ul style="list-style-type: none"> <li>• Cohesive and non-cohesive soils.</li> <li>• Incorporates up to ten clay layers.</li> </ul>	<ul style="list-style-type: none"> <li>• Width-averaged flow not accounted for.</li> <li>• Individual models run for each grain size in bed load.</li> </ul>
		SRH-2D	<ul style="list-style-type: none"> <li>• Flexible mesh for accuracy.</li> <li>• Accounts for structures and bends.</li> <li>• Wetting-drying algorithm.</li> </ul>	<ul style="list-style-type: none"> <li>• Specification of mesh (such as a fine mesh) need to be adapted.</li> <li>• Width-averaged flow not accounted for.</li> </ul>
3D	3D Momentum Equation or Navier-Stokes Equations.	CCHE3D	<ul style="list-style-type: none"> <li>• Incorporates sediment and pollutant transport and water quality.</li> <li>• Solid grid stability.</li> <li>• Irregular walls, etc. applied as boundary conditions.</li> <li>• Computes hydrostatic and dynamic pressure.</li> </ul>	<ul style="list-style-type: none"> <li>• No mixed mesh, but hexahedral elements.</li> </ul>
		Delft3D	<ul style="list-style-type: none"> <li>• Water quality, waves, and ecology accounted for.</li> <li>• Large range of time scale.</li> </ul>	<ul style="list-style-type: none"> <li>• Bed load transport directly related to flow velocities, not bed shear stress.</li> </ul>

			<ul style="list-style-type: none"> <li>• Dredging and dumping scenarios simulated.</li> </ul>	
		MIKE 3	<ul style="list-style-type: none"> <li>• Sand transport, mud transport and sediment tracking.</li> <li>• Dredging module.</li> <li>• Flexible mesh.</li> </ul>	<ul style="list-style-type: none"> <li>• Does not compute non-cohesive sediment.</li> </ul>

### 2.7.2.1 Empirical Bed Load Transport Equations

#### Meyer-Peter and Muller (1948)

The empirical bed load transport equation by Meyer-Peter and Muller (1948) only applies to large sediment grain and wide channels.

$$q^* = 8(\tau^* - \tau_c^*)^{3/2} \quad (2.41)$$

where the critical Shields parameter,  $\tau_c^*$  is assumed as 0.047.

Dimensionless bed flux,  $q^* = \frac{q_b}{\sqrt{(s-1)gd^3}}$ , and dimensionless shear stress/Shields parameter,  $\tau^* = \frac{\tau_b}{\rho(s-1)gd}$

$q_b$  is the Bed load discharge per unit width (ton/day/m),  $s$  is the specific gravity ( $\rho_s/\rho$ ) in which  $\rho$  is the density of water and  $\rho_s$  is the density of sediment, and  $g$  is the gravitational constant.

#### Van Rijn (1984)

The bed-load transport,  $q_b$ , (m<sup>2</sup>/s) formula is only applicable to particles in the size range 200 – 2,000  $\mu\text{m}$ .

$$\frac{q_b}{[(s-1)g]^{0.5} D_{50}^{1.5}} = 0.053 \frac{T^{2.1}}{D_*^{0.3}} \quad (2.42)$$

where, Particle parameter,  $D_* = \left[ \frac{g(s-1)}{v^2} \right]^{1/3} D_{50}$ .

Transport stage parameter, 
$$T = \frac{(u'_*)^2 - (u_{*,cr})^2}{(u_{*,cr})^2} \tag{2.43}$$

where, bed shear velocity related to grains,  $u'_* = \left( \frac{g}{c'} \right)^{0.5} \bar{u}$

where, the chézy-coefficient related to surface (or grain) roughness of the sediment bed,  $C' = 18 \log \left( \frac{12R_b}{3D_{90}} \right)$ ,  $\bar{u}$  is the mean flow velocity,  $u_{*,cr}$  is the Shields critical bed shear velocity (Fig. 2.12),  $D_{90}$  is the grain diameter just larger than the diameters of 90% of the soil grain,  $R_b$  is the hydraulic radius =  $\frac{A}{P}$ , where A is the area of the cross-section and P is the wetted perimeter.

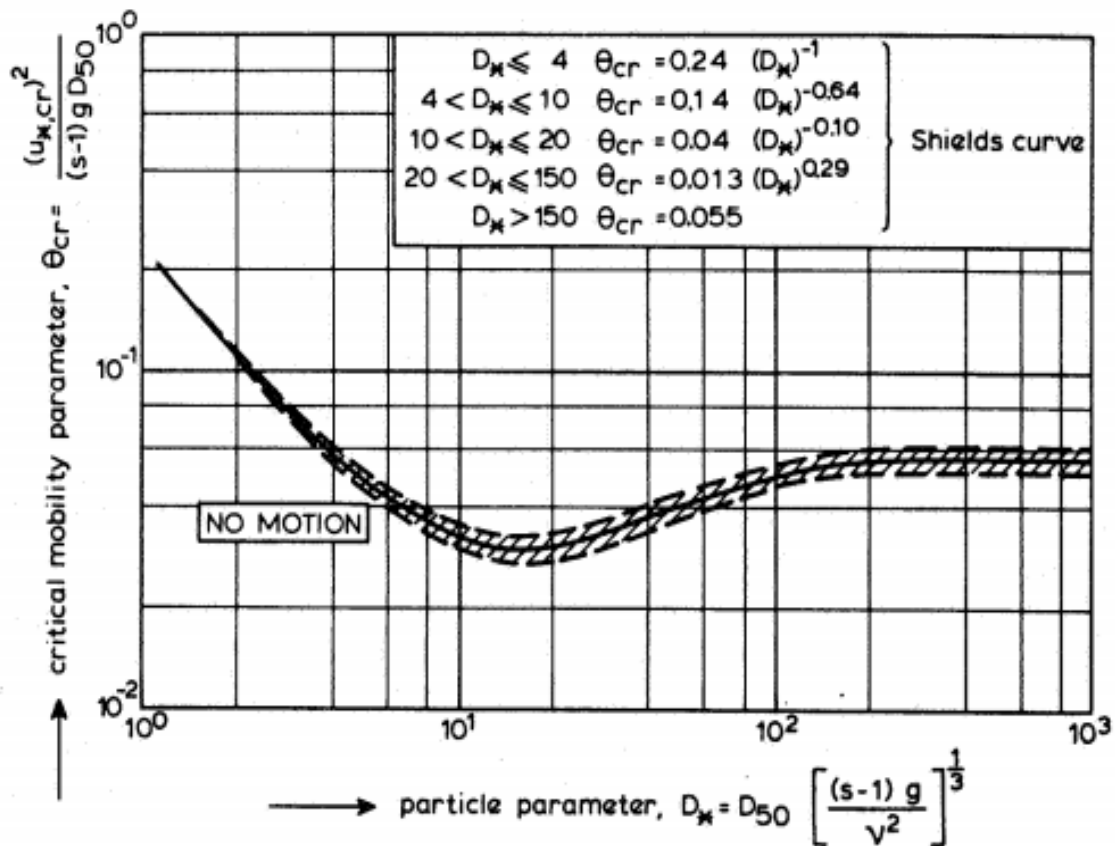


Figure 2.12. Initiation of motion according to Shields (Van Rijn, 1984).



### **Other empirical bed-load transport formula**

Several formulae have been proposed empirical and semi-empirical correlations to predict bed load transport rate (Table 2.7). The French hydraulic engineer, Du Boys is the first to propose a bed load transport model in 1879. His model was incomplete but generally agreed well with large laboratory measurements. Although, there have been improved models to determine the characteristics of the bed-load layer, large variations in the calculated values persist. Great caution is necessary when employing any formula for real-life situations. The real-life scenario must be similar to the boundary conditions that govern the formula.

Table 2.7. Empirical and semi-empirical correlations of bed load transport (Chanson, 1999).

Reference (1)	Formulation (2)	Range (3)	Remarks (4)
Boys (1879)	$q_s = \lambda \tau_o (\tau_o - (\tau_o)_c)$		$\lambda$ was called the characteristic sediment coefficient.
	$\lambda = \frac{0.54}{(\rho_s - \rho)g}$ Schoklitsch (1914)		Laboratory experiments with uniform grains of various kinds of sand and porcelain.
	$\lambda \propto d_s^{-3/4}$ Straub (1935)	$0.125 < d_s < 4 \text{ mm}$	Based upon laboratory data.
Schoklitsch (1930)	$q_s = \lambda' (\sin \theta)^k (q - q_c)$ $q_c = 1.944 \times 10^{-2} d_s (\sin \theta)^{-4/3}$	$0.305 < d_s < 7.02 \text{ mm}$	Based upon laboratory experiments.
Shields (1936)	$\frac{q_s}{q} = 10 \frac{\sin \theta}{s} \frac{\tau_o - (\tau_o)_c}{\rho g (s-1) d_s}$	$1.06 < s < 4.25$ $1.56 < d_s < 2.47 \text{ mm}$	
Einstein (1942)	$\frac{q_s}{\sqrt{(s-1)g d_s^3}} = 2.15 \exp\left(-0.391 \frac{\rho(s-1)g d_s}{\tau_o}\right)$	$\frac{q_s}{\sqrt{(s-1)g d_s^3}} < 0.4$ $1.25 < s < 4.25$ $0.315 < d_s < 28.6 \text{ mm}$	Laboratory experiments. Weak sediment transport formula for sand mixtures. Note: $d_s \approx d_{35}$ to $d_{45}$ .
Meyer-Peter (1949,1951)	$\frac{\dot{m}^{2/3} \sin \theta}{d_s} - 9.57(\rho g (s-1))^{10/9} = 0.462(s-1) \frac{(\rho g (\dot{m}_s)^2)^{2/3}}{d_s}$	$1.25 < s < 4.2$	Laboratory experiments. Uniform grain size distribution.
	$\frac{q_s}{\sqrt{(s-1)g d_s^3}} = \left(\frac{4\tau_o}{\rho(s-1)g d_s} - 0.188\right)^{3/2}$		Laboratory experiments. Particle mixtures. Note: $d_s \approx d_{50}$ .
Einstein (1950)	Design chart $\frac{q_s}{\sqrt{(s-1)g d_s^3}} = f\left(\frac{\rho(s-1)g d_s}{\tau_o}\right)$	$\frac{q_s}{\sqrt{(s-1)g d_s^3}} < 10$ $1.25 < s < 4.25$ $0.315 < d_s < 28.6 \text{ mm}$	Laboratory experiments. For sand mixtures. Note: $d_s \approx d_{35}$ to $d_{45}$ .
Schoklitsch (1950)	$\dot{m}_s = 2500(\sin \theta)^{3/2} (q - q_c)$ $q_c = 0.26(s-1)^{5/3} d_{40}^{3/2} (\sin \theta)^{-7/6}$		Based upon laboratory experiments and field measurements (Danube and Aare rivers).
Nielsen (1992)	$\frac{q_s}{\sqrt{(s-1)g d_s^3}} = \left(\frac{12\tau_o}{\rho(s-1)g d_s} - 0.05\right) \sqrt{\frac{\tau_o}{\rho(s-1)g d_s}}$	$1.25 < s < 4.22$ $0.69 < d_s < 28.7 \text{ mm}$	Re-analysis of laboratory data.

Notes:  $\dot{m}$  = mass water flow rate per unit width;  $\dot{m}_s$  = mass sediment flow rate per unit width;  $q$  = volumetric water discharge;  $q_s$  = volumetric sediment discharge per unit width;  $(\tau_o)_c$  = critical bed shear stress for initiation of bed load.

According to Chanson (1999), the bed load transport rate per unit width,  $q_s$ , can be applied to flat channels (i.e.,  $\sin \theta < 0.001$  to  $0.01$ ) with plane beds (Table 2.8).

$$q_s = C_s \delta_s V_s \quad (2.44)$$

where  $V_s$  is the average sediment velocity in the bed load layer,  $C_s$  is the mean sediment concentration, and  $\delta_s$  average saltation height measured perpendicular to the bed (Fig. 2.13).

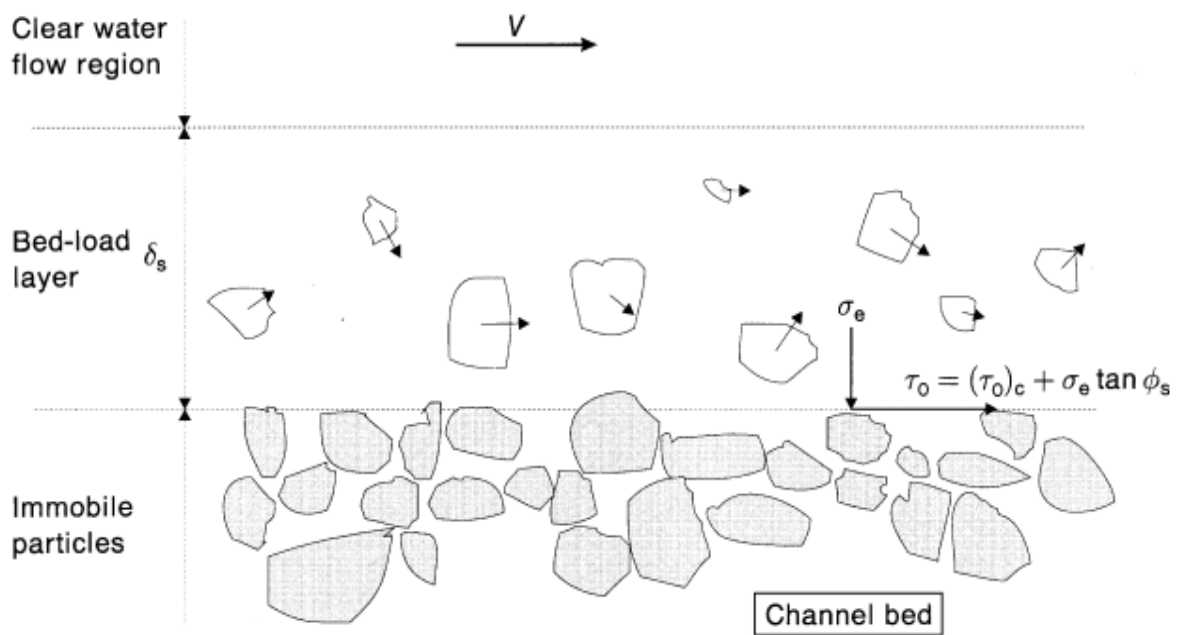


Figure 2.13. Bed-load motion at equilibrium (Chanson, 1999).

Table 2.8. Bed-load transport rate calculations (Chanson, 1999).

Reference (1)	Bed-load layer characteristics (2)	Remarks (3)
Fernandez-Luque and van Beek (1976)	$\frac{V_s}{V_*} = 9.2 \left( 1 - 0.7 \sqrt{\frac{(\tau_*)_c}{\tau_*}} \right)$	Laboratory data $1.34 \leq s \leq 4.58$ $0.9 \leq d_s \leq 3.3 \text{ mm}$ $0.08 \leq d \leq 0.12 \text{ m}$
Nielsen (1992)	$C_s = 0.65$ $\frac{\delta_s}{d_s} = 2.5(\tau_* - (\tau_*)_c)$ $\frac{V_s}{V_*} = 4.8$	Simplified model.
Van Rijn (1984a,1993)	$C_s = \frac{0.117}{d_s} \left( \frac{\nu^2}{(s-1)g} \right)^{1/3} \left( \frac{\tau_*}{(\tau_*)_c} - 1 \right)$ $\frac{\delta_s}{d_s} = 0.3 \left( d_s \left( \frac{(s-1)g}{\nu^2} \right)^{1/3} \right)^{0.7} \sqrt{\frac{\tau_*}{(\tau_*)_c} - 1}$ $\frac{V_s}{V_*} = 9 + 2.6 \log_{10} \left( d_s \left( \frac{(s-1)g}{\nu^2} \right)^{1/3} \right) - 8 \sqrt{\frac{(\tau_*)_c}{\tau_*}}$ $C_s = \frac{0.117}{d_s} \left( \frac{\nu^2}{(s-1)g} \right)^{1/3} \left( \frac{\tau_*}{(\tau_*)_c} - 1 \right)$ $\frac{\delta_s}{d_s} = 0.3 \left( d_s \left( \frac{(s-1)g}{\nu^2} \right)^{1/3} \right)^{0.7} \sqrt{\frac{\tau_*}{(\tau_*)_c} - 1}$ $\frac{V_s}{V_*} = 7$	For $\frac{\tau_*}{(\tau_*)_c} < 2$ and $d_s = d_{50}$ . Based on laboratory data $0.2 \leq d_s \leq 2 \text{ mm}$ $d > 0.1 \text{ m}$ $Fr < 0.9$  $d_s = d_{50}$ . Based on laboratory data $0.2 \leq d_s \leq 2 \text{ mm}$ $d > 0.1 \text{ m}$ $Fr < 0.9$

Notes:  $V_*$  = shear velocity;  $(\tau_*)_c$  = critical Shields parameter for initiation of bed load.

### 2.7.2.2 Two-phase Equation by Cheng and Hsu (2014)

Cheng and Hsu (2014) employed a two-phase formula to develop a sediment transport model; twoPhaseEulerSedFoam, through OpenFOAM; a free open-source CFD library. The model was validated for sheet flow in steady and oscillatory flows.

The mass conservation equations for fluid phase and sediment phase can be expressed as (Assumption: no mass transfer between the phases):

$$\frac{\partial(1-\phi)}{\partial t} + \frac{\partial(1-\phi)u_i^f}{\partial x_i} = 0 \quad (2.45)$$

$$\frac{\partial\phi}{\partial t} + \frac{\partial\phi u_i^s}{\partial x_i} = 0 \quad (2.46)$$

where,  $\phi$  is the sediment volumetric concentration,  $u_i^s$  and  $u_i^f$  are  $i$  velocity component of the sediment phase and fluid phase respectively, and  $i = 1, 2, 3$  is the streamwise, spanwise, and vertical components.

The momentum for the fluid phase and sediment phase can be expressed as:

$$\frac{\partial \rho^f (1-\phi) u_i^f}{\partial t} + \frac{\partial \rho^f (1-\phi) u_i^f u_j^f}{\partial x_j} = -\frac{\partial (1-\phi) p^f}{\partial x_i} + \frac{\partial (1-\phi) \tau_{ij}^f}{\partial x_j} + \rho^f (1-\phi) g \delta_{i3} + M_i^{fs} \quad (2.47)$$

$$\frac{\partial \rho^s \phi u_i^s}{\partial t} + \frac{\partial \rho^s \phi u_i^s u_j^s}{\partial x_j} = -\frac{\partial \phi p^f}{\partial x_i} - \frac{\partial p^s}{\partial x_i} + \frac{\partial \tau_{ij}^s}{\partial x_j} + \rho^s \phi g \delta_{i3} + M_i^{sf} \quad (2.48)$$

where,  $\rho^f$ ,  $\rho^s$  are density of fluid and sediment phase,  $g_i$  is gravitational constant,  $p^f$  is the fluid pressure, and  $\tau_{ij}^f$  is the shear stress of the fluid; viscous stress and turbulence stresses,  $p^s$  is the particle pressure,  $\tau_{ij}^s$  is the particle stress,  $M_i^{sf}$  and  $M_i^{fs}$  ( $-M_i^{sf}$ ) and represent the interphase momentum transfer between sediment and fluid phases.  $p^s$  and  $\tau_{ij}^s$  are determined from the kinetic theory of granular flow and phenomenological closure of frictional contact stresses.

The momentum between the sediment and fluid phases are coupled through the interphase momentum transfer term.

$$M_i^{fs} = -M_i^{sf} = -\phi \beta (u_i^f - u_i^s) - \beta \overline{\phi \Delta u_i^f} + p^f \frac{\partial (1-\phi)}{\partial x_i} \quad (2.49)$$

$p^f \frac{\partial (1-\phi)}{\partial x_i}$  is the interphase pressure correction term,  $\phi \beta (u_i^f - u_i^s)$  represents the averaged drag force due to mean relative velocity between both sediment and fluid phases and  $\beta \overline{\phi \Delta u_i^f}$  is called turbulent suspension; obtained from the Reynolds averaging. Both terms are due to drag force.

$$\tau_{ij}^s = \mu^{sf} \left[ \frac{\partial u_i^s}{\partial x_j} + \frac{\partial u_j^s}{\partial x_i} \right] - \frac{2}{3} \mu^{sf} \frac{\partial u_k^s}{\partial x_k} \delta_{ij} \quad (2.50)$$

where, frictional viscosity,  $\mu^{sf} = \frac{\sqrt{2} p^s \sin(\theta_f)}{2 \sqrt{S^s_{ij} \cdot S^s_{ij}}}$

$\theta_f$  is the angle of repose of the sand (taken as  $28^\circ$ ), the deviatoric part of strain rate tensor for sediment phase,  $S^s_{ij} = \frac{1}{2} \left[ \frac{\partial u_i^s}{\partial x_j} + \frac{\partial u_j^s}{\partial x_i} \right] - \frac{1}{3} \mu^{sf} \frac{\partial u_k^s}{\partial x_k} \delta_{ij}$

The standard projection method is used to solve fluid and particle velocities.

### 2.7.2.3 Sediment Transport Model by Zhang and Shi (2016)

Zhang and Shi (2016) employed the finite volume method to solve the governing equation of the fluid flow and the finite difference method to solve the governing equation of the sediment transport model to investigate the local scouring around an underwater pipeline.

The bed load sediment transport rate at the slope is adjusted according to:

$$q_{bi} = q_0 \frac{\tau_i}{|\tau|} - C q_0 \frac{\partial h}{\partial x_i} \quad (2.51)$$

where,  $\tau_i$  is the shear stress at  $i$  direction,  $C$  is the correction factor in range 1.5 -2.3 (1.5 was used in the study),  $h$  is the sand bed level,  $q_0$  is the sediment transport rate by Soulsby (1997);

$$q_0 = 12 \sqrt{g(s-1)d_{50}^3 \theta(\theta - \theta_{cr})} \quad (2.52)$$

where, the shields number,  $\theta = \frac{\tau}{\rho g(s-1)d_{50}}$ , the critical shields number,  $\theta_{cr}$ , adjusted based on the sediment motion up or down the bed slope.

$$\theta_{cr} = \theta_{cro} \left( \cos \alpha + \frac{\sin \alpha}{\tan \varphi} \right) \quad (2.53)$$

where, the critical shields number at the horizontal bed,  $\theta_{cro} = \frac{0.3}{1+1.2D_*} + 0.055[1 - \exp(-0.02D_*)]$ ,  $\alpha$  is the angle of slope of the bed and  $\varphi$  is the angle of repose of the sediment.

Dimensionless sediment size,  $D_* = \left[ \frac{g(s-1)}{v^2} \right]^{1/3} d_{50}$

The change of sandy bed level was expressed using the mass balance theory:

$$\frac{\partial h}{\partial t} = \frac{-1}{(1-n)} \left( \frac{\partial q_{bi}}{\partial x_i} \right) \quad (2.54)$$

where,  $n$  is the porosity.

Adjustments were made to the bed slope using the sand slide model to ensure the value is less than the angle of repose of the sand to guarantee stability during scouring process. Dynamic mesh technology is then implemented in ANSYS Fluent to simulate the process.

## 2.8 Summary

An extensive review has been carried out before experimental and computational studies to understand better the methods that have been employed to investigate tsunami wave characteristics. The evolution of the study has been shown in the description of the physical and numerical studies, flooding and tsunami mitigation measures for resilient coastal dike in Japan, early history and development of numerical simulation, and computational fluid dynamics theories. The review has shown that development of tsunami-induced scour and effects of coastal structure geometry on scour holes need further exploration.

The review shows the classification and characteristics of a tsunami wave. Impact standing and overflowing wave pressures are identified as having the highest impact on coastal structures with the possibility of negative uplift pressure but the insufficient relationship of its effect on scouring process. There are limited publications about the dam break method of tsunami wave generation and resulting scour damage at the landward region of coastal structures. Also, the description of the sediment transport mechanism and sediment transport models will form the basis of laboratory work, numerical studies, and analyses of the scouring process.

The evaluation of the RANS turbulence models and wall functions for near-wall modelling is crucial in deciding the appropriate model and function to employ in this study. It shows the advantages of improved flow variable results with realizable  $k-\epsilon$  Model and use of scalable wall function for a coarse mesh.

## **Chapter 3**

# **Tsunami Wave Propagation over Sea Dikes**

The destructive power of tsunami generates catastrophic damages to coastal infrastructure such as defences and buildings as well as the hinterland of such area. The fundamental physics of interactions between tsunami wave propagation and impact with coastal structures need to be understood before applying any prevention strategies for future events.

Extensive studies of tsunami flow propagation have been carried out in large-scale wave flumes using solitary waves by many researchers (e.g., Tonkin et al., 2003; Hsiao and Lin, 2010; Rossetto et al., 2011). However, there are not very many detailed tsunami research studies carried out on structures using dam break wave (DBW) conditions (Mikami and Shibayama, 2013).

This chapter begins with an introduction of various methods of experimental study of tsunami waves. The experimental data of flow quantities are described and statistically compared to other published studies, and the effect of geometry on wave characteristics are presented and discussed.

### **3.1 Introduction**

Several physical investigations of tsunami waves have been conducted, which have contributed to the understanding of the wave characteristics near-shore and off-shore, and particularly its impact on coastal structures. Chen et al. (2015) used a piston type wave generator to create steep solitary waves to study its reflection at a vertical wall. The wave run-up characteristics were found to have been underestimated by many past theoretical results. The collision was discovered to cause the occurrence of Rayleigh-Taylor instability. Lynett et al. (2010) conducted a laboratory investigation on the interactions between a breaking solitary wave and 3-D shallow water shelf. The experiment shows that when considering the mixing and transport processes, the turbulence created by bore fronts and spatial velocity gradients is more significant than that due to the bottom stress.

A piston type wave generator was used by Schimmels et al. (2014) to produce a tsunami-like wave as opposed to solitary wave. The long wave produced can prevent



the usual high turbulence caused by the air-water mixing immediately after generation. Using a pump-driven wave generator, Shito et al. (2014) generated a long-period tsunami wave to study its behaviour around a bay-mouth breakwater and an onshore tank. Their results showed the reduction of wave height due to the presence of breakwater. Also, the tsunami wave load and pressure values agreed well with other published values.

The use of a vertical water volume release method was employed by Wüthrich et al. (2016) to generate tsunami-like waves. In this technique, gravity is employed to transport a large volume of water from an upper tank into a lower reservoir, and then into the propagation channel. The comparison of results to theoretical solutions revealed that the method could produce waves with behaviour similar to the dam-break mechanism. Prasetyo et al. (2016) used a hybrid wave generator that combined both piston-type and pump driven wave-maker to investigate the effect of tsunami run-up and force around building structures with 1:20 length scale. The distance of the structures from the coastline, number of structures and distance of buildings from each other had a significant effect on the tsunami inundation and pressure on the structures.

Rahman et al. (2014) used the dam-break method to conduct an experimental study on the potency of sea wall in mitigating tsunami forces on onshore buildings. Different types of sea wall with varying heights and positions were studied, and findings showed greater force reduction in higher sea wall closer to the physical models. Efficacy of solid and perforated sea walls was also investigated, with results showing similar results in both cases. The economic advantage of constructing perforated sea wall over solid sea wall was also suggested. An experimental study was performed by Nistor et al. (2009) to understand better the time development and hydrodynamic forces generated by a fast advancing tsunami bore on varying shapes of a structural element. The impact of debris was also modelled by using wooden logs and results showed increased total force values.

The prime objective of this chapter is to show the suitability of small-scale DBW experiments to model tsunami wave and then compare the results to other hydrodynamic literature. The study will investigate tsunami bore flow over different geometries of sea dikes in an open channel flow to determine velocity and pressure distributions. It would ultimately assist in the understanding of scour profiles behind

sea dikes and thus improve the design of coastal defences built in tsunami-prone regions, which is discussed in detail in the next chapter.

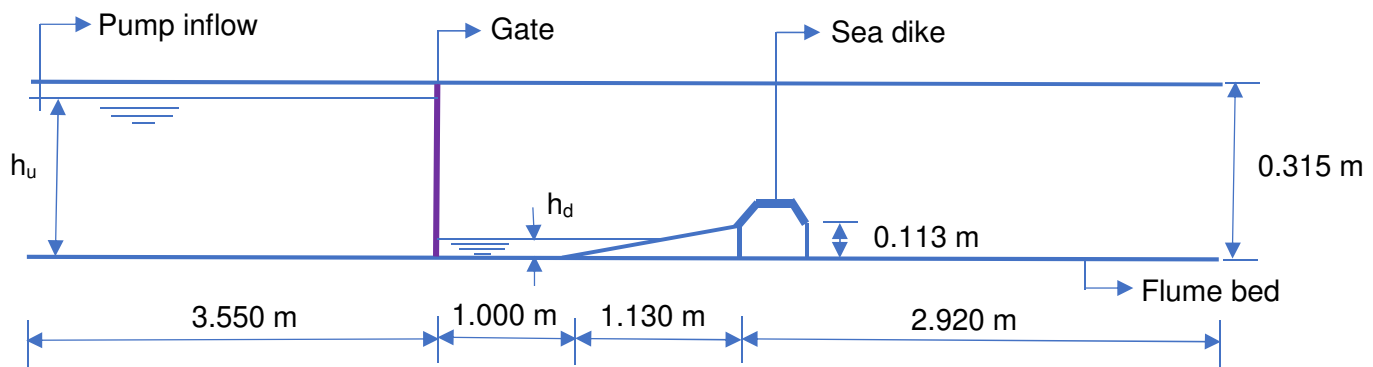
### 3.2. Laboratory Experiments

The difficulty of scaling the very long tsunami waves flow has been a major challenge in the laboratory studies of such phenomenon as they produce a much steeper wave. The introductory reviews above and in chapter two show how experimental studies of quasi-tsunamis have been carried out using solitary waves, long wave generated by wavemaker and dam-break waves. It is possible to produce a dam-break wave whose flow variables is qualitatively similar to actual tsunami waves. However, the difficulty of downscaling the length and time scales of real tsunamis in a small-scale experiment according to Froude similarity law persists.

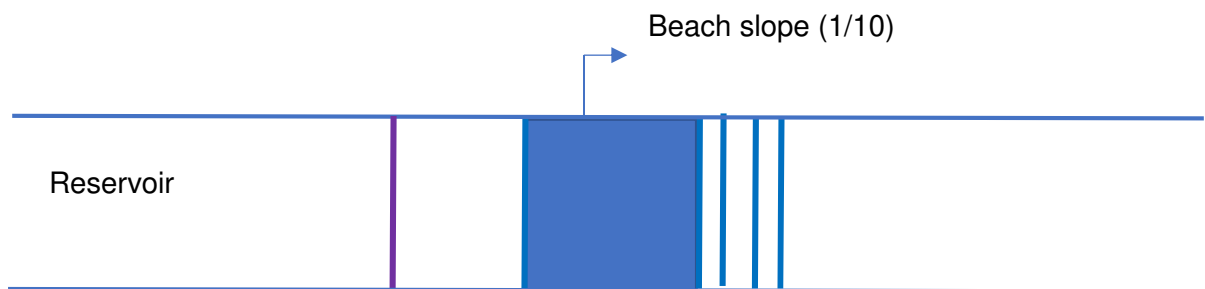
A series of comprehensive fully-controlled laboratory experiments were conducted in University of East London 's hydraulics testing facility with four 0.10 m high coastal dike models of scale 1:50 in a hydraulic flume, 8.60 m in length, 0.315 m in depth, and 0.305 m in width. Two of the model geometries (B and C types) were fabricated to scale of 1:50 by considering dikes that were affected in Iwanuma and Soma cities in Japan by the 2011 Great East Japan Earthquake and Tsunami (Jayaratne et al., 2014). The dam- break method was used to generate a tsunami bore with the gate located at 1.0 m from the toe of the 1:10 beach slope. The upstream water depth,  $h_u$ , was maintained at 0.3 m, while the downstream water depth,  $h_d$ , maintained at 0.015 m, 0.03 m, and 0.05 m were varied to generate hydraulic condition types I, II and III respectively using dimensionless initial downstream water depth,  $\alpha_i, \left(\frac{h_d}{h_u}\right)$  (after studies from Leal, Ferreira, and Cardoso, 2009). Pressure sensors ( $P_1 - P_5$ ) were placed on the seaward slope, crest and landward slope of the models to measure the vertical pressure distribution. Horizontal velocity of the bore front was tracked by 30 fps video camera and by using PhysMo software, a frame-by-frame analysis was employed to derive the velocity at different sections of the flume. The measured data were digitised at the time interval of 0.00004 s (25 kHz).



Figure 3.1. Front view of hydraulic flume channel.



a) Lateral view



b) Plan view

Figure 3.2. The layout of hydraulic flume (Not to scale).

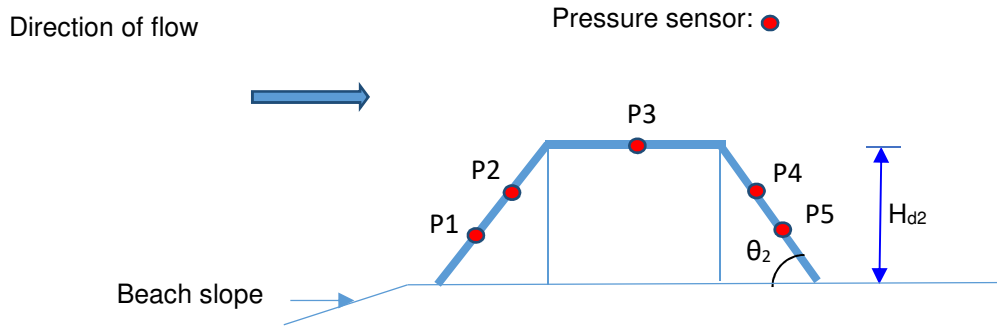


Figure 3.3. Location of pressure sensors.

The scaling of experimental results to prototype conditions is done using the Froude scaling, which is typical of gravity flow. The hydraulic properties of the tsunami bore were scaled as follows:

$$\begin{array}{ll}
 \text{Velocity:} & V_p = V_m \times \sqrt{L_R} \\
 \text{Time:} & T_p = T_m \times \sqrt{L_R} \\
 \text{Pressure:} & P_p = P_m \times L_R
 \end{array} \quad \left. \vphantom{\begin{array}{l} V_p \\ T_p \\ P_p \end{array}} \right\} \quad (3.1)$$

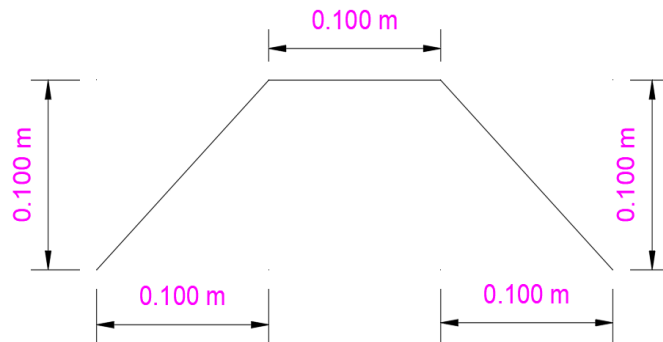
where,  $L_R$  is the scale factor; length ratio between prototype ( $L_p$ ) and model ( $L_m$ ),  $L_R = \frac{L_p}{L_m} = 50$ .

Table 3.1. Hydraulic conditions used in experiments.

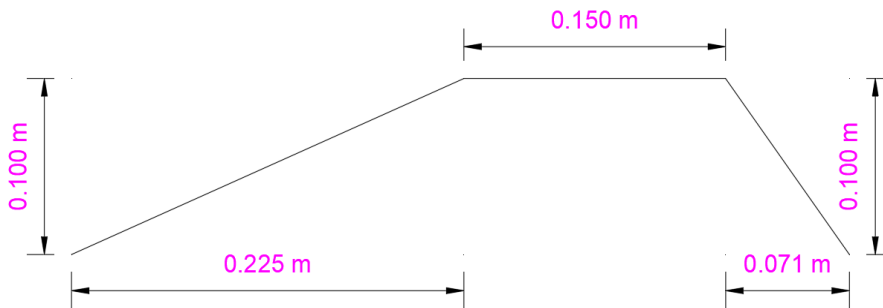
Type	$h_u$ (m)	$h_d$ (m)	$\alpha_i, \left(\frac{h_d}{h_u}\right)$
I	0.3	0.015	0.050
II	0.3	0.030	0.100
III	0.3	0.050	0.167

Table 3.2. Coastal dike model geometry.

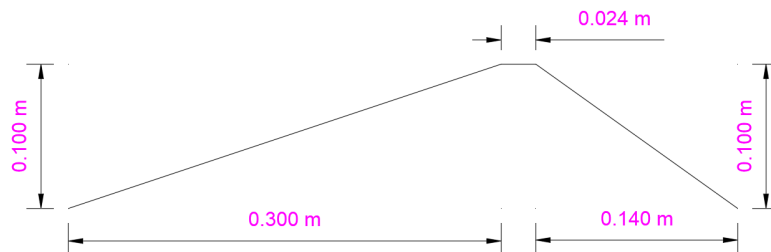
Dike model	Crest width (m)	Seaward slope	Landward slope
A	0.100	1: 1.00	1: 1 .00
B	0.150	1: 2.25	1: 0.71
C	0.024	1: 3.00	1 :1.40
D	0.053	1:1.40	1:2.15



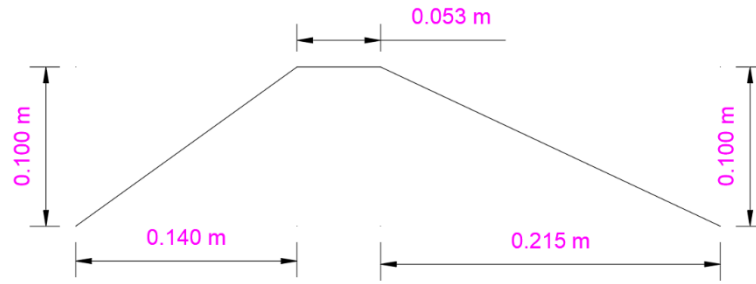
a. Model A



b. Model B



c. Model C



d. Model D

Figure 3.4. Sea dike model geometry.

### 3.3. Tsunami Wave Flow over Sea Dike

The bore from hydrodynamic waves is turbulent and destructive. In certain locations, field observation from 2004 Indian Ocean tsunami showed velocities between 3 to 8 m/s, and 10 to 13 m/s was recorded near Sendai airport during the March 2011 Japan tsunami (Wüthrich et al., 2016). Roh et al. (2012) used Particle Image Velocimetry (PIV) to estimate tsunami velocity at Sunaoshi River during the 2011 tsunami. It avoids the conventional disadvantages of unsteady camera motion and oblique viewpoint and offered reasonable agreement with Particle Tracking Velocimetry (PTV) and theoretical approach. About 8 m/s tsunami flow velocity was estimated within 1 km from the shoreline of the north of Natori river, Fujitsuka, and a maximum velocity value of about 15 m/s was recorded at the town of Onagawa during the 2011 Tohoku earthquake tsunami (Koshimura, Hayashi and Gokon, 2014). In this study, the spatial horizontal velocity of the hydraulic bore of the waves is tracked by an open-source video motion analysis program, PhysMo.

#### 3.3.1 Velocity distribution

Figure 3.4 shows the classification of different sections of the hydraulic flume. The sudden release of the gate generated large turbulence which contributed to the high velocity readings in the downstream section of the channel. There was a reduction of the velocity values as the bore propagates over the beach slope. The noticeably reduced speed was dependent on the hydraulic conditions in the downstream water depth,  $h_d$ .

Considering hydraulic conditions I, the models with steeper seaward slope, A and D, recorded lower maximum velocity; 2.17 m/s and 2.16 m/s respectively, while the

models with milder seaward slope, B, and C, recorded higher values of 2.44 m/s and 2.31 m/s respectively. A reversed trend was noticed for highest downstream water depth; hydraulic condition III. Models A and D both had a velocity of 2.16 m/s while models B and C had values of 2.14 m/s and 2.00 m/s respectively. However, a clear trend was not observed for the type II hydraulic condition (Table 3.3).

The velocity distribution over the crests of models B, C and D revealed a general decrease in bore velocity as the downstream water depth increased, whereas Model A showed an opposite trend. Model B decreased from 2.37 m/s to 2.08 m/s, Model C decreased from 2.26 m/s to 2.00 m/s, Model D decreased from 2.13 m/s to 2.02 m/s for type III hydraulic condition, but with an initial increase to 2.27 m/s for type II hydraulic condition. The opposing trend in Model A was the increase from 1.99 m/s to 2.07 m/s for type II hydraulic condition and then 2.16 m/s for type III hydraulic condition.

There was a general decrease in velocity of the bore over the landward slope for all the models as the downstream water depth increased. Model A decreased from 1.95 m/s to 1.91 m/s, Model B decreased from 2.20 m/s to 2.00 m/s, Model C decreased from 2.20 m/s to 2.01 m/s, and a minimal decrease from 2.00 m/s to 1.99 m/s for Model D. A noticeable increase in velocity was seen in Models C and D for type II hydraulic condition. Model C increased to 2.13 m/s, while Model D increased to 2.15 m/s before a final decrease.

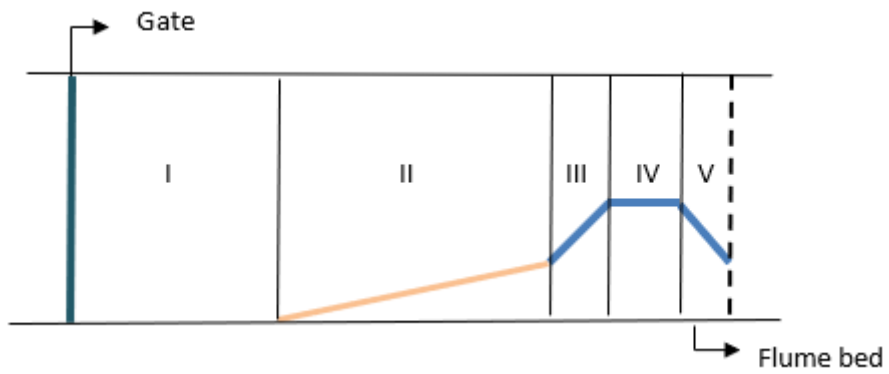


Figure 3.5. Section classification of the hydraulic flume.

Key:

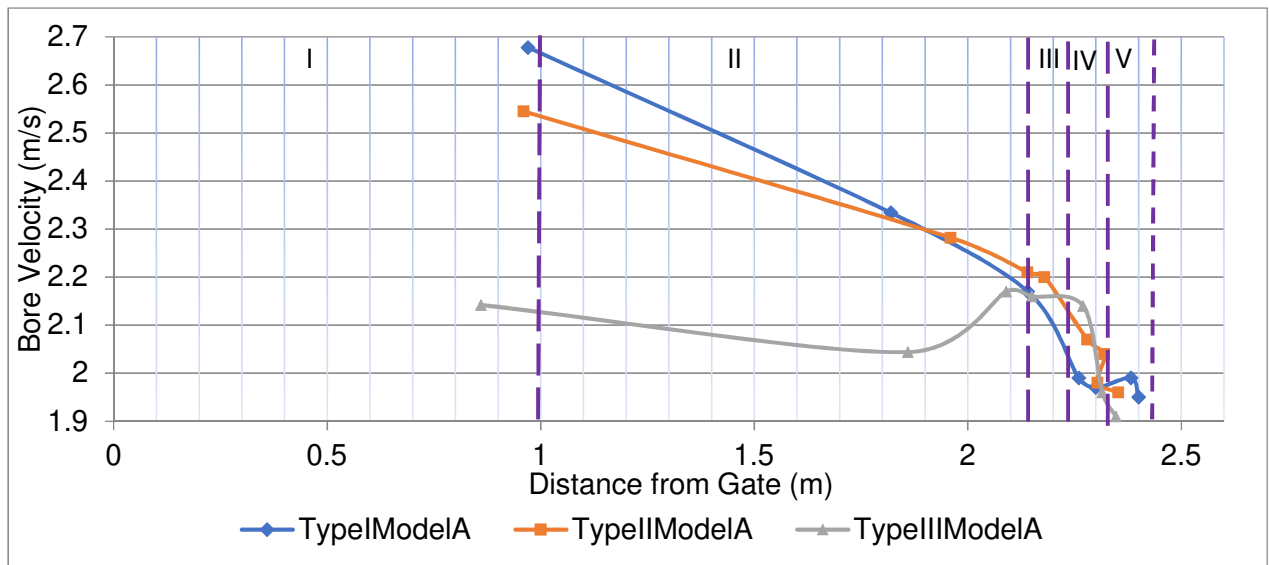
I - Downstream Section

II - Beach slope section

III - Seaward slope section

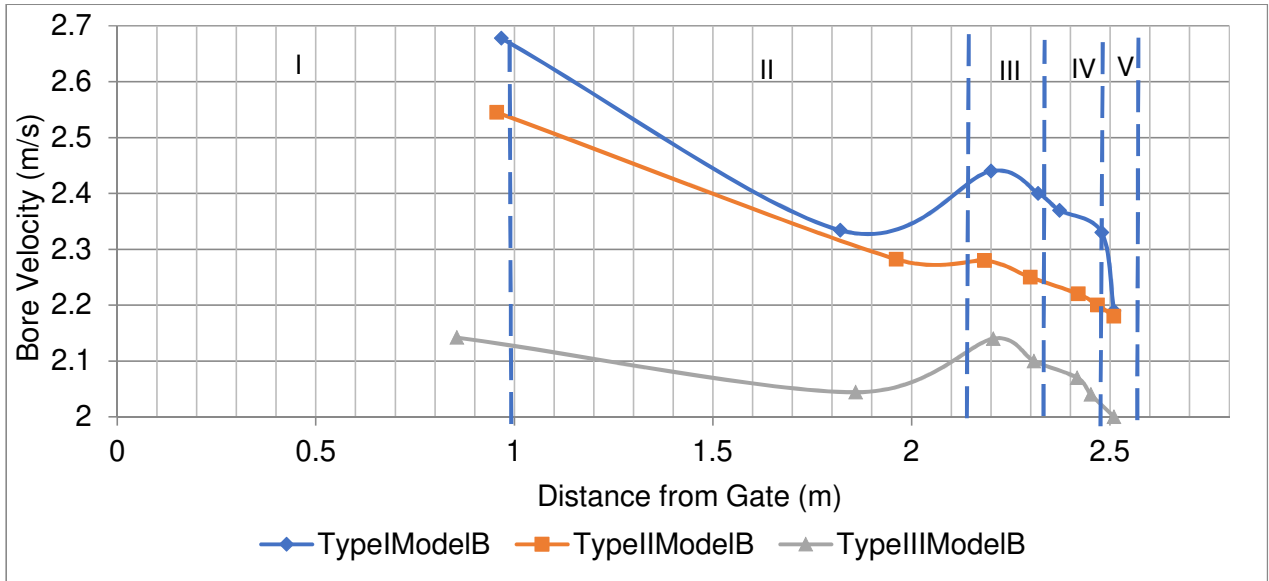
IV - Crest section

V – Leeward/landward slope section

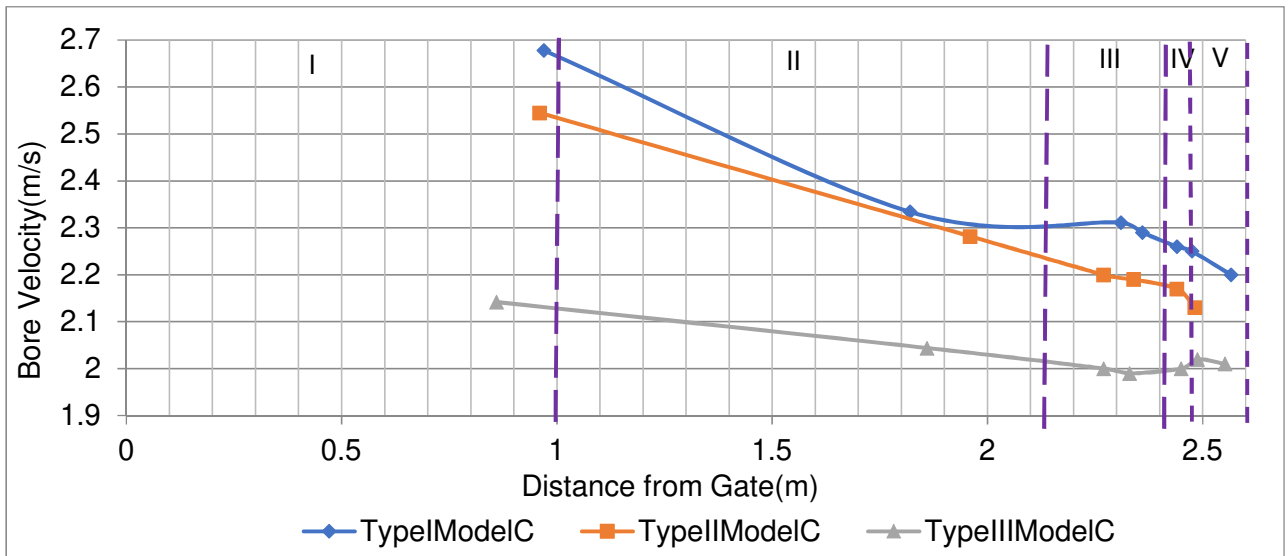


a) Model A

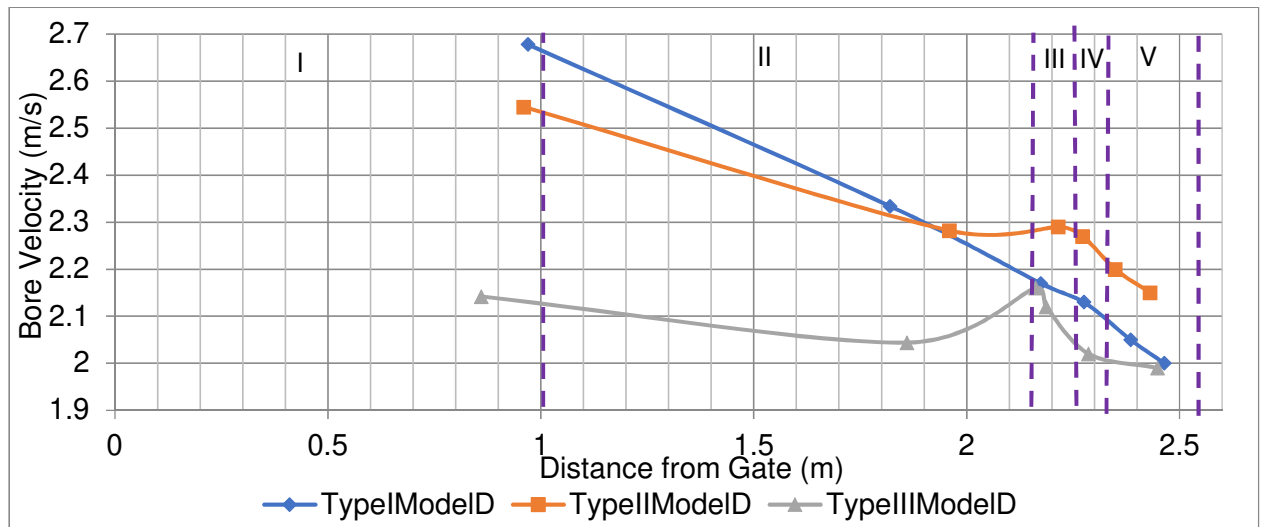




b) Model B



c) Model C



d) Model D

Figure 3.6. Velocity distribution in the hydraulic flume.

Table 3.3: Bore velocity readings for model dikes (Models A, B, C, and D).

Model A

Downstream depth, $h_d$	0.015m		0.03m		0.05m	
	Distance (m)	Velocity (m/s)	Distance (m)	Velocity (m/s)	Distance (m)	Velocity (m/s)
Downstream section	0.97	2.68	0.96	2.55	0.86	2.14
Beach slope section	1.82	2.33	1.96	2.28	1.86	2.04
Seaward slope	2.14	2.17	2.14	2.21	2.15	2.16
Crest	2.20	1.99	2.28	2.07	2.23	2.16
	2.23	1.97	2.32	2.04	2.27	2.14
Landward slope	2.40	1.95	2.40	1.96	2.35	1.91

### Model B

Downstream depth, $h_d$	0.015m		0.03m		0.05m	
	Distance (m)	Velocity (m/s)	Distance (m)	Velocity (m/s)	Distance (m)	Velocity (m/s)
Downstream section	0.97	2.68	0.96	2.55	0.85	2.14
Beach slope section	1.82	2.33	1.96	2.28	1.86	2.04
Seaward slope	2.20	2.44	2.18	2.28	2.21	2.14
Crest	2.37	2.37	2.37	2.24	2.36	2.08
	2.42	2.34	2.42	2.22	2.42	2.07
Landward slope	2.52	2.20	2.53	2.18	2.52	2.00

### Model C

Downstream depth, $h_d$	0.015m		0.03m		0.05m	
	Distance (m)	Velocity (m/s)	Distance (m)	Velocity (m/s)	Distance (m)	Velocity (m/s)
Downstream section	0.97	2.68	0.96	2.55	0.85	2.14
Beach slope section	1.82	2.33	1.96	2.28	1.86	2.04
Seaward slope	2.31	2.31	2.27	2.2	2.27	2.00
Crest	2.41	2.26	2.39	2.17	2.40	2.00
Landward slope	2.57	2.20	2.48	2.13	2.56	2.01

### Model D

Downstream depth, $h_d$	0.015m		0.03m		0.05m	
	Distance (m)	Velocity (m/s)	Distance (m)	Velocity (m/s)	Distance (m)	Velocity (m/s)
Downstream section	0.97	2.68	0.96	2.55	0.86	2.14
Beach slope section	1.82	2.33	1.96	2.28	1.86	2.04
Seaward slope	2.16	2.16	2.22	2.29	2.16	2.16
Crest	2.28	2.13	2.27	2.27	2.29	2.02
Landward slope	2.47	2.00	2.43	2.15	2.45	1.99

### 3.3.2 Configuration of a pressure analog input measurement

LabVIEW is a graphical programming platform that helps engineers scale from design to test, and from small to large systems. It provides integration with all measurement hardware.

A blank Virtual Instrument, VI, was created from the LabVIEW platform (Fig. A1). The DAQ Assistant Express VI was automatically launched once dropped on the diagram after right-clicking on the block diagram and going to Express » Input on the Functions palette (Fig. A2). The DAQ Assistant is a step-by-step wizard that allows quick configuration of measurements.

To configure a pressure analog input measurement was then configured by first selecting Acquire Signals » Analog Input » Pressure » Pressure (Bridge) (Figs. A3, A4, and A5).

The physical channel for the pressure measurement task was then selected. Here the supported data acquisition hardware device, NI 9237 four-channel simultaneous bridge module appeared in the tree control and was then expanded to select physical channel a0 which was used for the task (Figs. A6 and A7).

The natural output of a pressure transducer is a voltage. Most strain based pressure transducers will output a small mV voltage. This small signal requires several signal conditionings to amplify the signal and a data acquisition device to measure the signal. The NI 9237 module singularly provides the excitation voltage, signal conditioning, and data acquisition.

Next, the channel-specific and task-specific settings such as; signal input range, vex value, scaling and timing settings were configured. The inputs limits of the pressure transducers, found on the calibration certificate, were specified, 1 bar for Maximum value and 0 bar for the minimum value. Vex Value of 10 volts was also inputted as specified on the certificate. Continuous Samples was selected for the Acquisition Mode under the Timing Settings on the Configuration tab (Fig. A8).

Two-Point Linear method was used to configure the scale to map physical values to electrical values (Fig. A9). Information on the calibration certificate of the pressure transducer was used to set this scale. For the physical values, 0 was set as the first

value being the lower pressure input limit, and 1 was set as the second value being the upper pressure limit of the transducer. For the electrical value, 0 was set as the first value, while 3.786; the second value is the sensitivity (mV/V) of the transducer  $\left(\frac{\text{Full Scale Output (FSO), mV}}{\text{Excitation Voltage, V}}\right)$ .

The Waveform Graph Indicator was created by right-clicking on the output of the DAQ assistant and going to Create » Graph Indicator (Figs. A10 and 11).

The Write to Measurement File Express VI was launched by right-clicking on the block diagram and going to Express » Output » Write Measurement File on the Functions palette (Fig. A12). This was then configured to a Binary (TDMS) File Format for easy access on MS Excel (Fig. A13).

The Write to Measurement File Express VI was then wired from its terminal to the DAQ Assistant. After scaling the signal and before commencing each experiment, the reference position of the device was identified as 2.0 amplitude. At this position, the pressure transducer produced 0 bar. Finally, the Run button at the top block diagram was then clicked to perform the pressure task (Fig. A14).

### **3.3.3 Total tsunami wave pressure**

Tsunami wave pressure is the sum of the hydrostatic pressure and pressure based on conservation of momentum. Arimitsu (2013) illustrated how the magnitude of these two components could be significantly influenced by the part of the wave that impacted on the structure. Small hydrostatic pressure and large dynamic pressure occur when the bore acts on the structure, while large hydrostatic pressure and small dynamic pressure occur when the main body of tsunami acts on the structure. Dynamic pressure is the difference between total pressure and hydrostatic pressure, and Constantin (2016) showed that 'the dynamic pressure in an irrotational regular wave train attains its maximum value at the wave crest and its minimum value at the wave trough if there are no underlying currents.'

The limitation of the experimental set-up made it difficult to accurately ascertain, from the removal of the flume gate, the exact start time of the wave pressure development over the sea dike models. The approximate times the waves hit the different sections of the models were determined using the video camera.

### **3.3.3.1 Model A**

Figure 3.6 shows the total wave pressure for the three hydraulic conditions. The total wave pressure increased from 0.38 bar at P1 (the toe of seaward slope) and reached its maximum at the crest (0.50 bar) in Type I hydraulic condition (Fig. 3.6a), where the maximum negative pressure was also recorded. The values of the overflowing wave pressure were higher at the landward slope than at the crest in all the hydraulic condition types, though its time duration was only about 1.8 s. This is mainly due to the very steep seaward slope directing the flow away from the landward slope. As shown in Type II hydraulic condition (Fig. 3.6b), the maximum total wave pressure decreased from 0.38 bar at the seaward slope, P2, to 0.33 bar at the crest, P3. Similar to Type II hydraulic condition, the maximum total wave pressure occurred at the seaward slope, P2, and decreased from 0.52 bar to 0.40 bar at the crest, P3, in the Type III hydraulic condition (Fig. 3.6c). Types II and III hydraulic conditions recorded their maximum overflowing wave pressure at the landward slope, on the other hand, Type I hydraulic condition recorded it at the crest.

### **3.3.3.2 Model B**

Type I hydraulic condition in Figure 3.7a shows that the maximum total wave pressure of 0.49 bar occurred at the seaward slope, P1, and decreased to 0.35 bar on impacting on the crest, P3. This trend was consistent with the other two hydraulic conditions. Maximum total wave pressure of 0.40 bar at the seaward slope, P2, reduced to 0.36 bar at the crest, P3, in the Type II hydraulic condition (Fig. 3.7b) and in Type III hydraulic condition (Fig. 3.7c), maximum total wave pressure of 0.43 bar at the seaward slope, P1, reduced to 0.37 bar at the crest. The overflowing wave pressure was more sustained at the crest than at seaward slope. Like Model A, the duration of the overflowing wave pressure at the landward slope was about 2.2 s, with P5 which is closer to the toe of the landward slope readings before P4. This is mostly due to the very steep slopes and long crest width directing the flow away from the slopes. Reduced maximum impact pressure readings at seaward slope were recorded in both Types II and III hydraulic conditions. Similar to Model A, the largest negative total wave pressure occurred for Type I hydraulic condition.

### **3.3.3.3. Model C**

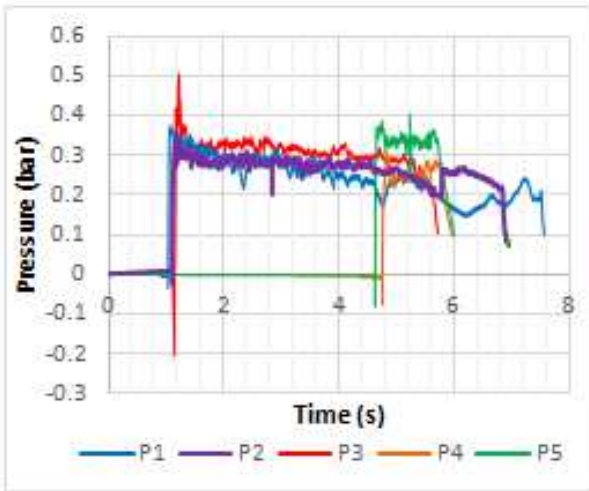
Figure 3.8 provides the instantaneous distribution of total wave pressure for Model C. Maximum wave pressure of 0.60 bar was recorded immediately after the impact of the bore on the seaward slope at the time,  $t = 0.95s$ . The reduction of wave pressure to 0.38 bar was noticed during the overflowing of the wave over the crest and later increased to 0.48 bar at P5. There would be the possibility of more significant damage to the crest and landward slope of the dike than at the seaward slope as evident by the large pressures sustained during the overflowing phase.

Unlike occurrences of Models A and B, there were more sustained overflowing wave pressures on the landward slope, and the bore first impacted the landward slope at P4 before P5. The maximum impact wave pressure values at the seaward slope and maximum overflowing wave pressure values at the landward slope reduced with increasing downstream depth condition,  $h_d$ . The overflowing pressure values at the crest are larger than at landward slope as the downstream depth,  $h_d$ , increases.

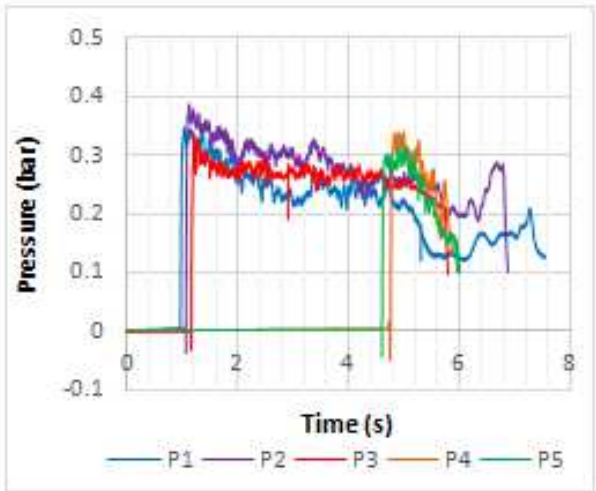
### **3.3.3.4 Model D**

The result of Type I hydraulic condition (Fig. 3.9a) showed that large values of overflowing wave pressure were sustained at the landward slope during the flow, suggesting the occurrence of the greatest damage when compared to other parts of the dike. As shown in Type III hydraulic condition (Fig. 3.9c), there were similar maximum wave pressure values of 0.37 bar during the impact and overflowing phases, except at the landward slope, P4, with a value of 0.34 bar.

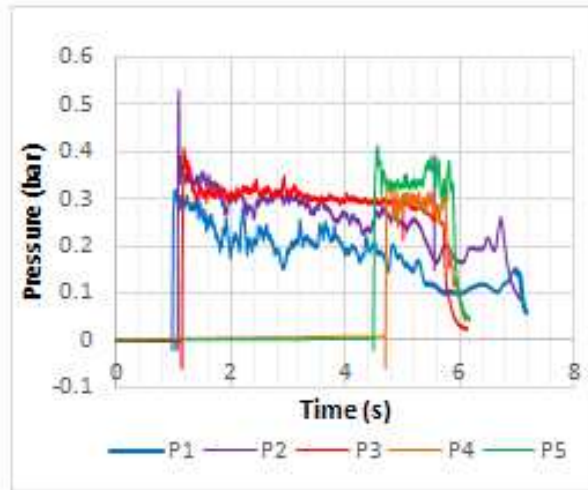
The maximum impact wave pressure occurred close to the toe of the seaward slope, P1. Similar to Model C, the maximum overflowing wave pressure at the landward slope decreased with increasing downstream water depth,  $h_d$ , and the overflowing pressure values at the crest were larger than at landward slope as the downstream depth,  $h_d$ , increased.



a. Type I hydraulic condition



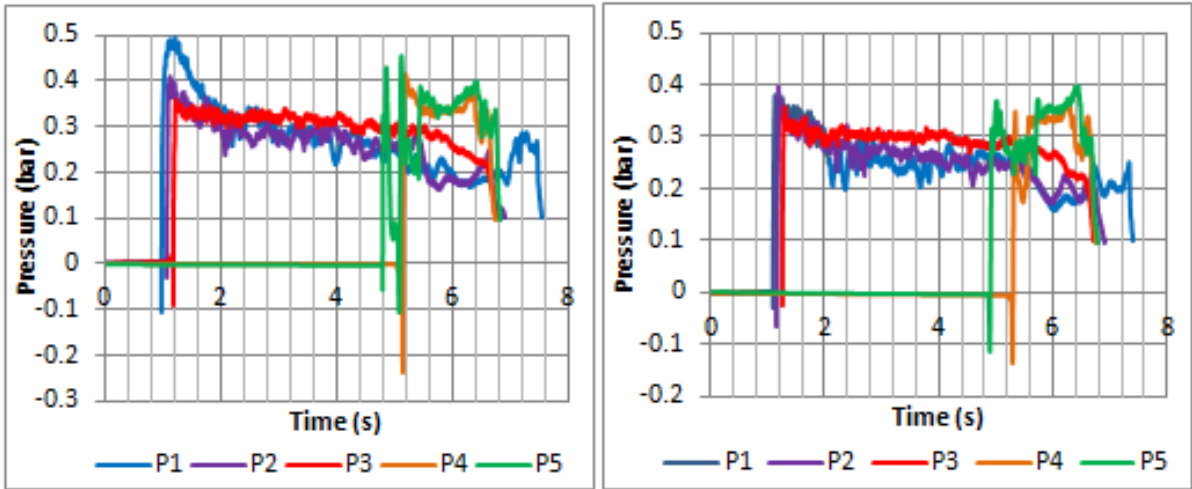
b. Type II hydraulic condition



c. Type III hydraulic condition

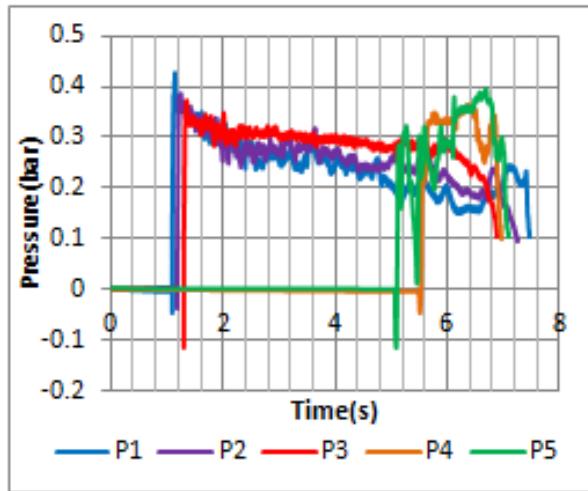
Figure 3.7. Total wave pressure distribution in Model A under various hydraulic conditions.





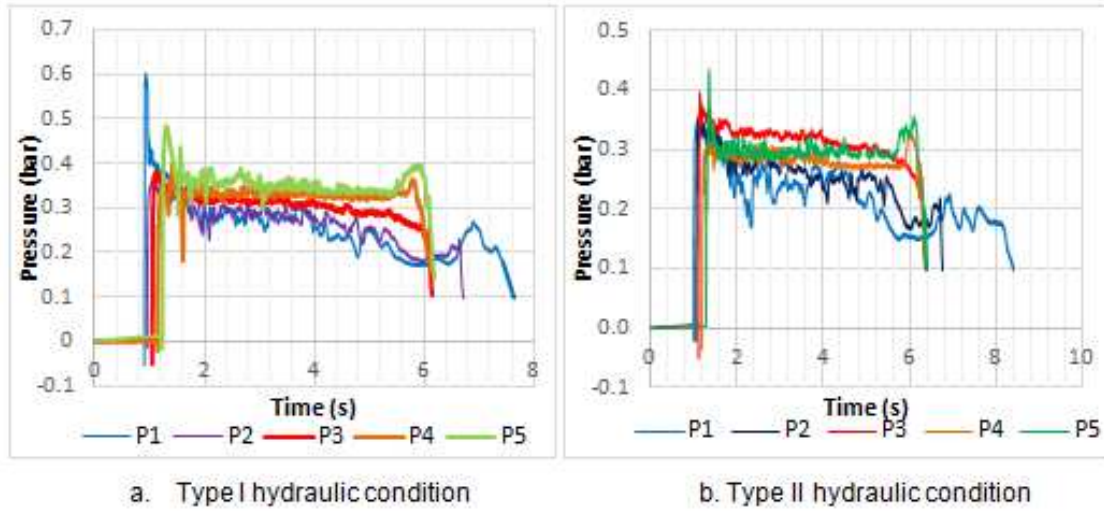
a. Type I hydraulic condition

b. Type II hydraulic condition



c. Type III hydraulic condition

Figure 3.8. Total wave pressure distribution in Model B under various hydraulic conditions.



I

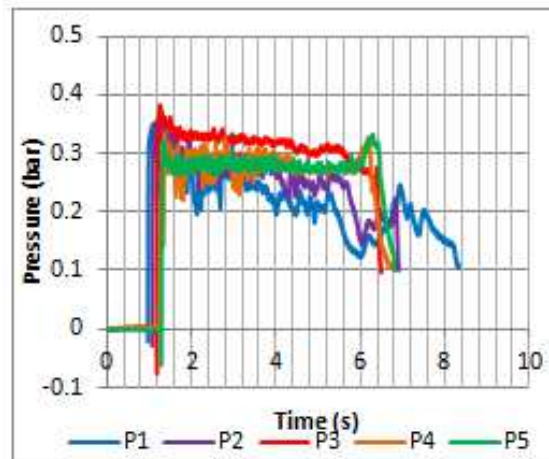
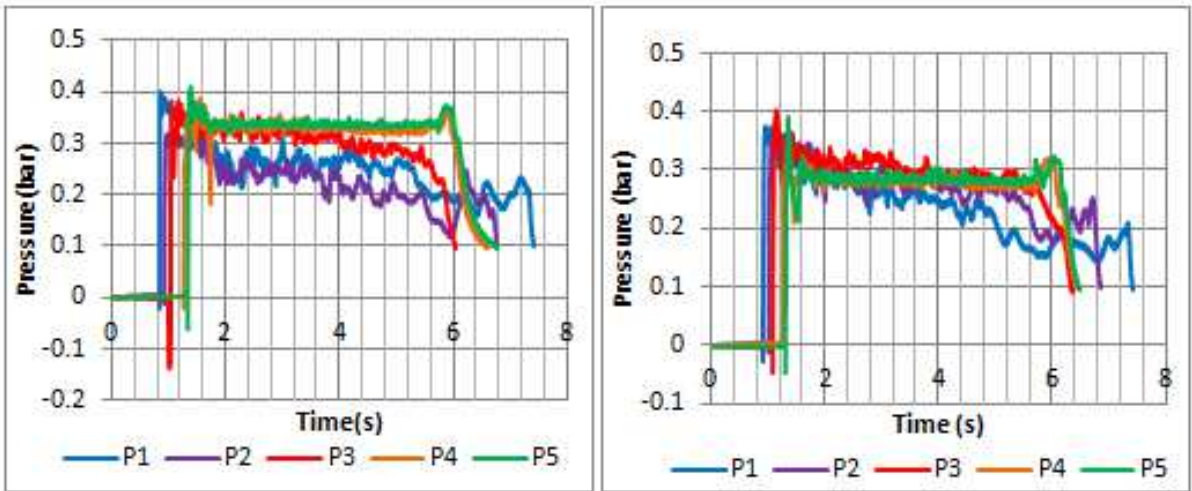
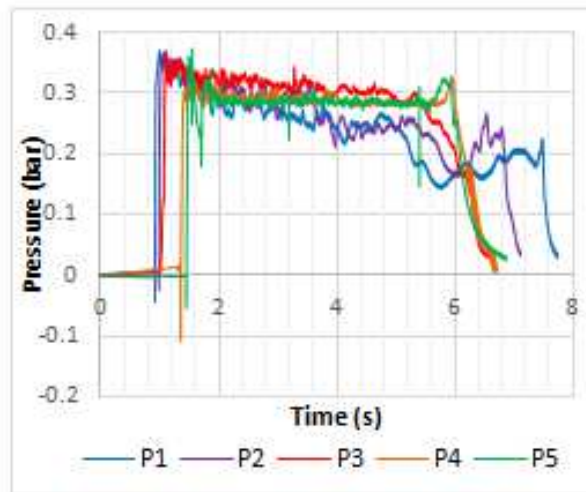


Figure 3.9. Total wave pressure distribution in Model C under various hydraulic conditions.



a. Type I hydraulic condition

b. Type II hydraulic condition



c. Type III hydraulic condition

Figure 3.10. Total wave pressure distribution in Model D under various hydraulic conditions

### 3.3.4 Overflowing Wave Pressure

The collision of the overflowing bore with the back of the model generates a maximum overflowing pressure,  $P_{om}$ , with maximum velocity over the crest measured at the landward region,  $V_m$ , angle of landward slope,  $\theta_2$ , density of water,  $\rho$ , gravitational constant,  $g$ , and height of dike crest measured on landward side,  $H_{d2}$ , as its essential model parameters.

$$\frac{P_{om}}{\rho g H_{d2}} = 2\sqrt{2} \frac{V_m \sin \theta_2}{\sqrt{g H_{d2}}} \quad (3.2)$$

Hydraulic conditions for Models A, B and C seem to best fit the formula for the maximum overflowing pressure with a combined coefficient of the determinant (r-squared) of 0.72, while the introduction of the Model D with the mildest landward slope reduced the coefficient to 0.36 (Fig. 3.10).

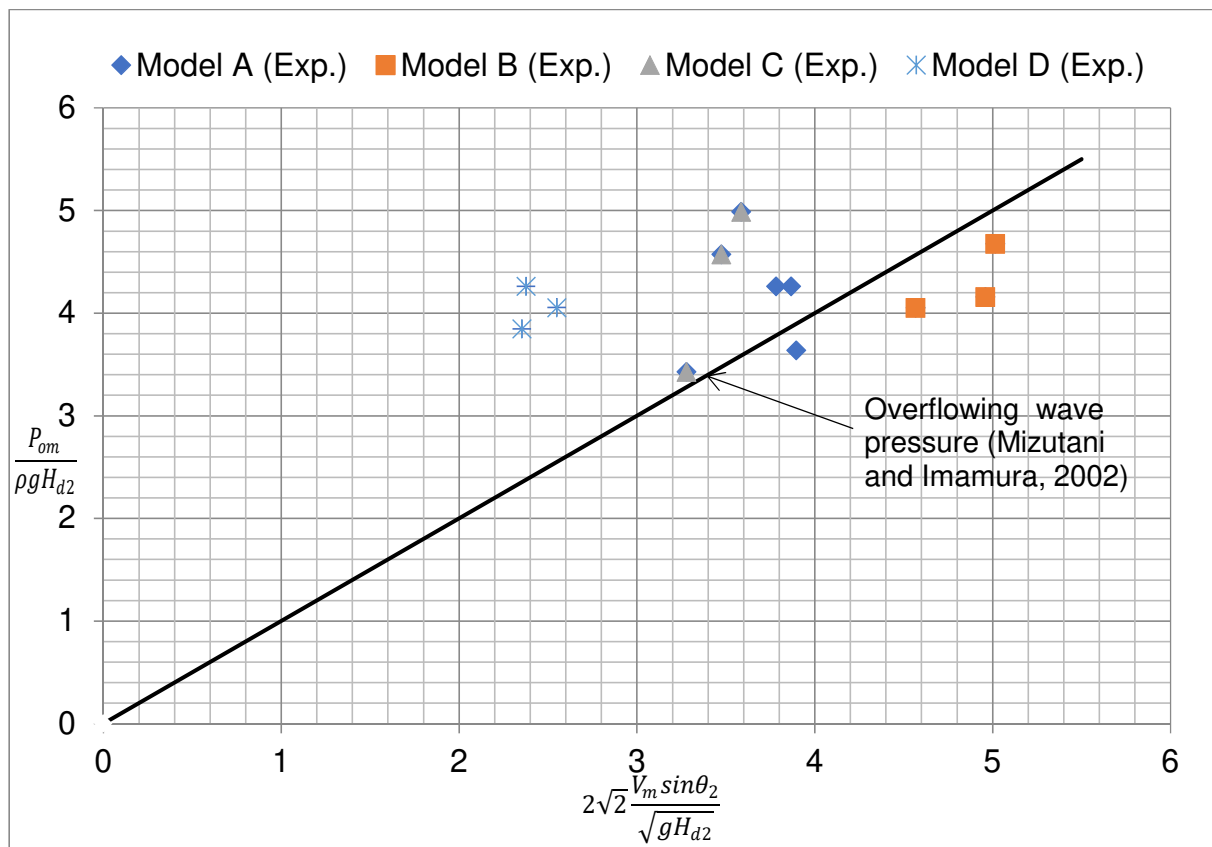


Figure 3.11. The relationship between overflowing wave pressure and flow quantities from experimental (Exp.) studies.

Average error, E, which indicates the suitability of a model to observed data shows that coastal dike model D data, with the mildest landward slope, has the largest deviation from the model equation of overflowing wave pressure (Table 3.4). It is expressed mathematically as:

$$E = \frac{\sqrt{\sum_{i=1}^N (\hat{Y} - Y_i)^2}}{N} \quad (3.3)$$

where  $\hat{Y}$  is the model data,  $Y_i$  is the observed data and N is the total number of data.

Table 3.4. Average Error of the observed data from the overflowing wave pressure model.

Model	$\hat{X} = 2\sqrt{2} \frac{V_m \sin \theta_2}{\sqrt{gH_{dz}}}$	$Y_i$ (Observed data)	$\hat{Y}$ (Model data)	E (Average error)
A	3.87	4.26	3.87	0.22
	3.89	3.64	3.89	
	3.78	4.26	3.78	
B	5.02	4.68	5.02	0.34
	4.96	4.16	4.96	
	4.57	4.05	4.57	
C	3.59	4.99	3.59	0.60
	3.47	4.57	3.47	
	3.28	3.43	3.28	
D	2.37	4.26	2.37	0.95
	2.55	4.05	2.55	
	2.35	3.85	2.35	

### 3.4 Conclusions

This chapter started with the introduction of the experimental methods that have been used to study tsunami waves: piston type wave generator and pump driven wave generator to produce solitary wave and long wave with tsunami-like characteristics, and vertical water volume release method and dam break mechanism to generate dam break wave.

The description of the experimental set-up to investigate the propagation of the tsunami-like wave over sea dike models and instrumentation were adequately presented. This included the geometry of the four sea dike models, the three hydraulic conditions, and configuration of the pressure sensors.

In these experiments, a dam-break bore, like the one occurring during a tsunami inundation was generated by the sudden opening of a vertical gate and afterwards impacted coastal dike models of various geometries. The flow velocities and pressures exerted on the seaward, and landward slopes of the model dikes were recorded and analysed in detail to estimate the flow variables around the structures. Also, the characteristics of the interaction between bore and coastal models were discussed.

The velocity distribution revealed a general decrease in the bore velocity as the downstream water depth increased. This could be due to the frictional resistance between the upstream and downstream water. The final bore velocity at the landward slope has an average prototype value of 14 m/s which is significantly close to the maximum of 15 m/s that was recorded inland at Onagawa during the 2011 Tohoku tsunami. The angle of the seaward slope affected the percentage decrease in velocity value over the three hydraulic conditions. The mildest seaward slope, Model C, produced 5% decrease in velocity value, and 3% decrease in velocity value was estimated for Model B with the second mildest seaward slope. Model D with the third mildest seaward slope produced about 0.5% decrease in velocity value, while the steepest models, Model A, gave about 1% decrease in velocity value.

In general, the experimental results revealed that the overflowing pressure values at crest increased above that at the landward slope as downstream depth increased for dike with a mild landward slope. Overflowing pressure values were larger at landward slope than crest for dikes with the steep landward slope for all the three hydraulic

condition types. The average error statistical measure showed a good agreement of the experimental results with the linear formula for overflowing wave pressure (Eq. 3.2). This pressure could be reduced by introducing a wave wall. Also, coastal dikes with steep landward slope and longer crest width have lower impact duration of overflowing pressure on the landward slope, hence their suitability for the reduction of tsunami wave pressure.

## Chapter 4

### Tsunami Induced Scour Profile on Erodible Boundaries

The scour profile and depth prediction that develops on the leeward side of coastal structures can play an integral role in their design. The Great Japan Tsunami of 2011 revealed the destructive impact scour could have on coastal defence structures. The prediction of the depth and the shape of scour holes that develop behind coastal defences can play a significant role in their stability design. The high cost of protecting the long stretch foundation necessitates the study of the maximum scour depth and length to assess the risk of failure (Karim and Ali, 2000).

There is limited research into understanding this tsunami-related phenomenon. Kato et al. (2007) after large-scale hydraulic experiments proposed ground improvement technique to produce a resilient coastal dike foundation. Jayaratne et al. (2014) using field survey data developed a simple mathematical model to predicts representative scour depth that can be employed in their foundation design.

In this chapter, the work will focus on the geometry of the scour profiles and its temporal development, scour validation with Shields parameter and Hjulstrom curve, representative scour depth predictive model, statistical comparison of the model to field survey and laboratory data, and proposing coastal dike section capable of resisting landward toe scour. Appropriate conclusions will also be deduced.

#### 4.1 Introduction

Coastal structures near the shorelines are susceptible to local scouring damage caused by tsunami runup and drawdown. Many of these structures have shown to be inadequate against higher levels of tsunami waves as revealed by the 2004 Indian Ocean Tsunami and 2011 Eastern Japan Tsunami. Numerous researches have made many design considerations to be given to these infrastructures; bridges, roadways, buildings, and port facilities.

Chen et al. (2013) employed laboratory study to understand tsunami-induced scour at a road model on a sandy beach. They discovered that tidal variation which affected the variation of the distance between the shoreline and road model was a critical factor that affected the scour depth. Their results also showed that equilibrium scour depth



might not be reached in typical tsunamis. Scouring mechanisms caused by tsunamis around vertical coastal cylindrical structure was studied by Yeh et al. (2004). The end of the drawdown phase of the tsunami runup when the flow velocities and shear stresses have greatly reduced, accounted for the most rapid scour occurrence. Also, the critical fraction of the buoyant weight of the sediment  $\Lambda$  was discovered to affect the scour results.

Riggs et al. (2008) investigated the risk posed by tsunami-like waves to coastal infrastructures. Their study also focused on the study of sediment transport and scour. The results indicated a significant sand erosion and high influence of wave type and bathymetry on the scour and deposition pattern. Chen et al. (2015) studied the protective capability of submerged and emerged breakwater in preventing tsunami-induced scour. The emerged breakwater was shown to have the more significant effect on tsunami scour reduction on the sandy beach than the submerged breakwater.

Daghighi et al. (2015) used an experimental study to examine tsunami-induced sediment transport, bed deformation, and sustainability of sandy beaches with varying grain diameters. Results showed that bed deformation and sustainability were significantly affected by the wave breaking point. The quantity of transported sand material is greatly affected by the grain sizes. Two types of flow pattern – hydraulic jump and submerged flow - were observed by Mitobe et al. (2014) in their study of the scouring process at the landward toe of coastal dike models.

Experimental and numerical studies were conducted by Tsujimoto et al. (2014) on the effects of artificial trenches in reducing the turbulent kinematic energy that ultimately affected the development of scour hole behind seawalls. The kinematic energy was discovered to influence the scour development and its decay rate was depended on the scale and not the shape of the trench. The shape of the trench was discovered to affect the reduction of tsunami energy, with a trapezoidal shape more effective than the rectangular. Also, the rapid development of a scour hole was seen immediately after the start of the overflow.

The reviews above have not provided a detailed quantitative understanding of the influence of tsunamis on the landward region of a coastal defence structure. The chapter will seek to provide improved insight into the development of soil profile behind a sea dike by investigating tsunami bore flow over different geometries of sea dikes in

the open channel flume described in Chapter three. The suitability of small-scale DBW experiments to model tsunami-induced scour is shown, and a coastal dike section capable of resisting extensive damage to landward toe is proposed.

## 4.2 Experimental Work

The difficulty of physically modelling sediment grain to study tsunami-scour is a concern for coastal engineers. Scaling effects of small-scale sediment scour laboratory studies are undoubtedly relevant since typically the sediments are modelled at full scale, while the tsunami waves are modelled at a reduced scale. Modelling the sediments at reduced scale will result in the use of very fine cohesive grains and thus an inaccurate representation of real sand substrate. Natural sediment grains have been used in existing research of tsunami-induced sediment transport (Kato, Sato and Yeh, 2000; Tonkin et al., 2003; Jiang et al., 2015; Chen et al., 2015).

Extensive laboratory experimental set-up discussed in Section 3.2 was adjusted to accommodate a layer of sand at the landward region. The experiments were performed with erodible sediment sand with mean grain diameter,  $D_{50}$ , of 0.35 mm. Sandpit, levelled to a uniform depth of 0.113 m, was built at the toe of the landward slope of the coastal dikes, and its depth was judged accordingly to prevent it from being exceeded by the scour depth (Figs. 4.1 and 4.2). The engineering properties of the sand particle were determined by grain size analysis experiment (Fig. 4.3).

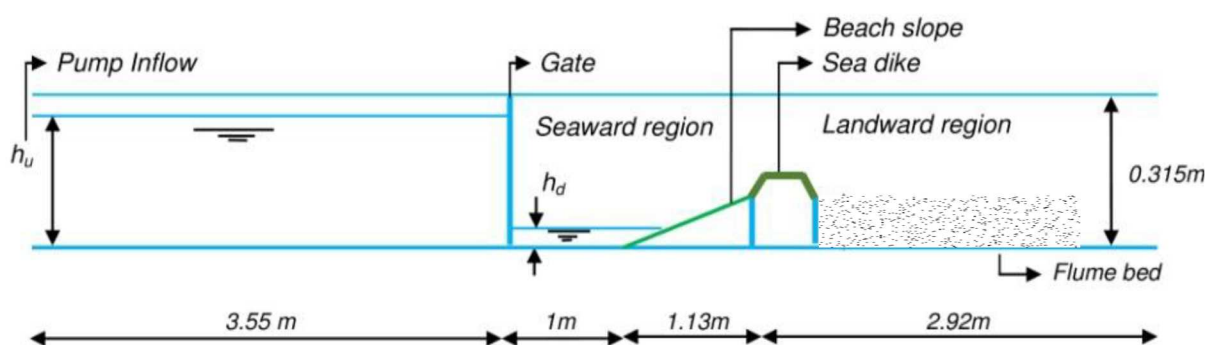


Figure 4.1. Schematic sketch of the experimental set-up at UEL.

(Image reproduced with permission of the rights holder, World Scientific, Appendix C)



Figure 4.2. Lateral view of representation of the experimental set-up.

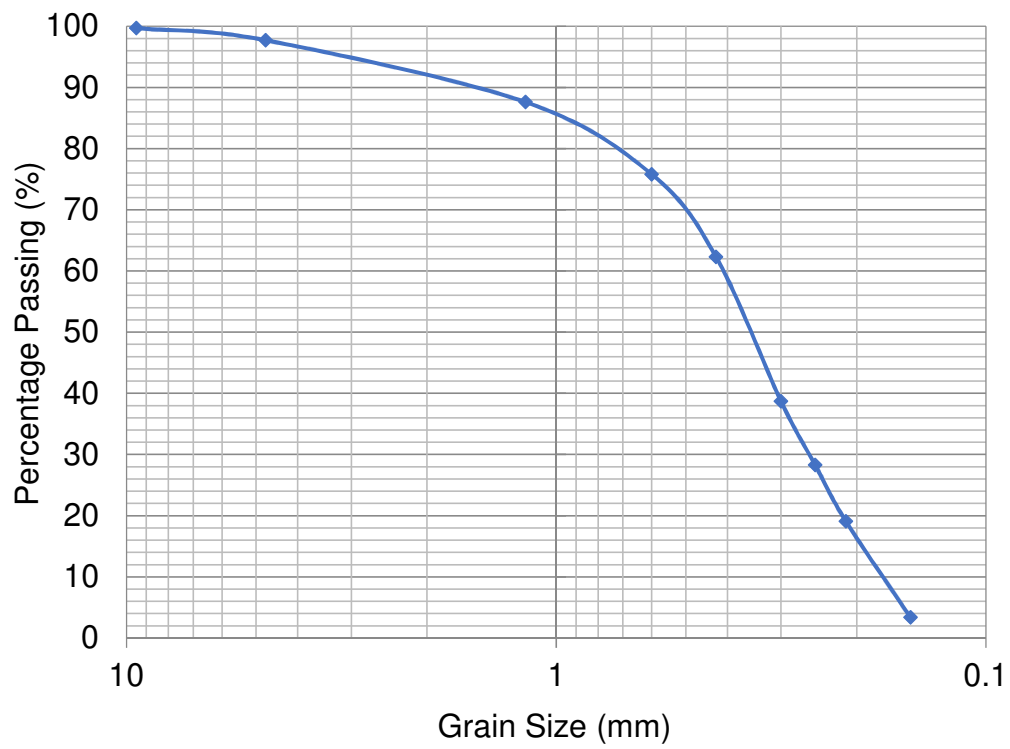


Figure 4.3. Grain size distribution curve.

From Grain size distribution curve:

Percentage of sand = 97.7

% Fine sand = 62.3

% Medium sand = 25.3

% Coarse Sand = 10.1

Percentage of gravel = 2.3

% Fine Gravel = 2.3

Uniformity Coefficient,  $C_u = \frac{D_{60}}{D_{10}} = \frac{0.4}{0.18} = 2.22$

Coefficient of Curvature,  $C_c = \frac{(D_{30})^2}{D_{10} \times D_{60}} = \frac{(0.25)^2}{0.18 \times 0.4} = 0.868$

Soil Permeability,  $K \text{ (m/s)} = 0.01 D^2_{10} = 0.01 \times (0.18)^2 = 2.56 \times 10^{-4} \text{ m/s}$

Using the Unified Soil Classification System, USCS, the material falls within the SW group because the sample is predominantly sand (97.7%) and less than 5% of the soil samples pass through the 75  $\mu\text{m}$  sieve. Therefore, the soil sample is a well-graded sandy soil.

A video camera of 30 FPS and a point-gauge (Fig. 4.4) were used to measure the duration of the scouring process and the depth of the scour hole respectively. The vertical movement of the scale measured scour depth readings at the point where the point-gauge just slightly touched the scoured bed surface.



Figure 4.4. Point gauge (manually operated) for measuring scour profile.

A point gauge is fixed to a sliding frame, which is clamped to the sides of the channel. The movable rod of the point gauge can slide upward and downward over the hydraulic flume. The end of the rod was lowered to the scour hole base, and the distance of rod displacement was measured at each horizontal location. The scour measurement was taken along the centreline of the channel in both horizontal and vertical directions.

The change in the bed surface level was recorded after every run of the experiment. The procedure was run three times to ascertain the actual scour profiles for each hydraulic conditions of the different geometries of the dike models (Appendix B). The measured scour depth values,  $D_s$ , and corresponding scour length,  $L_s$  were recorded. The sand particles and waste water were then carefully removed from the flume. An example of the aftermath of the scouring process is shown in Fig. 4.5.

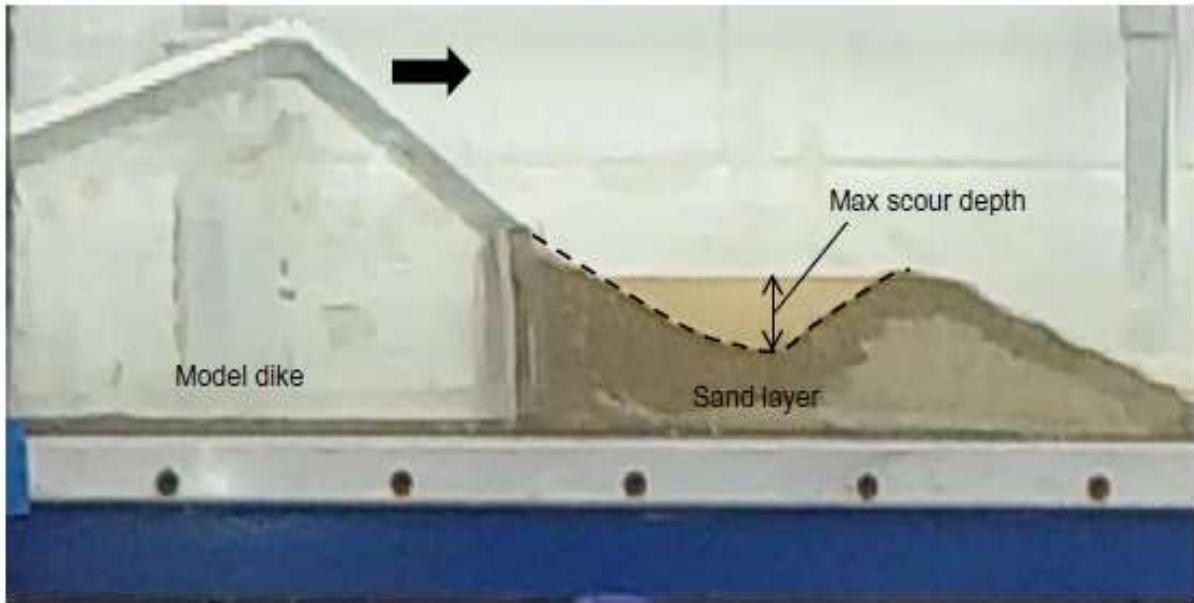


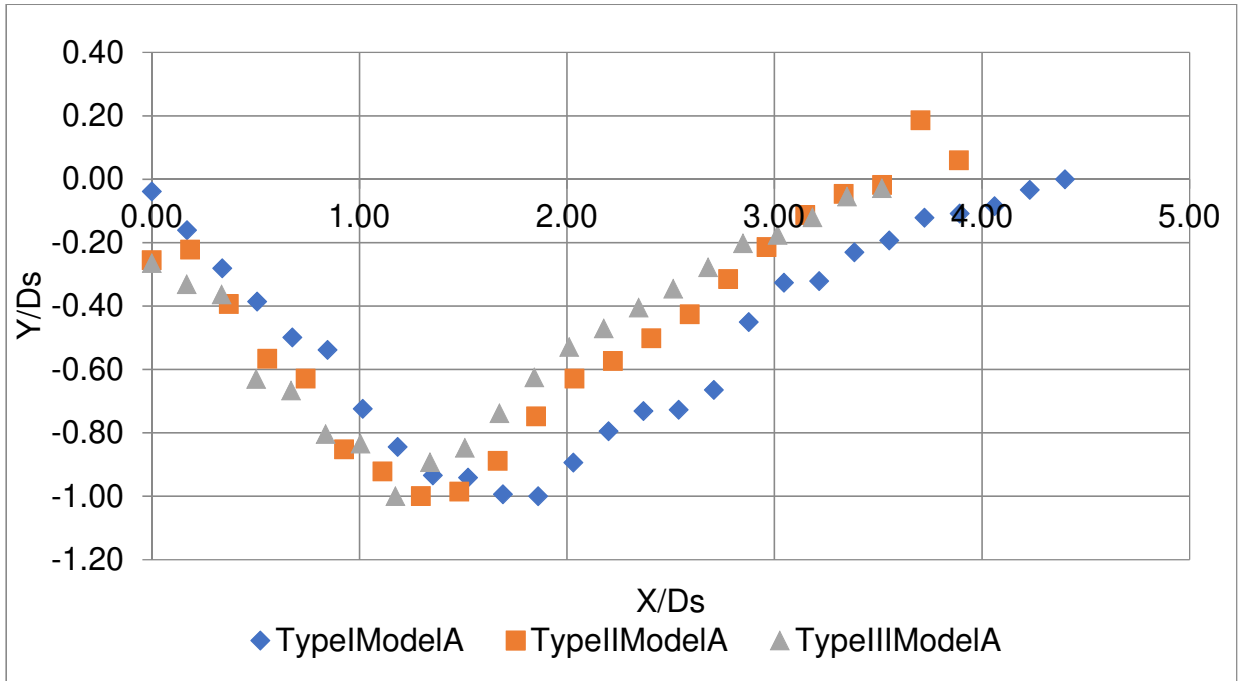
Figure 4.5. Snapshot of model C scour experiments.

(Image reproduced with permission of the rights holder, World Scientific, Appendix C)

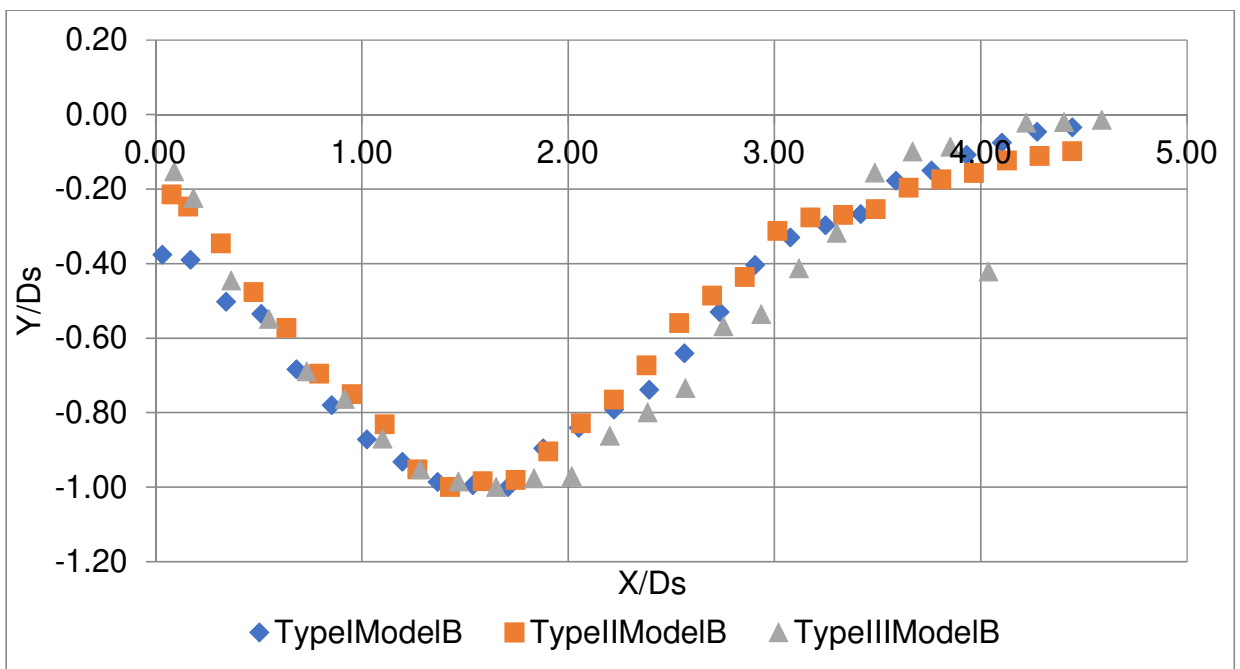
### 4.3 Scour Profile Characteristics

A moving point gauge with a vernier scale was used to measure the size of the scour holes behind the model coastal dike, and a level was used to position a layer of sand during the scour process. The dynamic changes in scour depth and extent from the initial leveled plane-bed were recorded and analyzed using video imagery technique. It was estimated that the prototype scour duration is approximately 42 s.

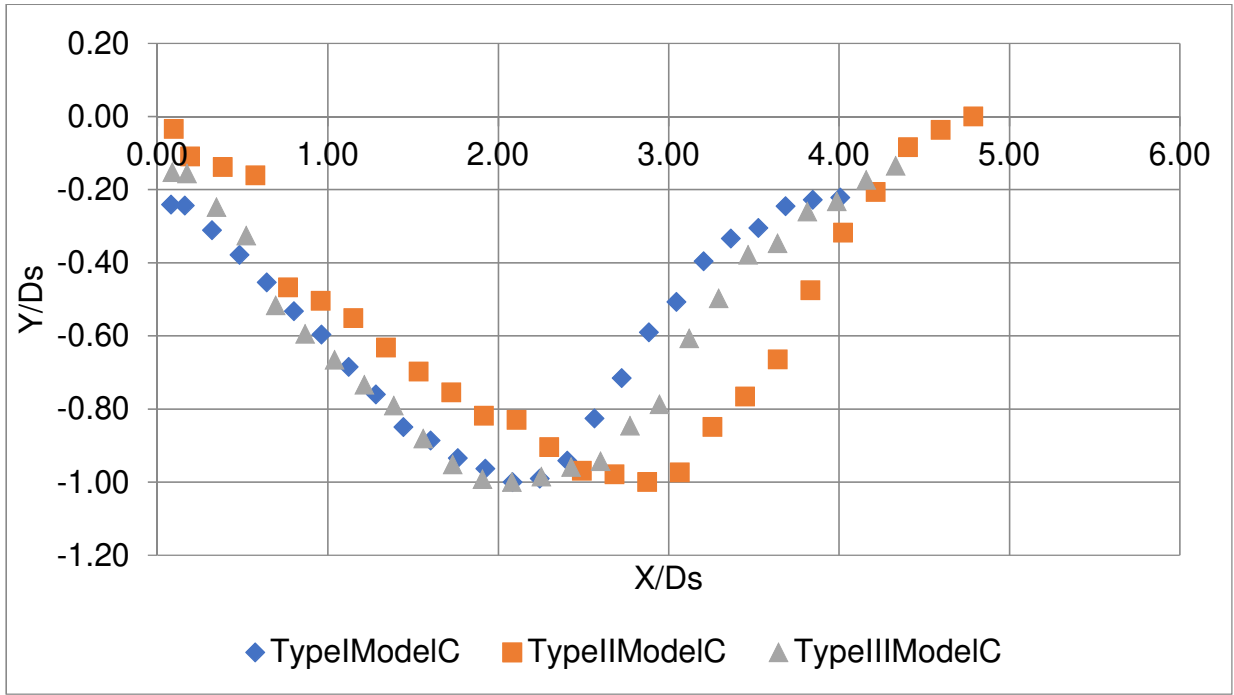
The scour profiles were established by plotting the profiles in terms of non-dimensional depth against non-dimensional horizontal distance (Fig. 4.6). The landward slope toe is at coordinate (0, 0), while the ground level is along coordinates (0, 0) and (5, 0). In general, the corresponding horizontal location of the maximum scour depth is closer to the dikes of hydraulic conditions II and III than the condition I. The steeper the landward slope, the closer the maximum scour depth to the landward toe.



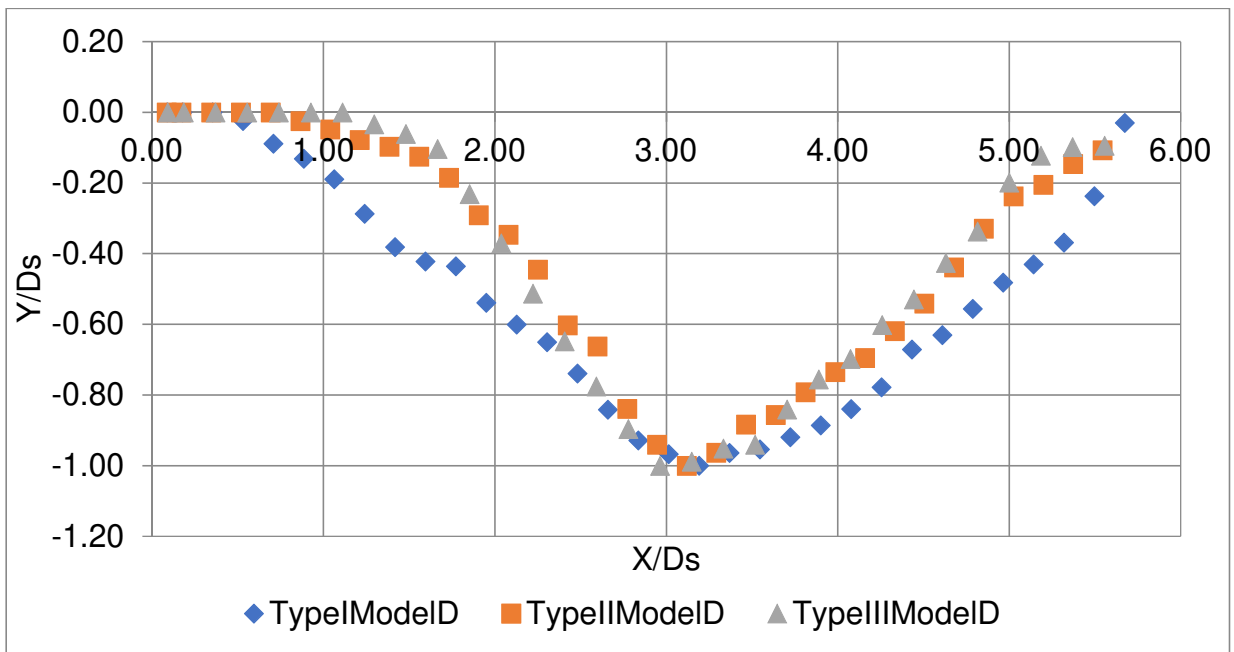
a) Model A



b) Model B



c) Model C

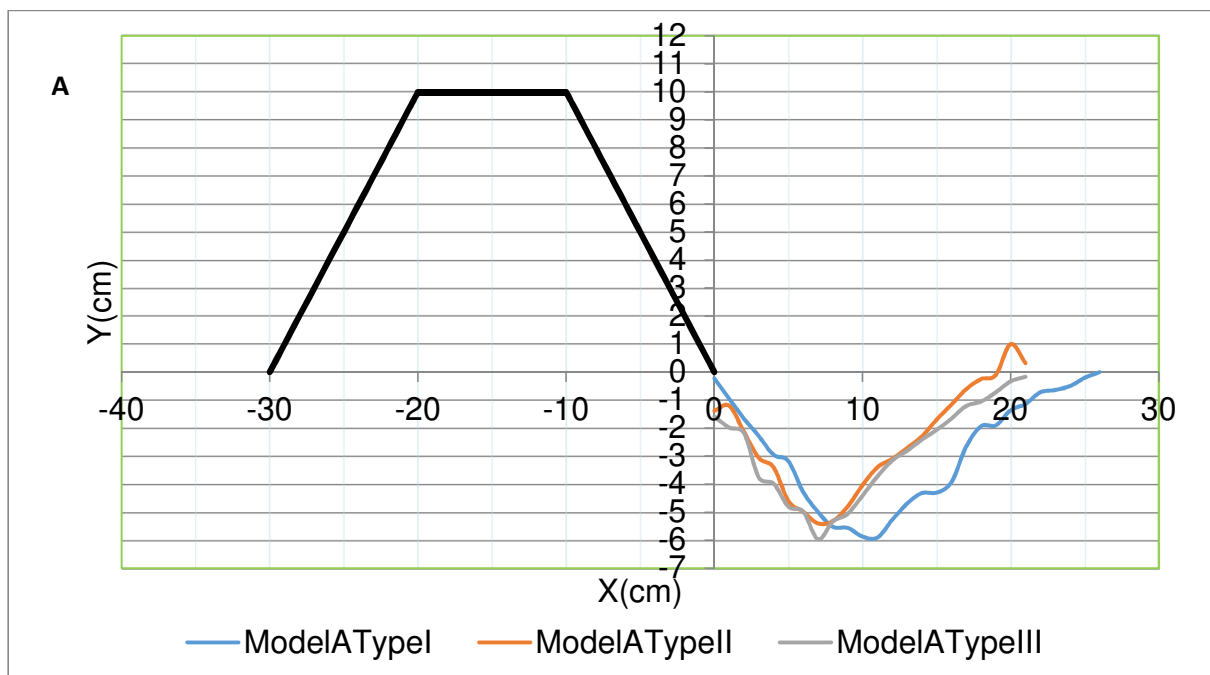


d) Model D

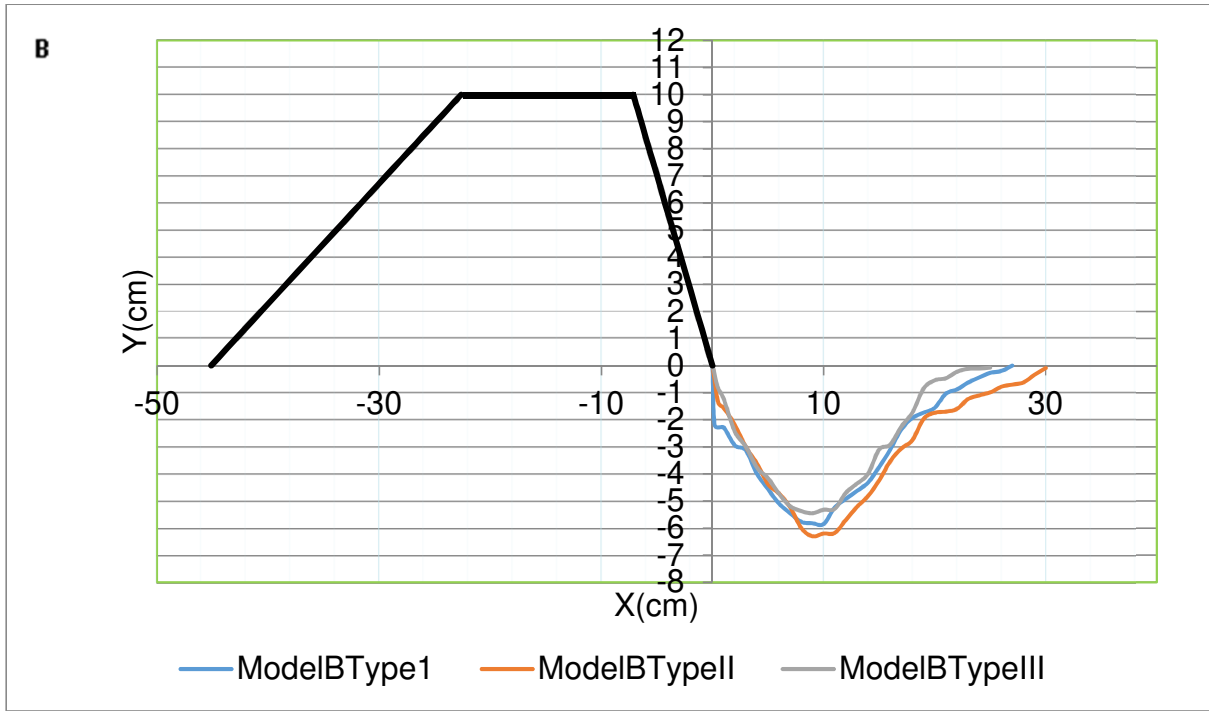
Figure 4.6. Non-dimensional scour profiles of sea dike models (Models A, B, C, and D).



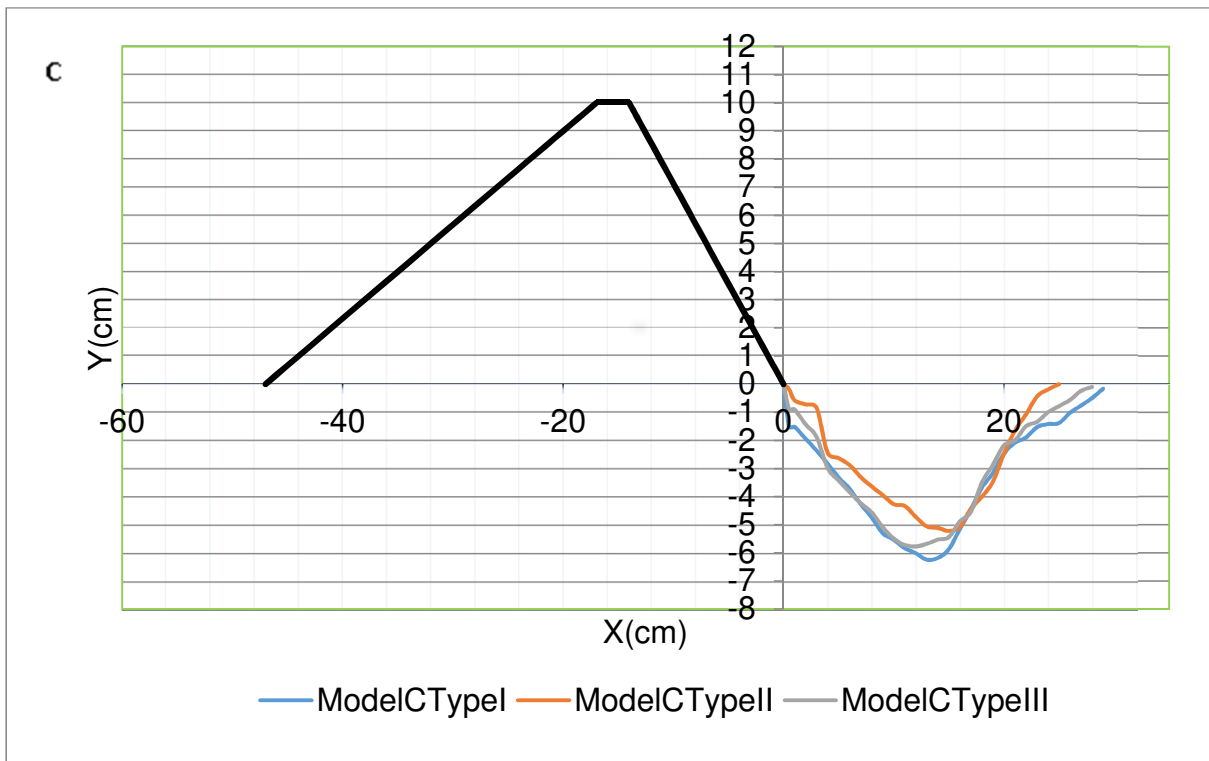
The average horizontal location of the maximum scour depth occurred at 0.083 m, 0.087 m, 0.13 m and 0.173 m from the landward toe of Models A, B, C and D respectively (Fig. 4.7). Figures 4.8 and 4.9 provide the  $R^2$  value which represents simple correlation and indicate how much of the total variation in the dependent variable can be explained by the independent variable. The  $R^2$  value when the angle of the seaward slope is the non-dimensional independent variable is 0.023, which is insignificant than the  $R^2$  value of 0.95 when the angle of the landward slope is the non-dimensional independent variable. These suggest that a stronger correlation exists between the average horizontal location of maximum scour depth  $L_{ms}$ , and angle of the landward slope than for angle of seaward slope. It also suggests that the milder the landward slope, the further away the location of the maximum scour depth that could significantly affect the structural integrity of the dike, thus suggesting length reduction of landward toe protection which would ultimately minimise their design and construction cost.



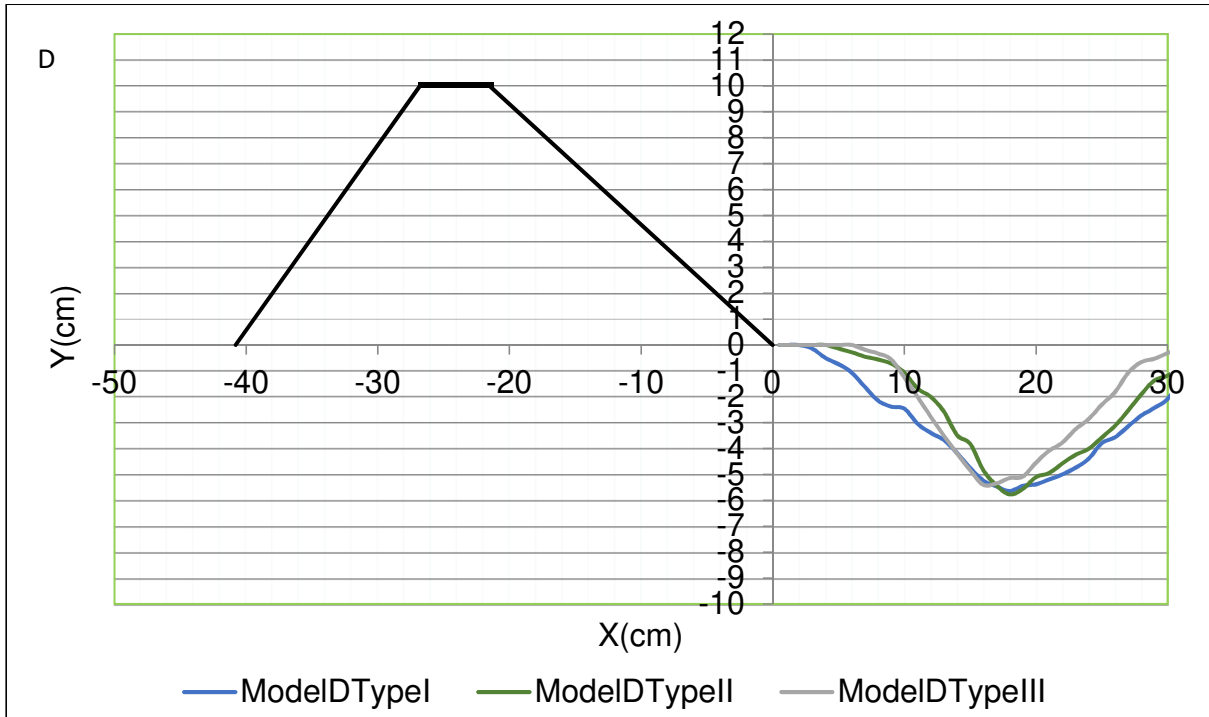
a) Model A



b) Model B



c) Model C



d) Model D

Figure 4.7. Scour development profile (Models A, B, C, and D).

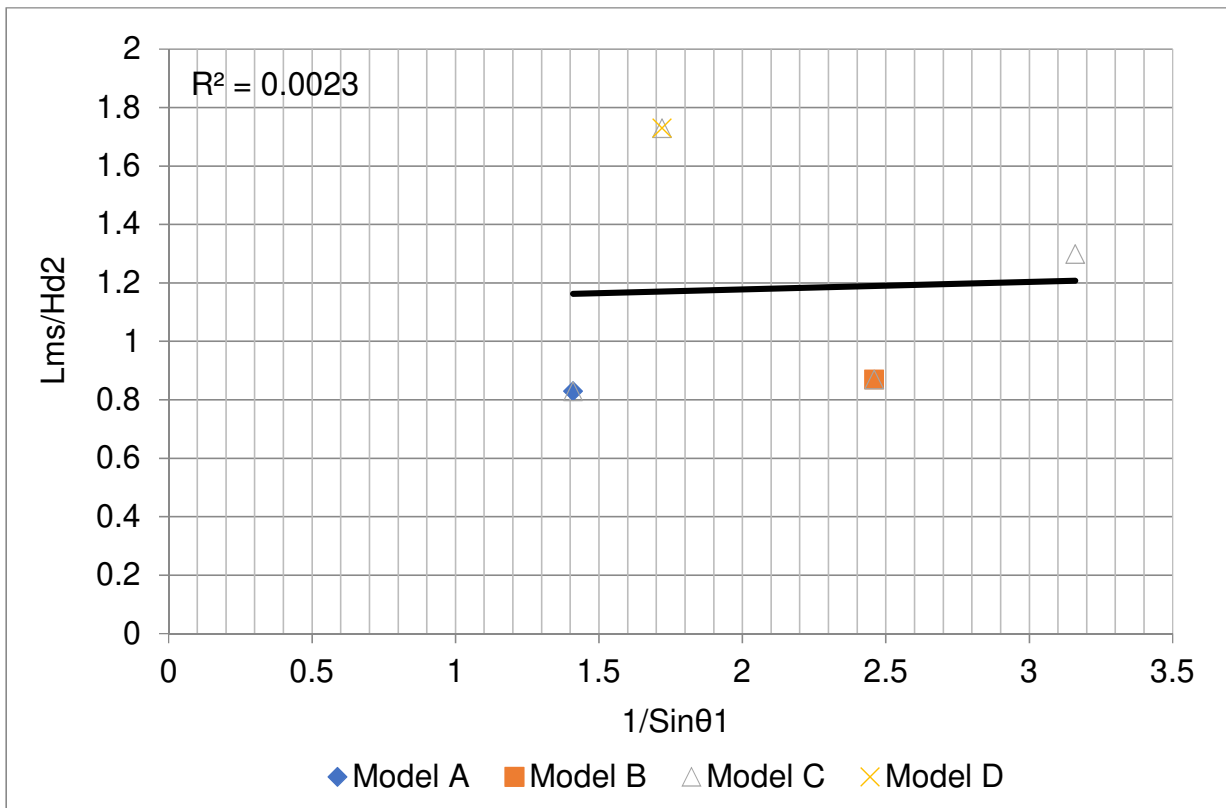


Figure 4.8. The non-dimensional relationship between the average horizontal location of maximum scour depth and angle of seaward slope.

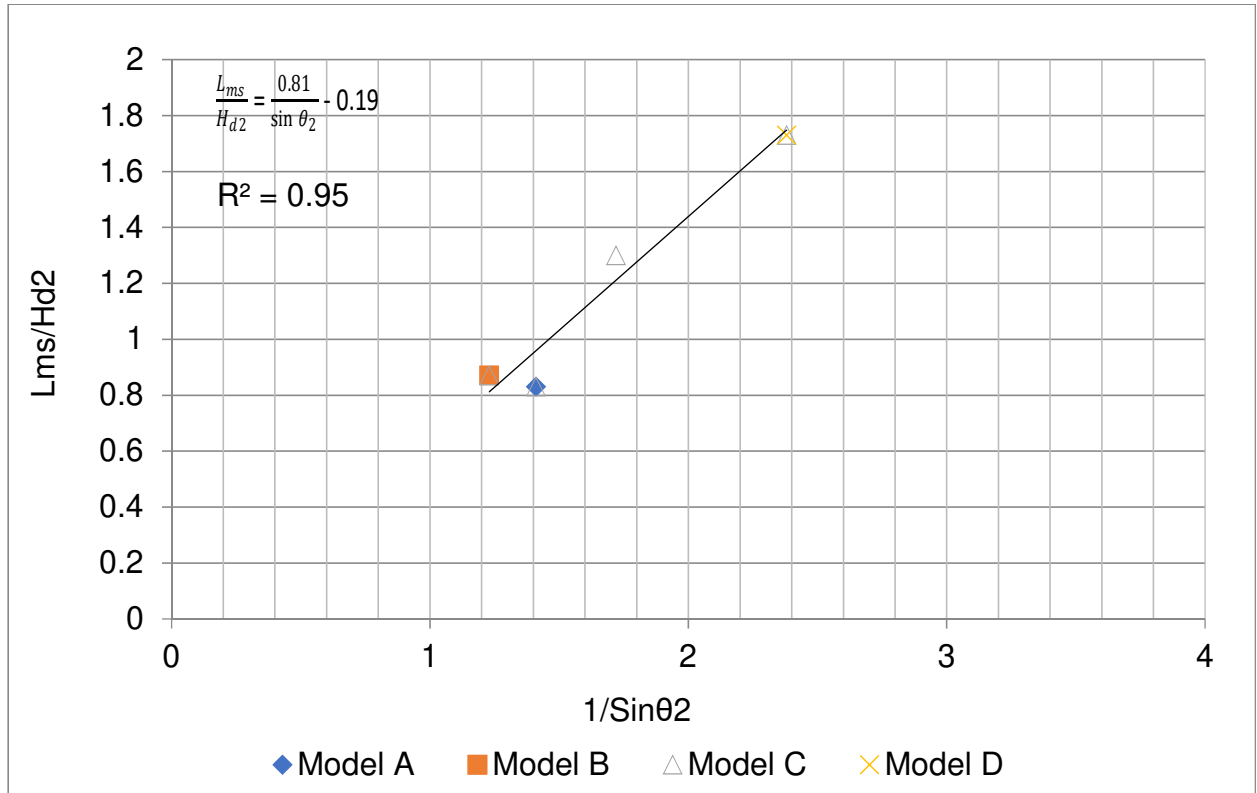


Figure 4.9. The non-dimensional relationship between the average horizontal location of maximum scour depth and angle of landward slope.

#### 4.4 Scour Occurrence Validation with Shields Parameter

The possibility for a tsunami scour is estimated by using the Shields parameter  $\theta$  which determines incipient sediment motion on a bed.

$$\theta = \frac{\tau_0}{\rho g d (s-1)} \quad (4.1)$$

where  $\tau_0$  is the bed shear stress,  $\rho$  is the water density,  $g$  is the gravitational acceleration,  $s$  is the specific gravity, and  $d$  is the grain diameter (taken as  $D_{50}$ , the median grain diameter).

Incorporating shear velocity,  $u_* = \sqrt{\frac{\tau_0}{\rho}}$ , into Eq. 4.1, the Shields parameter becomes;

$$\theta = \frac{u_*^2}{g d (s-1)} = \frac{u_*^2}{g d R_d} \quad (4.2)$$

where,  $R_d$  is the relative density.

Other equations and curves have been created to approximate the Shields Curve because of the inconvenience of determining the shear velocity,  $u^*$ . An approximate Shields Curve was created using an alternative parameter called Bonneville parameter or dimensionless grain diameter,  $D_*$  (Fig. 4.10).

$$D_* = d^3 \sqrt{\frac{R_d g}{\nu^2}} \quad (4.3)$$

where  $\nu$ , the kinematic viscosity is  $1.004 \times 10^{-6} \text{ m}^2/\text{s}$  and  $R_d$  is 1.602.

The experimental grain diameter,  $D_{50}$ , of 0.35 mm will equal a  $D_*$  value of 8.5.

Using Van Rijn (1993) graphical approach (Fig. 4.10 – see red dot), the critical Shields parameter,  $\theta_{cr} = 0.04$ .

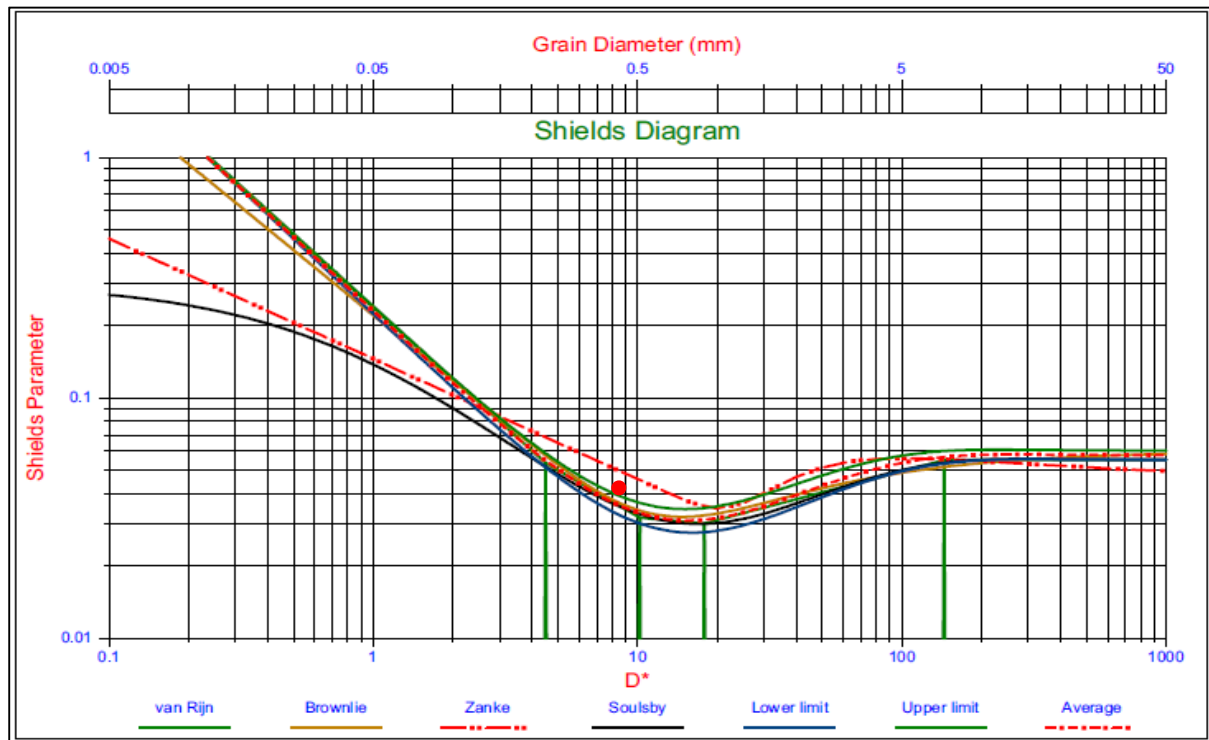


Figure 4.10. The Shields parameter as a function of the dimensionless diameter (Miedema, 2008).

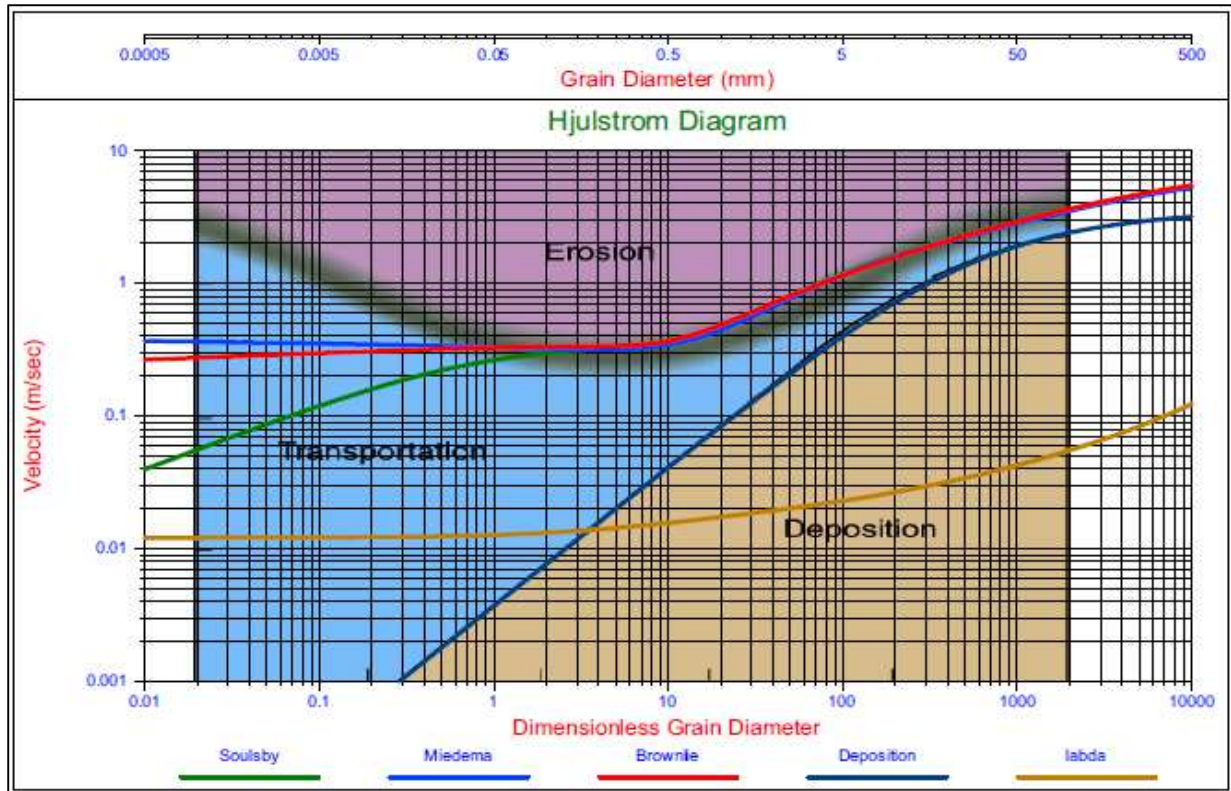


Figure 4.11. A comparison between the Hjulstrom curve and the Shields curve (Miedema, 2008).

Alternatively, using approximation equations by Van Rijn (1993) and Soulsby & Whitehouse (1997); Eqs. 4.4 & 4.5,  $\theta_{cr} = 0.04$ .

$$\theta_{cr} = \frac{0.14}{D_*^{0.64}} \quad 4.5 < D_* < 10.2 \quad \text{Van Rijn} \quad (4.4)$$

$$\theta_{cr} = \frac{0.30}{(1+1.2 \cdot D_*)} + 0.055 (1 - e^{-0.02 \cdot D_*}) \quad \text{Soulsby \& Whitehouse} \quad (4.5)$$

Miedema (2008) explained the erosion phenomenon using the loading process of a Trailing Suction Hopper Dredgers, TSHD and developed the equation of the critical average velocity above the bed,  $U_{cr}$ , that will erode a grain of diameter,  $d_s$  (Eq. 4.6).

$$U_{cr} = \sqrt{\frac{8 \cdot \theta_{cr} \cdot R_d \cdot g \cdot d_s}{\lambda_f}} \quad (4.6)$$

Adapting Eq. (4.6) to the experimental set-up, with the friction coefficient,  $\lambda_f$ , of 0.01 for fine grains and a smooth bed, the average velocity above the bed that will erode a grain diameter,  $D_{50}$ , of 0.35mm is 0.42 m/s. This value agrees well with the Hjulstrom diagram developed by comparison with Shields curve, (Fig. 4.11).

This validates the presence of scour at the landward toe during the laboratory experiment because the average maximum velocity at the landward slope, near the toe, is around 2.0 m/s which is higher than 0.42 m/s.

#### 4.5 Representative Scour Depth Predictive Model

This section focuses on the development of the scour depth predictive model to develop suitable dimensions that will improve the structural resilience of coastal dikes. The scour predictive model (Eq. 1) has been refined by making a comparison with scour data from laboratory experiments carried out at the University of East London's hydraulic facility to produce an actual field scenario. The mathematical modelling technique by Giordano et al. (2009) is summarized in Fig 4.12, and was used to explain the scour damage caused by tsunami based on the Buckingham  $\pi$  theorem and the equation of the maximum overflowing wave pressure as against impact overflowing wave pressure (Fig. 3.24) at the landward slope of a coastal dike.

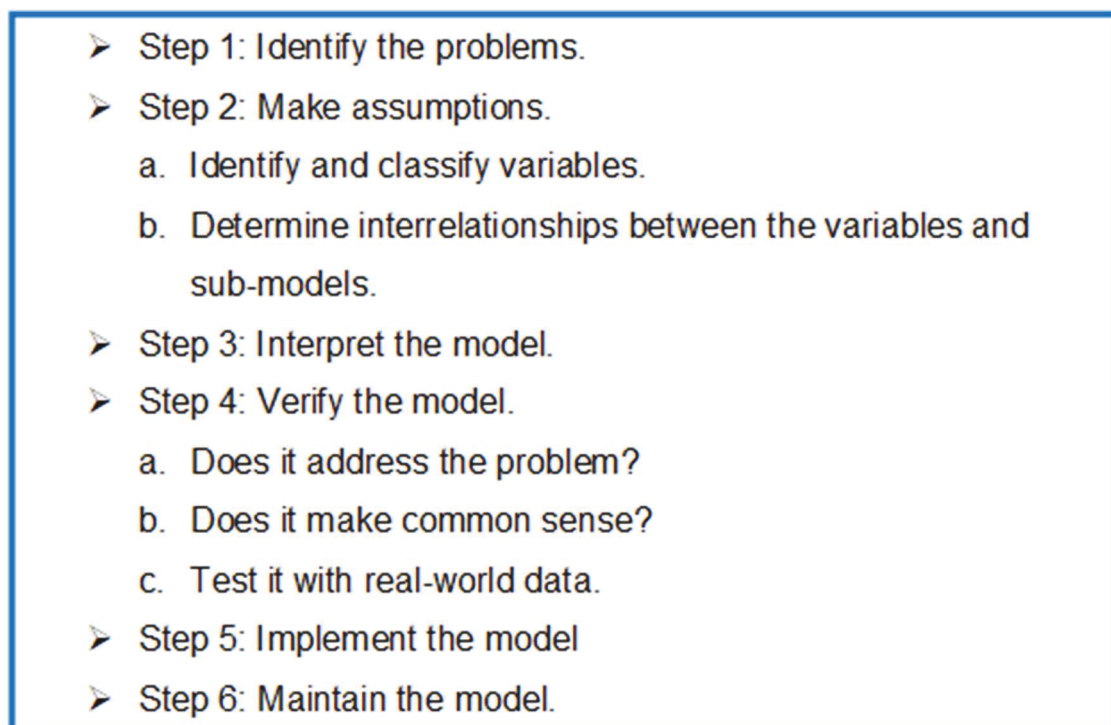
- 
- Step 1: Identify the problems.
  - Step 2: Make assumptions.
    - a. Identify and classify variables.
    - b. Determine interrelationships between the variables and sub-models.
  - Step 3: Interpret the model.
  - Step 4: Verify the model.
    - a. Does it address the problem?
    - b. Does it make common sense?
    - c. Test it with real-world data.
  - Step 5: Implement the model
  - Step 6: Maintain the model.

Figure 4.12. Mathematical modelling construction steps (Giordano et al., 2009).

The assumed variables of the scour process are:

$$f(D_s, \rho, g, H_{d2}, P_{om}) = 0 \quad (4.7)$$

where  $D_s$  is the measured scour depth,  $\rho$  is the sea water density,  $g$  is the gravitational acceleration,  $H_{d2}$  is the height of structure measured on the landward side, and  $P_{om}$  is the maximum overflowing wave pressure. The dimensional analysis reveals that the non-dimensional scour depth  $\frac{D_s}{H_{d2}}$  depends on the inverse of maximum overflowing pressure,  $\frac{\rho g H_{d2}}{P_{om}}$ , an expression derived by Mizutani and Imamura [2002] (Eq. 3.2). The mathematical form of the relationship is:

$$\frac{D_s}{H_{d2}} = f \left( \frac{\rho g H_{d2}}{P_{om}} \right) \quad (4.8)$$

Tsunami flow velocity during run-up process is an essential parameter to determine fluid forces on structures and other tsunami flow parameters. Bottom slope, inundation depth, bottom roughness, wave set-up and distance from the shoreline are factors that make it difficult to derive an accurate value for velocity (Matsutomi et al., 2010). Chock et al. (2013) used captured video and satellite imagery tools to analyse flow velocities after the 2011 Tohoku Tsunami, but due to the absence of videos at the exact locations of interest, the maximum flow velocity over the structure,  $V_m$ , given in Eq. (3.2) was assumed to be the upper bound inundation flow velocity derived by Matsutomi et al. (2010). This velocity exerts the largest fluid force and is related to the inundation height ( $h$ ), as  $U = 1.2\sqrt{gh}$ . This will change the Eq. (4.8) to:

$$\frac{P_{om}}{\rho g H_{d2}} = 3.4 \frac{\sqrt{h} \sin \theta_2}{\sqrt{H_{d2}}} \quad (4.9)$$



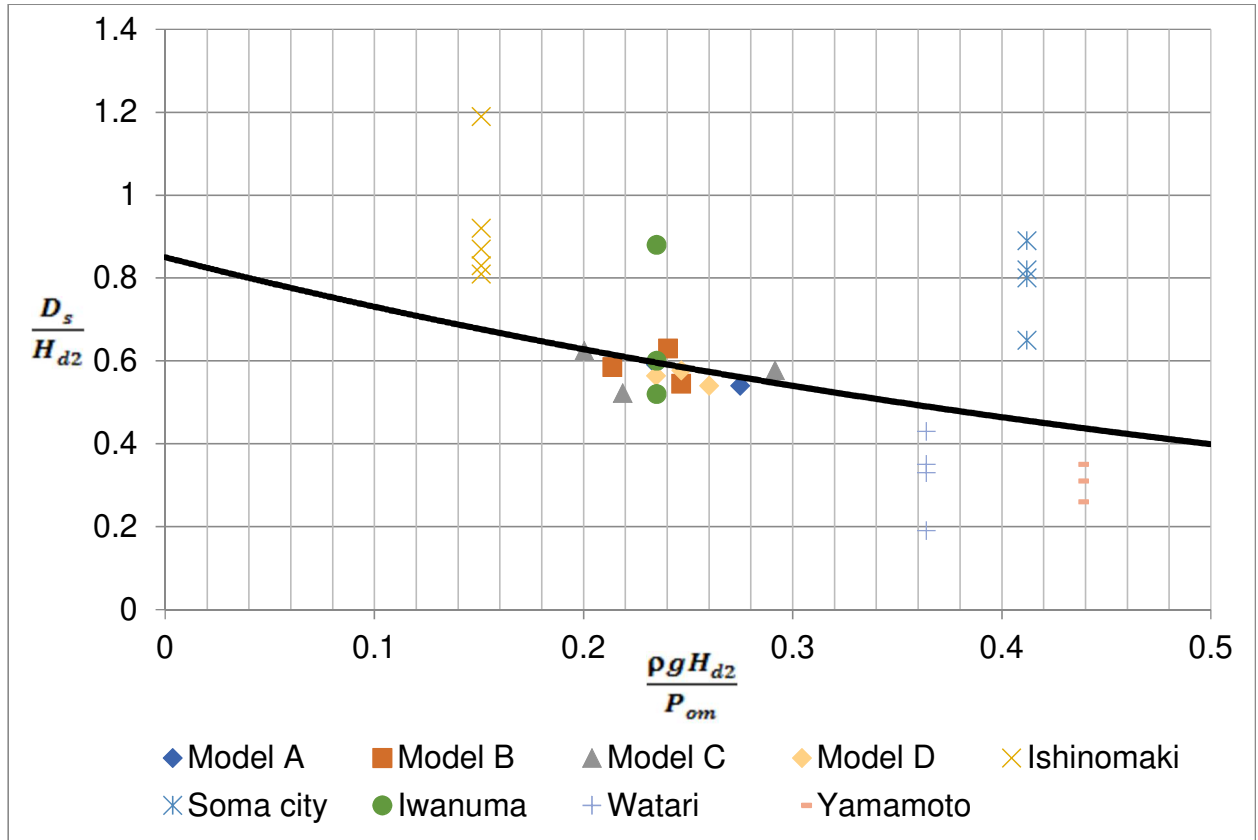


Figure 4.13. The relationship between relative scour depth and maximum overflowing wave pressure.

From Fig. 4.13, the relative mean scour depth becomes:

$$\frac{D_s}{H_{d2}} = 0.85 \left( \exp \left( -16 \frac{\rho g H_{d2}}{P_{om}} \right) \right) \left. \vphantom{\frac{D_s}{H_{d2}}} \right\} \frac{P_{om}}{\rho g H_{d2}} > 0 \quad (4.10)$$

Putting Eq. (4.9) into Eq. (4.10), the final model that incorporates the measurable in-situ quantities is generated and provided below.

The scour depth predictive equation can be presented as:

$$\frac{D_s}{H_{d2}} = \lambda \left( \exp \left( - \frac{\sqrt{H_{d2}}}{2.5 \lambda \sqrt{h} \sin \theta_2} \right) \right) \left. \vphantom{\frac{D_s}{H_{d2}}} \right\} h > H_{d2} \quad (4.11)$$

with a fitted coefficient  $\lambda = 0.85$ .

An exponential relationship is shown to exist between relative measured scour depth, height of structures measured on the landward face, inundation height as a function of flow velocity and landward slope angle. The expression is valid when the inundation height is higher than landward slope height, and the coefficient of permeability,  $k$ , in m/s is greater than  $10^{-4}$  but less than  $10^{-3}$ .

Root mean square error, RMSE, is used to measure the predictive power of the differences between values observed from field survey and laboratory data compared to the corresponding values predicted by the model. It is expressed mathematically as:

$$RMSE = \sqrt{\frac{\sum_{i=1}^N (\hat{Y} - Y_i)^2}{N}} \quad (4.12)$$

where  $\hat{Y}$  is the model data,  $Y_i$  is the observed data and N is the total number of data.

Table 4.1. Root mean square error of the field survey data compared with the scour predictive model.

Model	$\hat{X} = \frac{\rho g H_{d2}}{P_{om}}$	$Y_i$ (Observed data)	$\hat{Y}$ (Model data)	$(\hat{Y} - Y_i)^2$
Ishinomaki	0.151	0.87	0.668	0.041
	0.151	1.19	0.668	0.273
	0.151	0.92	0.668	0.064
	0.151	0.83	0.668	0.026
	0.151	0.81	0.668	0.020
Soma city	0.412	0.65	0.440	0.044
	0.412	0.89	0.440	0.203
	0.412	0.82	0.440	0.145
	0.412	0.80	0.440	0.130
Iwanuma	0.235	0.88	0.584	0.088
	0.235	0.52	0.584	0.004
	0.235	0.60	0.584	0.000
Watari	0.364	0.43	0.475	0.002
	0.364	0.19	0.475	0.081
	0.364	0.35	0.475	0.016
	0.364	0.33	0.475	0.021
Yamamoto	0.437	0.35	0.422	0.005
	0.437	0.26	0.422	0.026
	0.437	0.31	0.422	0.013
				$\Sigma = 1.202$

$$\text{RMSE} = \sqrt{\frac{1.202}{19}} = 0.25$$

Table 4.2. Root mean square error of the experimental data compared with the scour predictive model.

Model	$\hat{X} = \frac{\rho g H_{d2}}{P_{om}}$	$Y_i$ (Observed data)	$\hat{Y}$ (Model data)	$(\hat{Y} - Y_i)^2$
Model A	0.235	0.591	0.584	0.0000498
	0.275	0.540	0.548	0.0000570
	0.235	0.597	0.584	0.000170
Model B	0.214	0.585	0.604	0.000352
	0.241	0.630	0.578	0.00265
	0.247	0.545	0.573	0.000773
Model C	0.200	0.624	0.617	0.0000517
	0.219	0.522	0.599	0.00594
	0.292	0.577	0.533	0.00192
Model D	0.235	0.564	0.422	0.000398
	0.247	0.577	0.422	0.0000176
	0.260	0.540	0.422	0.000429
$\sum = 0.0128$				
$\text{RMSE} = \sqrt{\frac{0.0128}{12}} = 0.033$				

Tables 4.1 and 4.2 show excellent agreement between the laboratory and the predictive model, and a good agreement between the field scour data and the model. The field survey data shows the larger deviation from the scour predictive model with an RMSE value of 0.25, while the laboratory data shows a little deviation from the model with an RMSE value of 0.033.

## 4.6 Proposed Sea Dike Section to Resist Landward Toe Scour

Sensitivity analysis was performed to determine the best cost-effective coastal dike geometry for different ranges of tsunami wave inundation depth, by considering the landward slope area (Table 4.1). The model (Eq. 4.11) predicts that a coastal dike with a landward slope angle of  $28^{\circ}$  and height range between 4 – 5 m will result in a maximum scour depth that will range between 1.4 – 2.0 m under inundation height of between 5 – 9 m. The predictive model reveals that the higher the inundation height, the higher the possible scour depth. It also shows that milder landward slope would result in reduced scour depth. This agrees with the dike design approach of a landward face with gradients 1:2 ( $26.6^{\circ}$ ) and 1:3 ( $18.4^{\circ}$ ) of the Netherlands (Linham and Nicholls, 2010).

Also, applying the geometrical similarity requirement,  $L_R = 50$ , Figure 4.9 implies that the horizontal location of the maximum scour depth of a 5 m high coastal dike with a landward slope of  $28^{\circ}$  would be around 7.7 m from the landward toe. Therefore, it is safe to propose that the length of the toe protection be designed to the height of the coastal dike, 5 m, and the depth of the toe protection be designed to the maximum scour depth. This conclusion is consistent with Figure 4.7 which generally reveals the horizontal distance of the maximum scour depth from the landward toe at approximately the height of the sea dike models. Finally, Figure 4.14 is proposed as a design recommendation for a resilient coastal dike structure to mitigate landward toe scour.

Table 4.3. Sensitivity analysis for maximum scour depth  $D_s$  – the variation of landward slope  $\theta_2$ , inundation depth  $h$ , and dike height  $H_{d2}$ .

(Table reproduced with the permission of the rights holder, World Scientific.

Appendix C)

		$\theta_2 (25^\circ)$		$\theta_2 (28^\circ)$	
		$h$ (m)		$h$ (m)	
		5	9	5	9
$H_{d2}$ (m)	4	1.3	1.6	1.4	1.7
	5	1.4	1.9	1.6	2.0
	6	1.5	2.1	1.7	2.3
		$\theta_2 (30^\circ)$		$\theta_2 (32^\circ)$	
		$h$ (m)		$h$ (m)	
		5	9	5	9
$H_{d2}$ (m)	4	1.5	1.8	1.5	1.9
	5	1.7	2.1	1.7	2.2
	6	1.8	2.4	1.9	2.5

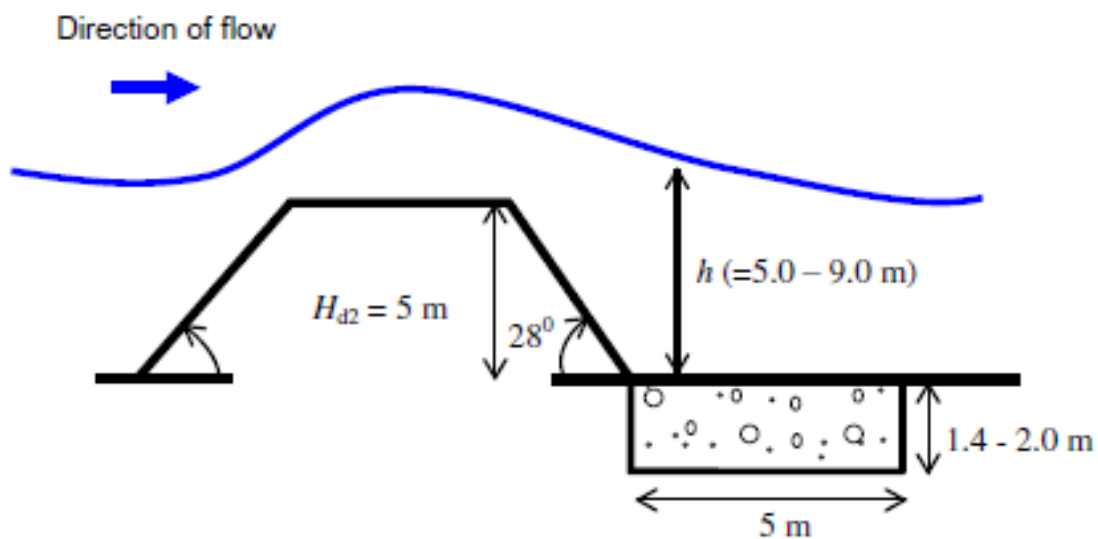


Figure 4.14. Design recommendation for a resilient coastal dike structure to mitigate the landward toe scour (Not to scale).

(Image reproduced with permission of the rights holder, World Scientific, Appendix C)

## 4.7 Conclusions

This chapter started with the introduction of the experimental studies of tsunami-induced scour. The description of the experimental set-up to investigate the development of the scour at the landward region of the four sea dike models are then adequately presented. The results of experiments conducted to investigate the effects of tsunami flow behind coastal dikes were presented. A moving point gauge with a vernier scale and a level were used to position the sand grain during the scouring process. In all 36 tests were performed, in which the dynamic changes in average maximum scour depth and length from plane-bed were recorded and finally used in analyses.

The results showed that the average maximum scour depth values do not vary significantly for all the four sea dike models, but the location of the maximum scour depth does significantly depend on the landward slope than the seaward slope. The horizontal position of the maximum scour depth was found to move slightly towards the landward toe as the slope steepened. Also, the presence of scour at the landward toe during the laboratory experiment was validated by the Shields parameter and Hjulstrom curve.

It was observed that an exponential relationship exists between relative scour depth and maximum overflowing wave pressure. Using the RMSE statistical measure, this relationship showed an excellent fit with the laboratory data and good agreement with tsunami field data. The difference in datasets is largely influenced by the difference in both laboratory and field velocity values, as Jayaratne et al. (2014) estimated the field velocity values of Iwanuma and Soma cities to be 8.97 m/s and 9.80 m/s respectively, compared with an average experimental value of 14 m/s. Also, the impact of the multiple tsunami wave train and sediment size scaling effects have not been modelled. The resulting scour predictive model revealed the importance of parameters like the height of sea dike, the angle of landward slope, and tsunami flow velocity; an independent variable of tsunami inundation height, in predicting a representative scour depth that can be used to design a more robust coastal defence structure.

Finally, using the scour predictive model and the non-dimensional relationship between the average horizontal location of maximum scour depth and angle of

landward slope, a sensitivity analysis was employed to propose a suitable sea dike section that can be constructed to minimize the effect of landward toe damage significantly.

## Chapter 5

### Numerical Simulation of Tsunami Waves

Different approaches are being used to model the turbulence in water waves; the statistical description of the eddies through Reynolds-averaged Navier-Stokes (RANS), the partial description of the eddies through Large Eddy Simulation (LES) and full description of vortical motions through Direct Numerical Simulation (DNS) (Rana, 2017). Direct Numerical Simulation is the most accurate approach because it directly and completely solves the Navier-Stokes equations for all the regime of the turbulent flow. This is possible when the grid size is less than or in the order of the Kolmogorov scale ( $N_x N_y N_z \approx Re^{9/4}$ , where  $Re$  is the Reynolds number). The high computational demand has limited its present application to low Reynolds number flows and in a small domain for high Reynolds flow problems.

In the study of many engineering flow problem, the mean properties of the turbulent flows are of significant interest. Therefore, Navier-Stokes equations are solved by averaging out the fluctuating properties, which are then considered in the modelling of turbulence by different approximation methods. Simulation done with RANS modelling approach require less computational resources and can be performed in a coarse grid when compared to LES and DNS. In this study, RANS would be employed to simulate two-dimensional tsunami waves

This chapter begins with a further introduction about various methods of numerical study of tsunami waves. The simulation data of flow quantities are described and statistically compared to experimental data in Chapter 3. The methodology employed for the CFD study is also compared to other published flow study to ascertain its accuracy and dependency.

#### 5.1 Introduction

The developments in the study of turbulence (as discussed in Section 2.4), numerical methods and increased computational power have enhanced the understanding of water wave characteristics. These have led to many innovative ideas into the investigation of tsunami waves using various modified numerical schemes, Smoothed



Particle Hydrodynamics (SPH), Large Eddy Simulation, and Direct Numerical Simulation.

Zou et al. (2006) outlined the application of Large Eddy Simulation for the simulation of compressible and incompressible turbulent flows. LES was described as an intermediate modelling technique between the Reynolds averaged Navier-Stokes equations and Direct Numerical Simulation. DNS offers the possibility of directly and accurately solving the Navier-Stokes equation which governs turbulent flows. There is also the difficulty of achieving the accuracy of the small-scale eddies with proper initial and boundary conditions, even with the possibility of direct simulation. Also, high-order numerical schemes will be required to minimise dispersion and dissipation error, but they offer limited flexibility in complex geometries and boundary conditions. The authors described the limitations of supercomputers in applying direct numerical simulation for high Reynolds number 3D turbulent flow, which would require a large number of grid points and very long computing time. In RANS, details of small eddies are not required as the emphasis is on averaged flow quantities. A coarse grid system might be enough to simulate practical flow examples on a simple computer. One of its disadvantages is the difficulty in predicting laminar-turbulent transitions. They opined that LES can simulate flows of larger Reynolds number than DNS and that the computational demand is not as heavy as DNS. Also, simulation accuracy is better than RANS for large turbulent flows.

In studying the interaction between non-breaking solitary wave and a group of three slender piles, Mo and Liu (2009) ignored the effects of viscosity and turbulence and employed a numerical model based on solving Navier-Stokes equations for incompressible fluids by finite volume scheme and tracked free surface displacement by Volume of Fluid (VOF) method. They obtained a good agreement between their numerical simulation and experimental works except for values of dynamic wave pressure due to instrumentation error.

Wu et al. (2015) performed a hydraulic experiment on the propagation and run-up of double solitary waves along a plane slope to determine their reflective behaviour, and numerical validation was provided by adopting the Reynolds averaged Navier-Stokes equations and RNG  $k - \epsilon$  turbulence model. Also, a two-phase model was developed to take account of the air and water flow in the computational domain.

Numerical and experimental studies of a drifting movement of motor vehicles in tsunami flooding were investigated by Yamauchi et al. (2015). A link-bounce-back

scheme based on the exchange of momentum was employed to study the interactions between inundation flow and the vehicles, and from one vehicle to another. A modified subgrid-scale (SGS) model and 3D Ladd's Lattice Boltzmann Method (LBM) model, which has been extended with free surface for particle suspension were employed. 80 car models were employed in the experiment, and their drift movements near the pillar of the evacuation tower were well modelled.

The numerical investigation of the interaction between a solitary wave and pile breakwater in the shape of a circular cylinder was studied by Liu et al. (2011). Depth-averaged shallow water equation, solved by the BGK-based finite volume methods, was used to model the free surface flow. A good agreement between numerical and experimental findings was observed when the wave height to water depth ratio was less than 0.25. There were deviations from the results of the two methods of study for relative wave height ratios larger than 0.25, and this was mostly due to the limitations of the depth-averaged shallow water equations in handling these large cases.

In studying transoceanic tsunami propagation, Ha and Cho (2015) employed a modified finite difference numerical scheme and adjusted the linear shallow water equations to reflect the different water depths. Different case studies and numerical schemes were used to verify the results of the proposed model after its application to tsunami propagation over a submerged shoal. Similar and reliable observations with other schemes were reported with an advantage of reduced computational time because of the larger uniform grid size that was employed.

In studying turbulent boundary layer flows, William and Fuhrman (2016) extended the one-dimensional Vertical (1DV) model, based on the horizontal component of the incompressible RANS equations, to incorporate a transitional two-equation  $k-\omega$  turbulence closure model. The results of the numerical simulations based on the developed models were compared with experimental results, and good agreement with various flow quantities was observed.

Smoothed particle hydrodynamics is a meshless method invented for the study of Astrophysics. The complexity of grid generation in many mesh-based numerical schemes generated compared with the simplicity of the SPH method generated interest in the field of mechanics and major development thereafter, especially in the 1990s. Sarfaraz and Pak (2017) employed smoothed particle hydrodynamics (SPH) to study the effect of tsunami wave on bridge superstructure and proposed equations for computing forces and moments applied by tsunami waves on the structure.

The concept behind the SPH method is presented by Xie et al. (2012). The authors also applied a 3D LES-SPH model to study breaking tsunami waves, and the turbulence was simulated by the Smagorinsky closure model. Rogers and Dalrymple (2008) also combined both SPH and LES schemes in simulating the generation and propagation of both 2D and 3D tsunamis. The scheme, a grid-less Lagrangian particle approach, was used to describe the viscous effect of the flow. In case of the 2D landslide-generated tsunami, the 2D models agreed well with other nonlinear numerical models but were shown to be inadequate for the 3D problems.

The objective of this chapter is to employ numerical investigation to model tsunami wave, and then compare the results to experimental data and hydrodynamic literature. The study will investigate tsunami bore flow over the different geometries of sea dikes, discussed in Section 3.2, to determine velocity distribution behind the structures and pressure distributions which would ultimately be used for the numerical study of scour development behind sea dikes, which is discussed in detail in Chapter 6.

## **5.2 Numerical Investigation of Dam Break Flow: two-phase flow**

### **5.2.1 Geometric Setup and Mesh Generation**

The schematic setup shown in Figure 3.1 of Chapter 3, and which has two flow phases of air and water is used to represent the domain of this study. This is to validate the experimental results of the flow variables. ANSYS Workbench 18.1 (Fig. 5.1) is used as the platform for the geometric representation in DesignModeler (Fig. 5.2), mesh generation in Meshing application (Fig. 5.3), and solution setup in Fluent.

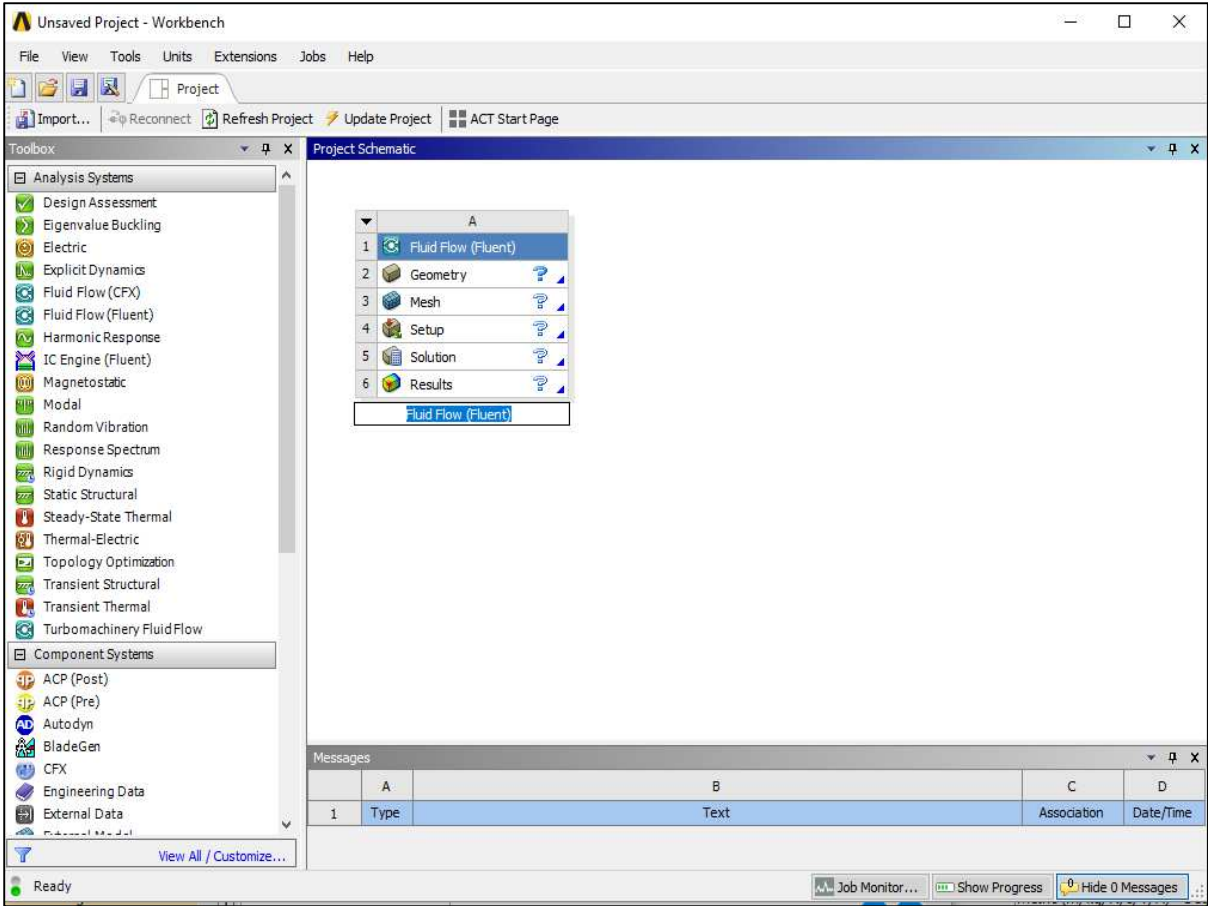


Figure 5.1. ANSYS Workbench project tab.

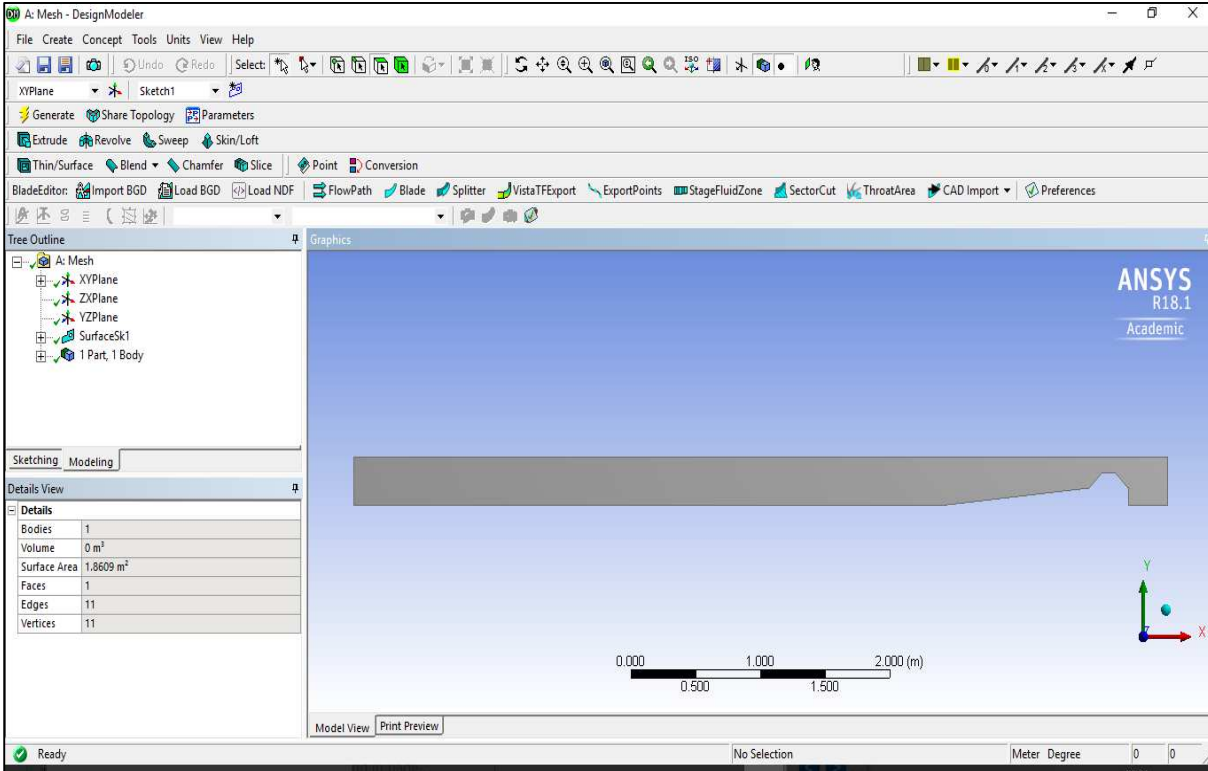


Figure 5.2. Geometry generation using DesignModeler.

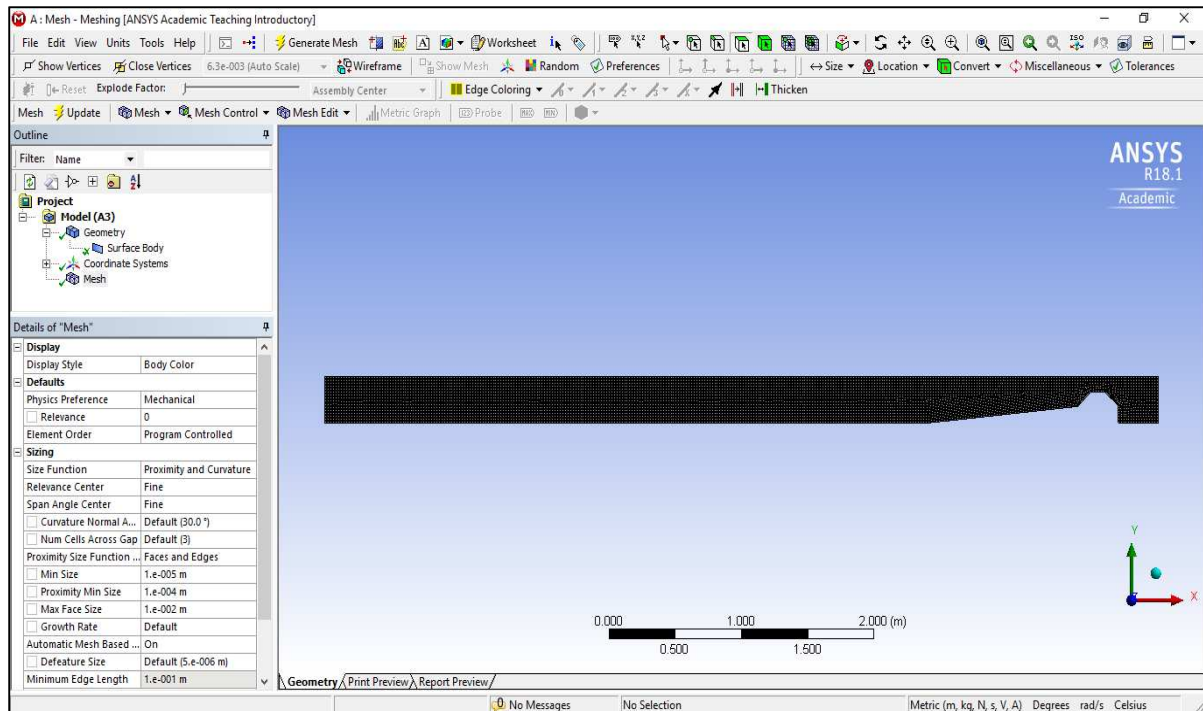


Figure 5.3. Mesh generation using meshing application.

Lines/Edges were created by interpolating through points using the sketching toolboxes; Draw, Modify and Dimensions. Surfaces of different geometric parts were then generated from the edges using the Concept menu option. Using the 'Create Named Selection' option upon right clicking on the edges, different parts were created from the surface to generate the boundary conditions required for the solution procedure (Fig. 5.4). The parts created were: Left\_Wall (Zone 1), Inlet (Zone 2), Free\_Surface (Zone 3), Seaward\_Slope (Zone 4), Crest (Zone 5), Landward\_Slope (Zone 6), Right\_Wall (Zone 7), Bottom\_Wall (Zone 8), Back\_Wall (Zone 9), Beach\_Slope (Zone 10), and Left\_Bottom\_Wall (Zone 11).

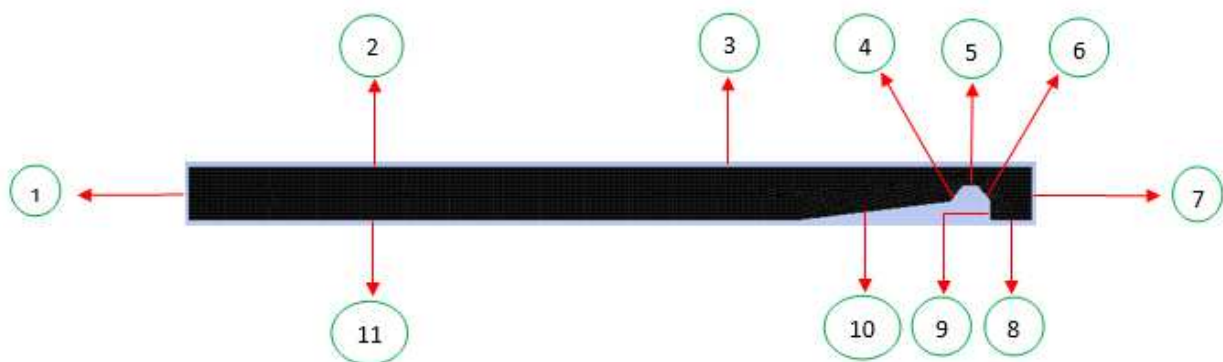


Figure 5.4. Different parts for boundary condition set up in Fluent.

The interior body representing the fluid was automatically generated by Fluent within the geometric volume from the surfaces.

### 5.2.2 Ansys Fluent setup

The mesh created in the Meshing application was imported to ANSYS Fluent through one of its GUI components; ribbon. The first task was to check the mesh for errors and improve its quality, to enhance the computational accuracy and stability. Orthogonal quality and aspect ratio criteria were employed for this diagnostic check (Fig. 5.5). Orthogonal quality has ranged between 0 and 1, where 0 is the worst and 1 is the ideal possible. The orthogonal quality for cells is computed using the face normal vector, the vector from the cell centroid of each adjacent cells, and the vector from the cell centroid to each of the faces. Aspect ratio indicated the stretching of a cell and computed as the ratio between the maximum value to the minimum value of either the normal distance between cell and face centroids or distance between cell centroid and nodes (ANSYS, 2015).

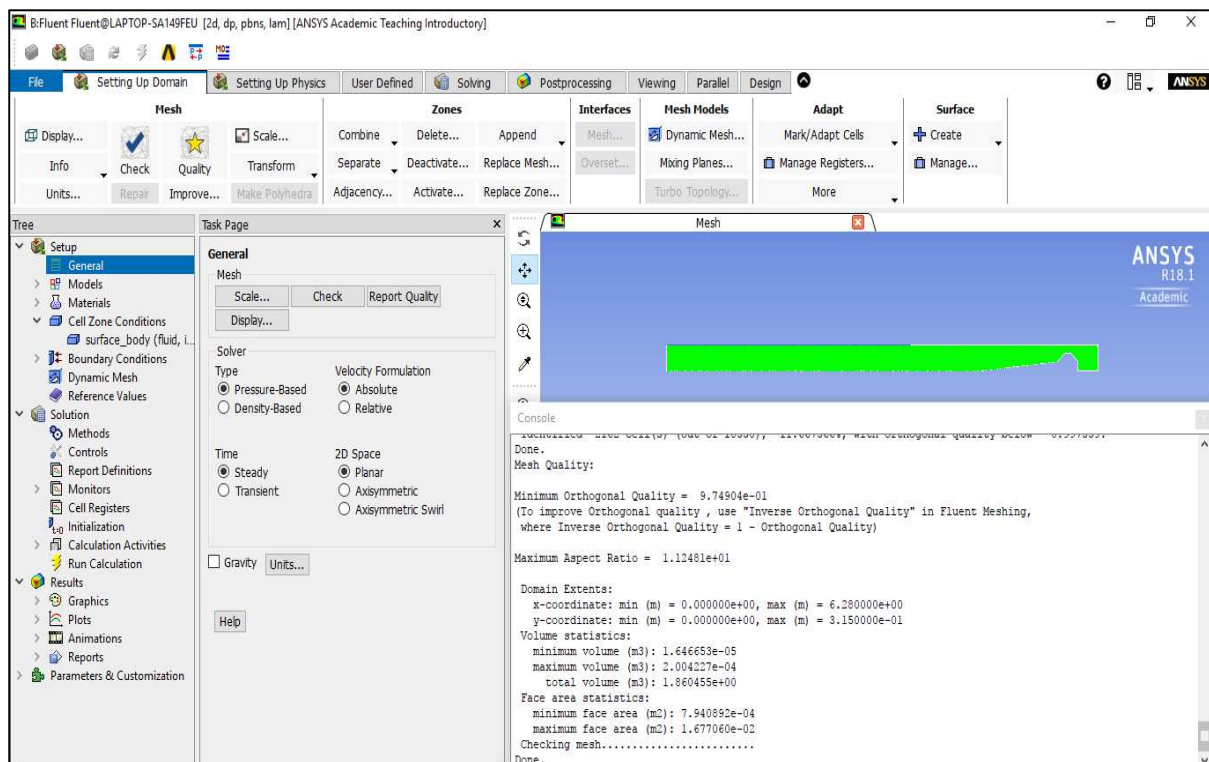


Figure 5.5. Quality metrics of mesh.

Different solver algorithms were employed throughout the setup, and sub-options include; segregated (de-coupled) and coupled, steady and unsteady (transient),

implicit and explicit. De-coupled, transient and implicit solvers were employed for this study.

In the general setup Tree, the pressure-based solver was chosen because it was developed for low-speed incompressible flows. This numerical method employs a finite-volume discretization technique in which the domain is divided into discrete control volumes using a grid system. In this pressure-based approach, the pressure or pressure correction equation is obtained from the manipulation of the continuity and momentum equations to produce the pressure field.

The multiphase model provides the different selection for the flow condition. The Volume of Fluid with two Eulerian phases; water and air, was employed with an Open Channel Flow sub-model with the activation of the implicit body force option (Fig. 5.6).

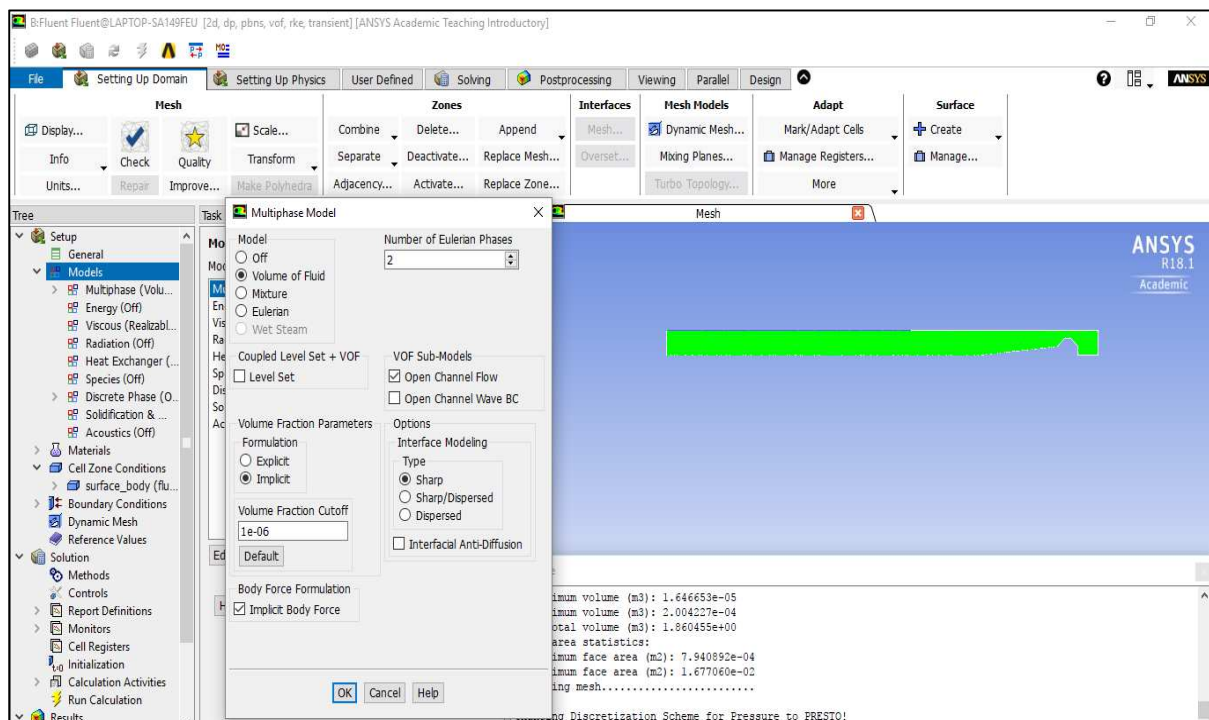


Figure 5.6. Multiphase model set-up.

The viscous model provides the option of different turbulence model selection. The Realizable  $k-\epsilon$  model with scalable wall function was employed for this study. The Realizable  $k-\epsilon$  model has been shown in various studies to provide better performance than other  $k-\epsilon$  models for separated flows and flows vortices and rotation (ANSYS, 2006). In general, the different wall functions help in the reduction of mesh resolution and simulation time. Scalable wall functions produce consistent results and offer the

advantage of log law, and standard wall functions approach by avoiding the deterioration of the latter under grid refinement below  $y^* < 11$ .

The materials, which are the two Eulerian phases specified in the VOF model are defined in the Tree panel of the GUI and presented in Table 5.1. The operating conditions of the fluid was specified in the Cell zone conditions; the gravitational acceleration was considered in the Y direction ( $-9.81 \text{ m/s}^2$ ), operating pressure of 101325 Pa at a reference pressure location of  $y = 0.305 \text{ m}$ , and operating density of  $1.225 \text{ kg/m}^3$  were specified to improve convergence behaviour.

Table 5.1 Physical properties of the Eulerian phases.

	Density	Viscosity
Air	$1.225 \text{ kg/m}^3$	$1.7894 \times 10^{-5} \text{ kg/m.s}$
Water	$998.2 \text{ kg/m}^3$	$0.001003 \text{ kg/m.s}$

The different parts generated when creating the geometry formed the surfaces on which the boundary conditions were defined. The pressure inlet boundary condition was specified at the inlet with the turbulence specification method of turbulent intensity and backflow turbulent viscosity ratio.

Turbulent intensity at the core of a fully-developed duct flow,  $I = 0.16 (Re_{DH})^{-1/8}$

Where,  $Re_{DH}$ , the Reynolds number is approximately  $8 \times 10^5$ .

Free surface level and total height were chosen as the flow specification method for the open channel sub-option in the Multiphase pressure inlet boundary condition. The pressure outlet boundary condition was specified at the outlet and free surface with the turbulence specification method of backflow turbulent intensity and viscosity ratio. The body fluid was set as the interior boundary condition type, and all other parts were defined as the wall boundary conditions (Table 5.2).



Table 5.2 Boundary conditions for geometry parts in Fluent.

Part	Zone	Boundary conditions
Left_Wall	1	Wall
Inlet	2	Pressure-inlet Turbulent Intensity = 3% (Reynolds number $\approx 8 \times 10^5$ ) Backflow Turbulent Viscosity Ratio = 10% Free surface level = 0.3m Total height = 0.315m Bottom level = 0m
Free-surface	3	Pressure outlet Backflow Turbulent Intensity = 3% Backflow Turbulent Viscosity Ratio = 10%
Seaward_Slope	4	Wall
Crest	5	Wall
Landward_Slope	6	Wall
Right_Wall	7	Pressure outlet Backflow Turbulent Intensity = 3% Backflow Turbulent Viscosity Ratio = 10%
Bottom_Wall	8	Wall
Back_Wall	9	Wall
Beach_Slope	10	Wall
Left_Bottom_Wall	11	Wall

Second order implicit or upwind discretisation schemes were selected for governing equations of transient formulation, turbulent dissipation rate, turbulent kinetic energy, and momentum equations (Fig. 5.7). The Pressure-Implicit with Splitting of Operators (PISO) pressure-velocity coupling scheme allows solution in either decoupled or coupled manner. It improves the efficiency of the pressure-correction equation to satisfy the momentum equation. Another advantage it offers through its skewness correction process is that the solution obtained is independent of the mesh skewness.

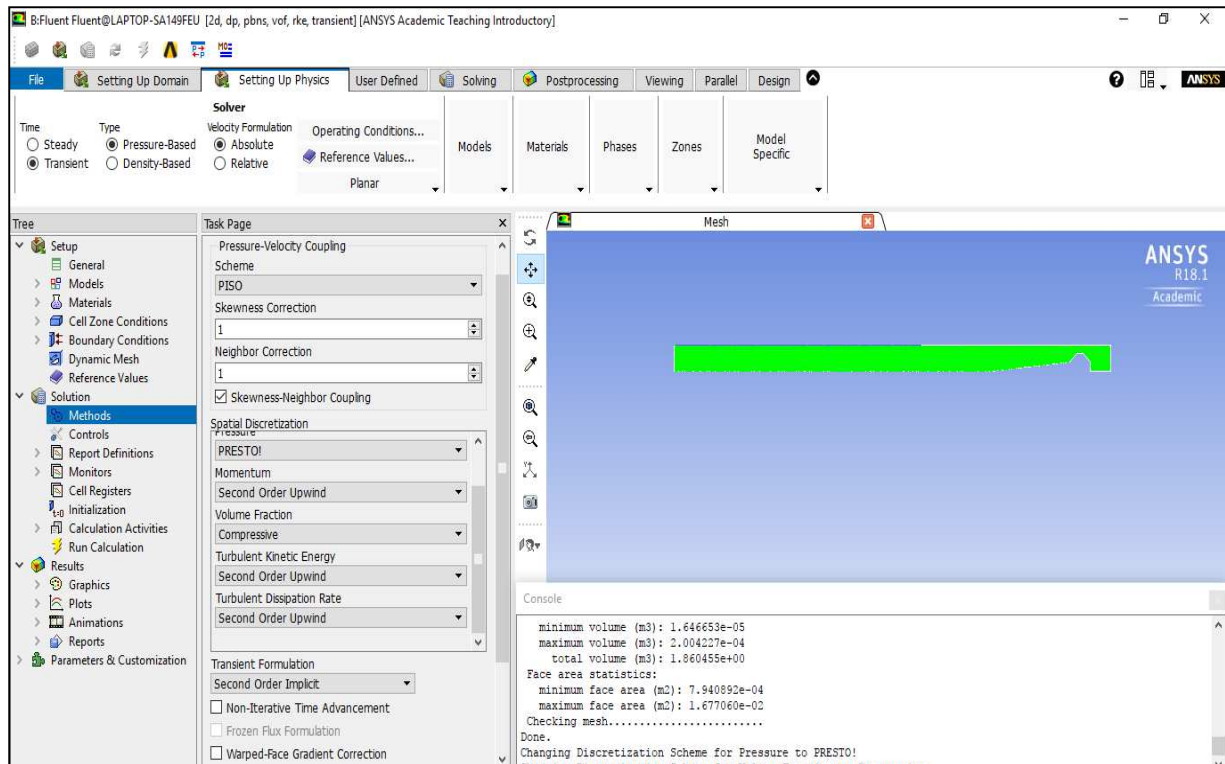


Figure 5.7. The solution method for setting up physics of flow.

Hybrid solution initialisation was employed to accelerate the convergence robustness of the simulation. Regions of the primary and secondary phases were then created within the domain and patched for localized control. The plotting of residuals was enabled to monitor the convergence of the simulation. The time step size of 0.001 s and maximum iterations per time steps of 20 were estimated by trial and error. The number of timesteps of 6000 was set for a 6 s flow. Figures 5.8 and 5.9 show the volume fraction of the phases during and after flow period respectively. Figure 5.10 shows the deduced flow chart for the set-up procedure. The CPU time is about 1h on a PC (Intel® Core (TM) i7-4790 CPU @3.60GHz, 16GB RAM).

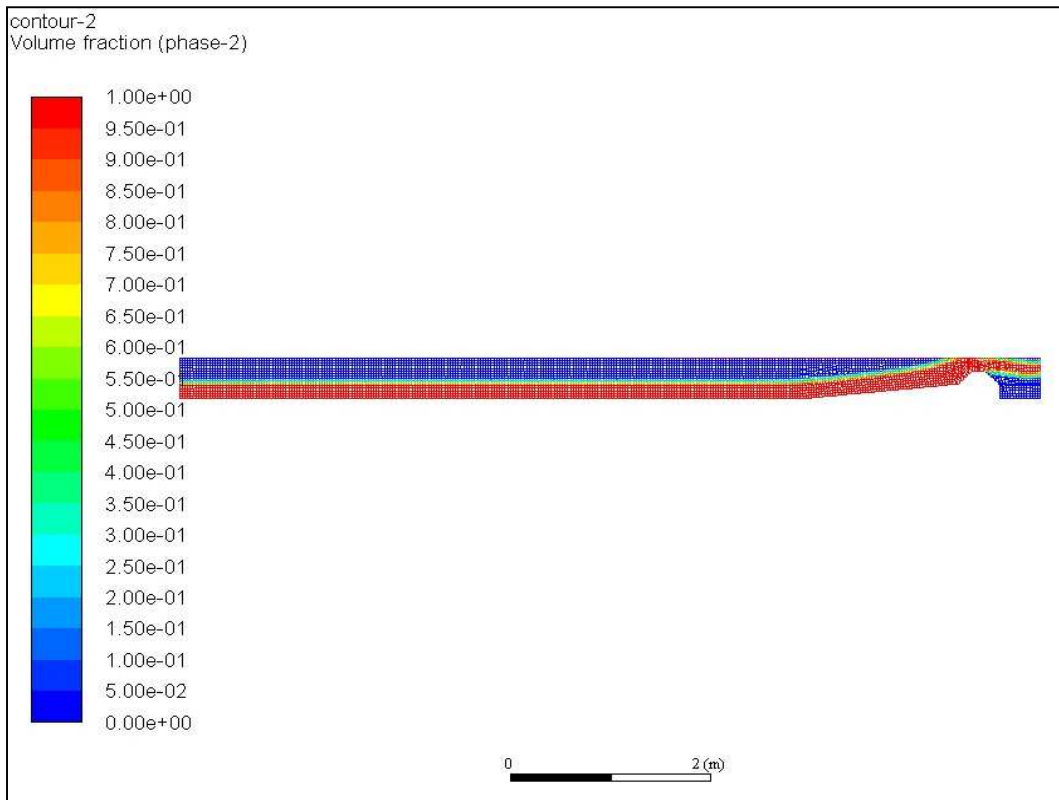


Figure 5.8. The volume fraction of the phases during flow over the sea dike model.

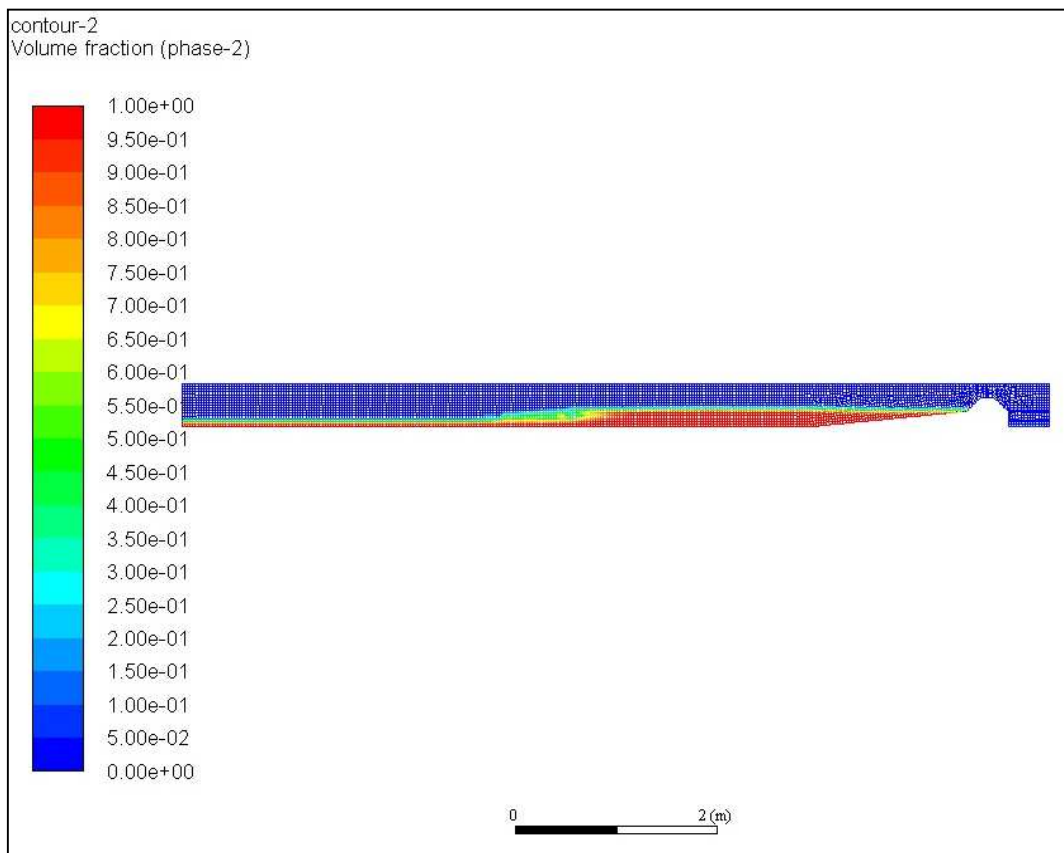


Figure 5.9. The volume fraction of the phases after flow over the sea dike model.

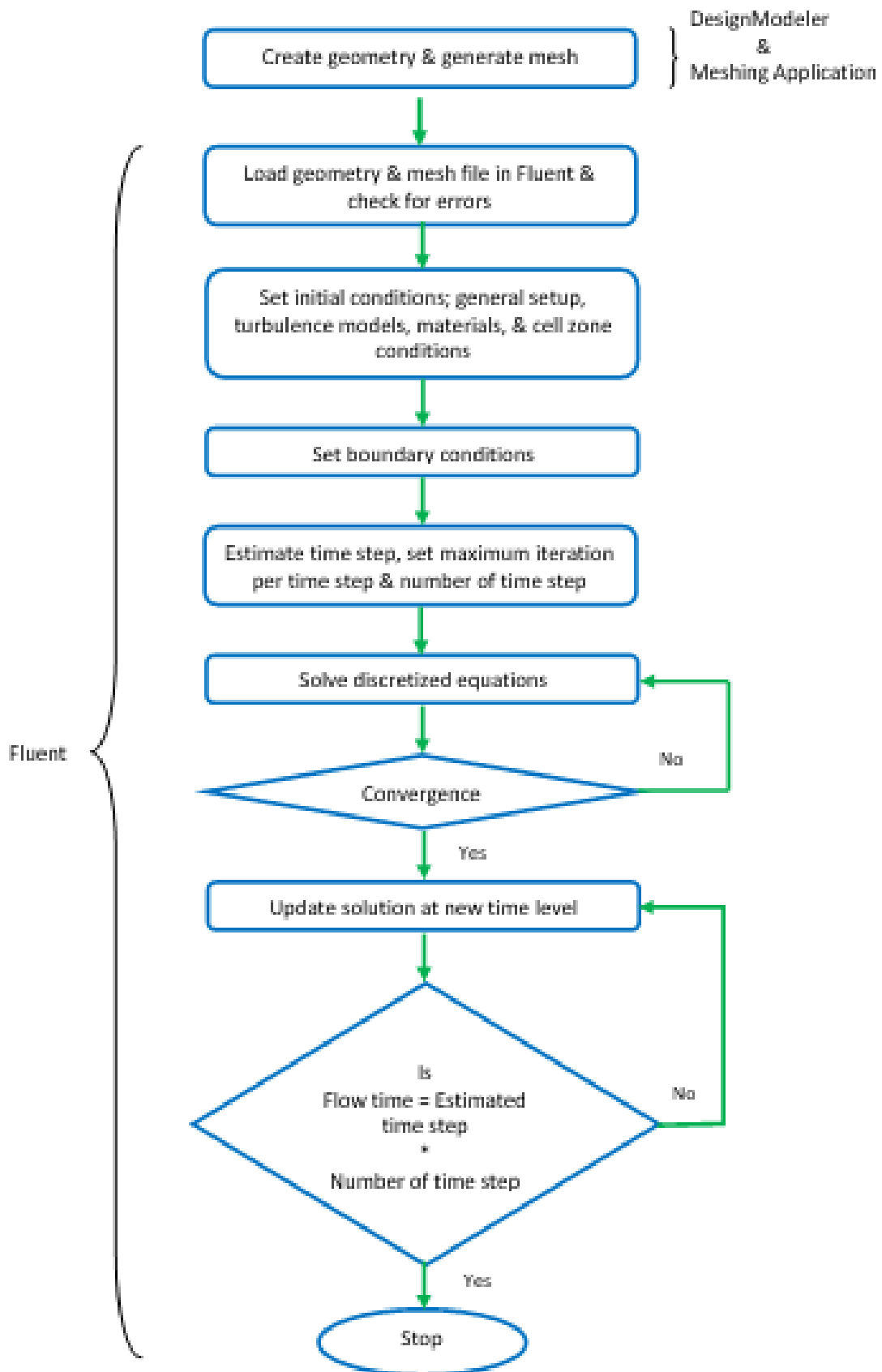


Figure 5.10. Solution procedure flowchart in ANSYS Workbench 18.1.

## **5.2.3 Total tsunami wave pressure**

### **5.2.3.1 Model A**

Figure 5.11 shows the total wave pressure for the three hydraulic conditions. The total wave pressure decreased from 0.43 bar at P1 (the toe of seaward slope) and reached its lowest at the landward slope, P5 (0.14 bar) in Type I hydraulic condition (Fig. 5.11a). There was an overall increase in the P1 and P2 pressure values from 0.43 bar to 0.64 bar and 0.28 bar to 0.43 bar respectively over the three hydraulic conditions. Also, there was an increase in experimental P2 pressure value from 0.35 bar to 0.53 bar.

As shown in Type II hydraulic condition (Fig. 5.11b), the maximum total wave pressure decreased from 0.28 bar at the seaward slope, P1, to 0.17 bar at the landward slope, P5. Like Types I and II hydraulic conditions, the maximum total wave pressure occurred at the seaward slope, P1, and decreased from 0.64 bar to 0.08 bar at the landward slope, P5, in the Type III hydraulic condition (Fig. 5.11c).

All the three hydraulic conditions recorded their maximum overflowing wave pressure at the crest, but the lowest value of 0.13 bar was recorded for Type III hydraulic condition because of the frictional resistance influenced by the large downstream water depths.

### **5.2.3.2 Model B**

Type I hydraulic condition in Figure 5.12a shows that the maximum total wave pressure of 0.33 bar occurred at the seaward slope, P1, and decreased to 0.17 bar on impacting on the landward slope, P5. This trend was consistent with the other two hydraulic conditions. Maximum total wave pressure of 0.20 bar at the seaward slope, P1, reduced to 0.17 bar at the landward slope, P5, in the Type II hydraulic condition (Fig. 5.12b) and in Type III hydraulic condition (Fig. 5.12c), maximum total wave pressure of 0.23 bar at the seaward slope, P1, reduced to 0.094 bar at the landward slope, P5. The overflowing wave pressure was more sustained at the crest than at seaward slope. Reduced maximum impact pressure readings at seaward slope were recorded in both Types II and III hydraulic conditions compared to Type I hydraulic condition. Like Model A, all the three hydraulic conditions recorded their maximum overflowing wave pressure at the crest.

### **5.2.3.3. Model C**

Figure 5.13 provides the instantaneous distribution of total wave pressure for Model C. Maximum wave pressure of 0.34 bar was recorded immediately after the impact of the bore on the seaward slope. This was reduced to 0.18 bar during the overflowing of the wave over the landward slope at P5 for Type I hydraulic condition. There would be the possibility of greater damage to the seaward slope and crest than the landward slope of the dike as evident by the large pressures sustained during the overflowing phase.

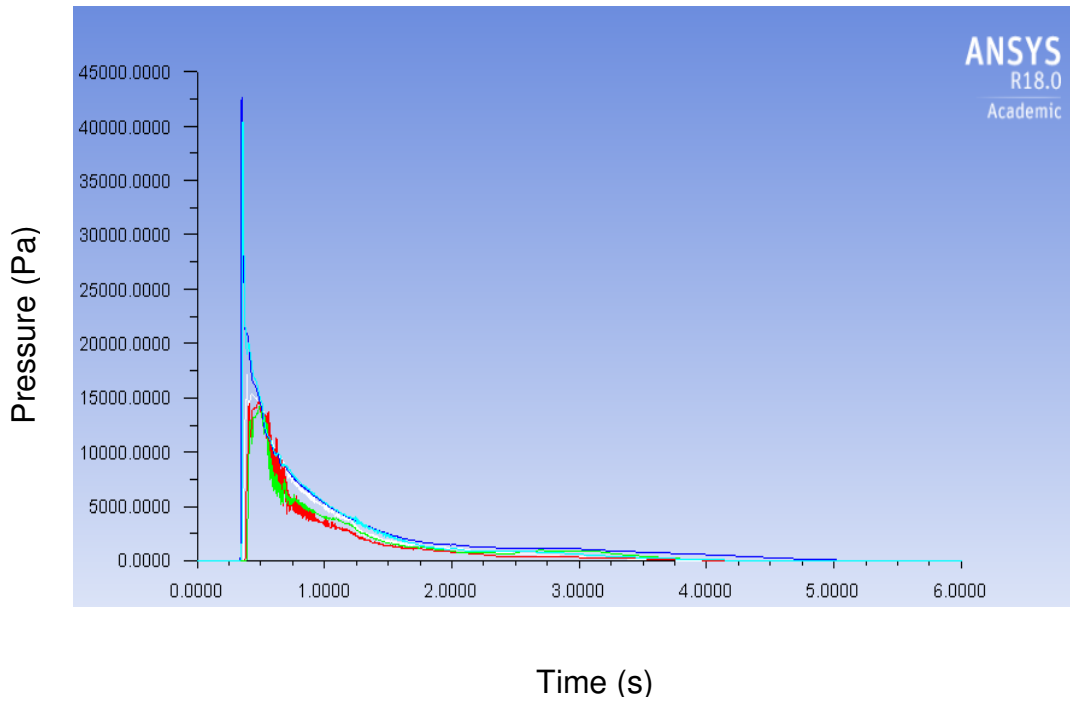
Unlike occurrences of Models A and B, there were more sustained overflowing wave pressures on the landward slope, and the bore first impacted the landward slope at P4 before P5. Like the experimental observation, the maximum impact wave pressure values at the seaward slope and maximum overflowing wave pressure values at the landward slope reduced with increasing downstream depth condition,  $h_d$ . Also, the overflowing pressure values at the crest were larger than at landward slope as the downstream depth,  $h_d$ , increases.

### **5.23.4 Model D**

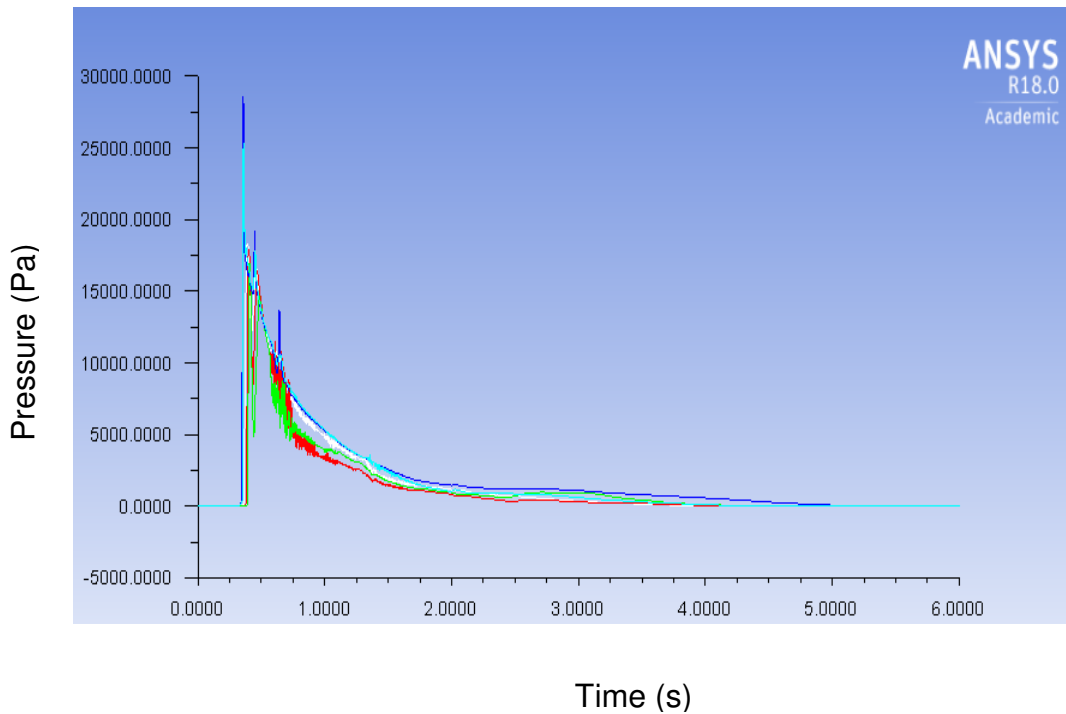
The result of Type I hydraulic condition (Fig. 5.14a), showed that large values of total wave pressure occurred immediately after impact of the flow, and these get reduced as it flows over the landward slope. As shown in Type III hydraulic condition (Fig. 5.14c), there were similar maximum wave pressure values of 0.37 bar during the impact and overflowing phases, except at the landward slope, P4, with a value of 0.34 bar.

The maximum impact total wave pressure occurred close to the toe of the seaward slope, P1, and this occurs for all sea dike models. Also, like all models, the maximum overflowing wave pressure at the landward slope decreased with increasing downstream water depth,  $h_d$ , and the overflowing pressure values at the crest were larger than at landward slope as the downstream depth,  $h_d$ , increased. This observation was also seen in the experimental results.

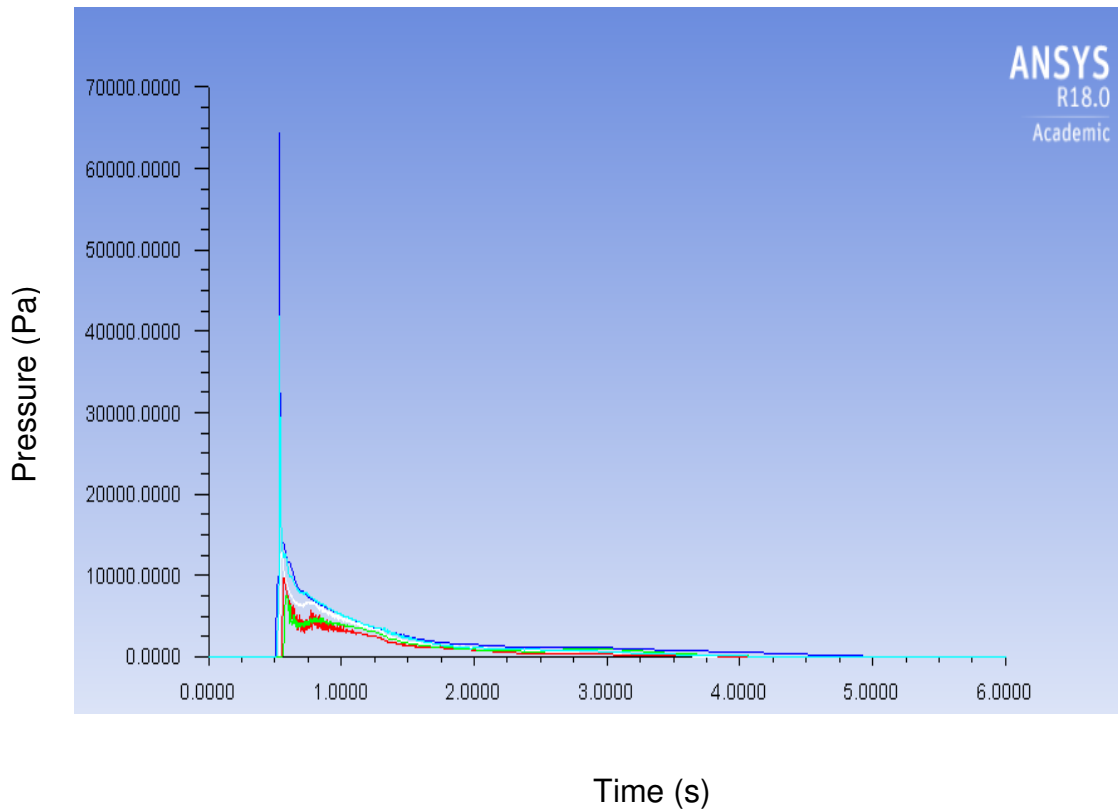
Legend: P1 P2 P3 P4 P3



a. Type I hydraulic condition



b. Type II hydraulic condition

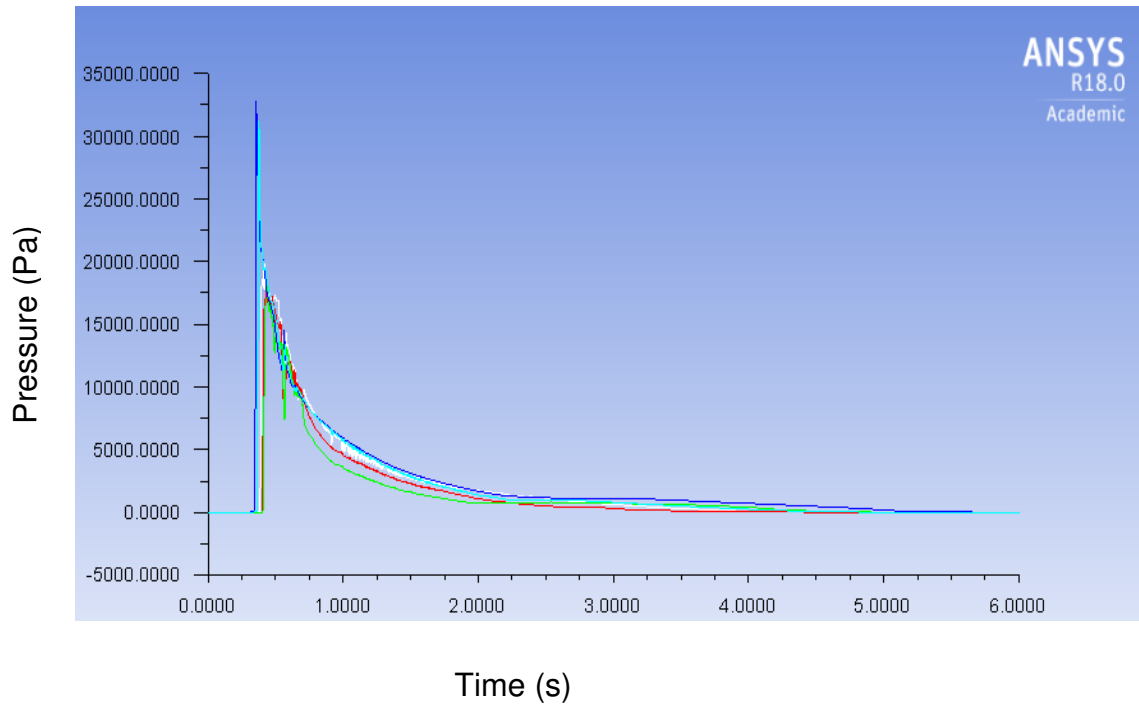


c. Type III hydraulic condition

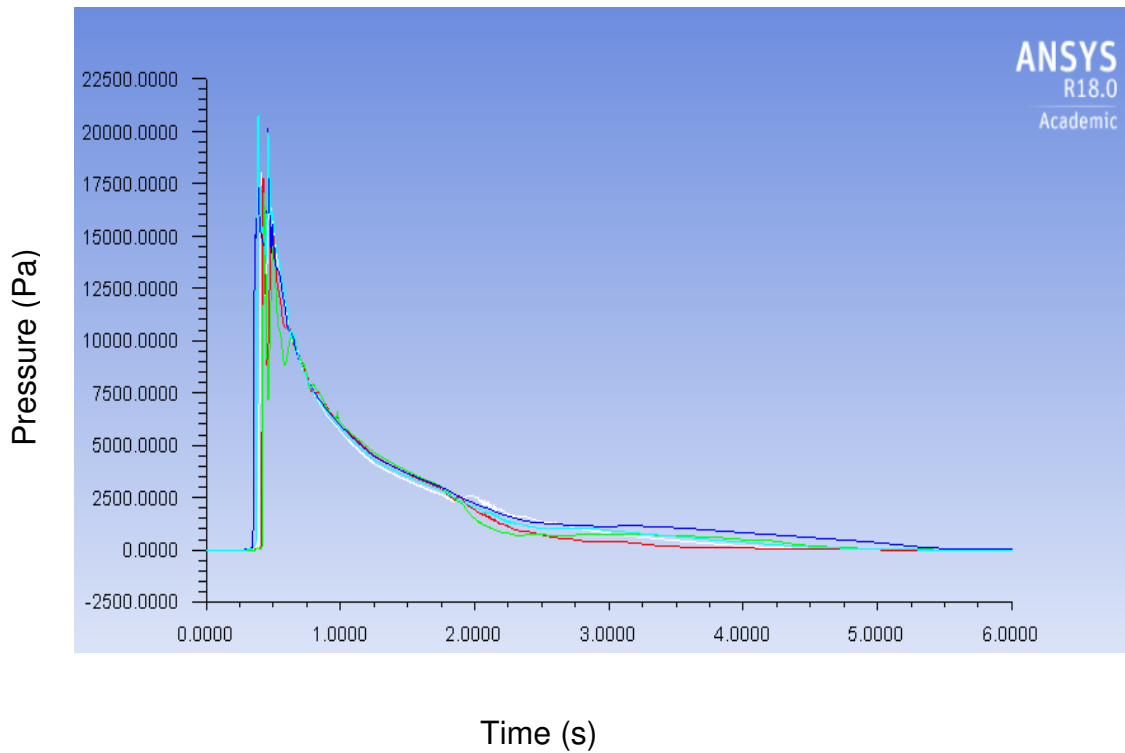
Figure 5.11. Total wave pressure distribution in Model A under various hydraulic conditions.



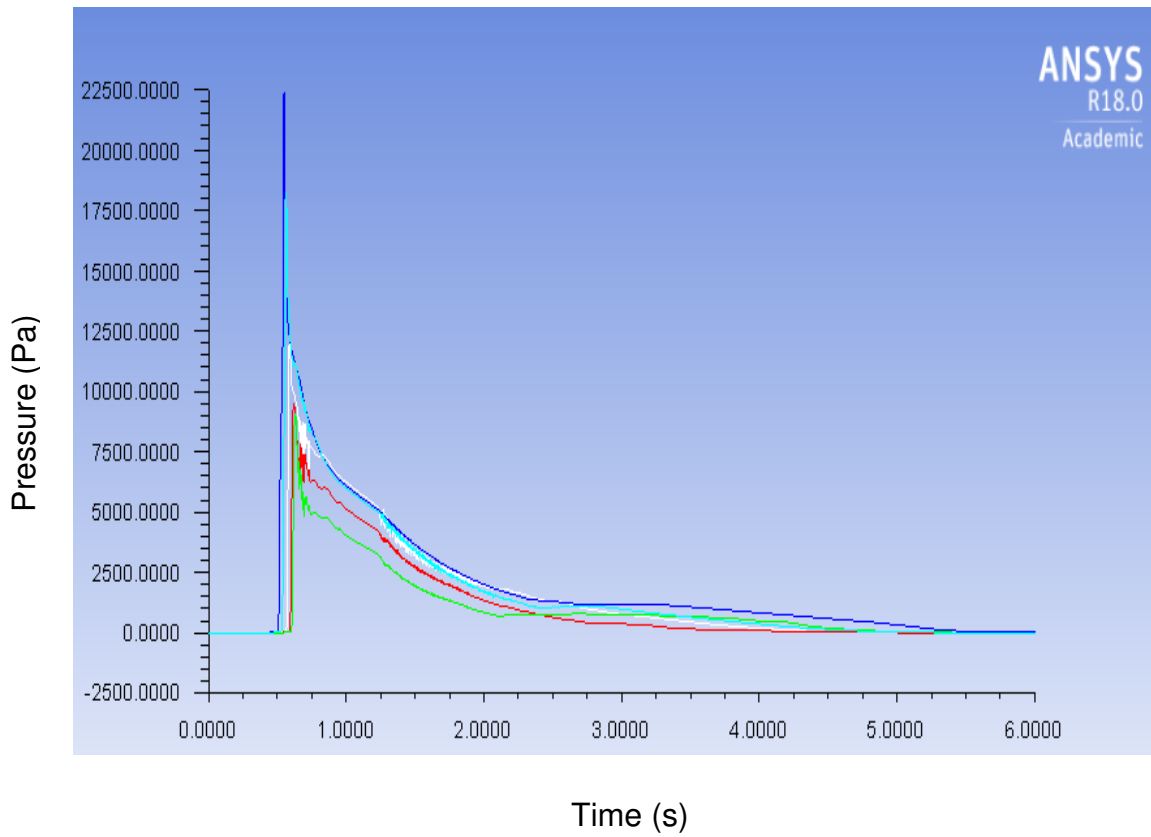
Legend: P1 P2 P3 P4 P3



a. Type I hydraulic condition



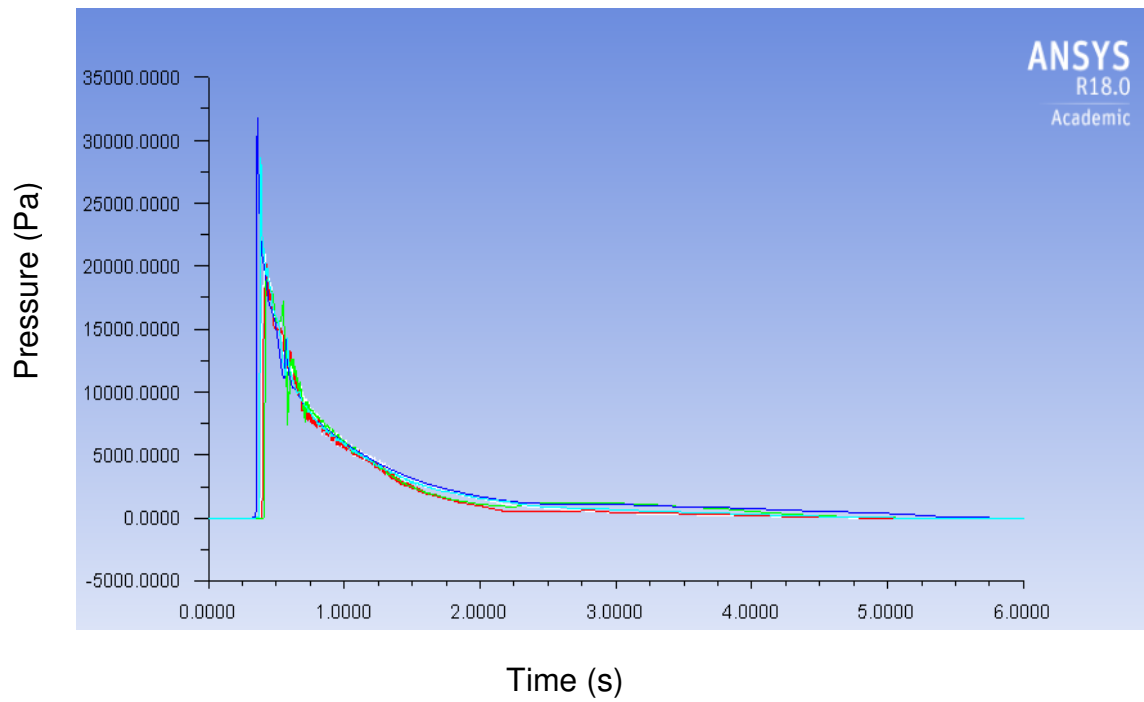
b. Type II hydraulic condition



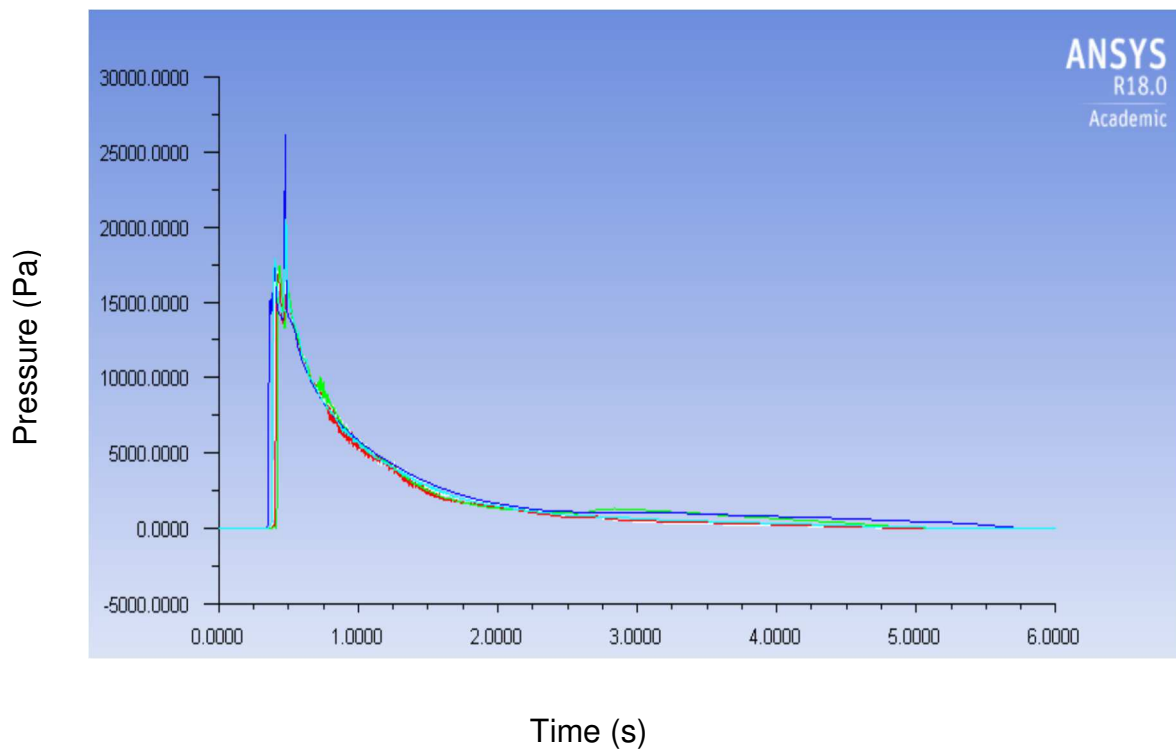
c. Type III hydraulic condition

Figure 5.12. Total wave pressure distribution in Model B under various hydraulic conditions.

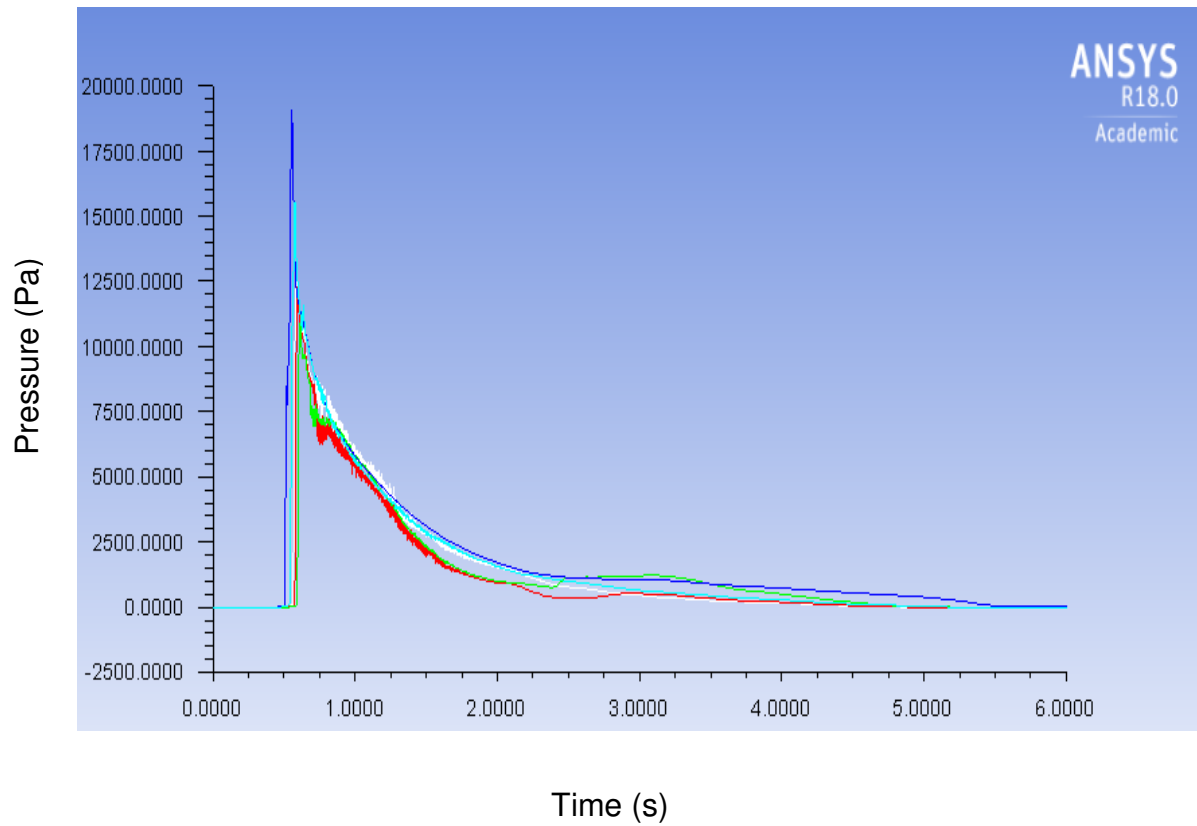
Legend: P1 P2 P3 P4 P3



a. Type I hydraulic condition



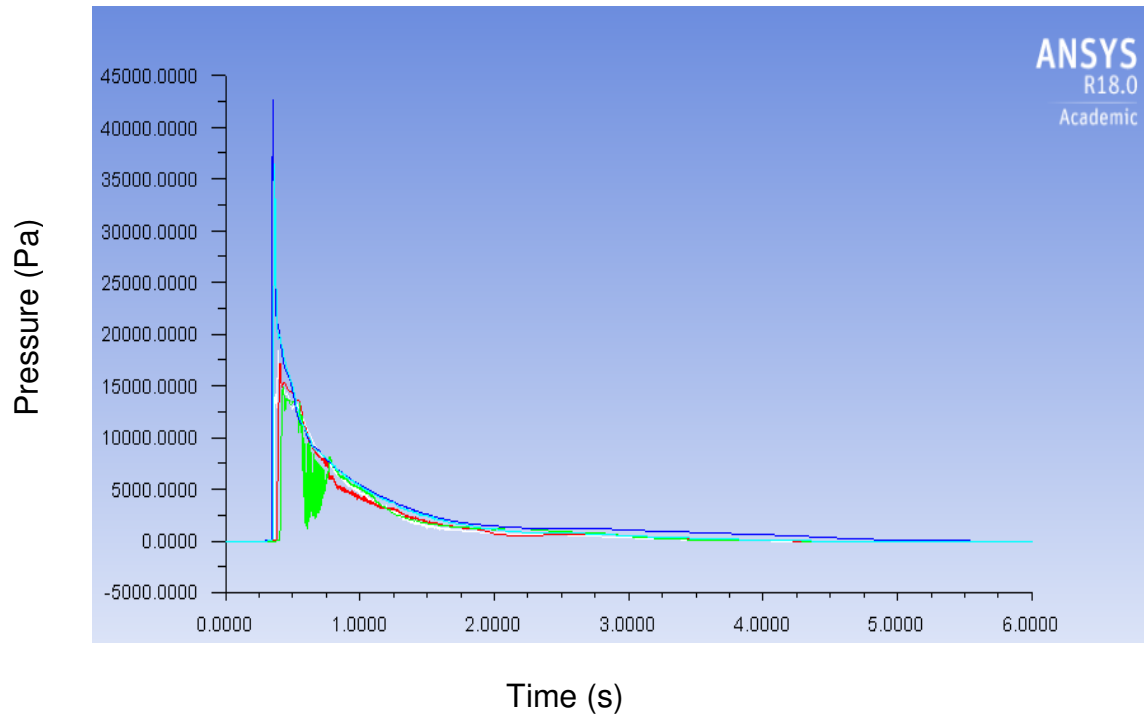
b. Type II hydraulic condition



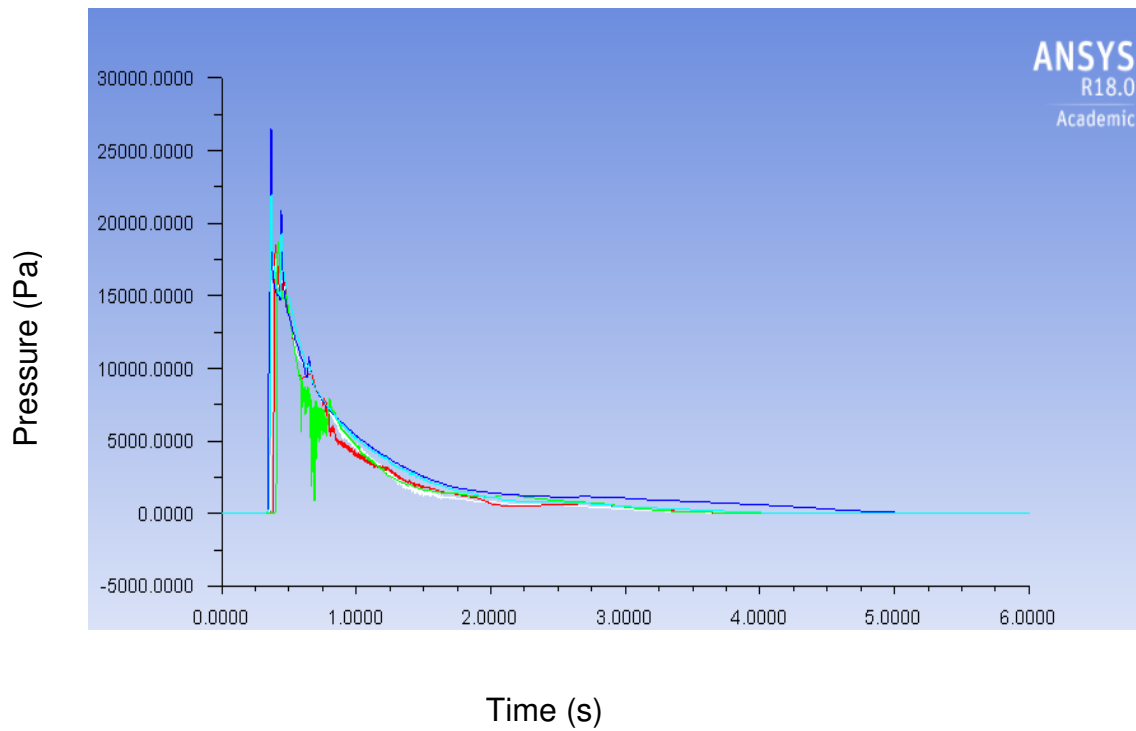
Type III hydraulic condition

Figure 5.13. Total wave pressure distribution in Model C under various hydraulic conditions.

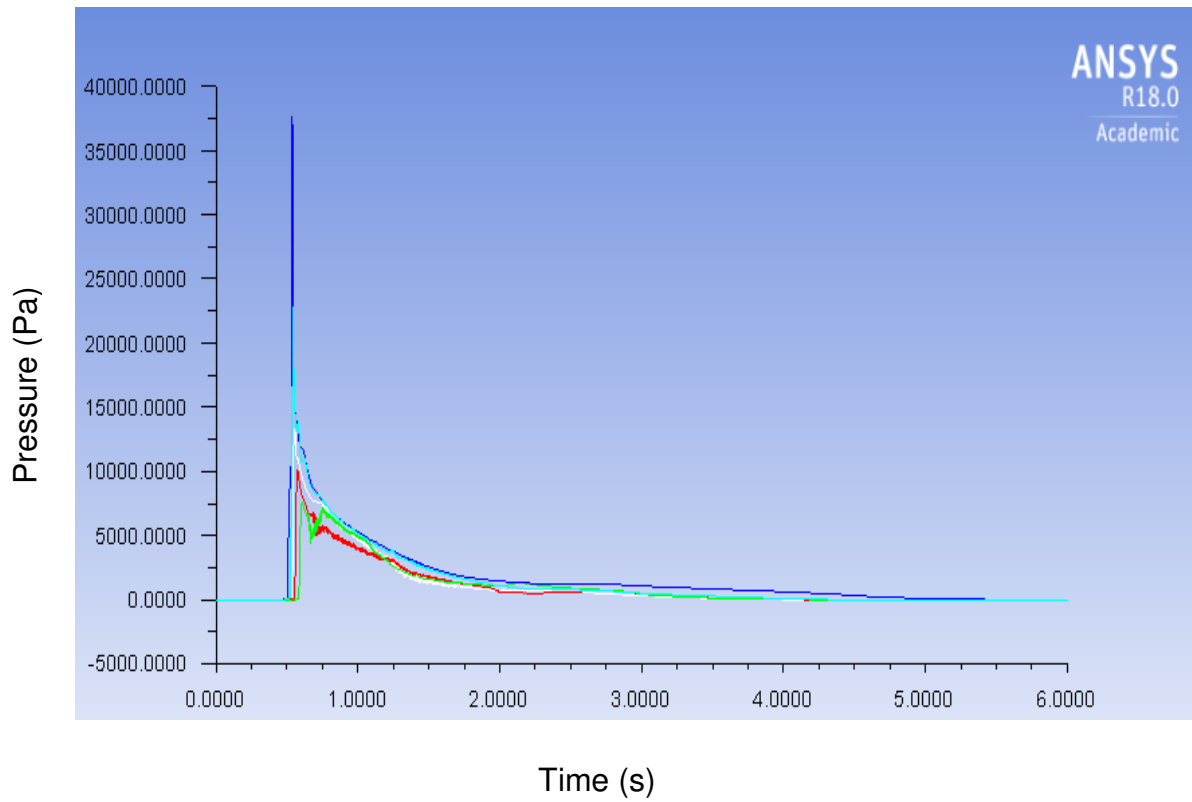
Legend: — P1 — P2 — P3 — P4 — P3



a. Type I hydraulic condition



b. Type II hydraulic condition



c. Type III hydraulic condition

Figure 5.14. Total wave pressure distribution in Model D under various hydraulic conditions.

## 5.2.4 Velocity distributions at the landward region

The post-processing of the computational velocity results generated at the sediment surface level; 0.30 m long and at 0.113 m high, immediately at the landward toe for each of the four sea dike models is presented. The values are employed as maximum velocity,  $V_m$ , measured at the landward region in maximum overflowing wave pressure expression (3.2).

The velocity distribution of models B, C, and D revealed a general decrease in bore velocity as the downstream water depth increased, whereas Model A showed an opposite trend. This is similar to the observation noticed in the experimental data of velocity distribution. Model B decreased from 2.58 m/s for the hydraulic condition I to 2.25 m/s for hydraulic condition II, but with an initial increase to 2.62 m/s for type II hydraulic condition. Model C decreased from 1.85 m/s to 1.79 m/s, and model D decreased from 2.23 m/s to 2.19 m/s for type III hydraulic condition, but with an initial increase to 2.59 m/s for type II hydraulic condition. The opposing trend in Model A was the decrease from 1.87 m/s to 1.79 m/s for type II hydraulic condition and then an increase back to 1.87 m/s for type III hydraulic condition (Figs.5.16 – 5.19). The comparison of both the numerical and laboratory data is shown in Fig. (5.15).

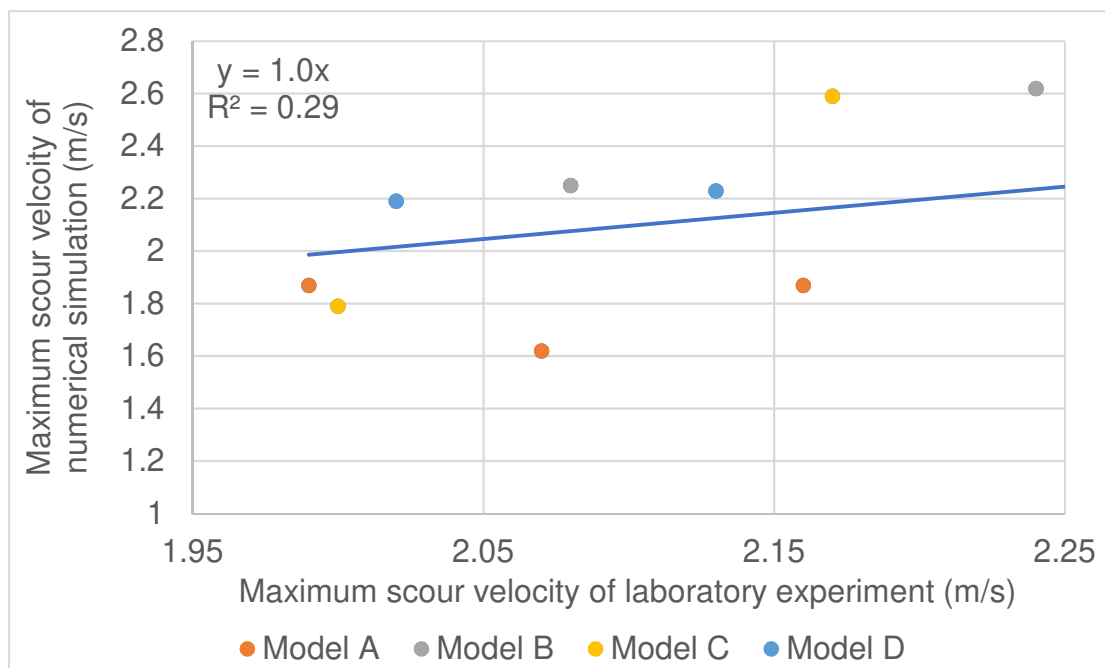
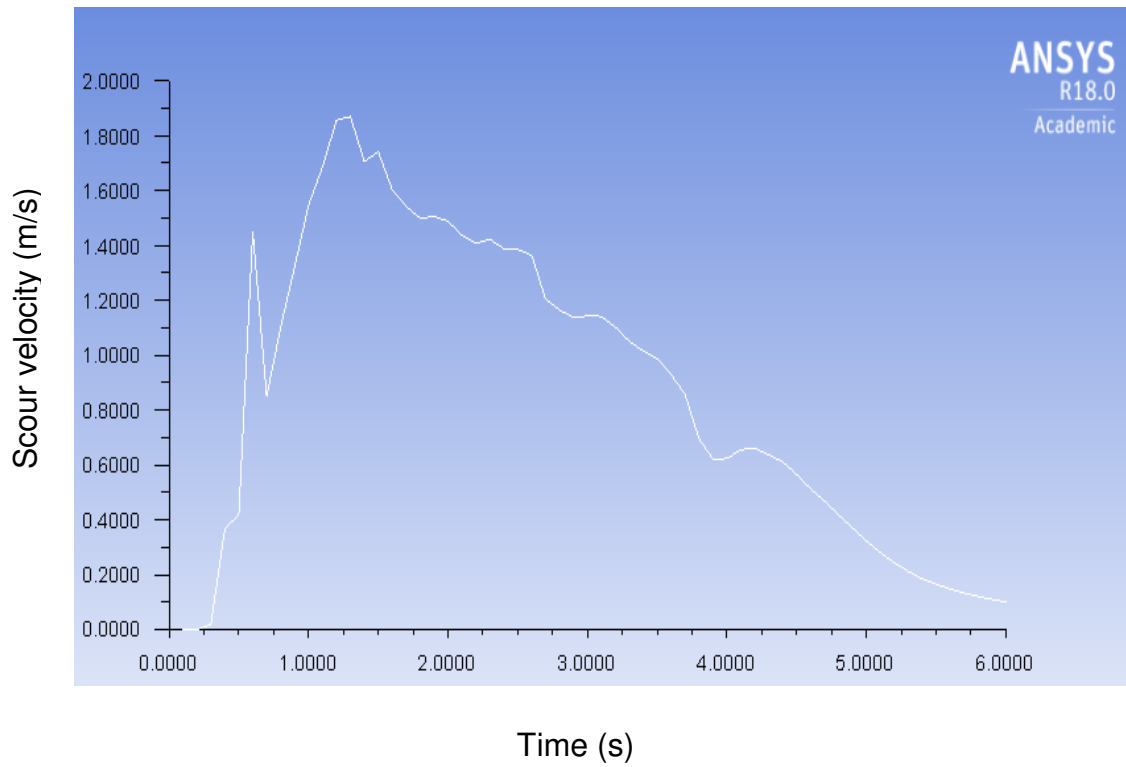
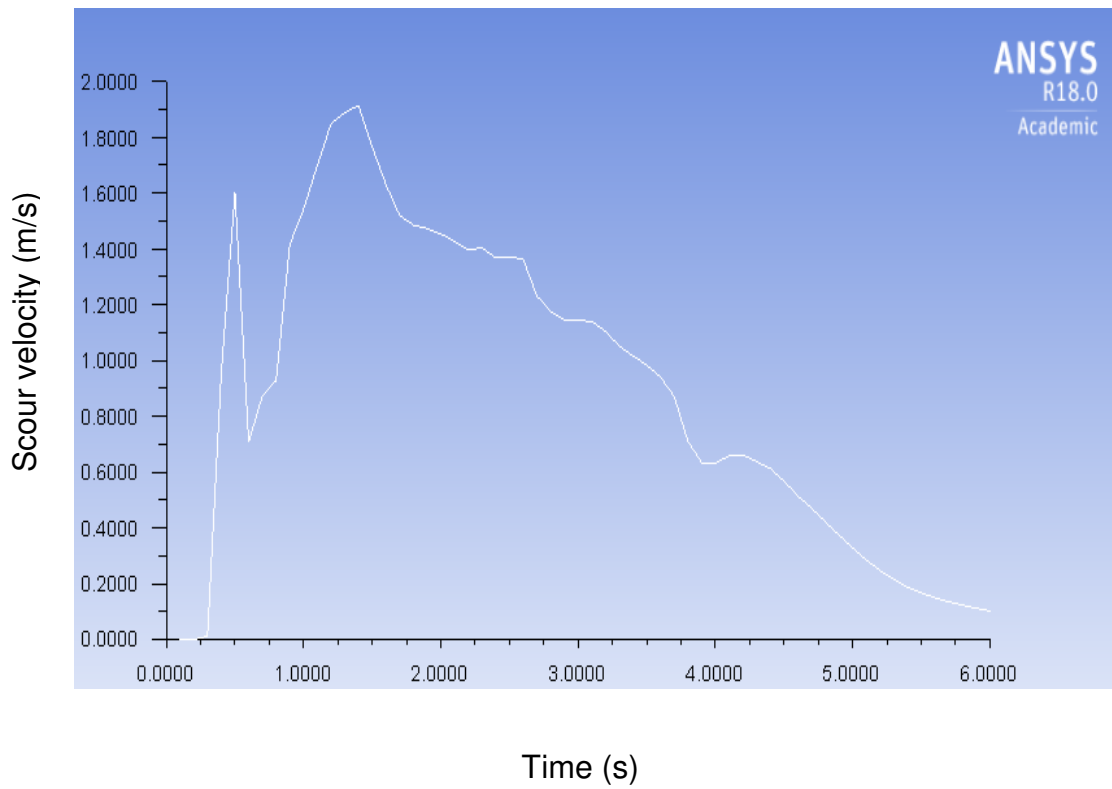


Figure 5.15. maximum scour velocity comparison between numerical and laboratory data.

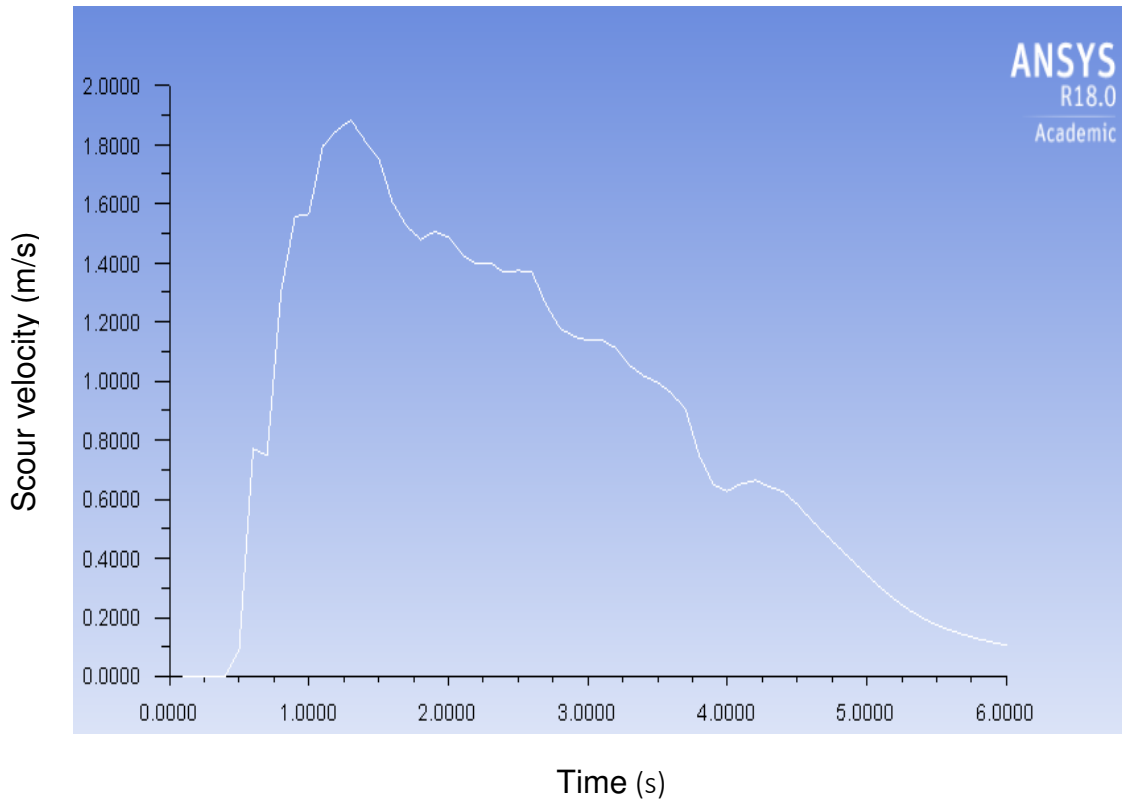


a. Type I hydraulic condition



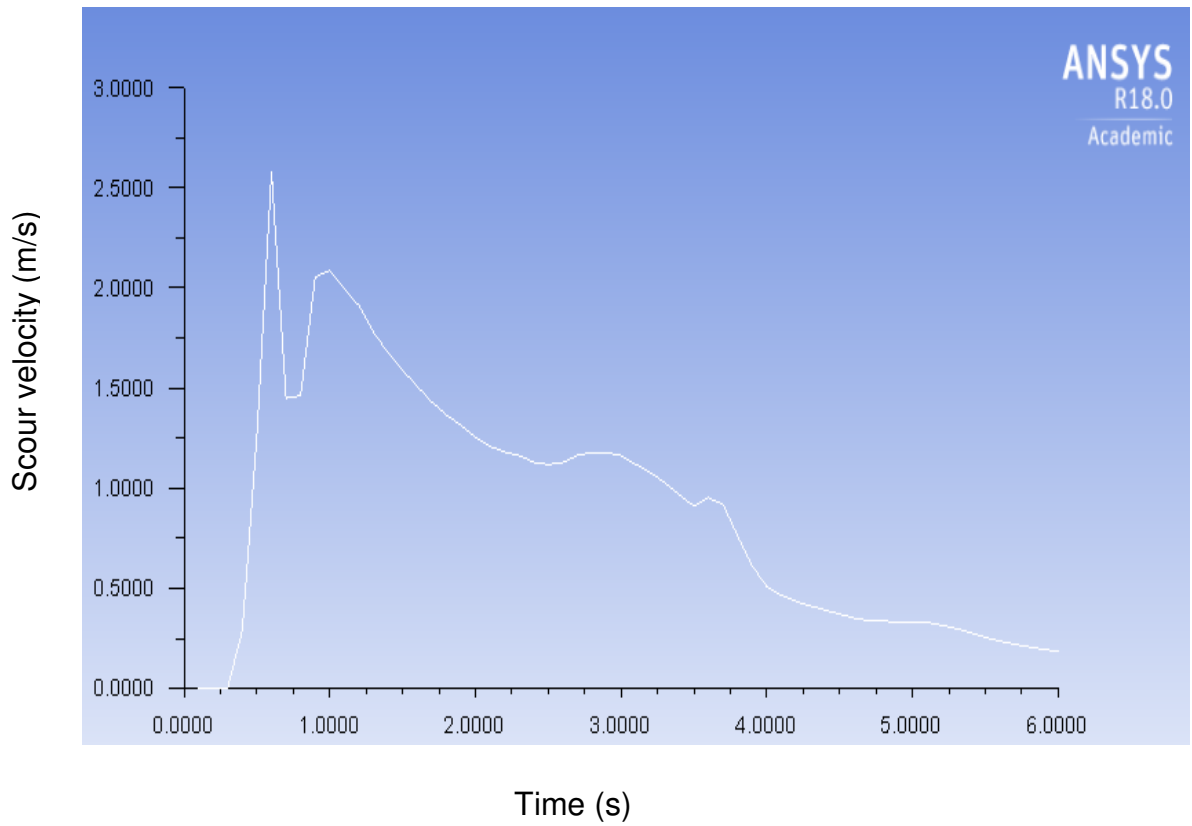
b. Type II hydraulic condition



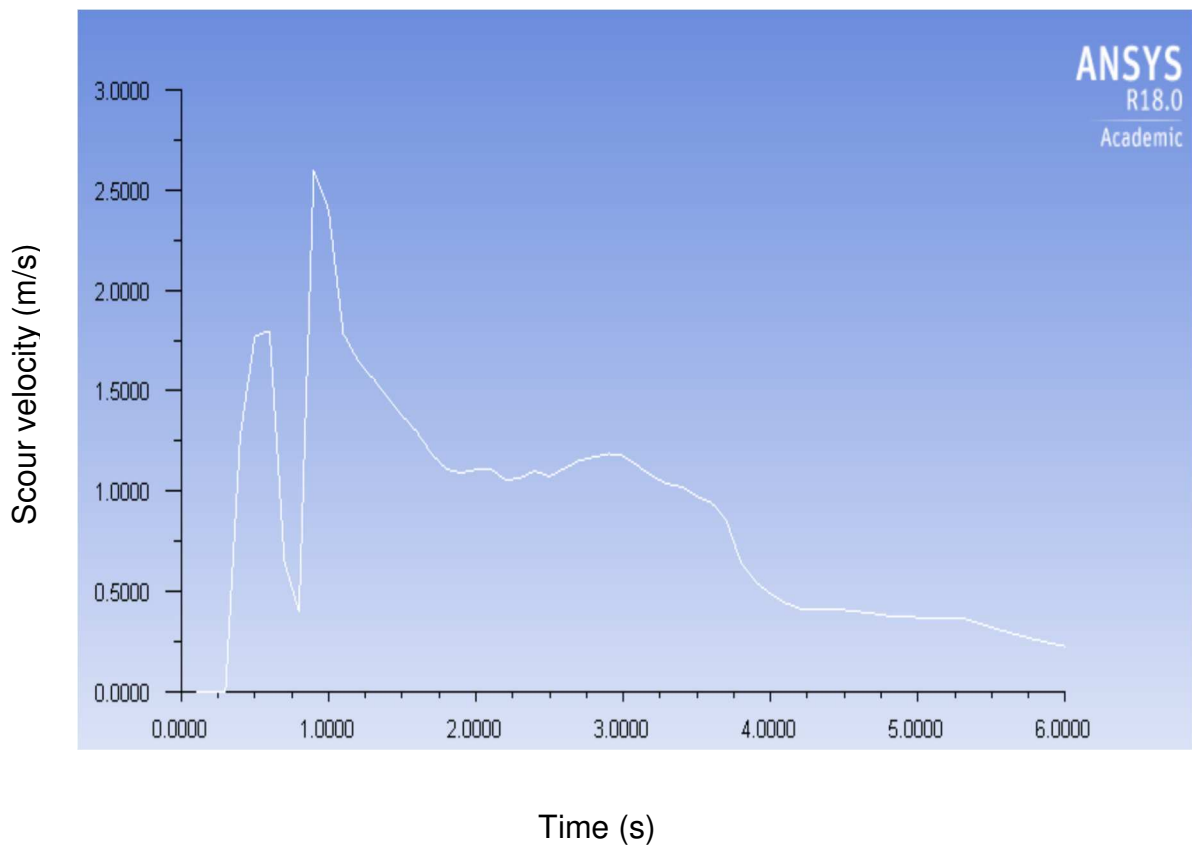


c. Type III hydraulic condition

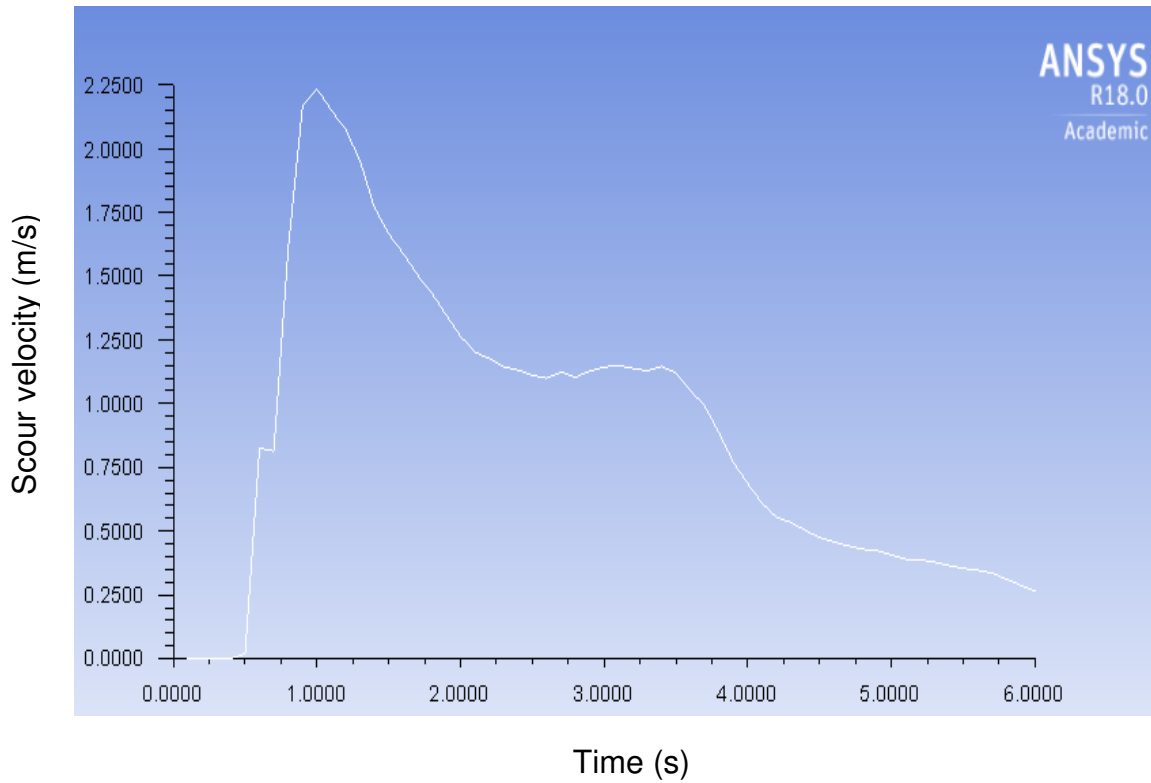
Figure 5.16. Velocity distribution behind Model A under various hydraulic conditions.



**a.** Type I hydraulic condition

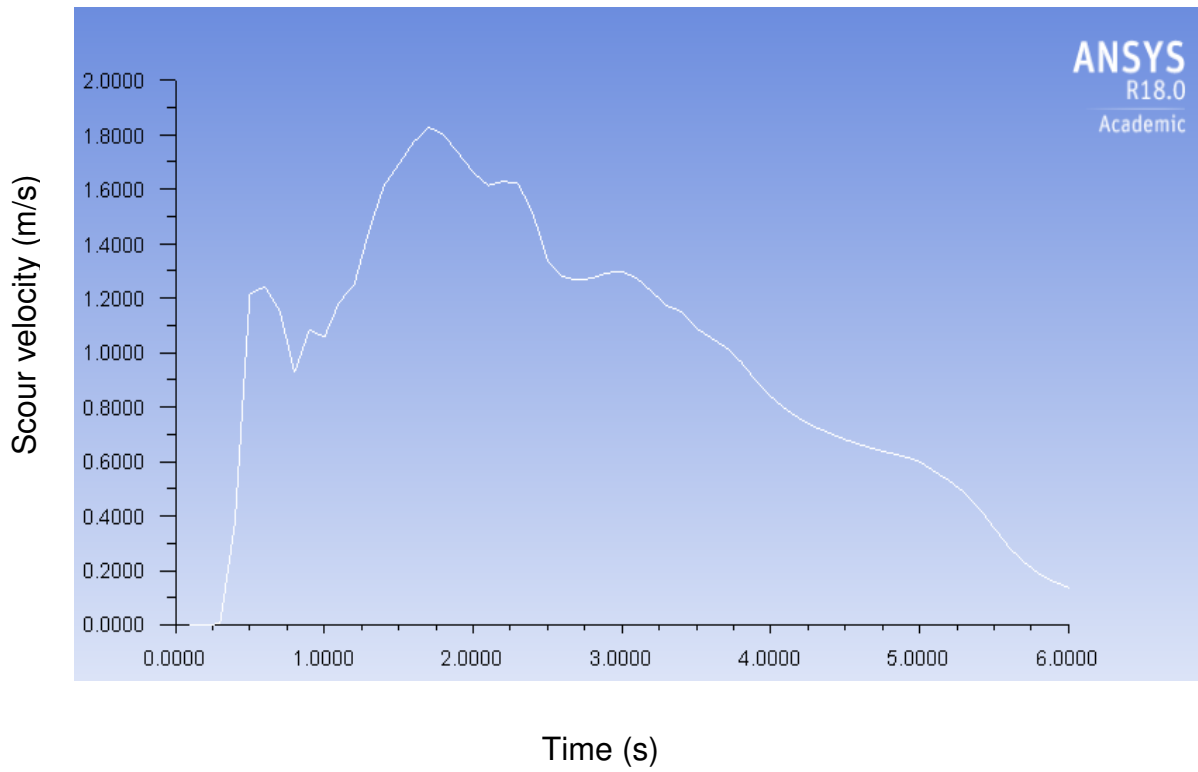


**b.** Type II hydraulic condition

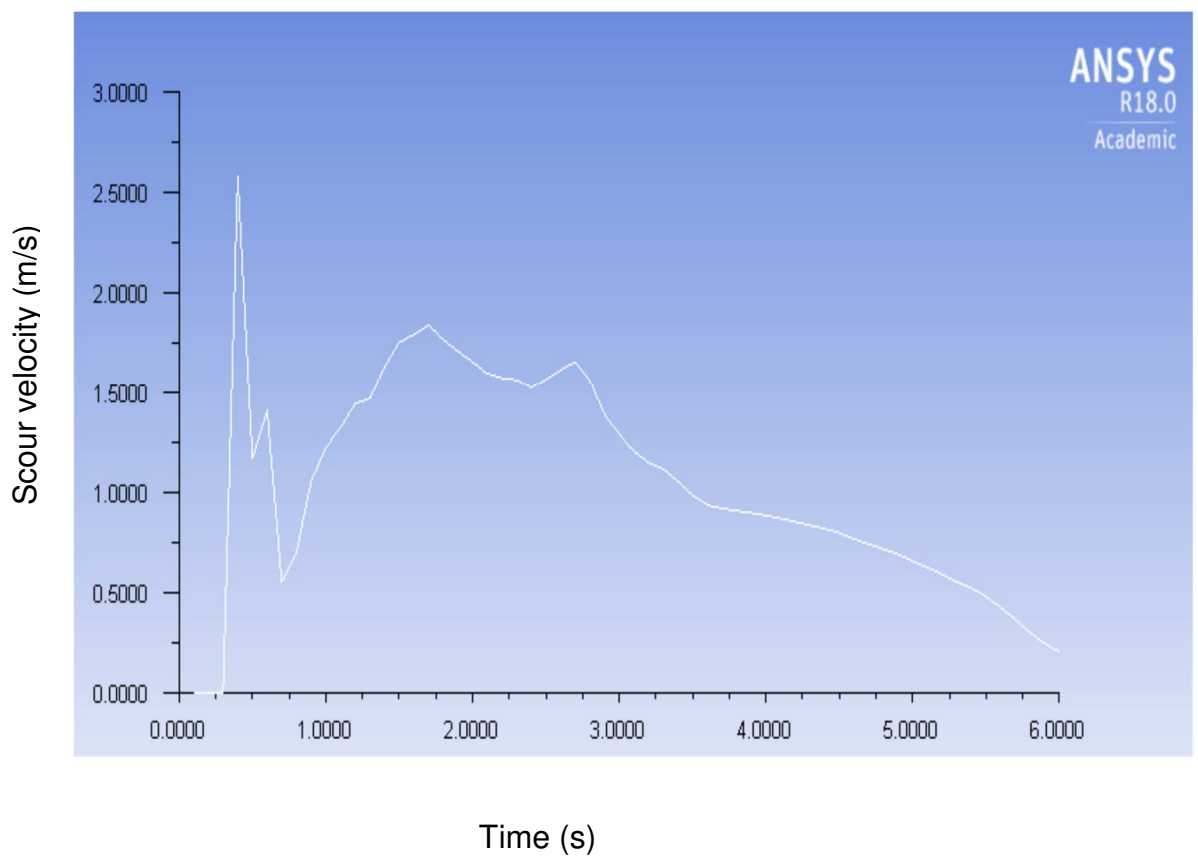


C. Type III hydraulic condition

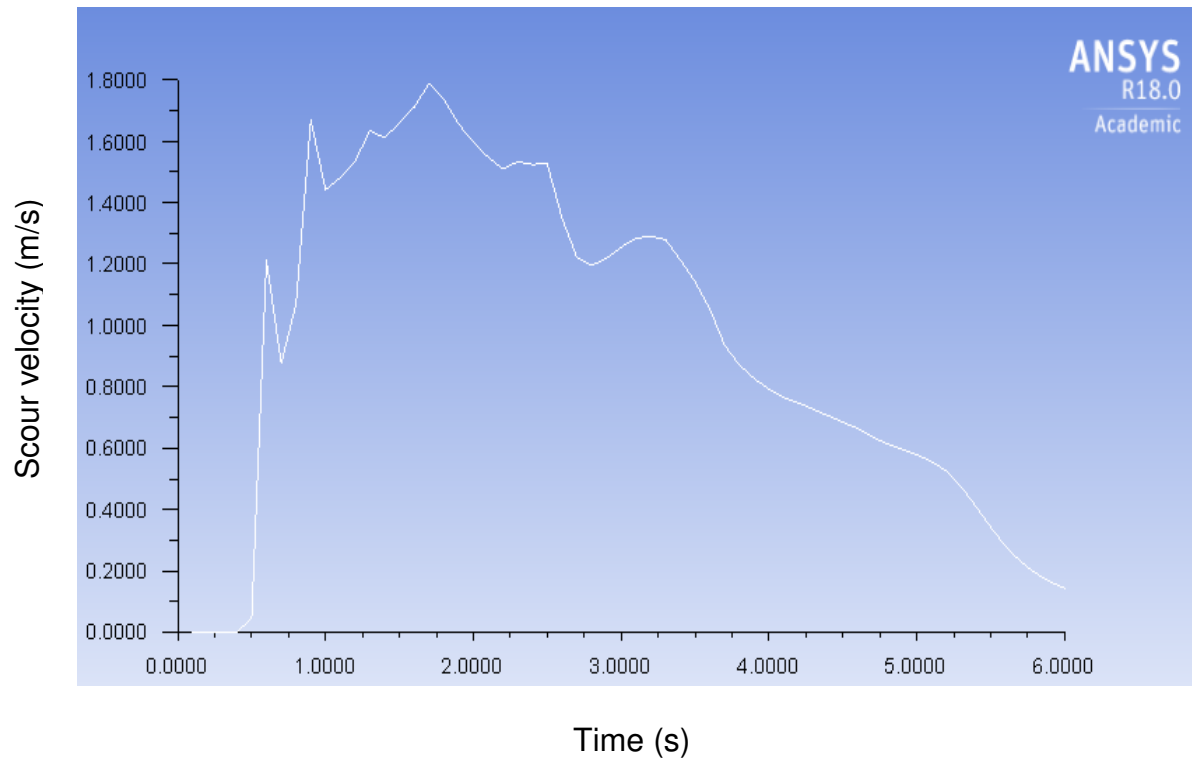
Figure 5.17. Velocity distribution behind Model B under various hydraulic conditions.



a. Type I hydraulic condition

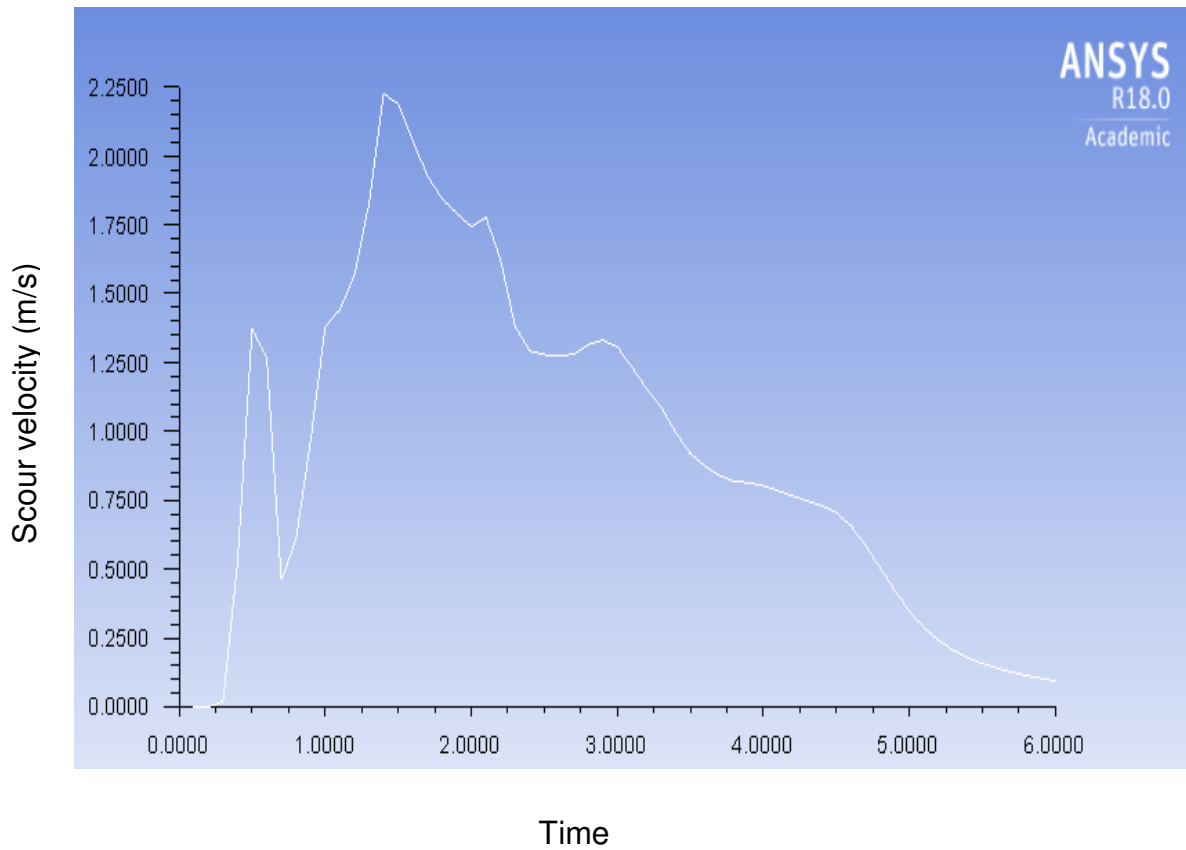


b. Type II hydraulic condition

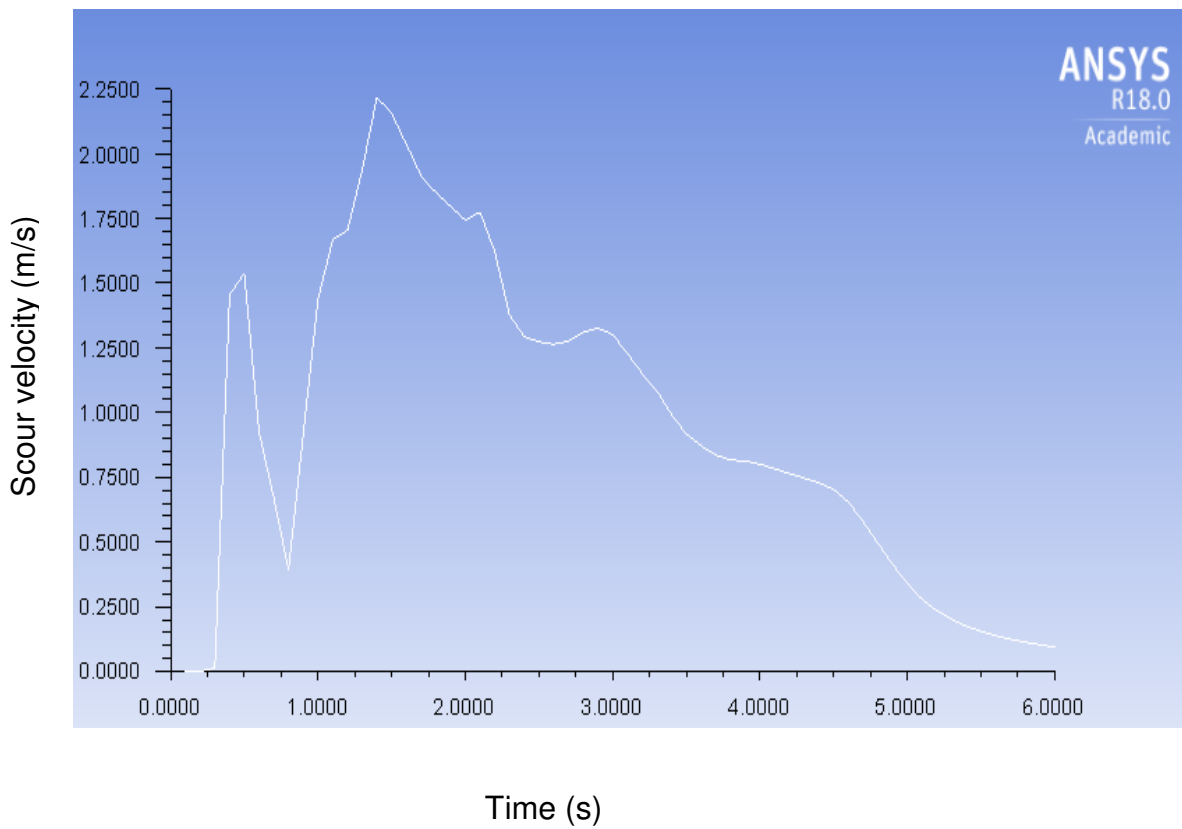


c. Type III hydraulic condition

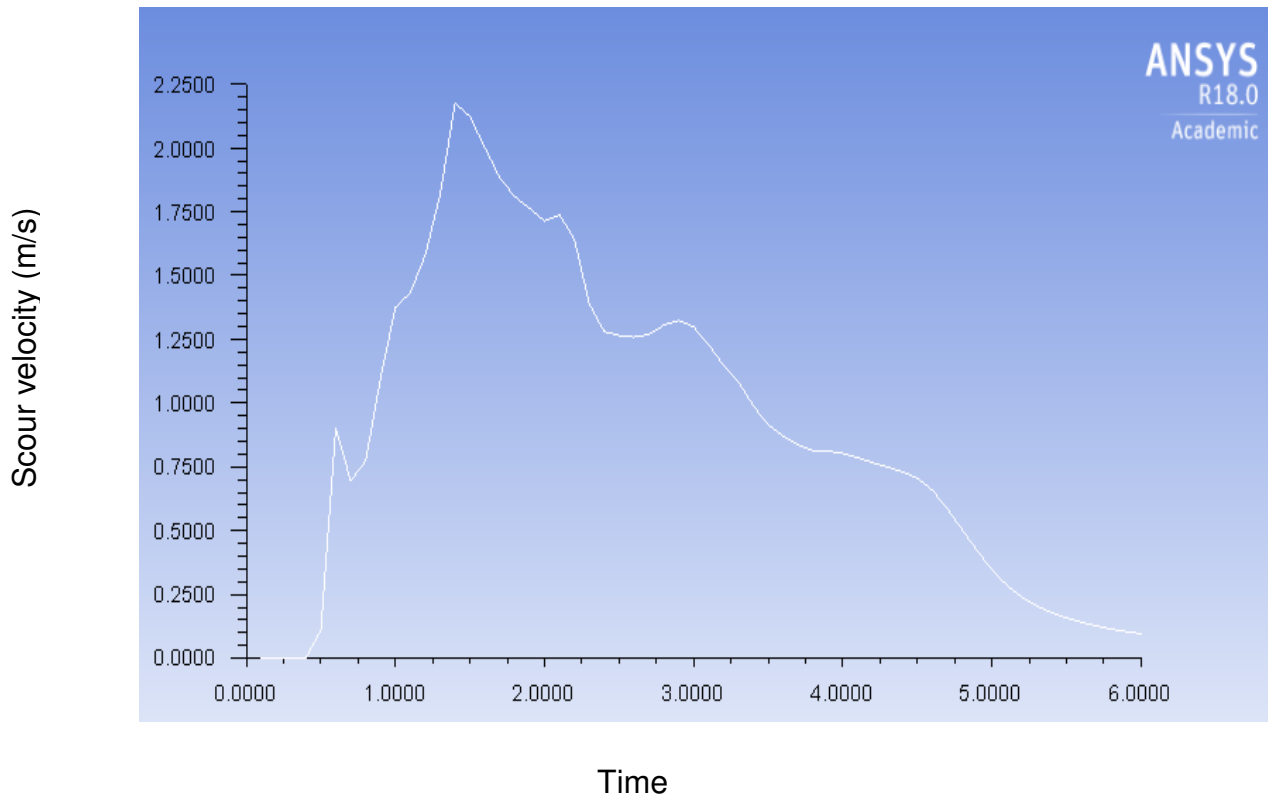
Figure 5.18. Velocity distribution behind Model C under various hydraulic conditions.



a. Type I hydraulic condition



b. Type II hydraulic condition



c. Type III hydraulic condition

Figure 5.19. Velocity distribution behind Model D under various hydraulic conditions.

### 5.2.5 Comparison between the numerical simulation and laboratory experiment

Hydraulic conditions for Models B and C seem to best fit the formula for the maximum overflowing pressure with average errors of 0.55 and 0.26 respectively (Fig. 5.20 & Table 5.3). Average error, E, which indicates the suitability of the model to numerical data shows that coastal dike models A and D data have the largest deviation from the model equation of overflowing wave pressure.

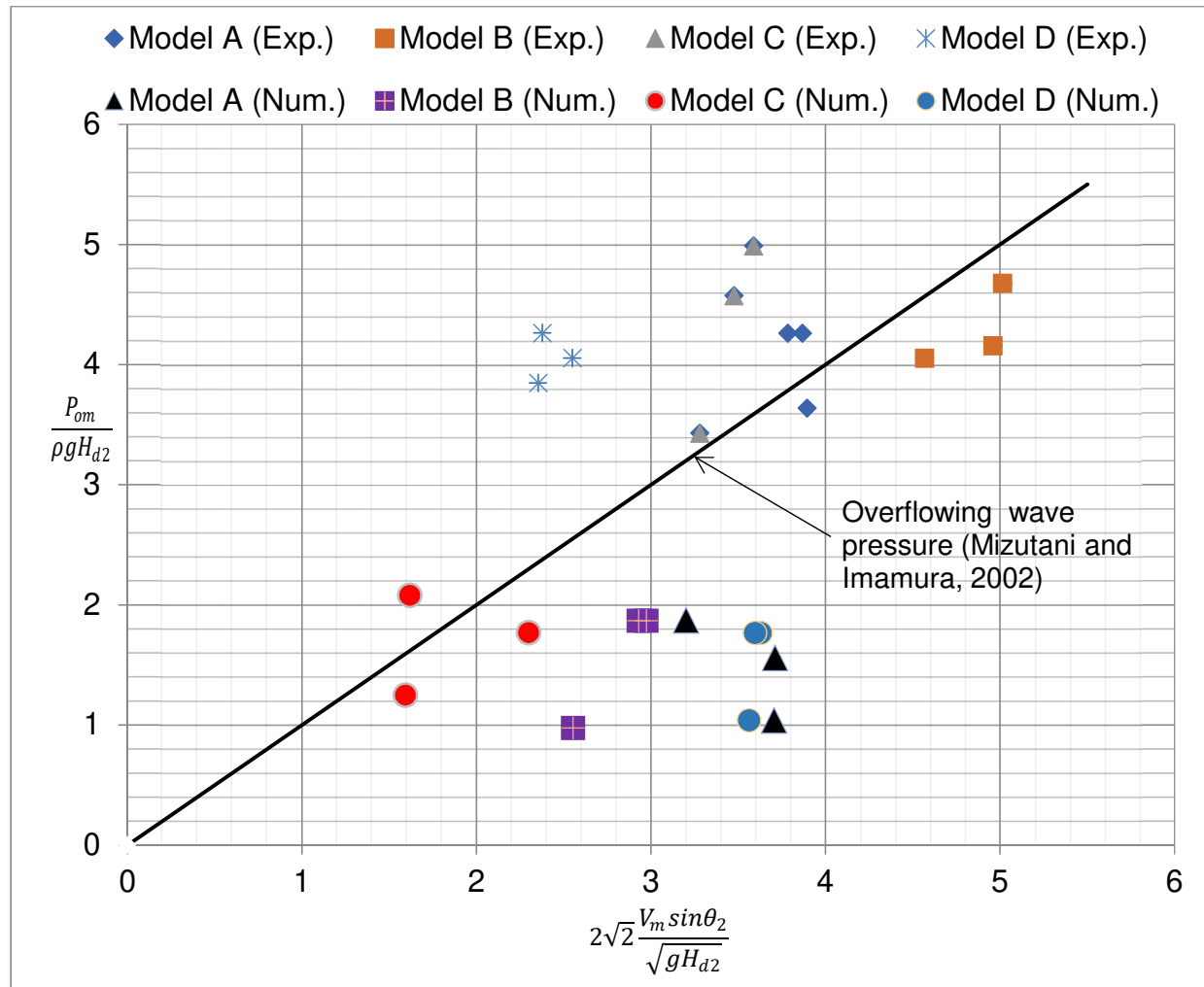


Figure 5.20. The relationship between overflowing wave pressure and flow quantities from experimental (Exp.) and numerical (Num.) simulation.



Table 5.3. Comparison of numerical and experimental average errors of the observed data from the overflowing wave pressure model

Model	$X = 2\sqrt{2} \frac{V_m \sin \theta_2}{\sqrt{gH_{d2}}}$ Numerical	$Y_i$ (Observed data) Numerical	$\hat{Y}$ (Model data)	E (Average error) Numerical	E (Average error) Experimental
A	3.71	1.56	3.71	1.22	0.22
	3.21	1.87	3.21		
	3.71	1.04	3.71		
B	2.93	1.87	2.93	0.55	0.34
	2.97	1.87	2.97		
	1.62	0.98	1.62		
C	1.62	2.08	1.62	0.26	0.60
	2.30	1.77	2.30		
	1.59	1.25	1.59		
D	3.63	1.77	3.63	1.21	0.95
	3.60	1.77	3.60		
	3.56	1.04	3.56		

### 5.3. Numerical Methodology of Dam Break Flow - Comparison Using ANSYS Fluent

#### 5.3.1 Introduction

The total wave pressures over the sea dike models are in the same order of magnitude but the substantial variation between both laboratory and numerical data revealed in Figure 5.20 necessitates the need to verify the numerical method employed with another peer-reviewed journal paper by Lobovsky et al. (2014). They performed extensive laboratory measurements on dam break flow over a dry horizontal bed to determine the dynamic wave pressure impacting on a vertical wall opposite the dam gate (Fig. 5.21).

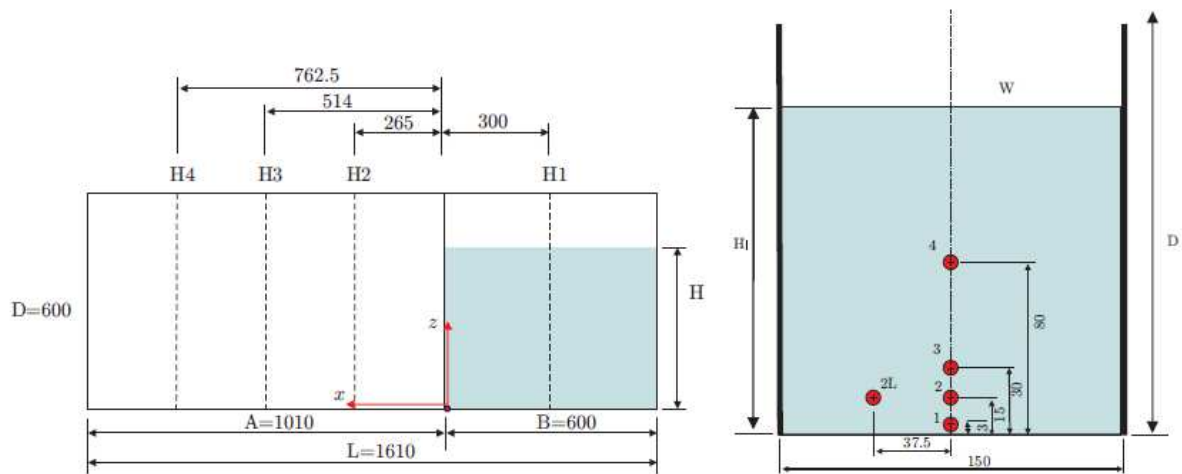


Figure 5.21. A side view of hydraulic flume with locations of water level measuring positions (left) and a front view showing the locations of pressure sensors at the impact wall downstream the dam (right). Dimensions in millimetres (Lobovsky et al., 2014). (Image reproduced with permission of the rights holder, Elsevier. Appendix D).

The numerical simulation set up comprises of two-phase flows of air and water. The water has a density of  $998 \text{ kg/m}^3$ , a dynamic viscosity of  $0.001003 \text{ kg/m.s}$  and surface tension of  $0.072 \text{ N/m}$  for the phase interaction. A grid size,  $\Delta x$ , and  $\Delta y$ , of  $0.01 \text{ m}$  with the same boundary conditions employed in this project was used for the numerical simulation.

In this 2D numerical simulation, the same maximum grid size, boundary conditions and other Fluent setup parameters employed for the numerical investigation of the laboratory dam break flow setup in Section 5.2 are used to verify the numerical methodology. Four points on the vertical downstream wall were set up to represent four of the five pressure sensors locations in the experimental arrangement shown in Figure 5.21. The dynamic pressure values were determined for sensors 1 - 4.

### 5.3.2 Computational setup

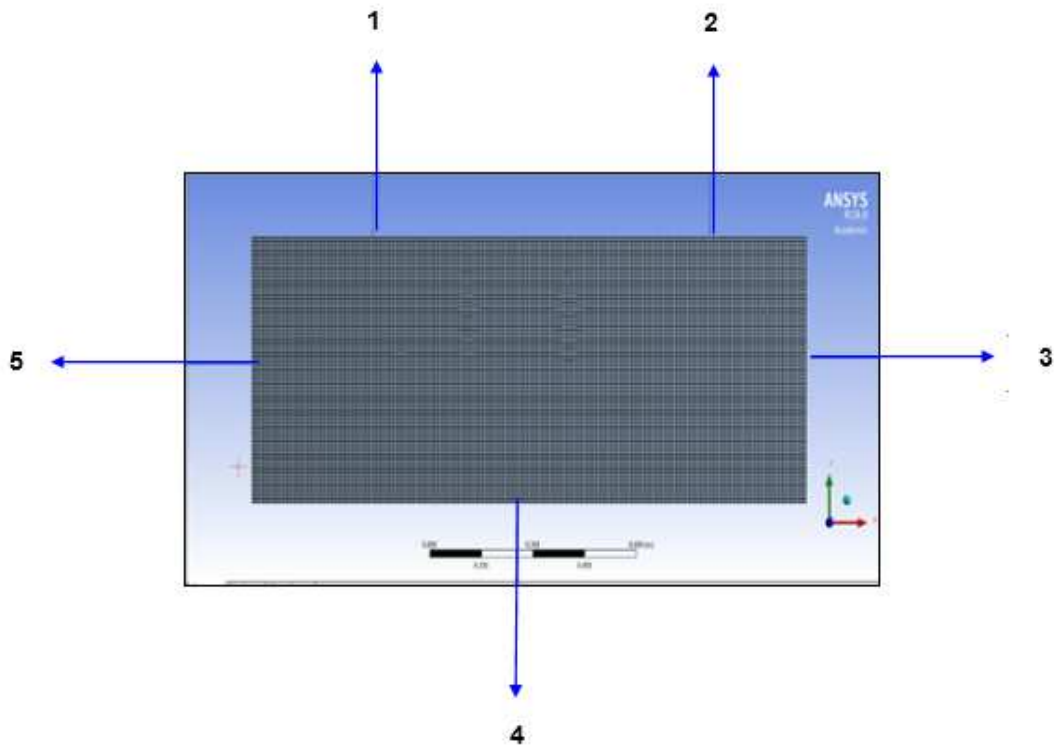


Figure 5.22. Different zones for boundary condition set up in Fluent (Zone 1: Free surface, Zone 2: Inlet, Zone 3: Right wall, Zone 4: Bottom wall, Zone 5: Left wall).

Table 5.4. Boundary conditions for geometry parts in Fluent.

Zone	Part	Boundary conditions
1	Free surface	Pressure outlet Backflow Turbulent Intensity = 3% Backflow Turbulent Viscosity Ratio = 10%
2	Inlet	Pressure-inlet Turbulent Intensity = 3% Backflow Turbulent Viscosity Ratio = 10% Free surface level = 0.3m Total height = 0.6m Bottom level = 0m
3	Right wall	Wall
4	Bottom wall	Wall
5	Left wall	Wall

### 5.3.3 Results and discussion

The highest peak was recorded by sensor 4, the sensor at the highest location, received the full impact of the flow while the lowest peak, sensor 1, received the lowest impact of the flow. This observation of the highest peak value of the dynamic wave pressure is the reverse of the experimental findings by Lobovsky et al. (2014) where the lowest sensor, sensor 1, recorded the highest peak of the dynamic pressure and the highest sensor, sensor 4, recorded the lowest peak (Fig. 5.25). This is due to the propagation pattern of the upstream wave. Careful observation revealed an upward inclined free surface in the experiment, while the numerical computation showed a downward inclined free surface (Figs. 5.23 & 5.24).

Figure 5.26 the peak pressure value of the numerical simulation agrees well with the typical peak pressure values of the experimental runs. Also, there is only a fair agreement of the time development of the flow between both investigations, because the flow period is faster in the computer simulation than in the laboratory experiment. This is probably due to the 2D nature of the simulation and the turbulence model employed. Further work should be carried out to ascertain this conclusion.

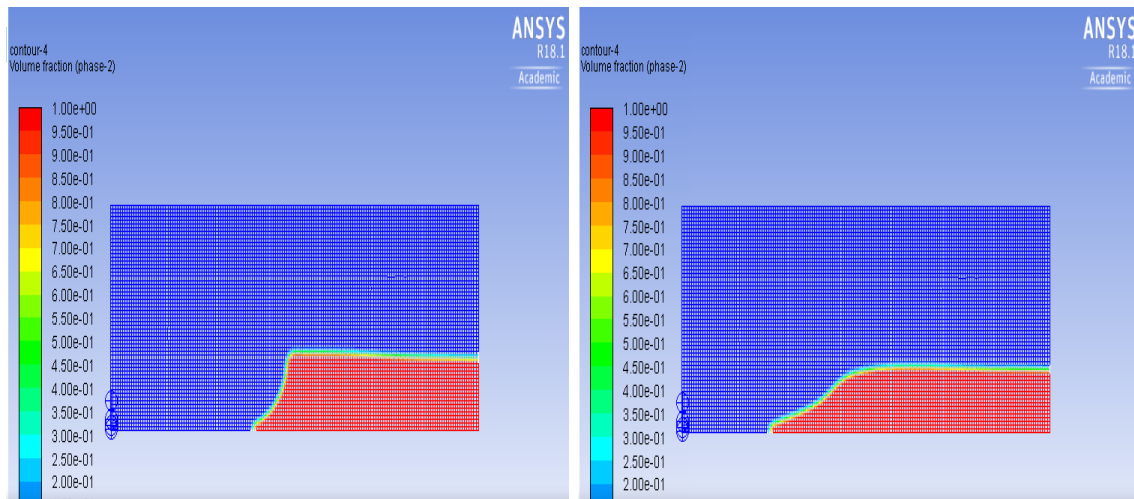


Figure 5.23.  $H = 300$  mm; free surface flow at 183 and 263 ms.



Figure 5.24. Free surface profile and upstream wave at the instant of complete dam gate removal.  $H = 300$  mm (left),  $H = 600$  mm (right).

(Image reproduced with permission of the rights holder, Elsevier. Appendix D).

Legend:

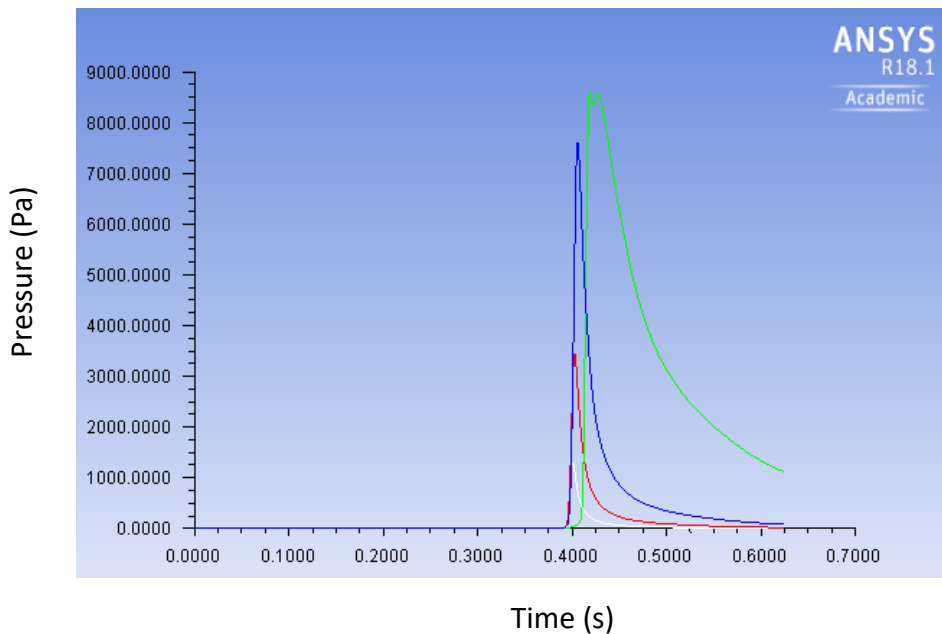
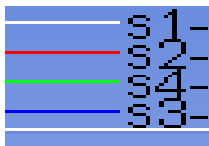


Figure 5.25. Numerical simulation value of dynamic pressure at sensors 1 – 4 (s1 - s4).

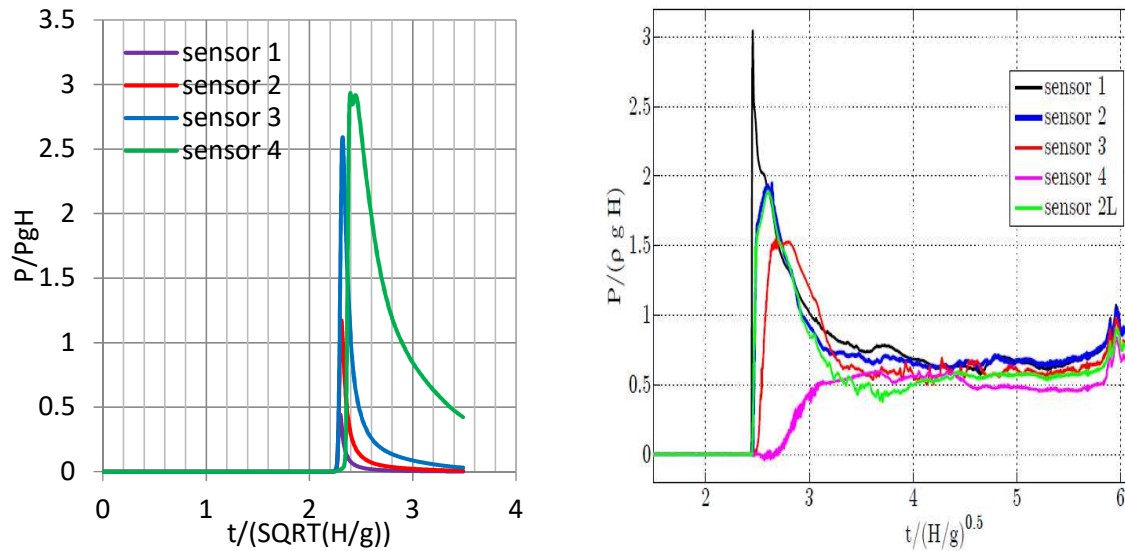


Figure 5.26.  $H = 300$  mm; numerical and experimental comparison of impact event pressure from four pressure sensors.

(Image [right] reproduced with the permission of the rights holder, Elsevier. Appendix D).

## 5.4 Conclusions

This chapter started with the introduction of the numerical schemes that have been used to study incompressible turbulent flows. The computational set-up was patterned after the laboratory experiment in Section 3.2. The flow velocities at the landward region and total wave pressures exerted on the seaward, crest and landward slopes of the model dikes were determined to estimate the flow variables around the structures. The characteristics of the interaction between bore and coastal models, and their agreement with the laboratory results were examined.

Like the laboratory findings, the final bore velocity at the landward region has a real-life average value of 14 m/s. The velocity distribution revealed a general decrease in the bore velocity as the downstream water depth increased. This could be due to the frictional resistance between the upstream and downstream water flows. This is the same trend noticed in the experimental data. Also, in the laboratory study, the bore of the flow was tracked at the toe of the landward slope and employed as the maximum velocity in the maximum overflowing pressure model. However, the numerical results reveal that the maximum velocity is not always at the bore; delayed maximum value was noticed within the body of fluid.

Time evolution of the pressure profiles was not identical to the experimental results provided in Section 3.3.3. However, statistical analysis of Table 5.3 reveals fair agreement with the maximum overflowing pressure formula, which is central to the underlying assumption of the scour predictive model. Using coarse mesh, the result shows that the solution of the Navier-Stokes equation with the RANS turbulence modelling along with a VOF approach for surface tracking should be carefully considered for dam-break flow predictions. Also, the data results should be useful for sediment scour validation as there is a fair agreement of maximum scour velocities in both experimental and numerical.

## Chapter 6

### Numerical Simulation of Tsunami-induced Sediment Scour

The significance of sediment transport study in the field of coastal engineering cannot be overemphasized. Its impact on coastal zone management, navigation, reservoirs, and aquatic ecosystems can lead to adverse effect on socio-economic and environmental systems. This has led to the development of numerical techniques to account for the hydro-sedimentary processes that can be used to understand better and predict sediment transport.

In this chapter, different numerical models that have been employed to study sediment transport are discussed first. The SedFoam-2.0, a two-phase flow solver, is then used to study sediment transport in the landward region of the coastal dike models employing shear stress numerical data of the tsunami wave propagation. This data was obtained with the same numerical methodology described in Chapter 5. After that, the numerical results are further compared to the experimental and field measurements presented in Figure 4.13.

#### 6.1 Introduction

Several numerical models have been developed to investigate sediment transport problems (Table 2.6), and their studies have been performed by using many commercial CFD software. However, their limitations have also spurred much research into numerical codes that can be embedded into them to solve complex sediment transport cases.

Kim and Chen (2014) coupled a 3D computational fluid dynamics solver for Reynolds-Averaged Navier-Stokes equations with a suspended sediment transport module to study flow around abutment in channel bend. Also, the two-layer turbulence model, that combines the one- and two-equation eddy-viscosity models, was utilized to resolve turbulence near smooth solid surfaces. The wall function approach is adopted to consider the roughness effects in the case of sediment beds. For velocity-pressure coupling, PISO/SIMPLER algorithms were used. They concluded that the 3D transport of the suspended sediment was well simulated. A more detailed description of a sediment transport module is presented by Hongwei and Rodi (2002). The authors developed a 3-D hydrodynamic module to study the flow and sediment transport in certain sections of the Yangtze River, China. The module included the standard  $k - \epsilon$  model, and bed-load and suspended load sediment transport modules with an



empirical model for calculating the interchange between them. The bed-load transport and the suspended load was calculated by solving the convection-diffusion equation for sediment concentration, and then the bed deformation was calculated from the depth-integrated sediment mass balance equation.

Tofany et al. (2014) coupled an empirical sediment transport formula to a 2D RANS-VOF based model to study scouring simulation in front of an impermeable vertical breakwater. The results showed that the model is very accurate for predicting the near bottom velocity. Ota, Sato, and Nakagawa (2015) suggested a 3D numerical model for flow simulation and bed evolution around a slit weir. The analysis was performed by solving RANS equations coupled with the VOF method. A momentum equation of sediment particles and the stochastic model was employed to account for the transition of sediment pick up from bed load to suspension and effect of non-equilibrium bed-load transport. Adequate accuracy was observed when experimental and numerical measurements were compared. Morichon, Desombre and Simian (2013) proposed a sediment transport model to simulate the scouring process induced by a dam break flow downstream of a rigid step. The free surface flow was simulated using a VOF-Navier stokes model, and the air-water interface tracking was achieved with the Piecewise Linear Interface Calculation (PLIC) volume of fluid method. A rheological model, the Bingham plastic fluid model, was used to simulate the flow of the sediment layer.

Burkow and Griebel (2016) coupled both NaSt3D to solve Navier-Stokes equations for 3D fluid flow and Exner's bed level equation for sediment bed deformation to reproduce bed load transport processes under clear water conditions. Large Eddy Simulation with Smagorinsky approach was employed for turbulence effect and results from the laboratory, and numerical simulations were in good agreement. Zhang and Shi (2016) redeveloped Fluent software to study the scouring process under an underwater pipeline. The authors embedded a bed-load sediment transport equation that is dependent on relative wall shear force into the software using the user-defined function (UDF). The morphological change of the sediment bed was achieved by dynamic mesh technology.

Numerous scour related numerical simulations have been carried out using commercial computational fluid dynamics models. Sreedhara et al. (2016) applied REEF3D, a CFD model, to study local scour and velocity profile around both circular and round nosed pier. Their results showed good agreement with experimental

observations. Afzal, Bihs and Arntsen (2014) applied REEF3D sediment transport module to determine contraction scour and deposition pattern. They found good agreement with physical experiments employed in their study. Ahmad et al. (2015) in their study of scouring around piles employed REEF3D to calculate flow field and sediment transport patterns.

Vasquez and Walsh (2009) applied FLOW-3D, CFD model, to study the initial stages of scour development in complex piers, and there was good qualitative agreement with experimental data. Ghasemi and Soltani-Gerdefaramarzi (2017) also employed FLOW-3D to study local scouring around a cylindrical pier in non-cohesive sediment bed. Although there was a considerably large disparity between some of the numerical and experimental results, there was good agreement with many of the flow variables. Li, Lang, and Ning (2013) used FLOW-3D to simulate the 3D flow, and local scour around a non-submerged spur dike and observed three stages of scour pit development: initial, main scour and balance stages. They observed that most scour process occurred in the first two stages. Abdelaziz, Bui and Rutschmann (2010) developed a sediment transport module for open channel flows and incorporated it into FLOW-3D to simulate scour development downstream of an apron due to the submerged jet which produced good agreement with experimental results.

SedFoam-2.0, developed by Chauchat et al. (2017), was compiled in OpenFOAM 2.4.0 and employed for the numerical simulation of the tsunami-induced scour. The solver is extended from the TwoPhaseEulerFoam available in OpenFOAM; a CFD open-source library. It has been employed to model turbulent sheet flow, sedimentation of non-cohesive particles, laminar bed-load driven by Poiseuille flow, and scour at an apron. In this chapter, the solver is adapted to a dam break flow by using the shear stress results from the numerical study of dam break flow presented in Chapter 5. This is then incorporated into logarithmic velocity distribution in the solver to study the scour process. Also, the kinetic theory of granular flows and  $k-\epsilon$  model were implemented as the inter-granular stress model and the turbulence model respectively.

## 6.2 SedFoam-2.0 Model – Two-phase Flow Solver

### 6.2.1 The governing equations

The mass conservation equations for fluid phase and particle phase can be expressed as:

$$\frac{\partial \beta}{\partial t} + \frac{\partial \beta u_i^b}{\partial x_i} = 0 \quad (6.1)$$

$$\frac{\partial \alpha}{\partial t} + \frac{\partial \alpha u_i^a}{\partial x_i} = 0 \quad (6.2)$$

where  $\alpha$  is the particle volumetric concentration,  $\beta = 1 - \alpha$  is the fluid volumetric concentration,  $u_i^a$ ,  $u_i^b$  are the  $i$  velocity component of the particle phase and fluid phase respectively, and  $i = 1, 2, 3$  is the streamwise, spanwise, and vertical components.

The momentum for the fluid phase and sediment phase can be expressed as:

$$\begin{aligned} \frac{\partial \rho^b \beta u_i^b}{\partial t} + \frac{\partial \rho^b \beta u_i^b u_j^b}{\partial x_j} = & -\beta \frac{\partial p}{\partial x_i} + \beta f_i + \frac{\partial \tau_{ij}^b}{\partial x_j} + \beta \rho^b g_i - \alpha \beta K (u_i^b - u_i^a) \\ & + S_{US} \beta K v_t^b \frac{\partial \alpha}{\partial x_i} \end{aligned} \quad (6.3)$$

$$\begin{aligned} \frac{\partial \rho^a \alpha u_i^a}{\partial t} + \frac{\partial \rho^a \alpha u_i^a u_j^a}{\partial x_j} = & -\alpha \frac{\partial p}{\partial x_i} - \frac{\partial \tilde{p}^a}{\partial x_i} + \frac{\partial \tau_{ij}^a}{\partial x_j} + \alpha f_i + \alpha \rho^a g_i + \alpha \beta K (u_i^b - u_i^a) \\ & - S_{US} \beta K v_t^b \frac{\partial \alpha}{\partial x_i} \end{aligned} \quad (6.4)$$

where  $\rho^a$  is the particle density,  $\rho^b$  is the fluid density,  $g_i$  is the gravitational acceleration,  $f_i$  is the external force that drives the flow,  $\tau_{ij}^b$  is the fluid shear stress comprising viscous stress, fluid-particle interaction effect on the grain scale and Reynolds stresses,  $\tau_{ij}^a$  is the particle shear stress, and  $\tilde{p}^a$  is the particle normal stress. The last two terms in Eqs. (6.3) and (6.4) represent the averaged drag force due to mean relative velocity between fluid and particle phases, and fluid turbulent suspension term respectively, in which  $K$  is the drag parameter,  $v_t^b$  is the turbulent viscosity,  $S_{US}$  is the inverse of Schmidt number.

## 6.2.2 Turbulence modelling

In this study, the  $k$ - $\varepsilon$  model was employed to close the eddy viscosity created due to the averaging of turbulence. The turbulent eddy viscosity  $\nu_t^b$  is calculated using,

$$\nu_t^b = c_\mu \frac{k^2}{\varepsilon} \quad (6.5)$$

The turbulent kinetic energy (TKE)  $k$  is computed from the solution of Eq. (6.6)

$$\begin{aligned} \frac{\partial k}{\partial t} + u_j^b \frac{\partial k}{\partial x_j} = & \frac{R_{ij}^{bt}}{\rho^b} \frac{\partial u_i^b}{\partial x_j} + \frac{\partial}{\partial x_j} \left[ \left( \nu^b + \frac{\nu_t^b}{\sigma_k} \right) \frac{\partial k}{\partial x_j} \right] - \varepsilon - \frac{2K(1-t_{mf})\alpha k}{\rho^b} \\ & - \frac{S_{US}}{\beta} \nu_t^b \frac{\partial \alpha}{\partial x_j} \left( \frac{\rho^a}{\rho^b} - 1 \right) \mathbf{g}_j \end{aligned} \quad (6.6)$$

The last two terms on the RHS in Eq. (6.6) represent the drag-induced damping term and buoyancy term.

The turbulent kinetic energy dissipation rate  $\varepsilon$  is expressed as:

$$\begin{aligned} \frac{\partial \varepsilon}{\partial t} + u_j^b \frac{\partial \varepsilon}{\partial x_j} = & c_{1\varepsilon} \frac{\varepsilon}{k} \frac{R_{ij}^{bt}}{\rho^b} \frac{\partial u_i^b}{\partial x_j} + \frac{\partial}{\partial x_j} \left[ \left( \nu^b + \frac{\nu_t^b}{\sigma_\varepsilon} \right) \frac{\partial \varepsilon}{\partial x_j} \right] - c_{2\varepsilon} \frac{\varepsilon^2}{k} - c_{3\varepsilon} \frac{\varepsilon}{k} \frac{2K(1-t_{mf})\alpha k}{\rho^b} - \\ & c_{4\varepsilon} S_{US} \frac{\varepsilon}{k\beta} \nu_t^b \frac{\partial \alpha}{\partial x_j} \left( \frac{\rho^a}{\rho^b} - 1 \right) \mathbf{g}_j \end{aligned} \quad (6.7)$$

where  $\nu^b$  is the fluid viscosity,  $t_{mf}$  is the turbulent drag parameter,  $c_{1\varepsilon} = 1.44$ ,  $c_{2\varepsilon} = 1.92$ ,  $c_{3\varepsilon} = 1.2$ ,  $c_{4\varepsilon} = 0$  or  $1$ ,  $c_\mu = 0.09$ ,  $\sigma_\varepsilon = 1.3$ ,  $\sigma_k = 1.0$ ,  $S_{US} = 1$ .

## 6.2.3 Kinetic theory model

In this model, interactions between the particles are assumed to be dominated by dual collisions for low to moderate sediment volumetric concentration, and the resulting shear stresses are quantified by the fluctuations in the particle velocity. This is represented by the granular temperature  $\Theta$ . The expression for the balance equation for granular temperature is:

$$\frac{3}{2} \left[ \frac{\partial \alpha \rho^a \Theta}{\partial t} + \frac{\partial \alpha \rho^a u^a \Theta}{\partial x_j} \right] = \left( -p^a \delta_{ij} + \tau_{ij}^a \right) \frac{\partial u_i^a}{\partial x_j} - \frac{\partial q_j}{\partial x_j} - \gamma + J_{int} \quad (6.8)$$

where  $q_j$  is the granular temperature flux,  $\gamma$  is the energy dissipation rate due to the inelastic collision,  $J_{int}$  is the fluid-particle interaction term,  $\tau_{ij}^a$  is the particle collision

stress,  $p^a$  is the particle pressure and the first term at the RHS of Eq. (6.8) is the production of granular temperature.

#### **6.2.4 Model setup, initial and boundary conditions, and mesh generation**

The sediment bed is made of sand with density,  $\rho^a = 1602 \text{ kg/m}^3$  and diameter  $d = 0.35 \times 10^{-3} \text{ m}$  (Fig. 6.1). The fluid is water, density  $\rho^b = 1000 \text{ kg/m}^3$  and kinematic viscosity  $\nu^b = 1 \times 10^{-6} \text{ m}^2/\text{s}$ . The flow depth  $h_b$  is taken to be 0.202 m, and the initial bed depth  $h_o$  is 0.113 m. The length of the scour bed is 0.3 m. A grid of 800,000 cells with  $\Delta x = 0.000375 \text{ m}$  and  $\Delta y = 0.305 \text{ m}$  in both water and sediment phase, while  $\Delta z = 0.000226 \text{ m}$  in the sediment region and  $\Delta z = 0.000404 \text{ m}$  in the water region (Fig. 6.2).

The bottom boundary, the sediment bed, and the left part of the sediment region, Inlet (sed), are set as the wall boundaries. The left part of the water region, inlet (flow), is the inlet boundary where the 1D velocity distribution profile according to the rough wall log law and constant values of turbulent quantities are imposed. The right sides of both regions are set as the outlet boundary conditions. The top boundary, free surface, is set as a symmetry plane.

The velocity of both water and sediment phases, the sediment concentration, the TKE ( $k$ ) and the TKE dissipation variables ( $\epsilon$ ) are set based on 1D simulation results using funkySetFields. The details of the boundary conditions are summarized in Table 6.1.

```

/*----- C++ -----*/
=====
  \ \ / / F i e l d           OpenFOAM: The Open Source CFD Toolbox
  \ \ / / O p e r a t i o n       Version: 1.7.1
  \ \ / / A n d                   Web:      www.OpenFOAM.com
  \ \ / / M a n i p u l a t i o n
=====
FoamFile
{
  version      2.0;
  format       ascii;
  class        dictionary;
  location     "constant";
  object       transportProperties;
}
// ***** sediment properties ***** //
phasea
{
  rho          rho [ 1 -3 0 0 0 ] 1602;
  nu           nu [ 0 2 -1 0 0 ] 1e-6;
  d            d [ 0 1 0 0 0 0 ] 0.35e-3;
  sF           sF [ 0 0 0 0 0 0 ] 0.5; // shape Factor to adjust settling velocity for non-spherical particles
  hExp        hExp [ 0 0 0 0 0 0 ] 2.65; // hindrance exponent for drag: beta^(-hExp) (2.65 by default)
}

phaseb
{
  rho          rho [ 1 -3 0 0 0 ] 1000;
  nu           nu [ 0 2 -1 0 0 ] 1.e-06;
  d            d [ 0 1 0 0 0 0 ] 10e-6;
  sF           sF [ 0 0 0 0 0 0 ] 1.;
  hExp        hExp [ 0 0 0 0 0 0 ] 2.65;
}
//***** //

alphaSmall    alphaSmall [ 0 0 0 0 0 0 ] 1e-6; // minimum volume fraction (phase a) for division by alpha
alphaAlpha    alphaAlpha [ 0 0 0 0 0 ] 0; // surface tension
Cvm           Cvm [ 0 0 0 0 0 ] 0; // Virtual/Added Mass coefficient
Cl            Cl [ 0 0 0 0 0 ] 0; // Lift force coefficient
Ct            Ct [ 0 0 0 0 0 ] 0; // Eddy diffusivity coefficient for phase a

transportModel Newtonian;

nu            nu [ 0 2 -1 0 0 0 ] 1e-06;

nuMax         nuMax [0 2 -1 0 0 0] 0.1; // viscosity limiter for the Frictional model (required for stability)
// ***** //

```

Figure 6.1. Transport properties.

```

=====
\\  /  F ield      OpenFOAM: The Open Source CFD Toolbox
\\  /  O peration  Version:  2.4.0
\\  /  A nd        Web:      www.OpenFOAM.org
\\  /  M anipulation
*-----*
Build   : 2.4.0-dcea1e13ff76
Exec    : blockMesh
Date    : Jan 18 2018
Time    : 22:06:20
Host    : "DESKTOP-1QGD1NB"
PID     : 2114
Case    : /home/wapz/sedfoam/tutorials/C3
nProcs  : 1
sigFpe  : Enabling floating point exception trapping (FOAM_SIGFPE).
fileModificationChecking : Monitoring run-time modified files using timeStampMaster
allowSystemOperations : Allowing user-supplied system call operations

// ***** //
Create time

Creating block mesh from
"/home/wapz/sedfoam/tutorials/C3/constant/polyMesh/blockMeshDict"
Creating curved edges
Creating topology blocks
Creating topology patches

Creating block mesh topology

Check topology

    Basic statistics
        Number of internal faces : 1
        Number of boundary faces : 10
        Number of defined boundary faces : 10
        Number of undefined boundary faces : 0
    Checking patch -> block consistency

Creating block offsets
Creating merge list .

Creating polyMesh from blockMesh
Creating patches
Creating cells
Creating points with scale 1
    Block 0 cell size :
        i : 0.000375 .. 0.000375
        j : 0.305 .. 0.305
        k : 0.000226 .. 0.000226

    Block 1 cell size :
        i : 0.000375 .. 0.000375
        j : 0.305 .. 0.305
        k : 0.000404 .. 0.000404

Writing polyMesh
-----
Mesh Information
-----
    boundingBox: (0 -0.113 -0.305) (0.3 0.202 0)
    nPoints: 1603602
    nCells: 800000
    nFaces: 3201800
    nInternalFaces: 1598200
-----
Patches
-----
    patch 0 (start: 1598200 size: 500) name: inandouthalf21
    patch 1 (start: 1598700 size: 500) name: inandouthalf12
    patch 2 (start: 1599200 size: 500) name: inandouthalf11
    patch 3 (start: 1599700 size: 500) name: inandouthalf22
    patch 4 (start: 1600200 size: 800) name: top
    patch 5 (start: 1601000 size: 800) name: walls
    patch 6 (start: 1601800 size: 1600000) name: frontAndBackPlanes

End

```

Figure 6.2. Fine grid size (Block 0 cell size is the sediment region, and Block 1 cell size is the water region).

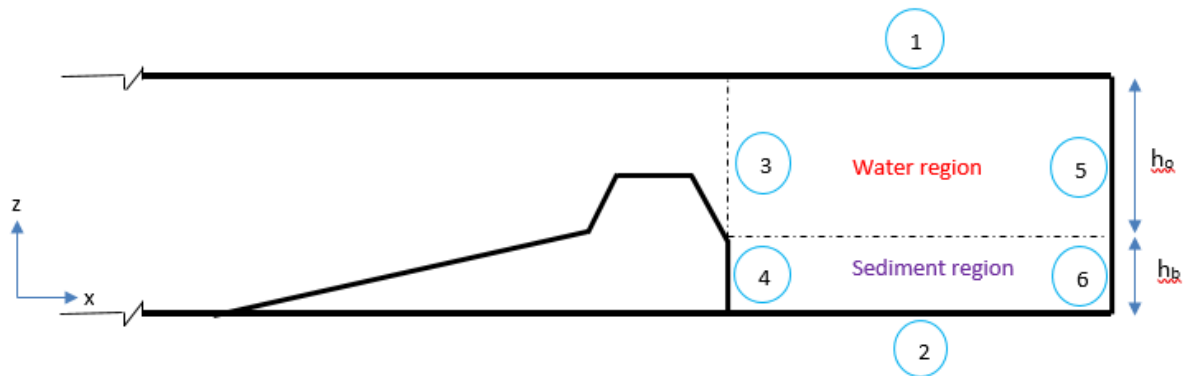


Figure 6.3. Schematics of the landward region (Refer to the boundary and zone columns in Table 6.1).

Table 6.1. Summary of boundary condition in the 2D sediment scour experimental configuration: zG = zeroGradient, fV = fixedValue, dM = directionMixed, fFP = FixedFluxPressure and hp = hydrostatic pressure.

Boundary	Zone	Type	$\alpha$	k	$\epsilon$	$u^a$	$u^b$	p	$\Theta$ (for kinetic Theory)
Top	1	patch	zG	zG	zG	zG	zG	zG	zG
Bottom	2	Wall	zG	zG	zG	fV, $u^a = 0$	fV, $u^b = 0$	zG	zG
Inlet (flow)	3	Patch	1D profile	fV, $k = 1 \times 10^{-4}$	zG	1D profile	1D profile	zG	fV, $k = 1 \times 10^{-6}$
Inlet (sed)	4	Wall	zG	fV, $k = 1 \times 10^{-12}$	zG	fV, $u^a = 0$	fV, $u^b = 0$	zG	zG
Outlet (flow)	5	Patch	zG	zG	zG	dM	dM	hp	zG
Outlet (sed)	6	Patch	zG	zG	zG	zG	zG	zG	zG



#### 6.2.4.1 Logarithmic Velocity Distribution

The universality of Von kármán's law of velocity distribution near a solid boundary is applied to determine the inlet velocity. Keulegan (1938) showed that the rough wall log-law could be written as:

$$\frac{u}{u_*} = \frac{1}{k} \ln \left( \frac{z}{z_o} \right) \quad (6.9)$$

Where,  $z$  is the vertical distance from the bottom wall,  $z_o (= \frac{k_s}{30}$  for hydraulically rough flow) is a constant of integration,  $k = 0.41$ ; Von kármán's constant,  $u$  is the velocity at the point,  $u_*$  is the bed friction velocity; it is responsible for the bed load transport and entrainment of sand from the bed.

$$\frac{u}{u_*} = \frac{1}{k} \ln \left( \frac{30z}{k_s} \right) \quad (6.10)$$

According to Fredsoe and Deigaard (1992),  $k_s = 2.5 d_{50}$ , which is the Nikuradse roughness length/equivalent roughness of the bed, where  $d_{50}$  is the median grain diameter.

$$u(z) = \frac{u_*}{k} \ln \left( \frac{30z}{2.5d_{50}} \right) \quad (6.11)$$

where,  $u_* = \sqrt{\frac{T_w}{\rho}}$ , and  $T_w$  is the bottom-wall shear stress, and  $\rho$  is the fluid density.

#### 6.2.4.2 Shear Stress at Bottom-wall

The post-processing of the computational shear stress results was generated with ANSYS Fluent using the same methodology described in Section 5.2. The average values at the 0.30 m long bed or bottom-wall were determined over the crucial 4 seconds of the 6 seconds flow for each of the four sea dike models. These values are employed as the bottom-wall shear stress,  $T_w$ , in the shear friction equation for the rough-wall log law (Eq. 611).

The average shear stress value of Model A increased from 2.52 Pa for Type I hydraulic condition to 2.92 Pa for hydraulic condition II, but with a minimal decrease to 2.88 Pa for Type III hydraulic condition. This observation was similar for model B, where there was an increase from 4.21 Pa to 6.23 Pa, before a decline to 4.65 Pa for hydraulic condition III. The average shear stress value of Model C increased from 2.88 Pa for Type I hydraulic conditions to 3.48 Pa for Type II hydraulic condition, and then a decline to 2.67 Pa for Type III hydraulic condition. An unchanged average shear

stress value of 3.43 Pa was noticed for Types I and II hydraulic conditions of Model D, while a minimal decline to 3.32 Pa was noticed for hydraulic condition III.

The shear stress distribution of models A, C, and D revealed a general delayed surge in maximum shear stress value, whereas Model B showed a general parabolic decline once the peak value was reached (Figs.6.4 – 6.7).

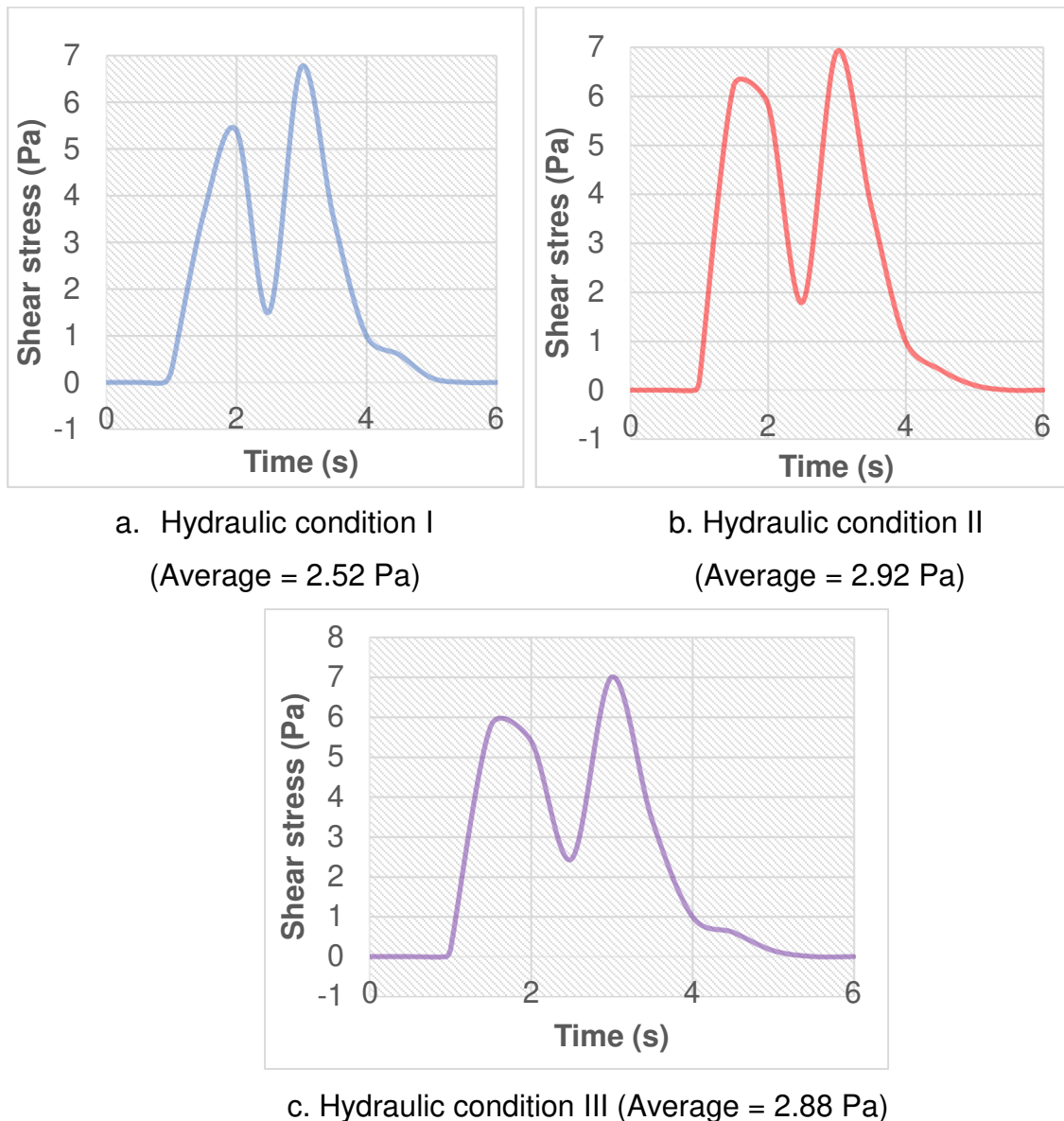
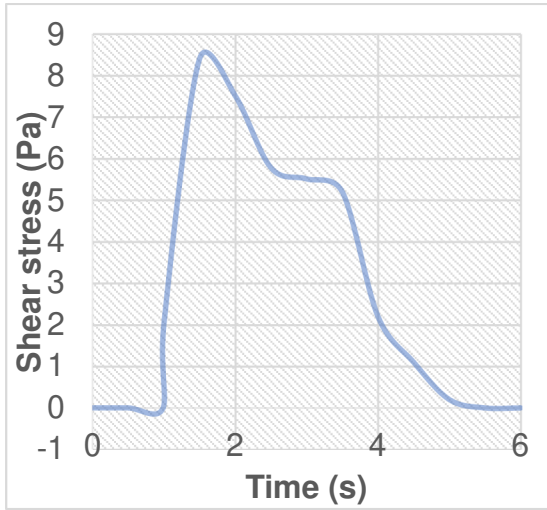
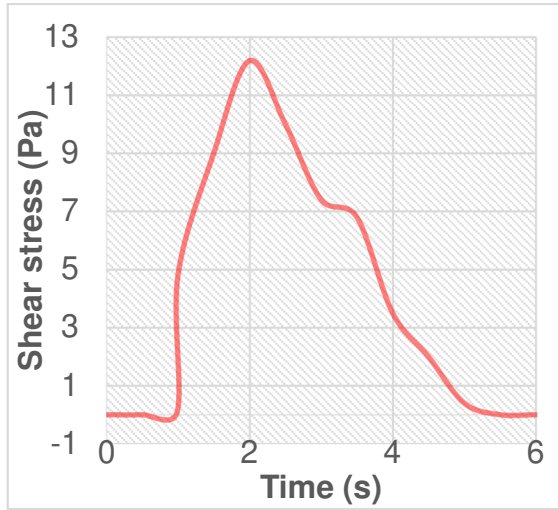


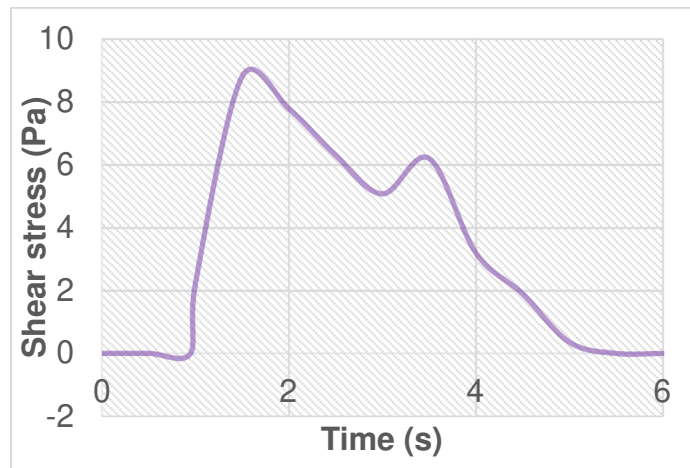
Figure 6.4 Shear stress distribution at bottom-wall (Zone 2) of Model A under various hydraulic conditions.



a. Hydraulic condition I  
(Average = 4.21 Pa)

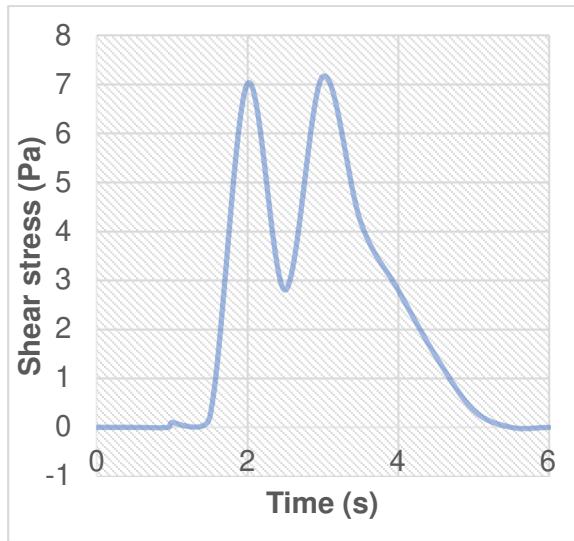


b. Hydraulic condition II  
(Average = 6.23 Pa)

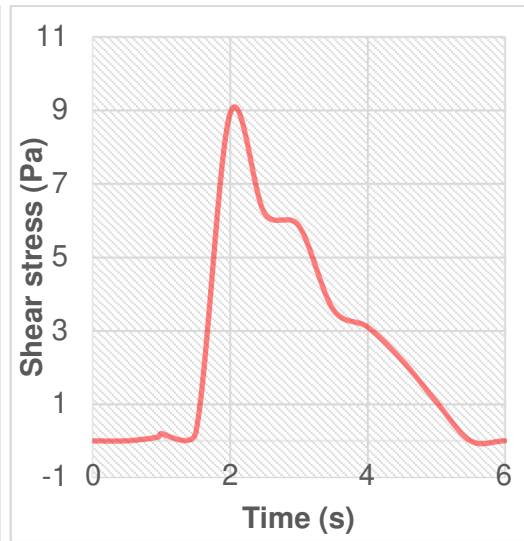


c. Hydraulic condition III (Average = 4.65 Pa)

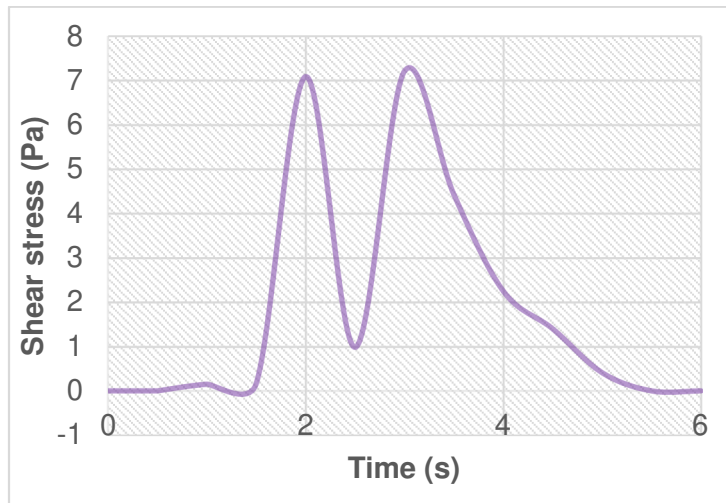
Figure 6.5 Shear stress distribution at bottom-wall (Zone 2) of Model B under various hydraulic conditions.



a. Hydraulic condition I  
(Average = 2.88 Pa)

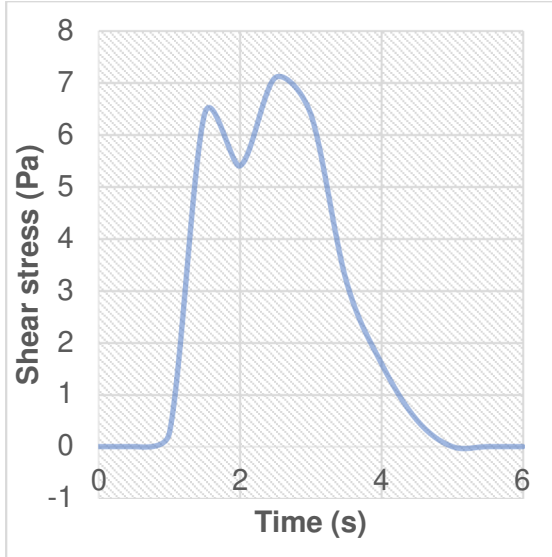


b. Hydraulic condition II  
(Average = 3.48 Pa)

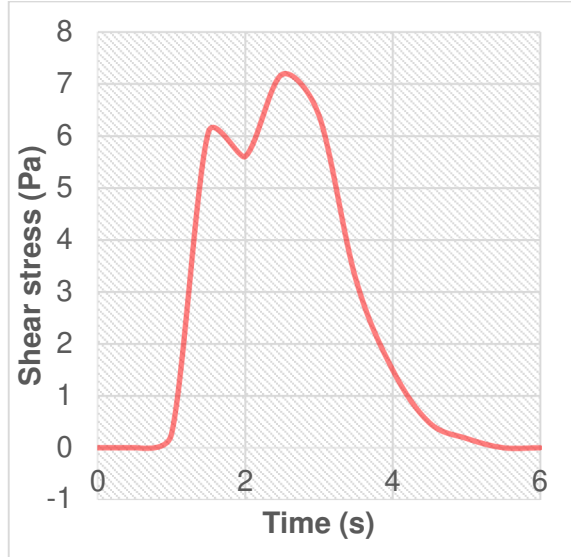


c. Hydraulic condition III (Average = 2.67 Pa)

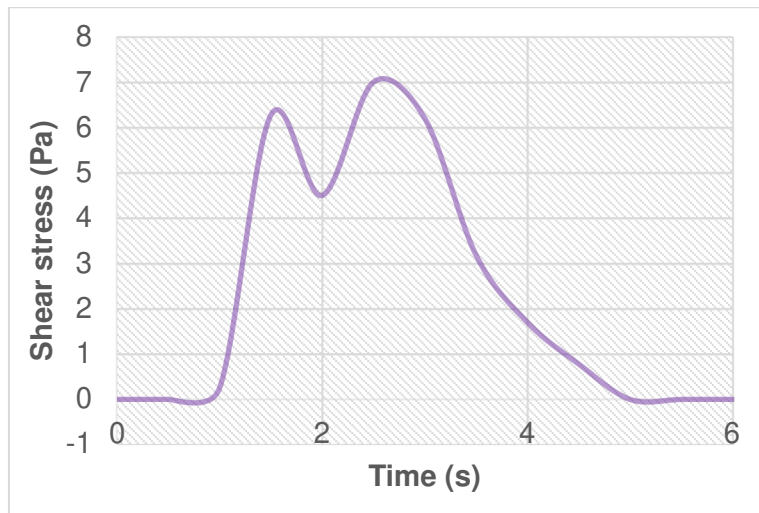
Figure 6.6. Shear stress distribution at bottom-wall (Zone 2) of Model C under various hydraulic conditions.



a. Hydraulic condition I  
(Average = 3.43 Pa)



b. Hydraulic condition II  
(Average = 3.43 Pa)



c. Hydraulic condition III (Average = 3.32 Pa)

Figure 6.7. Shear stress distribution at bottom-wall (Zone 2) of Model D under various hydraulic conditions.

### 6.2.5 Solution procedure

Figure 6.8 shows how two CFD tools are adapted to study the scour behind the coastal dikes models, while Figure 6.9 shows the summary of the numerical solution procedure for the SedFoam-2.0 solver.

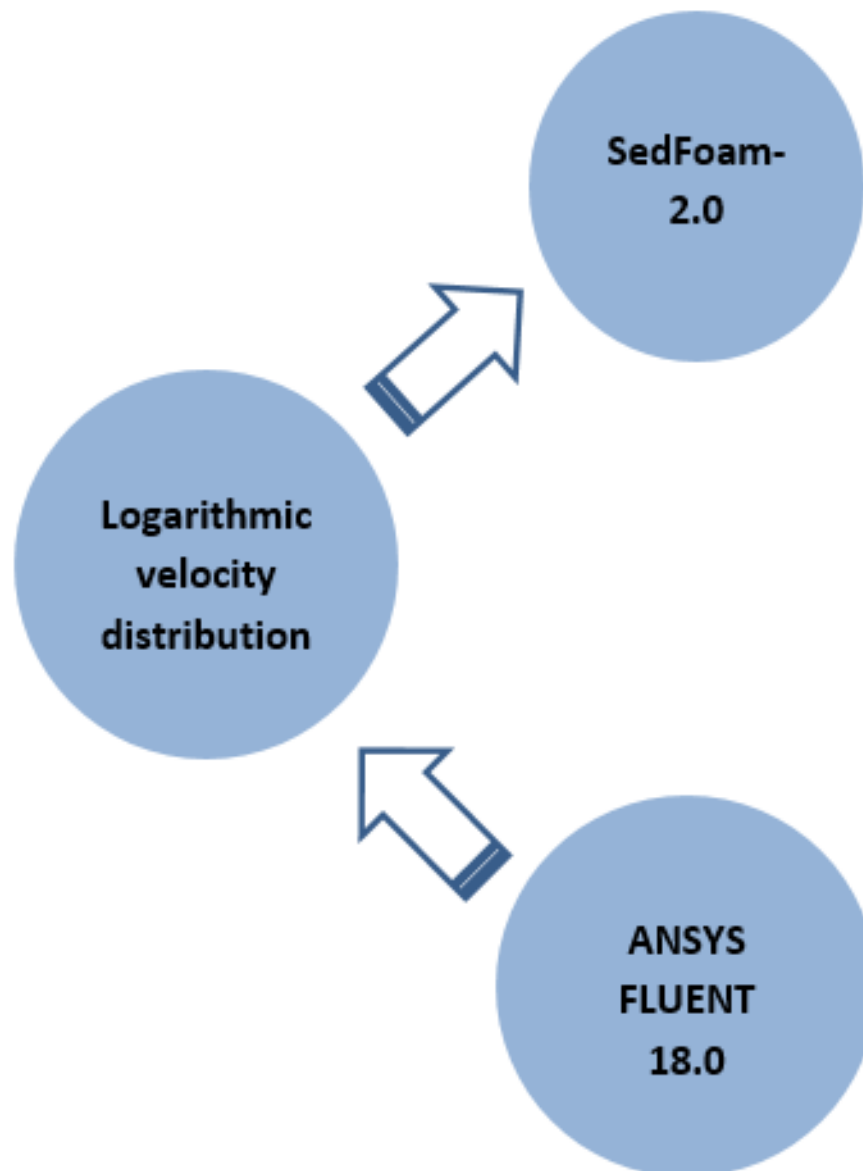


Figure 6.8. Using logarithmic velocity distribution to link two CFD tools for tsunami-induced scour process.

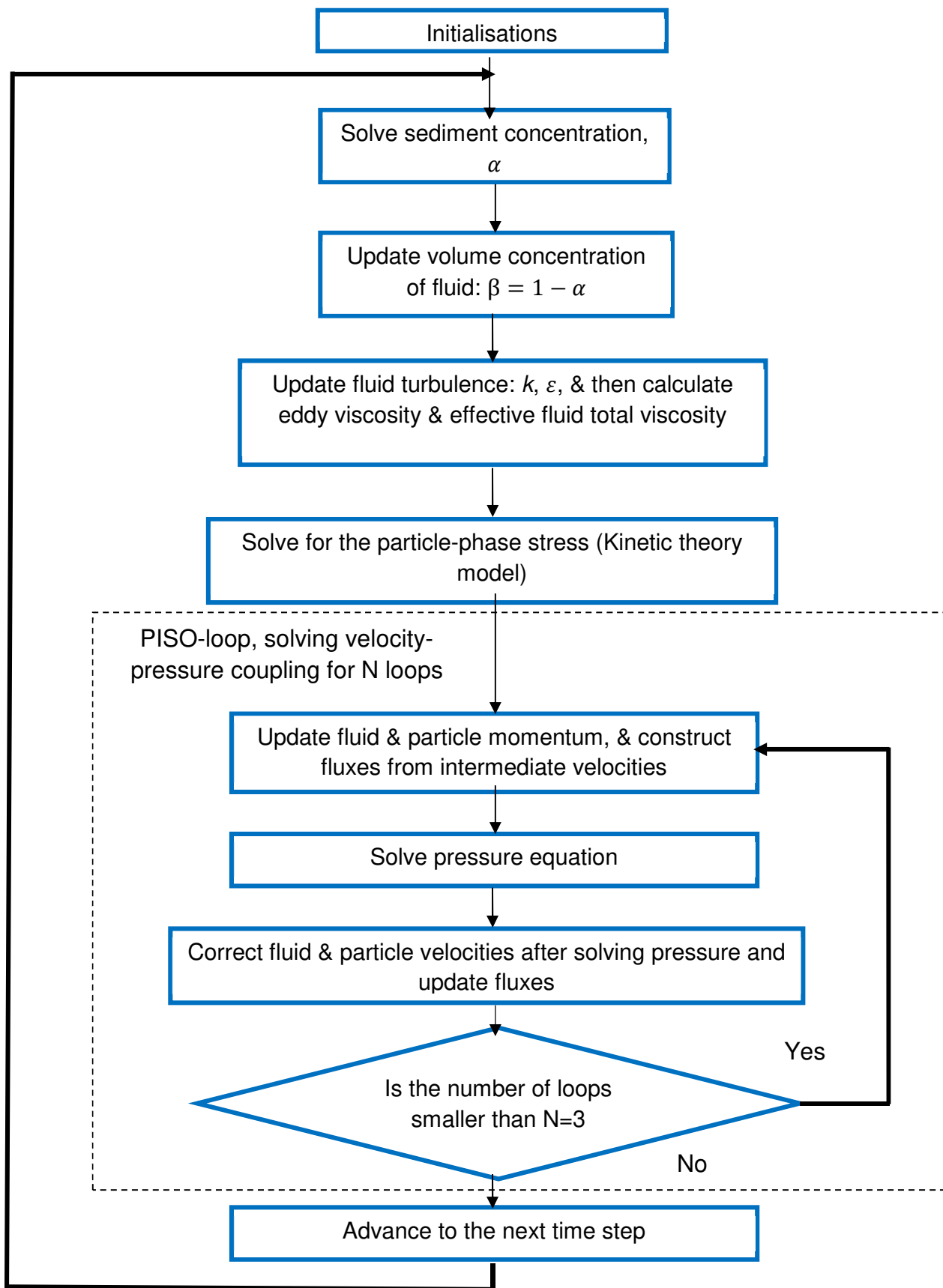


Figure 6.9. Solution procedure flowchart in SedFoam-2.0 (After Cheng and Hsu, 2014; Chauchat et al., 2017).

### 6.3 Scour Profile Characteristics

The fine grid employed for the scour study was compared with a coarse grid to understand the effect of grid size on the convergence or accuracy of the solution. The coarse grid used had 31,200 cells, with  $\Delta x = 0.00125$  m and  $\Delta y = 0.305$  m in both water and sediment phase, while  $\Delta z = 0.0014125$  m in the sediment region and  $\Delta z = 0.00404$  m in the water region (Fig. 6.3).

The ParaView-4.1.0 was used for the post-processing of the sediment concentration result, and the results show that spatial resolution plays a significant role in the stability of the scour profile, and therefore fine spatial resolution is a requirement for accurate simulation of the sediment transport problem (Figs. 6.11 & 6.12). It was also noticed that the two-phase calculation solved with the fine grid size was time-consuming for larger flow velocity.

```
=====
//      F i e l d      | OpenFOAM: The Open Source CFD Toolbox
//      O p e r a t i o n | Version: 2.4.0
//      A n d           | Web:      www.OpenFOAM.org
//      M a n i p u l a t i o n |
*-----*
Build : 2.4.0-dcea1e13ff76
Exec  : blockMesh
Date  : Jan 19 2018
Time  : 12:28:09
Host  : "LAPTOP-SA149FEU"
PID   : 16872
Case  : /home/wapz/sedfoam/tutorials/C1_1
nProcs : 1
sigFpe : Enabling floating point exception trapping (FOAM_SIGFPE).
fileModificationChecking : Monitoring run-time modified files using timeStampMaster
allowSystemOperations : Allowing user-supplied system call operations

// ***** //
Create time

Creating block mesh from
"/home/wapz/sedfoam/tutorials/C1_1/constant/polyMesh/blockMeshDict"
Creating curved edges
Creating topology blocks
Creating topology patches

Creating block mesh topology

Check topology

Basic statistics
Number of internal faces : 1
Number of boundary faces : 10
Number of defined boundary faces : 10
Number of undefined boundary faces : 0
Checking patch -> block consistency
```



```

Creating block offsets
Creating merge list .

Creating polyMesh from blockMesh
Creating patches
Creating cells
Creating points with scale 1
Block 0 cell size :
  i : 0.00125 .. 0.00125
  j : 0.305 .. 0.305
  k : 0.0014125 .. 0.0014125

Block 1 cell size :
  i : 0.00125 .. 0.00125
  j : 0.305 .. 0.305
  k : 0.00404 .. 0.00404

Writing polyMesh
-----
Mesh Information
-----
boundingBox: (0 -0.113 -0.305) (0.3 0.202 0)
nPoints: 63142
nCells: 31200
nFaces: 125170
nInternalFaces: 62030
-----
Patches
-----
patch 0 (start: 62030 size: 80) name: inandouthalf21
patch 1 (start: 62110 size: 50) name: inandouthalf12
patch 2 (start: 62160 size: 50) name: inandouthalf11
patch 3 (start: 62210 size: 80) name: inandouthalf22
patch 4 (start: 62290 size: 240) name: top
patch 5 (start: 62530 size: 240) name: walls
patch 6 (start: 62770 size: 62400) name: frontAndBackPlanes

End

```

Figure 6.10. Coarse grid size (Block 0 cell size is the sediment region, and Block 1 cell size is the water region).

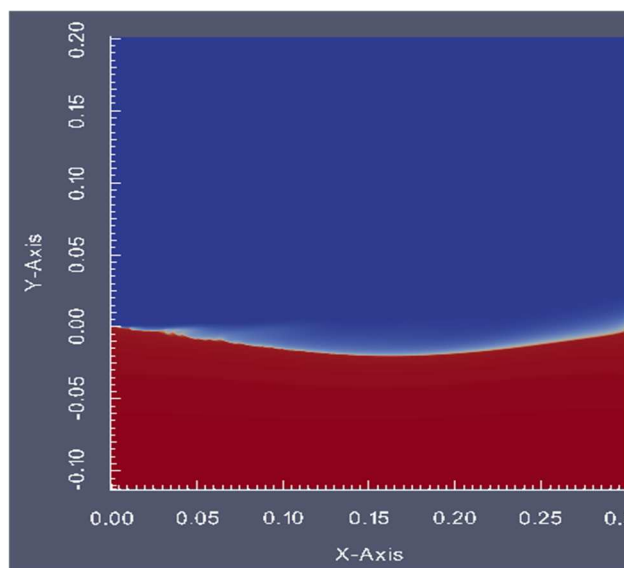


Figure 6.11. Stability of sediment concentration calculation at 4 s by using a fine grid.

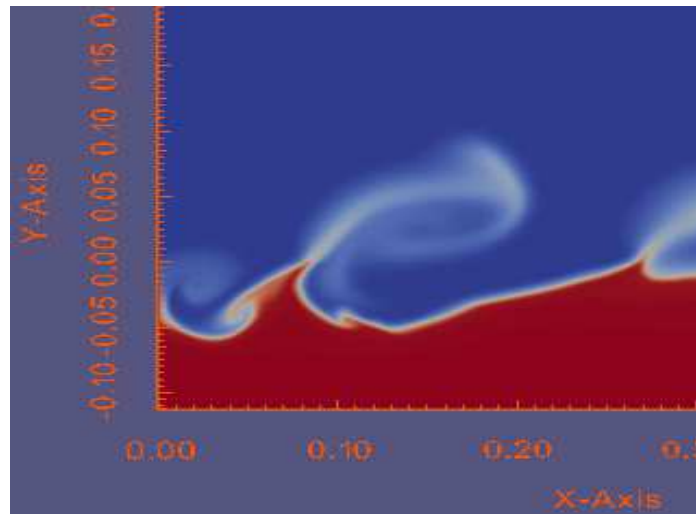


Figure 6.12. Instability of sediment concentration calculation at 0.5 s by using a coarse grid size.

The changes in scour depth and extent from the initially leveled plane-bed were recorded and analyzed using Paraview-4.1.0 and MS Excel. The scour duration was set to 4 seconds, which is the significant time of the shear stress readings. Scour profiles were established by plotting the profiles in terms of scour depth against scour horizontal distance (Figs. 6.13 - 6.16). The landward slope toe is at coordinate (0, 0), while the ground level is along coordinates (0, 0) and (3, 0).

In Model A, the scour depth data of Type I hydraulic condition (Fig. 6.13a) showed a low maximum scour value of 0.018 m at a horizontal distance of 0.14 m away from the landward toe. The maximum scour depth increased to 0.021 m for Type II hydraulic condition (Fig. 6.13b) and then slightly reduced to 0.0205 m for Type III hydraulic condition (Fig. 6.13c). It was observed that the horizontal position of the maximum scour depth moves farther away from the landward toe as the downstream water depth increases for Types II and III hydraulic conditions. In the latter hydraulic conditions, the horizontal location of the maximum scour depth was approximately 0.15 m from the landward toe.

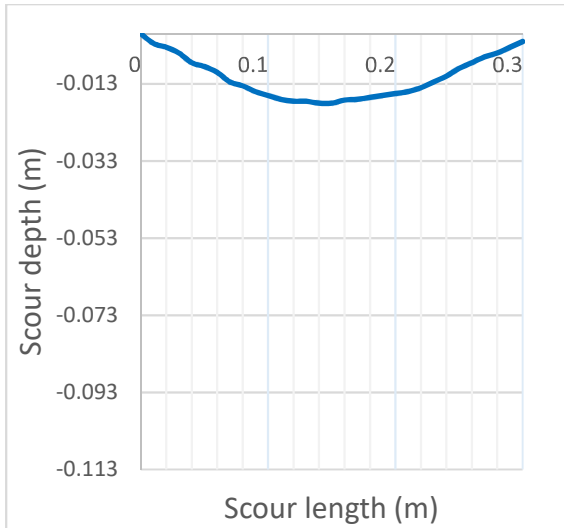
In Model B, parabolic scour profile shapes were observed for all the three hydraulic conditions. For Type I hydraulic condition, the maximum scour depth of 0.029 m occurred close to the toe of the landward slope at 0.21 m (Fig. 6.14a). Type II hydraulic condition, with the highest average shear stress value of 6.23 Pa, had the highest

maximum scour depth value of 0.041 m at 0.24 m away from the toe of the landward slope (Fig. 6.14b), and Type III hydraulic condition had a maximum scour depth value of 0.031 m at 0.22 m away from the toe of the landward slope (Fig. 6.14c).

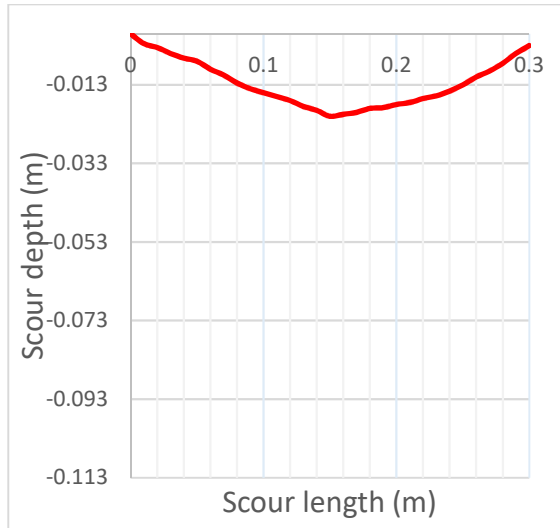
Figure 6.15 provides the scour profile characteristics for Model C. Maximum scour depth of 0.0205 m was measured at 0.15 m from the landward toe after the 4 seconds scour process for Type I hydraulic condition. The increase of scour depth to 0.024 m at 0.19 m away from the landward toe was noticed for the Type II hydraulic condition. A later decrease to 0.0196 m of the maximum scour depth value was measured at 0.16 m from the landward toe for the Type III hydraulic condition. The decrease can be attributed to the decrease in average shear stress value from 3.48 Pa for Type II hydraulic condition to 2.67 Pa for Type III hydraulic condition.

The results of hydraulic conditions I and II of Model D (Figs. 6.16a & 6.16b) showed the maximum scour depth of 0.022 m at 0.18 m away from the landward toe. Both hydraulic conditions have an average shear stress value of 3.43 Pa. As shown in the hydraulic condition III (Fig. 6.16c), a lower maximum scour depth of 0.021 m was measured at about 0.17 m from the toe of the landward slope.

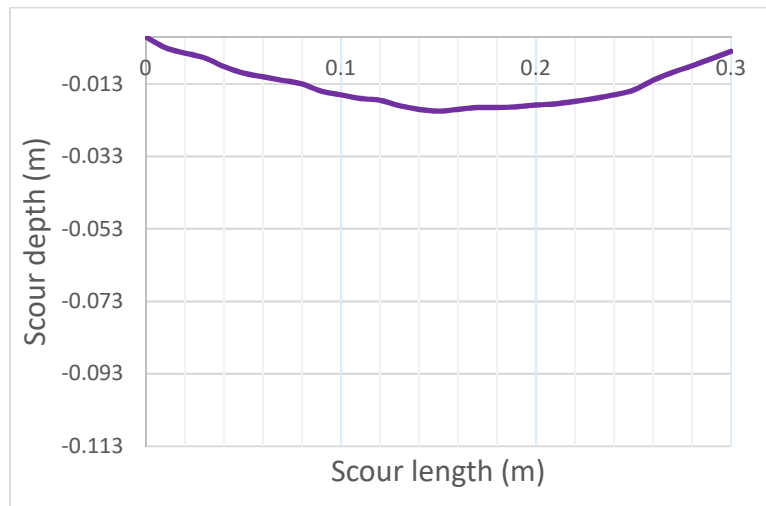
In general, the corresponding horizontal location of the maximum scour depth is dependent on the average shear stress. The larger the shear stress, the deeper the scour depth and the farther away the maximum scour depth from the landward toe.



a. Hydraulic condition I



b. Hydraulic condition II

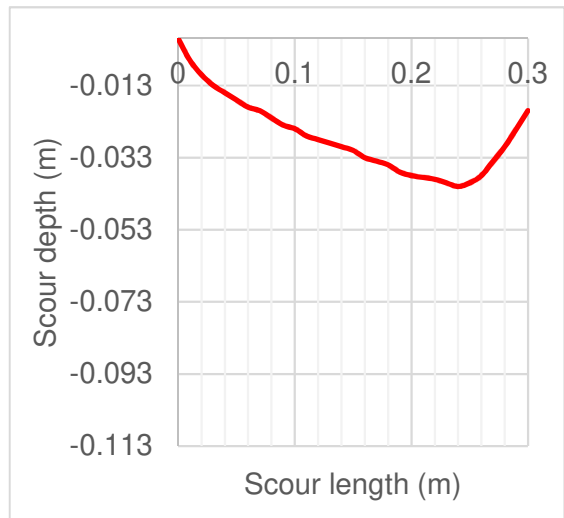


c. Hydraulic condition III

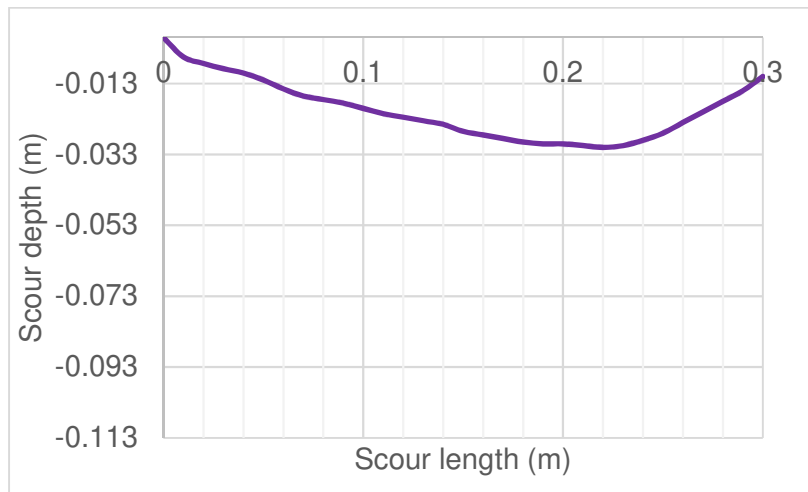
Figure 6.13. Scour profile of Model A under various hydraulic conditions.



a. Hydraulic condition

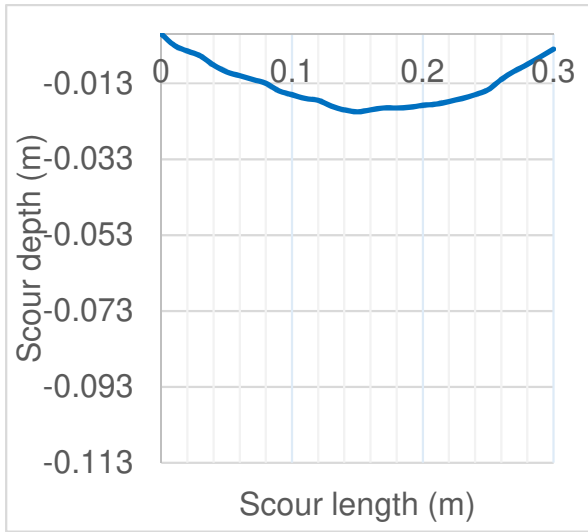


b. Hydraulic condition II

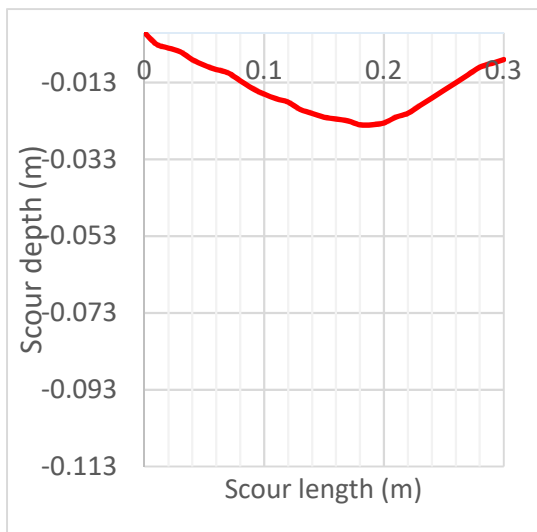


a. Hydraulic condition III

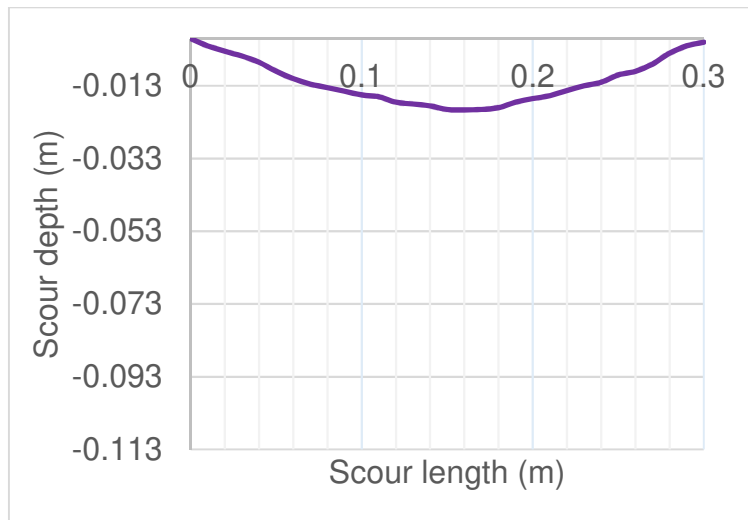
Figure 6.14. Scour profile of Model B under various hydraulic conditions.



a. Hydraulic condition I

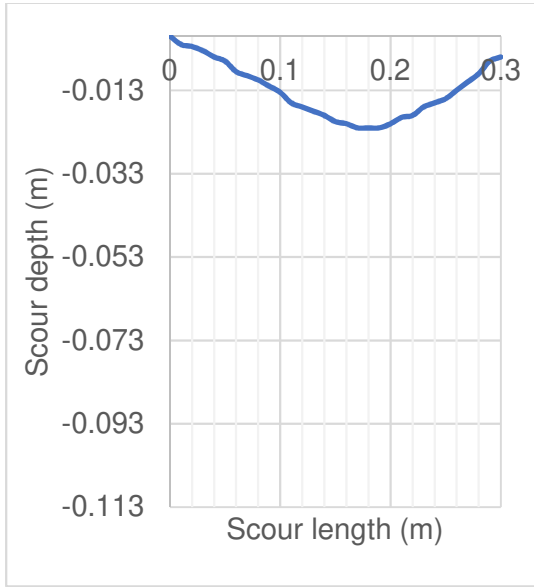


b. Hydraulic condition II

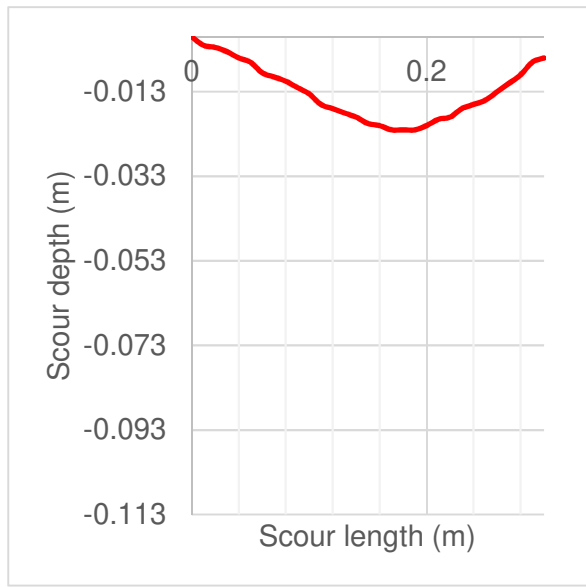


b. Hydraulic condition III

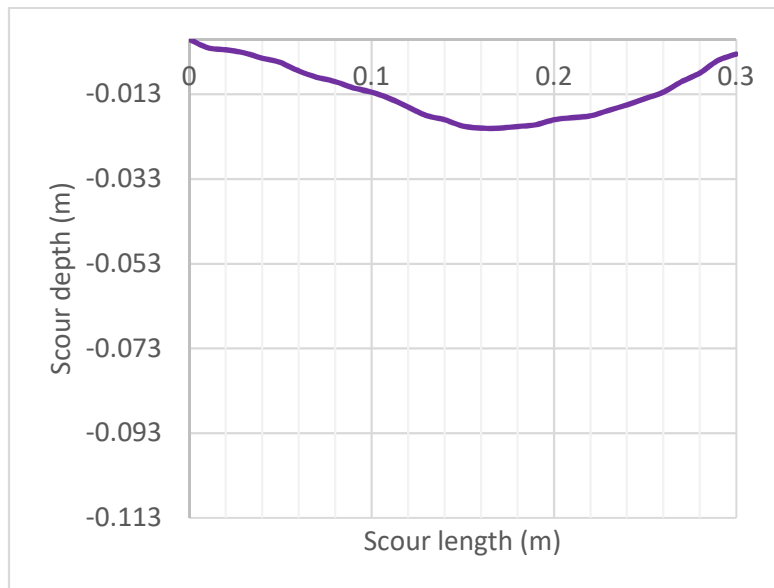
Figure 6.15. Scour profile of Model C under various hydraulic conditions.



a. Hydraulic condition I



b. Hydraulic condition II



c. Hydraulic condition III

Figure 6.16. Scour profile of Model D under various hydraulic conditions.

## 6.4 Comparison between the Numerical Simulation and Laboratory Experiment

Figure 6.18 shows the relationship between the non-dimensional scour depth on the vertical axis and the non-dimensional overflowing wave pressure on the horizontal axis. It shows the field survey result by Jayaratne et al. (2014), the experimental data reported in Chapters 3 & 4, and the numerical results analysed in Chapters 5 & 6. The graph shows that there is reasonable agreement with the scour predictive model. The numerical result is consistent with the exponential trend of the model. The lower maximum overflowing wave pressure values led to the lower maximum scour depth values when compared to the experimental results with higher maximum overflowing wave pressure.

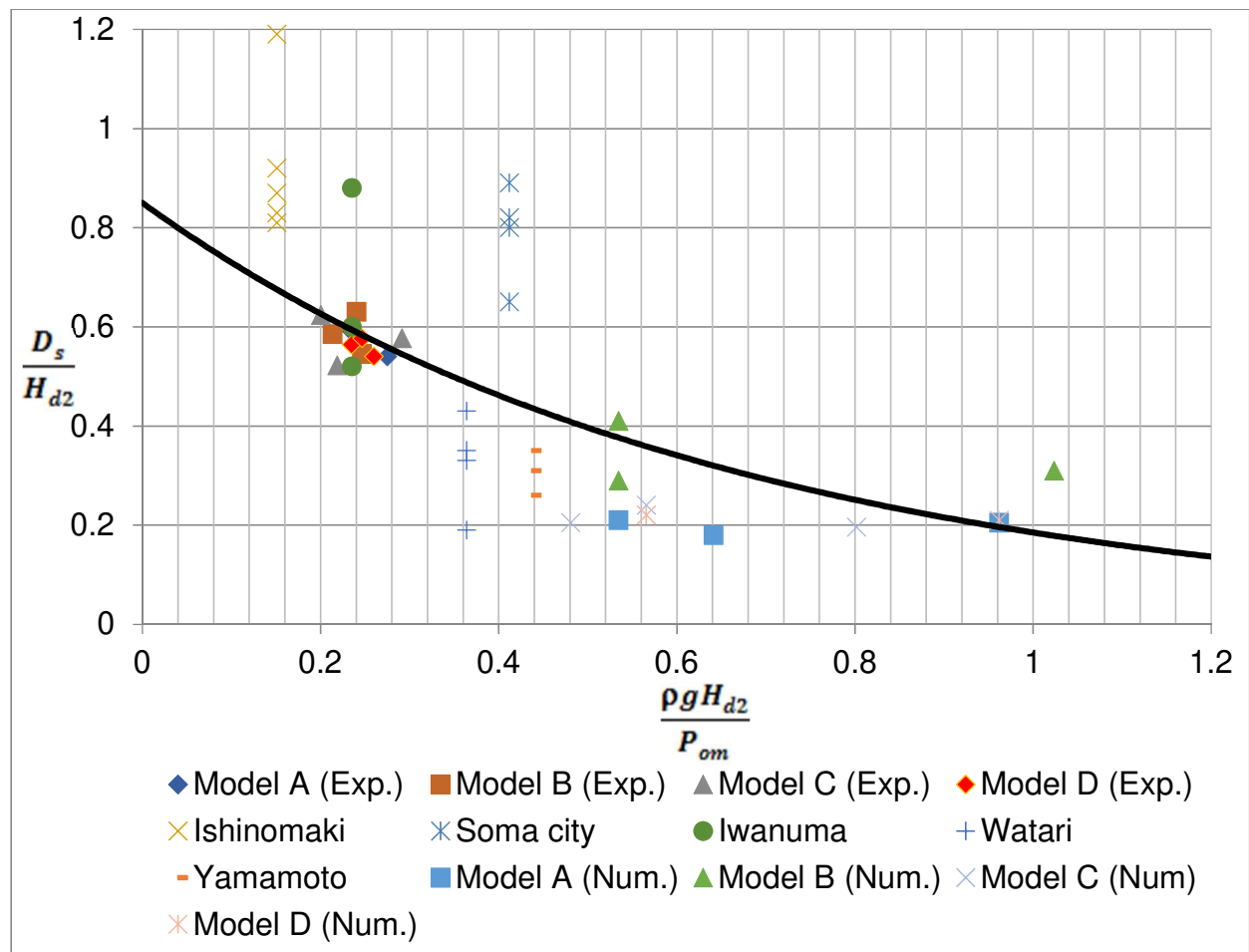


Figure 6.17. The relationship between relative scour depth and impact overflowing wave pressure.



Root mean square error, RMSE, is used to measure the predictive power of the differences between values observed from the numerical data compared to the corresponding values predicted by the model. Table 6.2 shows that the model is acceptable since the root mean square value of 0.11 is close to 0.

Table 6.2. Root mean square error of the numerical data compared with the scour predictive model.

Model	$\hat{X} = \frac{\rho g H_{d2}}{P_{om}}$	$Y_i$ (Observed data)	$\hat{Y}$ (Model data)	$(\hat{Y} - Y_i)^2$
Model A	0.641	0.180	0.305	0.0155
	0.534	0.210	0.361	0.0229
	0.962	0.205	0.182	0.00051
Model B	0.534	0.290	0.361	0.0051
	0.534	0.410	0.361	0.00236
	1.023	0.310	0.165	0.0209
Model C	0.481	0.205	0.394	0.0356
	0.566	0.240	0.344	0.0108
	0.802	0.196	0.236	0.00158
Model D	0.566	0.22	0.344	0.0153
	0.566	0.22	0.344	0.0153
	0.962	0.540	0.182	0.00076
$\sum = 0.147$				
$RMSE = \sqrt{\frac{0.147}{12}} = 0.11$				

## 6.5 Conclusions

This chapter started with the introduction of the numerical schemes that have been used to study sediment transport problems. The computational set-up was patterned after the landward region of the laboratory experiment in Section 4.2. The description of the numerical simulation model used to examine the effect of tsunami wave shear stress over fixed sediment bed is presented. The two-phase flow was considered using SedFoam-2.0 to analyse water and sediment flow in the landward region of the open channel. The characteristics of the scour profile and their agreement with the field survey data, laboratory results and predictive scour model were examined.

The average shear stress at the bottom-wall was employed in the logarithmic law of the wall to generate the inlet velocity into the water region and sediment region shown in Figure 6.3. The values revealed that the higher the shear stress, the deeper the scour depth and the farther away from the landward toe its horizontal location.

The influence of spatial resolution on the accuracy of numerical simulations is revealed in the study. The coarse grid gave an inaccurate solution of the sediment scour problem, while the fine grid resulted in the convergence of the solution. Large computational time was expended to achieve the accuracy of the sediment transport problem.

The RMSE statistical measure showed there was reasonable agreement with the scour predictive model considering the lower values of the maximum overflowing pressure. The results, however, revealed lower scour values compared to the experimental data with higher maximum overflowing wave pressure. However additional work is needed to accurately predict the maximum scour depth and its angle of attack of flow into the landward region.

## CHAPTER 7

### Conclusions and Recommendations

The main aim of the thesis is to perform extensive small-scale laboratory experiments and numerical simulation to elucidate further the scour failure of coastal dikes due to tsunami wave attack. In achieving this general aim, comprehensive experimental and numerical programmes were developed to study tsunami flow hydrodynamics and its associated hydro-sedimentary characteristics. A viable resilient coastal defence structure was proposed to minimize structural damage for future Level 1 and 2 tsunami events. Also, a predictive scour model, which is bounded by the sediment characteristics, the geometry of the coastal dike and tsunami flow variables, was improved. This model can be used to design sea dikes that are resistant to toe scour failure in the landward region and ultimately has significant benefit in coastal engineering and value engineering. In this chapter, the conclusions are summarised first, and then recommendations for further work are presented.

#### 7.1 Conclusions

##### **Experimental investigation of tsunami flows and tsunami-induced scour**

In Chapter 3, four sea dike models, of which two were fabricated to scale of 1:50 after dikes that were significantly affected in Iwanuma and Soma cities in Japan by the 2011 Great East Japan Earthquake and Tsunami, were employed in the study of the dam break experimental method of investigating tsunami wave propagation. The hydraulic flume set-up included a beach slope of 1:10 mounted at 1.0 m away from the dam gate. Also, three variations of downstream water depth  $h_d$ : hydraulic conditions I, II, and III, were employed to vary the flow variable measurements due to the small scale of the channel. The total wave pressure over different sections of the dikes was determined by using very sensitive 25 kHz pressure sensors, while the velocity distribution over different regions of the flume was established by tracking the wave bore using a motion tracking software.

In Chapter 4, the experimental set-up described above was extended by introducing a 0.113 m depth of a sediment layer behind the coastal dike models to study the characteristics of the tsunami-induced scour profile. Particle size analysis was

employed to ascertain the properties of the sand grain used for the scour experiment. The permeability and median grain size are in the range of the field result obtained by Jayaratne et al. (2014). The change in the bed surface level was measured by a point gauge at the centre of the sand grains.

The results of the tsunami wave and scour experimental studies are summarised as follows:

- The suitability of a small-scale experiment for tsunami wave studies has been shown. The velocity measurements have been shown to be similar to a prototype tsunami runup velocity measurements.
- The gradual reduction of the velocity distribution at the seaward region of the channel reveals that the presence of obstacles would contribute to the reduction of the tsunami energy at the landward region of the sea dike.
- The instantaneous wave pressure readings revealed a delayed sudden jump in values during the overflowing phase of the propagation. This reveals possible tsunami energy stored in the fluid body because of collision with the beach slope and dike slopes thus, leading to an increased interaction between the eddies formed.
- The variation of downstream water depth has been shown to have considerable influence on the total wave pressure and velocity values. The frictional resistance contributes to the reduced values of these flow variables.
- The landward slope was shown to broadly influence the horizontal location of the maximum scour depth. This helps in determining the extent of landward toe protection.
- The dimensionless grain diameter and approximation equations were employed to determine the critical Shields parameter, which was then used to determine the critical average velocity above the bed. This velocity was compared with the average experimental velocity value, and the result supported scour occurrence. Also, the Hjulstrom diagram was employed to further support the evidence of sediment movement.
- The existence of an exponential relationship between the non-dimensional maximum overflowing wave pressure and scour depth, which formed a basis for the derivation of the extrapolative scour model.

- The predictive scour depth model is:

$$\frac{D_s}{H_{d2}} = \lambda \left( \exp\left(-\frac{\sqrt{H_{d2}}}{2.5\lambda\sqrt{h} \sin\theta_2}\right) \right) \} \quad h > H_{d2}$$

where,  $D_s$  is the scour depth,  $H_{d2}$  is the height of structure measured on the landward side (m),  $\theta_2$  is the landward slope angle,  $h$  is the inundation height as a function of flow velocity (m), and  $\lambda$  is the fitted coefficient = 0.85. It applies to sediments with the coefficient of permeability (m/s),  $K$ , between  $10^{-4}$  and  $10^{-3}$ .

- Statistical validation of the impact overflowing pressure was carried out on the experimental data results, and three of the four models showed a good agreement with maximum overflowing pressure formula.
- Root mean square error was employed for the statistical validation of the scour predictive model by making comparisons with the field survey and laboratory data. The two approaches showed a good agreement with the model.
- Design recommendation for a resilient coastal dike structure to mitigate the landward toe scour was provided based on a sensitivity analysis of the experimental data. The recommended design was the appropriate structurally cost-effective section based on the geometry of the sea dikes.

### **Numerical simulation of tsunami flows and tsunami-induced scour**

Chapter 5 details the numerical study of the experimental work discussed in Chapter 3. The ANSYS Fluent; a CFD tool that combines governing flow equations and numerical schemes to solve fluid flow problems, was employed for the 2-D investigation of tsunami wave propagation over four different geometry of sea dikes.

In Chapter 6, SedFoam-2.0; a comprehensive two-phase model for sediment transport, has been implemented to study the sediment transport experimental study presented in Chapter 4.

The results of the tsunami wave and scour experimental studies are summarised as follows:

- There was a fair agreement between the experimental and numerical maximum flow velocity values in the landward region of the sea dikes. A prototype inundation velocity value of about 14 m/s occurs in both methodologies.

- Similar to the laboratory study, the increase in the downstream water depth caused a reduced total wave pressure and velocity values at the seaward and landward slopes. This can be attributed to the frictional interaction between the upstream and downstream water flows.
- The result of the simulation showed that maximum velocity value is not always contained at the tsunami wave bore as assumed during the laboratory study to determine the maximum velocity of the tsunami wave. It revealed that the maximum tsunami force could be resident within the body of the fluid.
- The instantaneous pressure distribution was not identical with the laboratory study. The fluctuating component of the total wave pressure results has not been accurately represented by the turbulence modelling employed for the closure of the RANS equation.
- The use of coarse mesh with suitable near-wall modelling approach for 2-D numerical investigation of fluid flow in a small domain has been shown to give good agreement with experimental results. However, conclusions of numerical simulations in a large fluid domain must be cautiously implemented.
- The development of the scour profile characteristics is similar to the experimental investigation. However, the similarity and the accuracy of the simulation is shown to largely depend on the quality of the grid size.
- Statistical validation of the maximum overflowing pressure was carried out on the numerical simulation data results, and two of the four models showed fair agreement with maximum overflowing pressure formula.
- Numerical research of the scour process was carried out by employing the shear stress data from the ANSYS Fluent software to generate the inlet velocity in SedFoam-2.0 by using the logarithmic law of the wall. The scour depth results were consistent with the predictive scour model.
- Root mean square error was employed for the statistical validation of the scour predictive model by making comparisons with the numerical simulation data results. This showed a good agreement with the model.

## 7.2 Recommendations

This study should be regarded as a contribution towards understanding the kinematics and dynamics of tsunami-induced scour over the coastal dike. Due to the complexities between the fluid and sediment interactions, much research into these processes should be carried out. Recommendations regarding future works to the current research project are:

- The use of improved experimental technique and equipment such as acoustic Doppler velocimeters (ADV) and particle image velocimetry (PIV) Laser to accurately measure and ascertain flow and sediment parameters.
- The investigation of different sediment sizes and permeabilities could be carried out to broaden the practical significance of the project.
- The extensive studies of the effects of crest width and angle of seaward slope of sea dike structure on local scour at the landward toe, and the scour predictive model, to determine the best structural resilient and economically viable geometry.
- The laboratory and numerical studies can be extended to other forms of coastal defences: sea wall, offshore breakwater, and revetments, to determine the best economical solution for minimizing the destructive impact of tsunami run-up at the landward region.
- Only the Realizable  $k-\varepsilon$  model had been adopted as the turbulence models in the 2-D RANS. The turbulence effect can be investigated by using other improved turbulence models available in ANSYS Fluent. The effect of near-wall modelling can also be investigated by using various wall functions.
- OpenFoam CFD tool can be used to study the propagation of tsunami wave flow, and results of the flow properties compared to the ANSYS Fluent results presented in this project.
- The numerical computation has only been limited to 2-D calculations due to prolong CPU times and computational challenges for 3-D calculations. 3-D numerical investigation of a tsunami wave can be carried out by using either dam break wave or solitary wave generation methods. Generating a finer mesh than that employed in the study improve the result. Also, the mesh can be

adapted such that finer mesh used at the wall boundary while a coarse mesh is used in other areas of the fluid domain.

- Different angles of the beach slope and stepped slopes can be further studied to examine their influence on the tsunami wave properties, and sediment scour depth.
- The SedFoam-2.0 solver used for the numerical investigation of the scour is based on a two-phase solver. The real-life scenario of the problem includes the simultaneous interaction between air, water, and sand phases, and as such a solver based on interFoam solver in OpenFoam CFD library for dam break flow problems, could be developed to incorporate the three phases, and ascertain the time development of the scour depth and the upstream bed angle.
- The ANSYS Fluent 18.0 is not suitable for the sediment transport simulation of dense bed. However, a user-defined function in ANSYS Fluent could be developed to monitor the sediment scour profile development for multiphase flows.



## References

Abdelaziz, S., Bui, M. D. and Rutschmann P. (2010) 'Numerical simulation of scour development due to submerged horizontal jet', *River Flow. Process of the International Conference on Fluvial Hydraulics*, Braunschweig, Germany, pp. 1597-1604.

Abimbola, A. (2013) *Analysis of scour failure mechanism of coastal structures due to tsunami*, MSc. dissertation, University of East London, London.

Afzal, M., S., Bihs, H. and Arntsen A. (2014) '3D numerical modelling of contraction scour under steady current using the level set method', *11<sup>th</sup> International Conference of Hydroscience and Engineering, Hamburg, Germany*, pp. 525-530. Lehfeldt & Kopmann (eds).

Ahmad, N., Bihs, H., Kamath, A. and Arntsen, A. (2015) 'Three dimensional cfd modelling of wave scour around side-by-side and triangular arrangement of piles with REEF3D', *8<sup>th</sup> International Conference on Asian and Pacific Coasts (APAC), Procedia Engineering*, 116(2015), pp. 683-690.

Andersen, T. L. and Frigaard, P. (2007) *Lecture notes for the course in water wave mechanics*. Aalborg University.

ANSYS (2006) *Modeling turbulent flows: introductory fluent training*. Available at: [http://www.southampton.ac.uk/~nwb/lectures/GoodPracticeCFD/Articles/Turbulence\\_Notes\\_Fluent-v6.3.06.pdf](http://www.southampton.ac.uk/~nwb/lectures/GoodPracticeCFD/Articles/Turbulence_Notes_Fluent-v6.3.06.pdf) (Accessed: 08<sup>th</sup> December 2017)

ANSYS (2006) *Ansys fluent 12.0 theory guide – 12.4.3 Realizable  $k$ - $\epsilon$  model*. Available at: <https://www.sharcnet.ca/Software/Fluent6/html/ug/node480.htm> (Accessed: 08<sup>th</sup> June 2017)

ANSYS (2009) *Ansys fluent 12.0 theory guide – 16.3.2 volume fraction equation*. Available at: <http://www.afs.enea.it/project/neptunius/docs/fluent/html/th/node299.htm> (Accessed: 20<sup>th</sup> June 2017)

ANSYS (2015) *Ansys fluent 16.2 release – 5.2.2 mesh quality*. Available at: [https://www.sharcnet.ca/Software/Ansys/16.2.3/en-us/help/flu\\_ug/flu\\_ug\\_mesh\\_quality.html](https://www.sharcnet.ca/Software/Ansys/16.2.3/en-us/help/flu_ug/flu_ug_mesh_quality.html) (Accessed: 20<sup>th</sup> December 2017)

Arimitsu, T., Ooe, K. and Kawasaki, K. (2013). Evaluation method of tsunami Wave Pressure Acting on Land Structure Using 2D Depth-Integrated Flow Simulation, *Coastal Dynamics*, pp. 105 – 114.

Boussinesq, J. (1877) *Essai sur la théorie des eaux courantes*, Mémoires présentés par divers savants à l'Académie des Sciences, 23, pp. 1-680.

Burkow, M. and Griebel, M. (2016) 'A full three-dimensional numerical simulation of the sediment transport and the scouring at a rectangular obstacle' *Computer and Fluids*, Vol. 125, pp. 1-10.

Cengel, Y. A. and Cimbala, J. M. (2014) *Fluid mechanics: fundamentals and application*, 3<sup>rd</sup> edn. New York: McGraw-Hill.

Chanson, H. (1999) *The hydraulics of open channel flow*. 2<sup>nd</sup> edn. London: Edward Arnold.

Chauchat, J., Cheng, Z., Nagel, T., Bonamy, C. and Hsu, T. (2017) 'SedFoam-2.0: a 3D two-phase flow numerical model for sediment transport', *Journal of Geoscientific Model Development*, 10, pp. 4367-4392.

Chen, J., Jiang, C., Yang, W. and Xiao, G. (2015) 'Laboratory study on protection of tsunami-induced scour by offshore breakwaters', *Natural Hazards*, 81(2), pp. 1229-1247.

Chen, J., Huang, Z., Jiang, C., Deng, B. and Long, Y. (2013) 'Tsunami-induced scour at coastal roadways: a laboratory study', *Natural Hazards*, 69(1), pp. 655 – 674.

Chen, Y. Y., Kharif, C., Yang, J. H., Hsu, H. C., Touboul, J. and Chanbarel, J. (2015) 'An experimental study of steep solitary wave reflection at a vertical wall', *European Journal of Mechanics – B/Fluids*, 29 (A), pp. 20 – 28.

Constantin, A. (2016) 'Extrema of the dynamic pressure in an irrotational regular wave train' *Physics of Fluids*, 28(11), pp. 113604-1 - 113604-8. Available at: <https://doi.org/10.1063/1.4967362> (Accessed: 22<sup>nd</sup> December 2017)

Craft, T. J. (2011) 'Near-wall modelling'. Manchester: University of Manchester. Available at: [http://cfd.mace.manchester.ac.uk/twiki/pub/Main/TimCraftNotes\\_All\\_Access/flmsc-wallfns.pdf](http://cfd.mace.manchester.ac.uk/twiki/pub/Main/TimCraftNotes_All_Access/flmsc-wallfns.pdf) (Accessed: 23<sup>rd</sup> October 2017)

Craik, A. (2004) 'The origin of water wave theory' *Annual Review of Fluid Mechanics*, 36, pp. 1-28, Annual Reviews [online]. Available at: <http://www.annualreviews.org/eprint/ntKxUcsyXeywpgFQRASc/full/10.1146/annurev.fluid.36.050802.122118> (Accessed: 13 March 2014).

Daghighi, N., Chegini, A. H. N., Daliri, M. and Hedayati, D. (2015) 'Experimental assessment of sediment transport and bed formation of sandy beaches by tsunami waves' *International Journal of Environmental Research*, 9(3), pp. 795-804.

Dao, M.H. and Tkalich, P. (2007) 'Tsunami propagation modelling – a sensitivity study' *Natural Hazards and Earth System Sciences*, 7, pp 741 – 754.

Dey, S. (1999) 'Sediment threshold', *Journal of Applied Mathematical Modelling*, 23, pp. 399-417.

Dias, F. and Dutykh, D. (2006) *Dynamics of tsunami waves*. Available at: <http://hal.archives-ouvertes.fr/docs/00/64/34/37/PDF/FD-DD-2006.pdf> (Accessed: 19 March 2014).

ERC OFTAC Series (2011) Direct and large eddy simulation VIII. Springer Science + Business Media B. V.,15.

Francis, J. R. D. (1973) 'Experiments on the motion of solitary grains along the bed of a water-stream' *Proceedings of the Royal Society a Mathematical, Physical and Engineering Sciences*, 332, pp. 443-471.

Fredsoe, J. and Deigaard, R. (1992) *Mechanics of coastal sediment transport*. Advanced series on ocean engineering, 3. Singapore: World Scientific.

Fromm, J. E. and Harlow, F. H. (1963) 'Numerical solution of the problem of vortex street development', *Physics of Fluids*, 6, pp. 975-982.

Ghasemi, M. and Soltani-Gerdefaramarzi, S. (2017) 'The scour bridge simulation around a cylindrical pier using flow-3d'. *Journal of Hydrosiences and Environment*, 1(2), pp 46-54.

Gica, E., Spillane, M.C. and Titov, V.V. (2007): Tsunami hazard assessment using short-term inundation forecasting for tsunamis (SIFT) tool. EASTEC International Symposium 2007 - Dynamic Earth: its Origin and Future, Sendai, Japan.

Giordano, F., Fox, W., Horton, S. and Weir M. (2009) *A first course in mathematical modelling*. 4th edn. Canada: Cengage learning.

Ha, T. and Cho, Y. (2015) 'Tsunami propagation over varying water depths' *Journal of Ocean Engineering*, 101, pp. 67 – 77.

Hanna, R. (2014) *Implementation of a sediment transport model for CE-QUAL-W2*. Master's Project Reports. Portland State University. Available at: [http://pdxscholar.library.pdx.edu/cgi/viewcontent.cgi?article=1011&context=cengin\\_g radprojects](http://pdxscholar.library.pdx.edu/cgi/viewcontent.cgi?article=1011&context=cengin_g radprojects) (Accessed: 29<sup>th</sup> November 2017)

Harlow, F.H. and Welch, J. E. (1965) 'Numerical calculation of time-dependent viscous incompressible flow of fluid with a free surface', *The Physics of Fluids*, 8, pp. 2182-2189.

Hicken, E. J. (2010) *Chapter 4: Sediment transport*. Canada: Simon Fraser University. Available at: <http://www.sfu.ca/~hickin/RIVERS/Rivers4%28Sediment%20transport%29.pdf> (Accessed: 13<sup>th</sup> November 2017)

Hirota, I. and Miyakoda, K. (1964) 'Numerical solution of kármán vortex street behind a circular cylinder', *Journal of the Meteorological Society of Japan*, 43(1), pp. 30-41.

Hongwei, F. and Rodi, W. (2002) 'Three-dimensional mathematical model and its application in the neighbourhood of the three gorges reservoir dam in the Yangtze river' *Chinese Journal of Mechanics Press, Beijing, China*. 18(3), New York: Allerton Press, INC.

Imamura, F., Yalciner, A. C. and Ozyurt, G. (2006) *Tsunami modelling manual (TUNAMI model)* Available at: <http://www.tsunami.civil.tohoku.ac.jp/hokusai3/J/projects/manual-ver-3.1.pdf> (Accessed: 15 April 2014)

Japan International Cooperation Agency (2010) *Technical standards and guidelines for design of flood control structures*. Available at: [http://whrm-kamoto.com/assets/files/FinalDesignFC\[1\].pdf](http://whrm-kamoto.com/assets/files/FinalDesignFC[1].pdf) (Accessed: 20<sup>th</sup> June 2018)

Jayaratne, R. (2012) Lecture1: waves. CEM001 Hydraulic Structures, Coastal & River Engineering. 27<sup>th</sup> September. London: University of East London

Jayaratne, R., Abimbola A., Mikami T., Matsuba S., Esteban, M. and Shibayama, T. (2014). 'Predictive model for scour depth of coastal structure failures due to tsunamis'. *Proceedings of the 33<sup>rd</sup> International Conference on Coastal Engineering ICCE*, No. 34, Structures Paper No: 56.

Jayaratne, R., Premaratne, B., Abimbola, A., Mikami, T., Matsuba, S., Shibayama, T., Esteban, M. and Nistor, I (2016) 'Failure mechanisms and local scour at coastal structures induced by tsunami', *Coastal Engineering Journal*, 58(4), World Scientific. Available at: <http://www.worldscientific.com/worldscinet/cej> (Accessed: 21<sup>th</sup> December 2016)

Jiang, C., Chen, J., Yao, Y., Liu, J. and Deng, Y. (2015) 'Study on threshold motion of sediment and bedload transport by tsunami waves', *Ocean Engineering*, 100, pp. 97–106

Julien, P. Y. (2010). *Erosion and sedimentation*, 2nd edn. New York: Cambridge University Press.

Karim, O.A. and Ali, K. H. M. (2000). 'Prediction of flow patterns in local scour holes caused by turbulent water jets', *Journal of Hydraulic Research*, 38, pp. 279 – 287.

Kato, F., Inagaki, S. and Fukuhama M. (2007) 'Wave force on coastal Dike due to tsunami', *Proceedings of the 30<sup>th</sup> International Conference on Coastal Engineering*, ASCE, pp 5150 – 5161. Available at: <http://pwweb1.pwri.go.jp/eng/ujnr/joint/37/paper/13kato.pdf> (Accessed: 29 March 2014)

Kato, F., Sato S. and Yeh H. (2000) 'Large-scale experiment on dynamic response of sand bed around a cylinder due to tsunami', *Proceedings of 27<sup>th</sup> International Conference on Coastal Engineering*, ASCE, pp. 1848–1859.

Kato, F., Suwa, Y., Watanabe, K. and Hatogai, S. (2012) 'Mechanisms of coastal dike failure induced by the great east Japan earthquake tsunami'. *Proceedings of the 33<sup>rd</sup> International Conference on Coastal Engineering*, ASCE.

Keetels, G. H., Goeree, J. C. and Rhee, V. (2017) 'Advection-diffusion sediment models in a two-phase flow perspective' *Journal of Hydraulic Research*, Available at: <http://www.tandfonline.com/doi/pdf/10.1080/00221686.2017.1289262?needAccess=true> (Accessed: 01<sup>st</sup> December 2017).

Keulegan, G. H. (1938) 'Laws of turbulent flow in open channels', *Journal of Research of the National Bureau of Standards*, 21(RP1151), pp. 707-741.

Kim, H. S. and Chen H. (2014) 'Three-dimensional numerical analysis of sediment transport around abutment in channel bend'. *Coastal engineering proceedings* (34). Available at: <https://icce-ojs-tamu.tdl.org/icce/index.php/icce/article/view/7183> (Accessed: 10 November 2017)

Kinsman, B. (1965) *Wind waves: their generation and propagation on the ocean surface*. Englewood Cliffs, N.J.: Prentice-Hall.

Komar, P. D. (1980) 'Modes of sediment transport in channelized water flows with ramifications to the erosion of the Martian outflow channels', *Icarus* 42, pp. 317–329.

Koshimura, S., Hayashi, S. and Gokon, H. (2014) 'The impact of the 2011 Tohoku earthquake tsunami disaster and implications to the reconstruction', *Soils and Foundations*, 54 (4), pp. 560-572.

Launder, B. E. and Spalding, D. B. (1972) *Lectures in mathematical models of turbulence*. London: Academic Press.

Launder, B. E. and Spalding, D. B. (1974) 'The numerical computation of turbulent flows', *Computer Methods in Applied Mechanics and Engineering*, 3, pp. 269-289.

Leal, J., Ferreira, R. and Cardoso, A (2009) 'Maximum level and time to peak of dam break waves on mobile horizontal bed', *Journal of Hydraulic Engineering, ASCE*, 135 (11), pp. 995 – 999.

Le roux, A. (2009) *A mathematical model for tsunami generation using a conservative velocity-pressure hyperbolic system*. Available at: <http://arxiv.org/abs/0905.3159v1> (Accessed: 12 March 2014).

Lilly D. K. (1967) 'The representation of small-scale turbulence in numerical simulation experiments'. *Proceedings of the IBM scientific computing symposium on environmental sciences*; Yorktown Heights, USA, pp. 195–210

Li, G., Lang, L. and Ning, J. (2013) '3d numerical simulation of flow and local scour around a spur dike', *35<sup>th</sup> Proceedings of International Association for Hydro-Environment Engineering and Research (IAHR) World Congress, Chengdu, China*, 1, pp 239-247.

Li, L., Qiu, Q. and Huang, Z. (2012) 'Numerical modelling of the morphological change in Lhok Nga, west Banda Aceh, during the 2004 Indian Ocean tsunami: understanding tsunami deposits using a forward modelling method', *Natural Hazards*, 64 (2) pp 1549-1574.

Liu, H., Ghidaoui, M. S., Haung, Z., Yuan, Z. and Wang, J. (2011) 'Numerical investigation of the interactions between solitary waves and pile breakwaters using BGK-based methods', *Journal of Computers and Mathematics with Applications*, 61, pp. 3668 – 3677.

Lobovsky, L., Botia-Vera, E., Castellana, F., Mas-Soler, J. and Souto-Iglesias, A. (2014) 'Experimental investigation of dynamic pressure loads during dam break' *Journal of Fluids and Structures*, 48, pp. 407 – 434.

Lynett, P., Swigler, D., Son, S., Bryant, D., Socolofsky, S. (2010) 'Experimental study of solitary wave evolution over a 3d shallow shelf' *Proceedings of 32<sup>nd</sup> Conference on Coastal Engineering, Shanghai, China*, No. 32. Available at: [https://icce-ojs-tamu.tdl.org/icce/index.php/icce/article/view/1385/pdf\\_364](https://icce-ojs-tamu.tdl.org/icce/index.php/icce/article/view/1385/pdf_364) (Accessed: 14<sup>th</sup> November 2017)

Mader, C. (2004) *Numerical modelling of water waves*. 2nd edn. Boca Raton, FL: CRC press.

Matsutomi, H., Okamoto, K., and Harada, K. (2010) 'Inundation flow velocity of tsunami on land and its practical use'. *Proceedings of 32<sup>nd</sup> Conference on Coastal Engineering*, ASCE. Shanghai, China. Available at: [http://journals.tdl.org/icce/index.php/icce/article/view/1141/pdf\\_215](http://journals.tdl.org/icce/index.php/icce/article/view/1141/pdf_215) (Accessed: 6 August 2015).

Meyer-Peter, E. and Muller, R. (1948) 'Formulas for bed-load transport' *Report on 2nd Meeting for International Association for Hydro-Environment Engineering and Research, Stockholm*, pp. 39-64.

Miedema, S. A. (2008). 'An analytical method to determine scour' *WEDA XXVIII & Texas A&M*, 39, pp. 8-11.

Mikami, T., Matsuba, S. and Shibayama, T. (2014) 'Flow geometry of overflowing tsunamis around coastal dikes' *Proceedings of 34<sup>th</sup> Conference on Coastal Engineering*, ASCE. Available at: [https://icce-ojs-tamu.tdl.org/icce/index.php/icce/article/viewFile/7615/pdf\\_839](https://icce-ojs-tamu.tdl.org/icce/index.php/icce/article/viewFile/7615/pdf_839) (Accessed: 15 January 2016).

Mikami, T. and Shibayama, T. (2013) 'Numerical analysis of tsunami flow around coastal dyke.' *Proceedings of the 7<sup>th</sup> international Conference on Asian and Pacific Coasts*, Bali, Indonesia, September 24 – 26.



Mintz, Y. (1965) 'Very long-term global integration of the primitive equations of atmospheric motion: An experiment in climate simulation', *WMO-IUGG Symposium on Research and Development Aspects of Long-range Forecasting*, WMO Technical Note 66, pp. 141-167.

Mitobe, Y., Adityawan, M. B., Tanaka, H., Kawahara, T., Kurosawa, T. and Otsushi, K. (2014) 'Experiments on local scour behind coastal dikes induced by tsunami overflow' *Proceedings of 34<sup>th</sup> Conference on Coastal Engineering, Seoul, Korea*. Available at: [https://icce-ojs-tamu.tdl.org/icce/index.php/icce/article/view/7671/pdf\\_855](https://icce-ojs-tamu.tdl.org/icce/index.php/icce/article/view/7671/pdf_855) (Accessed: 6<sup>th</sup> June 2017)

Mizutani, S. and Imamura, F. (2001) 'Dynamic wave force of tsunamis acting on a structure' *ITS Proceedings*. Available at: [http://nthmp-history.pmel.noaa.gov/its2001/Separate\\_Papers/7-28\\_Mizutani.pdf](http://nthmp-history.pmel.noaa.gov/its2001/Separate_Papers/7-28_Mizutani.pdf) (Accessed: 31 March 2014)

Mizutani, S. And Imamura, F. (2002). 'Design of coastal structure including the impact and overflow on tsunamis', *Proceedings of Coastal Engineering*, JSCE, 49.

Mo, W. and Liu, P. (2009) 'Three dimensional numerical simulations for non-breaking solitary wave interacting with a group of slender vertical cylinders', *Internal Journal of Naval Architecture and Naval Engineering*, 1, pp. 20 – 28.

Morichon, D., Desombre, J. and Simian, B. (2013) 'Vof simulation of sediment transport under high velocity flow case of a dam break over mobile bed', *Coastal Dynamics- 7<sup>th</sup> International Conference of Coastal Dynamics*, pp. 1241-1250.

National Instruments (2015) Using the dax assistant to automatically generate Labview code. Available at: <http://www.ni.com/tutorial/4656/en/> (Accessed: 16 March 2015).

Nistor, I., Nouri, Y., Palermo, D. and Cornett, A. (2009) 'Experimental investigation of the impact of a tsunami-induced bore on structures' *Proceeding of the 31<sup>st</sup> International Conference of Coastal Engineering, Hamburg, Germany*, pp. 3324-3336. Available at: [https://www.researchgate.net/publication/269117553\\_Experimental\\_investigation\\_of](https://www.researchgate.net/publication/269117553_Experimental_investigation_of)

[the impact of a tsunami-induced bore on structures](#) (Accessed: 15<sup>th</sup> December 2017).

NOAA, (2014) *Tsunami data and information*. Available at: <http://www.ngdc.noaa.gov/hazard/tsu.shtml> (Accessed: 19 March 2014).

NOAA Center for Tsunami Research (2014) *Tsunami modelling research*, Available at: <http://nctr.pmel.noaa.gov/model.html> (Accessed: 15 April 2014).

Noh, W.F. and Woodward, P. (1976). 'SLIC (Simple Line Interface Calculation)'. In: van de Vooren A.I., Zandbergen P.J. (eds)', *Proceedings of 5<sup>th</sup> International Conference on Numerical Methods in Fluid Dynamics*. June 28 – July 2, 1976. Twente University, Enschede. Lecture Notes in Physics, 59, pp. 330–340.

Ota, K., Sato, T. and Nakagawa, H. (2016) '3D numerical model of sediment transport considering transition from bed-load motion to suspension- application to a scour upstream of a cross-river structure'. *Journal of Japan Society of Civil Engineer*, 71(4), pp. 173-180.

Prasetyo, A., Tomiczek, T., Yasuda, T., Mori, N., Mase, H. and Kennedy, A (2016) 'Physical experiments of tsunami run-up and force on building cluster using a hybrid tsunami generator', *Proceeding of the 6<sup>th</sup> International Conference on the Application of Physical Modelling in Coastal and Port Engineering and Science, Ottawa, Canada, May 10 – May 13*. Available at: <http://rdio.rdc.uottawa.ca/publications/coastlab16/coastlab73.pdf> (Accessed: 15<sup>th</sup> December 2017).

Raby, A., Macabuag, J., Pomonis, A. and Wilkinson, S. (2015) 'Implications of the 2011 great east japan tsunami on sea defence design' *International Journal of Disaster Risk Reduction*, 14, pp. 332 – 346.

Rahman, S., Akib, S., Khan, M., T., R. and Shirazi, S., M. (2014) 'Experimental study on tsunami risk reduction on coastal building fronted by sea wall' *The Scientific World Journal*. Available at: <https://www.ncbi.nlm.nih.gov/pmc/articles/PMC3984855/pdf/TSWJ2014-729357.pdf> (Accessed: 15<sup>th</sup> December 2017).

Rana, Z. (2017) lecture notes: *Advanced turbulence modelling*. Advance Turbulence Modelling and Simulation. 30<sup>th</sup> January. Milton Keynes: Cranfield University.

Reynolds, O. (1895) 'On the dynamical theory of incompressible viscous fluids and the determination of the criterion', *Philosophical Transactions of the Royal Society of London*. A, 186, pp. 123-164.

Reynolds, W. C. (1974) 'Recent advances in the computation of turbulent flows', *Elsevier Advances in Chemical Engineering*, 9, pp. 193-246.

Riggs, H. R., Robertson, I. N., Cheung, K. F., Pawlak, G., Young, Y. L. and Yim, S. C. S. (2008) 'Experimental simulation of tsunami hazards to buildings and bridges', *Proceedings of 2008 NSF Engineering Research and Innovation Conference, Knoxville, Tennessee*, Available at: <http://teri.hawaii.edu/pdf/CMMI2008Riggs.pdf> (Accessed: 23<sup>rd</sup> December 2017).

Rogers, B. D. and Dalrymple R. A. (2008) 'SPH modeling of tsunami waves' *Advanced Numerical Models for Simulating Tsunami Waves and Runup*, 10, pp. 75-100. doi: 10.1142/9789812790910\_0003.

Roh, M., Tanaka, H., Aditaywan, M., B., Mano, A. and Udo, K. (2012) 'Evaluation of celerity and velocity for tsunami propagation into rivers', *33<sup>rd</sup> International Conference on Coastal Engineering, Santander, Spain*. Available at: <https://journals.tdl.org/icce/index.php/icce/article/view/6746> (Accessed: 15<sup>th</sup> December 2017).

Rosetto, T., Allsop, W., Charvet, I. and Robinson, D. (2011) 'Physical modelling of tsunami using a new pneumatic wave generator', *Coastal Engineering, Elsevier*, pp. 517 – 527.

Rueben, M., Holman, R., Cox, D., Shin, S., Killian, J. and Stanley, J. (2010) 'Optical measurements of tsunami inundation through an urban waterfront modeled in a large-scale laboratory basin'. *Coastal Engineering, Elsevier*, pp. 229 – 238.

Salim, S. M. and Cheah, S. C. (2009) 'Wall  $y^+$  strategy for dealing with wall-bounded turbulent flows' *Proceedings of the International MultiConference of Engineers and Computer Scientists*, II. Available at:

<http://citeseerx.ist.psu.edu/viewdoc/download?doi=10.1.1.149.722&rep=rep1&type=pdf> (Accessed: 09<sup>th</sup> December 2017).

Schimmels, S., Sriram, V., Didenkulova, I., and Fernandez, H. (2014) 'On the generation of tsunami in a large scale wave flume' *Proceedings of 34th Conference on Coastal Engineering, Seoul, Korea, 2014*, 34. Available at: [https://icce-ojs-tamu.tdl.org/icce/index.php/icce/article/view/7465/pdf\\_951](https://icce-ojs-tamu.tdl.org/icce/index.php/icce/article/view/7465/pdf_951) (Accessed: 15<sup>th</sup> December 2017).

Shibayama, T., Esteban, M., Nistor, I., Takagi, H., Danh Thao, N., Matsumaru, R., Mikami, T., Aranguiz, R., Jayaratne, R. and Ohira, K. (2013) 'Classification of tsunami and evacuation areas', *Journal of Natural Hazards*, 67 (2), pp. 365-386.

Shih, T., Liou, W., Shabbir, A., Yang, Z. and Zhu, J. (1995) 'A new  $k-\epsilon$  eddy viscosity model for high Reynolds number turbulent flows', *Elsevier Computers & Fluids*, 24(3), pp. 227-238.

Shito, M., Inuzuka, I., Amaya, I, Saito, H., and Kurata, J. (2014) 'Numerical simulations and experiments on tsunami for the design of coastal and offshore structures' *IHI Engineering Review*, 46(2), pp. 21 – 25.

Soulsby, R. (1997) *Dynamics of Marine Sands*. London: Tomas Telford Ltd.

Soulsby, R. and Whitehouse, R. (1997). 'Threshold of sediment motion in coastal environment', *proceedings pacific Coasts and Ports 1997 Conference*. University of Canterbury, Christchurch, New Zealand, pp. 149- 154.

Smagorinsky J. (1963) 'General circulation experiments with the primitive equations I. the basic experiment', *Monthly Weather Review*, 91(3), pp. 99–164.

Smagorinsky, J., Manabe, S. and Holloway, J. L. (1965) 'Numerical results from a nine-level general circulation model of the atmosphere', *Monthly Weather Review*, 93, p. 727-768.

Sreedhara, B. M., Sanooj, A., Manu and Mandal, S. (2016) 'Simulation of local scour around circular and round nosed bridge pier using reef3d', *International Journal of Innovative Research in Science, Engineering and Technology*, 5(9), pp. 149-154.

Suwa, Y., Kato, F. and Hatogai, S. (2013) *Technical support in relation to resilient structures of coastal dikes*. Available at: <http://www.nilim.go.jp/english/annual/annual2013/4.pdf> (Accessed: 20<sup>th</sup> June 2018).

Suwa, Y. and Watanabe, K. (2014) *New developments in coastal management – Introducing the concept of disaster mitigation and preventive maintenance*. Available at: <http://www.nilim.go.jp/english/annual/annual2014/38.pdf> (Accessed: 20<sup>th</sup> June 2018).

Thao, N. D. (2007) *Simulation of velocity field in front of breakwater and wave breaking impact*. PhD thesis, Yokohama National University.

Titov, V., Gonzalez, F., Mofjeld, H., and Newman, J. (2001) 'Project SIFT (short-term Inundation Forecasting for Tsunamis)', *ITS Proceedings*, session 7, Number 7-2, pp. 715-721.

Tofany, N., Ahmed, M. F., Mamat, M. and Husain, M. L. (2014) 'Simulation of scouring in front of an impermeable vertical breakwater using the rans-vof numerical model', *Journal of Environmental Science and Technology*, 7(6), pp. 314 – 325.

Tonkin, S., Yeh, H., Kato, F. and Sato, S. (2003) 'Tsunami scour around a cylinder', *Journal of Fluid Mechanics*, 496, pp. 165–192.

Torii, K. (2014) *Structural measures that promote non-structural measures*. Available at: <http://www.nilim.go.jp/english/annual/annual2014/d.pdf> (Accessed: 20<sup>th</sup> June 2018).

Tsujimoto, G., Mineura, R., Yamada, F., Kakinoki, T. and Uno, K. (2014) 'Scouring mechanism behind seawall from tsunami overflow and optimum conditions to reduce tsunami energy with an artificial trench', *Proceedings of 34<sup>th</sup> Conference on Coastal Engineering, Seoul, Korea*. Available at: <https://journals.tdl.org/icce/index.php/icce/article/view/7396> (Accessed: 23<sup>rd</sup> December 2017).

Van Rijn, L.C. (1984) 'Sediment transport, Part I: Bed load transport', *ASCE Journal of Hydraulic Engineering*, 110, pp. 1431-1456.

Van Rijn, L. C. (1993). *Principles of sediment transport in rivers, estuaries and coastal seas*, Aqua Publications, Oldemarkt, The Netherlands.

Vasquez, J. A. and Walsh, B. W. (2009) 'CFD simulation of local scour in complex piers under tidal flow', *33rd International Association of Hydraulic Engineering & Research Congress, Vancouver, Canada*, pp. 913-920.

Viot, P. (2016) Lecture in Master 2 *Physics of complex systems and modelling, statistics and algorithms for out-of-equilibrium systems*. Numerical simulation in statistical physics. 19<sup>th</sup> October. Paris: Laboratoire de Physique Theorique de la Matiere Condensee.

Wang, X (2009) *User manual for comcot version 1.7 (first draft)*. Available at: <http://ceeserver.cee.cornell.edu/pll-group/doc/COMCOT User Manual v1 7.pdf> (Accessed: 15 April 2014)

Wijetunje, J. J. (2009) 'Field measurements and numerical simulations of the 2004 tsunami impact on the south coast of Sri Lanka', *Coastal Engineering, Elsevier*, 36, pp. 960-973.

William, I. A., and Fuhrman, D. R. (2016) 'Numerical simulation of tsunami-scale wave boundary layers', *Journal of Coastal Engineering*, 110, pp. 17 – 31.

Wu, W., Liu, H. and Fang, Y. (2015) 'A study on runup of nonbreaking double solitary waves on plane slope', *8<sup>th</sup> International Conference on Asian and Pacific Coasts*, 116, pp. 738 – 745.

Wüthrich D., Nistor, I., Pfister, M., and Schleiss, A., J. (2016) 'Experimental generation of tsunami-like waves', *Proceeding of Coastal Structures. Boston, MA, USA*, pp. 9-11. Available at: [https://infoscience.epfl.ch/record/223800/files/2016-1097%20W%C3%BCthrich Nistor Pfister Schleiss Experimental%20generation%20of%20tsunami-like%20waves.pdf](https://infoscience.epfl.ch/record/223800/files/2016-1097%20W%C3%BCthrich%20Nistor%20Pfister%20Schleiss%20Experimental%20generation%20of%20tsunami-like%20waves.pdf) (Accessed: 15<sup>th</sup> December 2017)

Wüthrich D., Pfister, M., De Cesare, G. and Schleiss, A., J. (2016) 'Velocity profile measurements in bore waves' *10<sup>th</sup> International Symposium on Ultrasonic Doppler Methods for Fluid Mechanics and Fluid Engineering, Tokyo, Japan*, pp. 137 – 140.

Available at: [https://infoscience.epfl.ch/record/222950/files/2016-1107%20W%C3%BCthrich Pfister De%20Cesare Schleiss Velocity%20profile%20measurements%20in%20bore%20waves.pdf](https://infoscience.epfl.ch/record/222950/files/2016-1107%20W%C3%BCthrich%20Pfister%20De%20Cesare%20Schleiss%20Velocity%20profile%20measurements%20in%20bore%20waves.pdf) (Accessed: 15<sup>th</sup> December 2017).

Xie, J., Nistor, I. and Murty, T. (2012) 'A corrected 3-D SPH method for breaking tsunami wave modelling', *Natural Hazards*, 60, pp. 81 – 100.

Yalciner, A., Pelinovsky, E., Talipova, T., Kurkin, A., Kozelkov, A. and Zaitsev, A. (2004) 'Tsunamis in the black sea: comparison of the historical, instrumental, and numerical data', *Journal of Geophysical Research*, 109(C12).

Yamauchi, S., Kioka, W. and Kitano, T. (2015) 'Drifting motion of vehicles in tsunami inundation flow', *8<sup>th</sup> International Conference on Asian and Pacific Coasts*, 116, pp. 592 – 599.

Yeh, H., Tonkin, S., Heller, E., Arduino, P., Kato, F. and Sato, S. (2004) 'Mechanisms of scour induced by tsunami runup.' *Proceedings of Second International Conference on SCOUR and EROSION, Singapore, 2*, pp. 464–471.

Youngs, D. L. (1982) 'The time-dependent multi-material flow with large fluid distortion.' *Numerical Methods for Fluid Dynamics*, Edited By, K. W. Morton and M. J. Baines, Eds., pp. 273–285. New York: Academic Press.

Zhang, Z. and Shi, B. (2016) 'Numerical simulation of local scour around underwater pipeline based on fluent software', *Journal of Applied Fluid Mechanics*, 9(2), pp. 711-718.

Zhiyin, Y. (2015) 'Large-eddy simulation: past, present and the future', *Chinese Journal of Aeronautics*, 28(1), pp. 11-24.

Zou, G. W., Liu, S. L., Chow, W. K. and Gao, Y. (2006) 'Large eddy simulation of turbulent flows', *International Journal on Architectural Science*, 7(1), pp. 26 – 34.

## Bibliography

Cfd-online.com. (2011) *K-epsilon models -- CFD-Wiki, the free CFD reference*. Available at: [https://www.cfd-online.com/Wiki/K-epsilon\\_models](https://www.cfd-online.com/Wiki/K-epsilon_models) (Accessed: 17 November 2017).

Daad.wb.tu-harburg.de (2017) *Approaches for turbulent modelling*. [online] Available at: [http://daad.wb.tu-harburg.de/fileadmin/BackUsersResources/Flood\\_Probability/2D/Steffi-2D/pdf/Approaches\\_for\\_turbulent\\_modelling.pdf](http://daad.wb.tu-harburg.de/fileadmin/BackUsersResources/Flood_Probability/2D/Steffi-2D/pdf/Approaches_for_turbulent_modelling.pdf) (Accessed: 2 November 2017).

Daad.wb.tu-harburg.de (2017) *Reynolds average Navier-Stokes equations*. Available at: [http://daad.wb.tu-harburg.de/fileadmin/BackUsersResources/Flood\\_Probability/2D/Steffi-2D/pdf/Reynolds\\_average\\_Navier-Stokes\\_equation.pdf](http://daad.wb.tu-harburg.de/fileadmin/BackUsersResources/Flood_Probability/2D/Steffi-2D/pdf/Reynolds_average_Navier-Stokes_equation.pdf) (Accessed: 2 November 2017).

Ghoma, M. I. (2011) *The effect of wall jet flow on local scour hole development*. PhD thesis, University of Bradford, Bradford.

Jiang, X. and Lai, C. (2009). *Numerical techniques for direct and large-eddy simulations*. Boca Raton: Taylor and Francis Group, LLC.

LEAP CFD Team (2014) *Turbulence Part 3 - Selection of wall functions and  $Y^+$  to best capture the Turbulent Boundary Layer* [online] Available at: <https://www.computationalfluidynamics.com.au/turbulence-part-3-selection-of-wall-functions-and-y-to-best-capture-the-turbulent-boundary-layer/> (Accessed: 12 June 2017).

Robertson I., Paczkowski K., Riggs H. and Mohamed A. (2008) 'Experimental results of tsunami bore forces on structures. American Society of Mechanical Engineers', *27<sup>th</sup> International Conference on Offshore Mechanics and Arctic Engineering*. Available at: [https://www.researchgate.net/profile/Ian\\_Robertson12/publication/236168669\\_Experimental\\_Results\\_of\\_Tsunami\\_Bore\\_Forces\\_on\\_Structures/links/5441c01a0cf2a6a049a5c043/Experimental-Results-of-Tsunami-Bore-Forces-on-Structures.pdf](https://www.researchgate.net/profile/Ian_Robertson12/publication/236168669_Experimental_Results_of_Tsunami_Bore_Forces_on_Structures/links/5441c01a0cf2a6a049a5c043/Experimental-Results-of-Tsunami-Bore-Forces-on-Structures.pdf) (Accessed: 15 December 2017).



Sednet.org. (2017) *The importance of sediment and sediment processes for river basin management*. [online] Available at: [http://sednet.org/download/WG4\\_riverbasin.pdf](http://sednet.org/download/WG4_riverbasin.pdf) (Accessed: 17 November 2017).

Xie, Z. (2010) *Modelling of breaking waves under the influence of wind*, PhD thesis, University of Leeds, Leeds.

Yan H. (2013) *Experiments and 3D modelling of hydrodynamics, sediment transport, settling and resuspension under unsteady conditions in an urban storm water detention basin*. Other. INSA de Lyon, English.

## APPENDIX A

### Configuration of LabView; a Pressure Analog Input Measurement

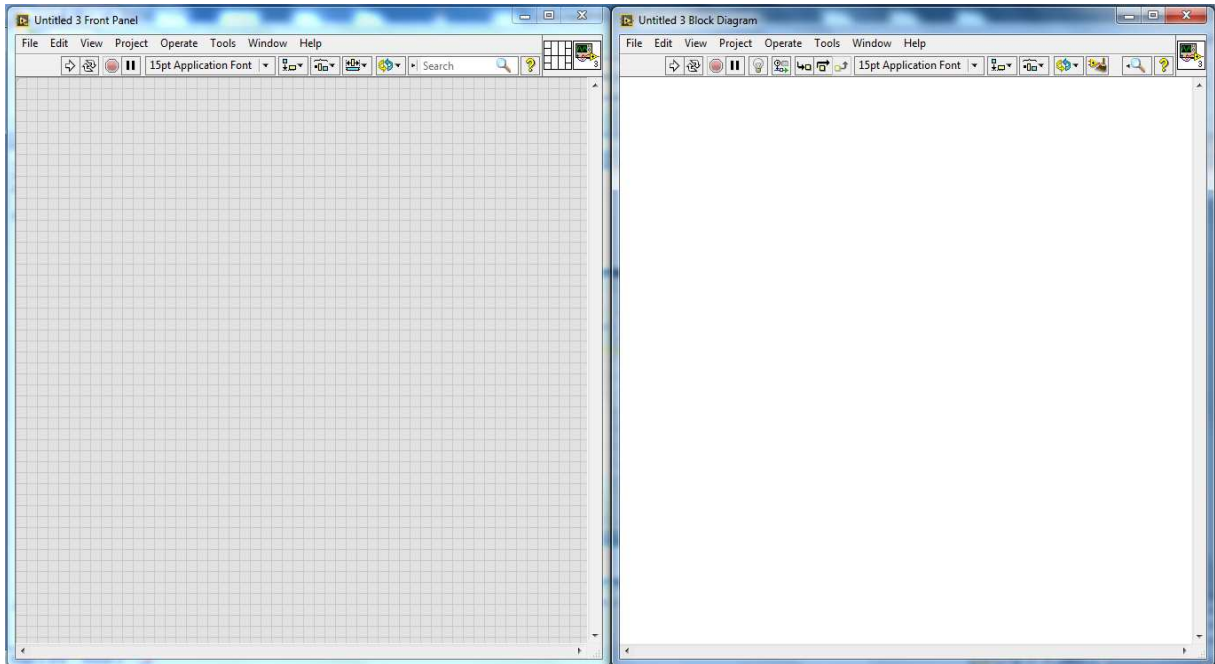


Figure A1. Blank Virtual Instrument, VI

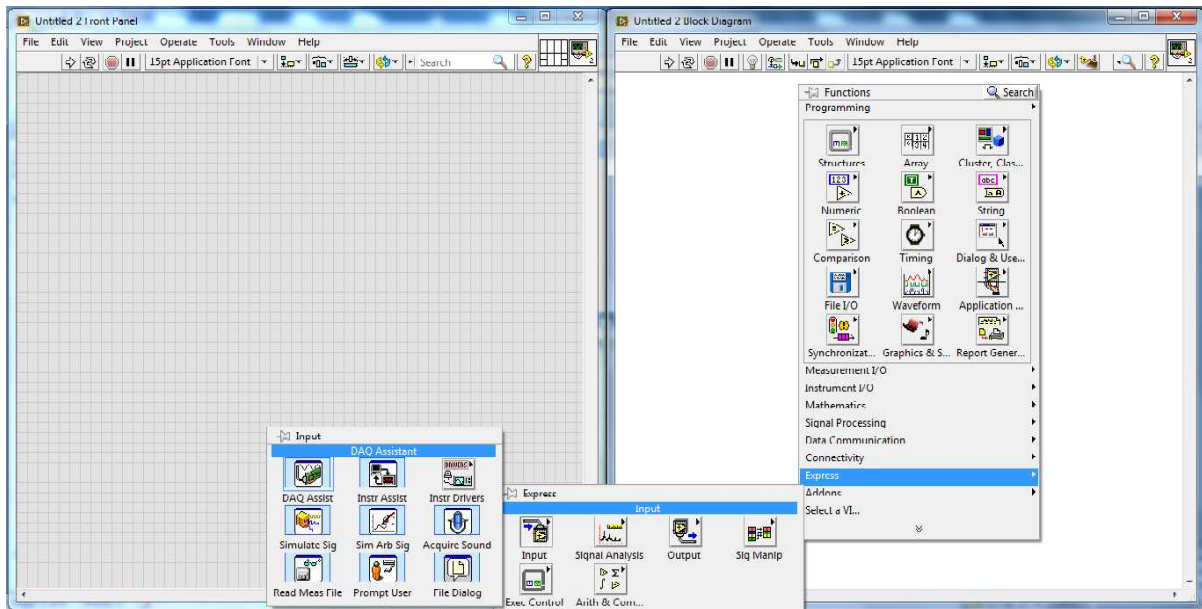


Figure A2. DAQ Assistant Express VI

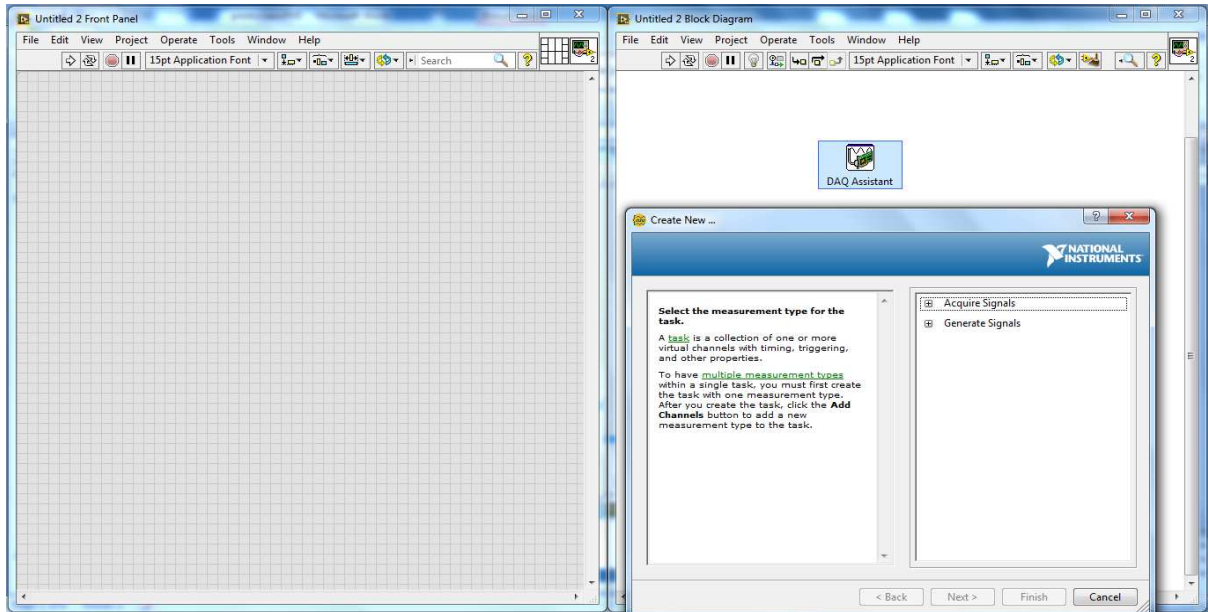


Figure A3. First step of pressure analog input measurement configuration

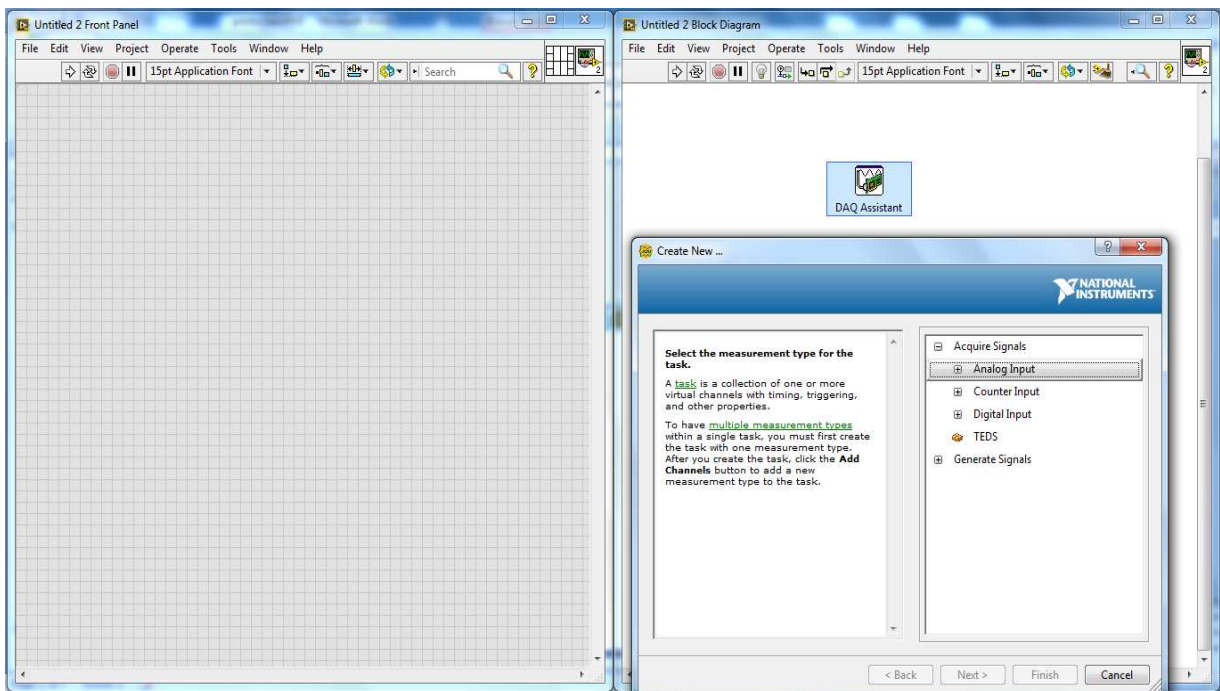


Figure A4. Second step of pressure analog input measurement configuration

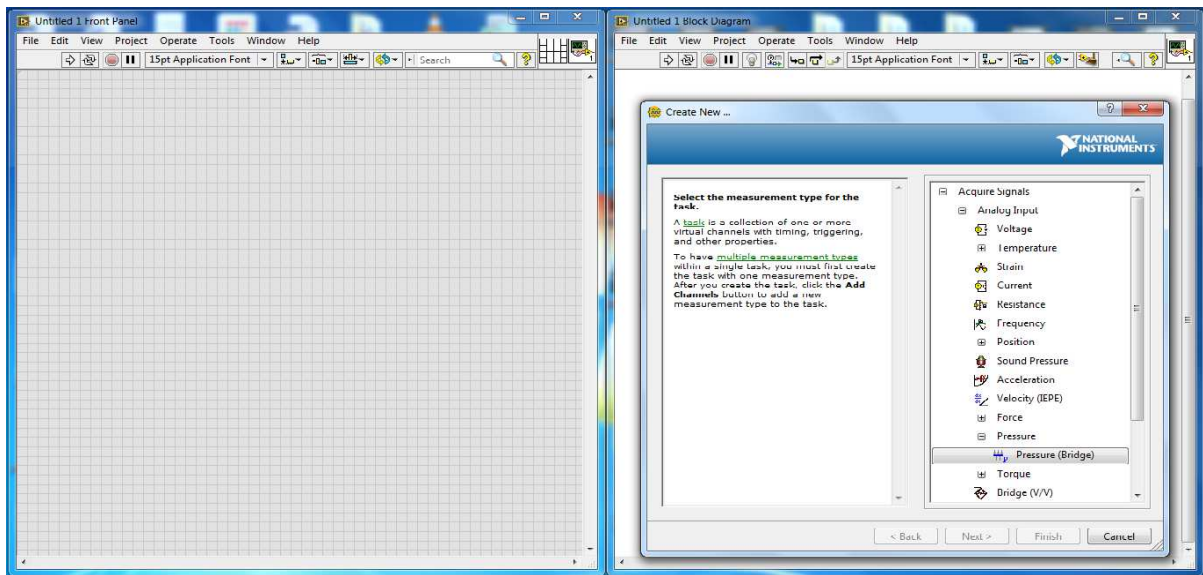


Figure A5. Third step of pressure analog input measurement configuration

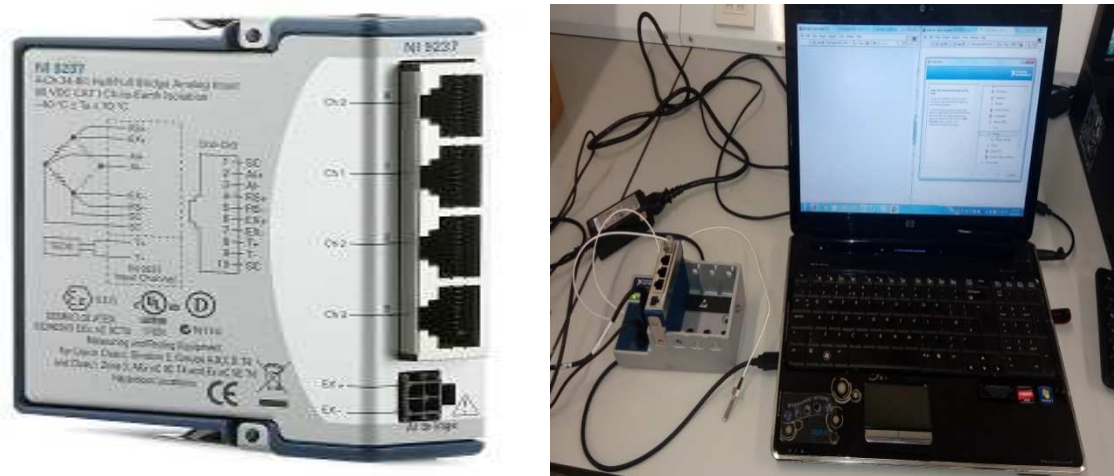


Figure A6. Data acquisition hardware device and pictorial representation of its connection

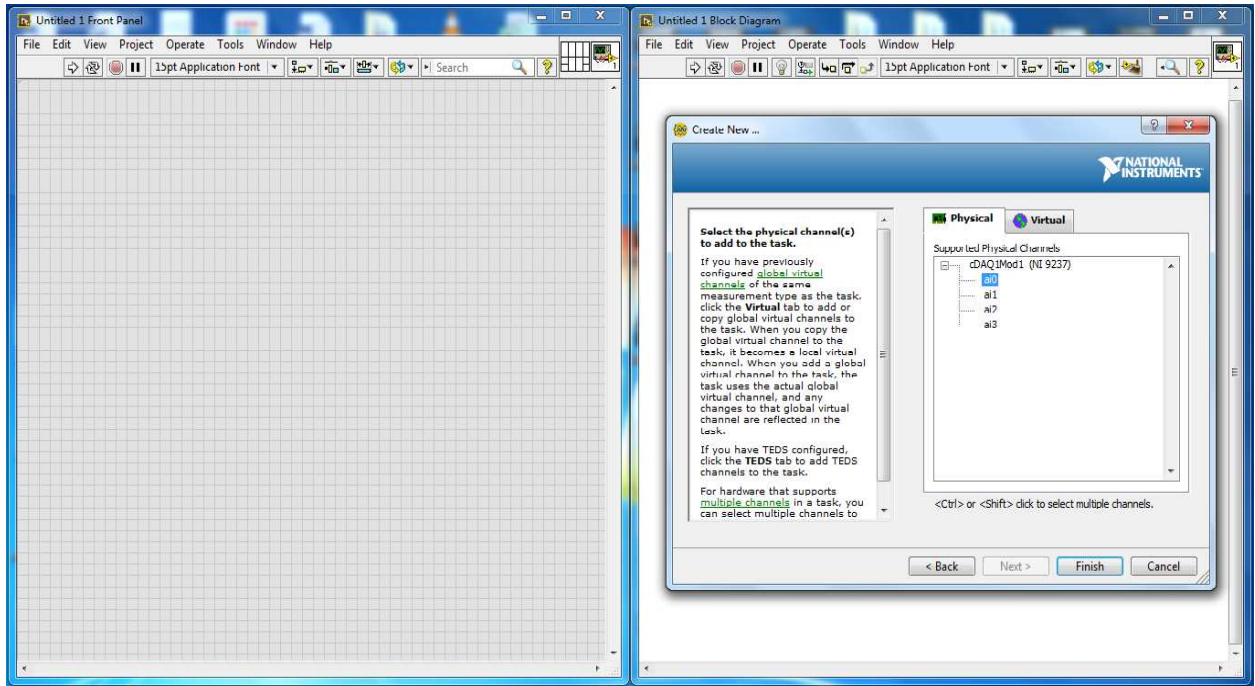


Figure A7. Physical channel a0 for pressure measurement

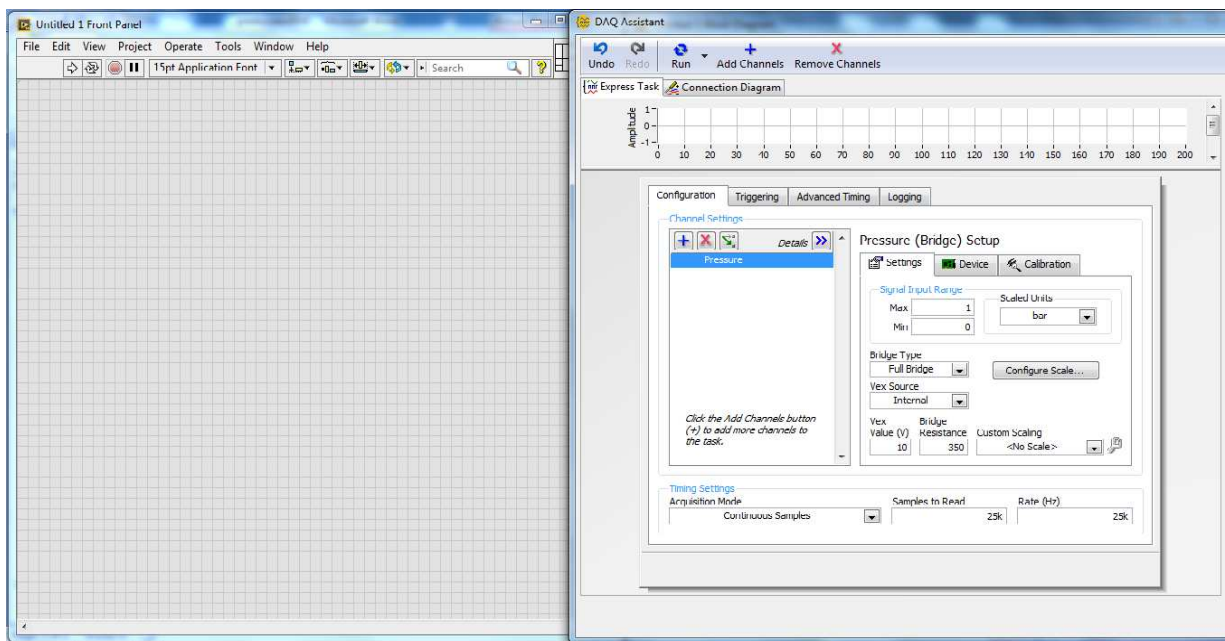


Figure A8. Configuration of channel-specific and task-specific settings

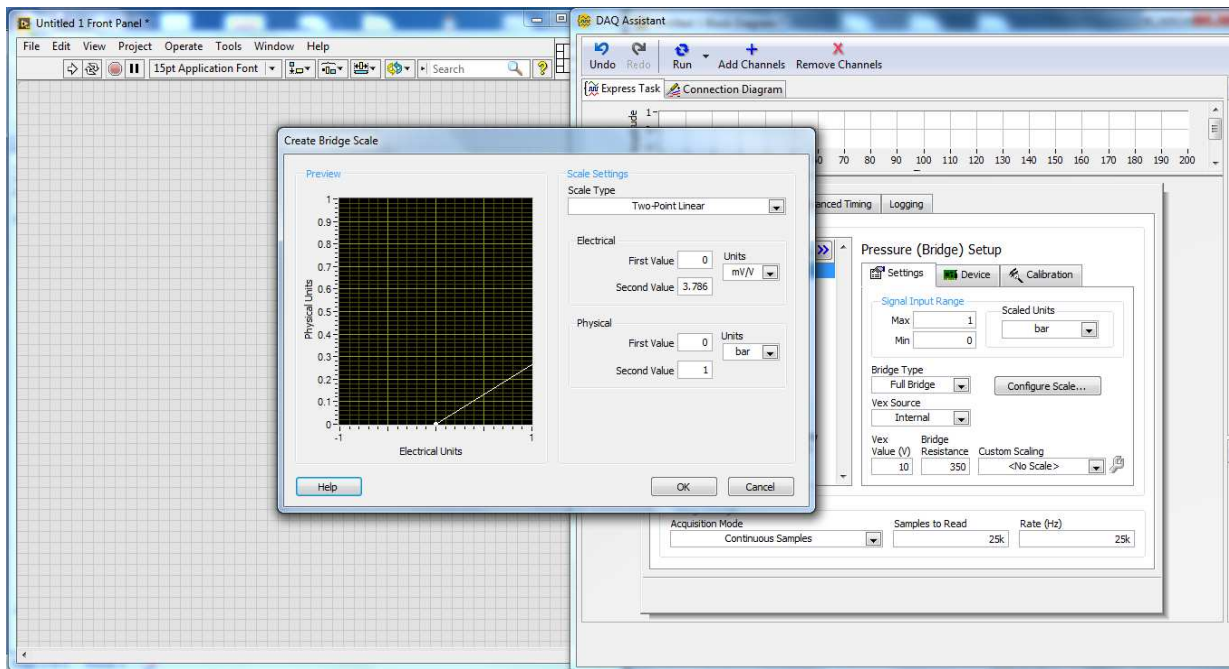


Figure A9. Configuration of the bridge scale to map physical values to electrical values

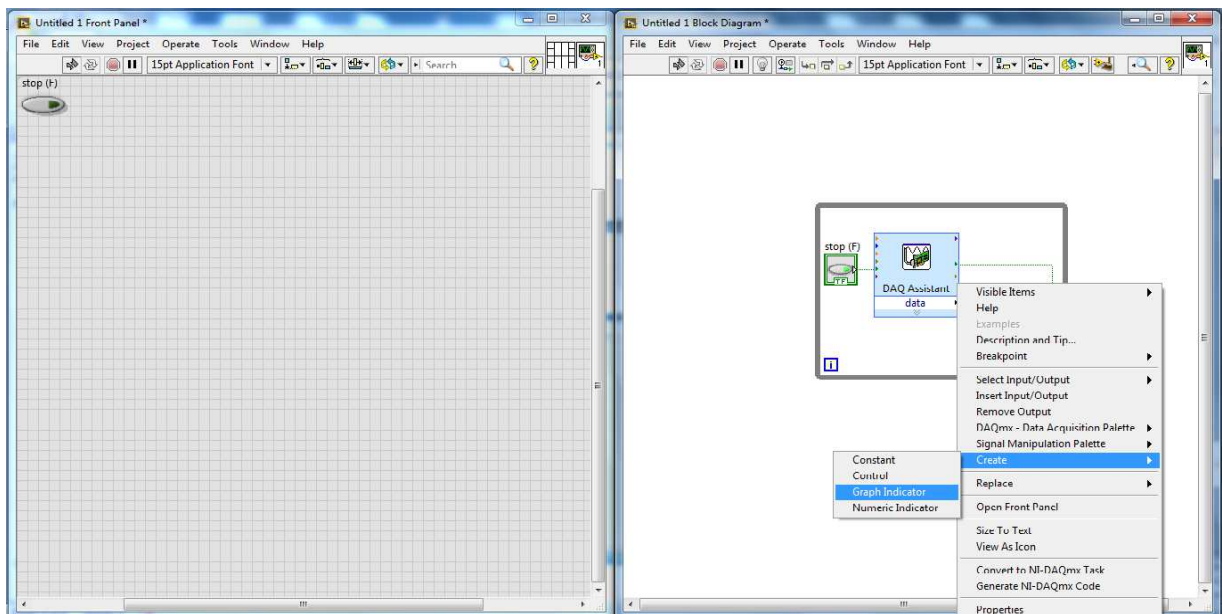


Figure A10. Creating graph indicator from DAQ assistant

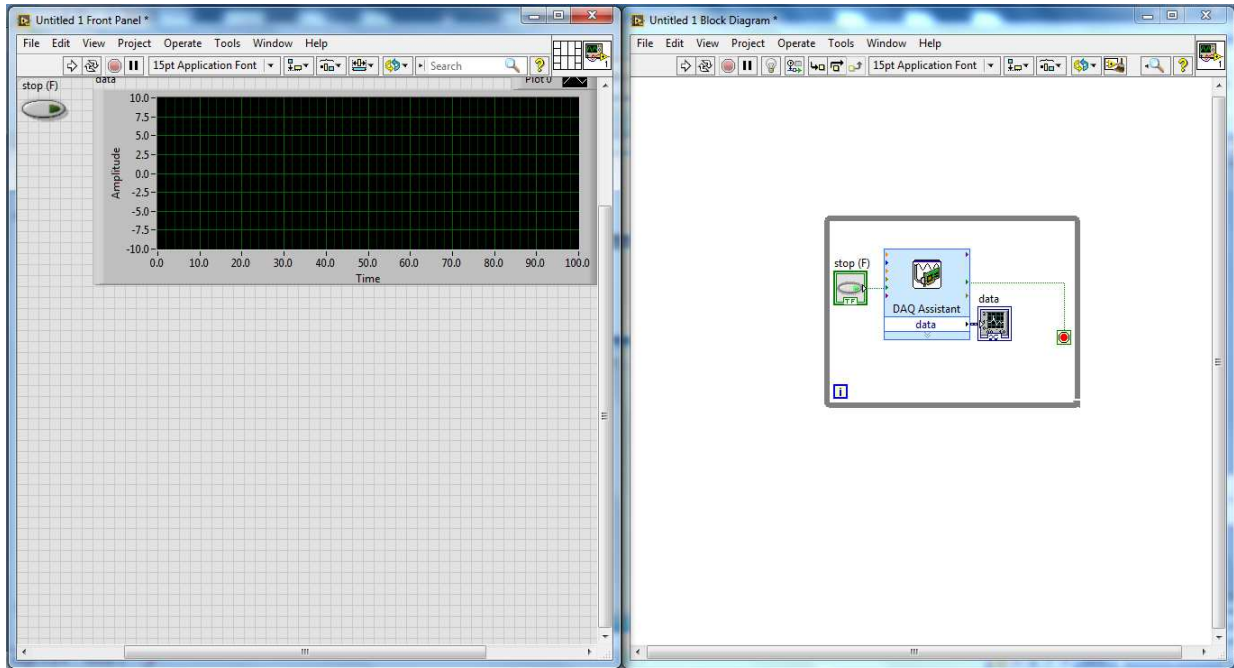


Figure A11. The Waveform Graph Indicator

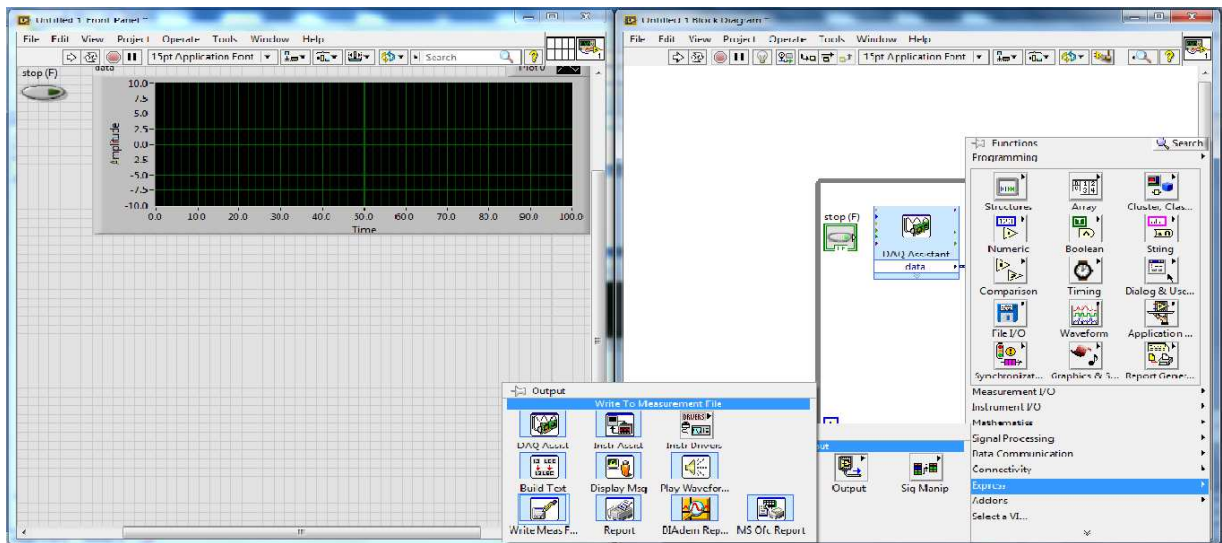


Figure A12. Launching the Write to Measurement File Express VI.

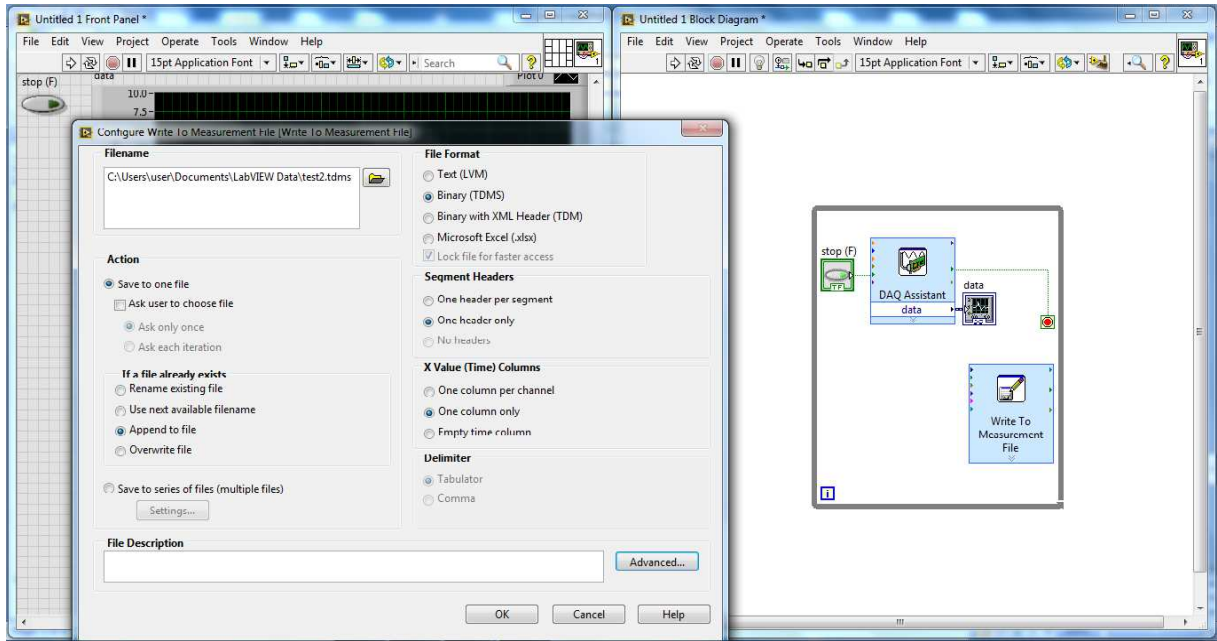


Figure A13. Configuration of the Write to Measurement File Express VI to a Binary (TDMS) File Format

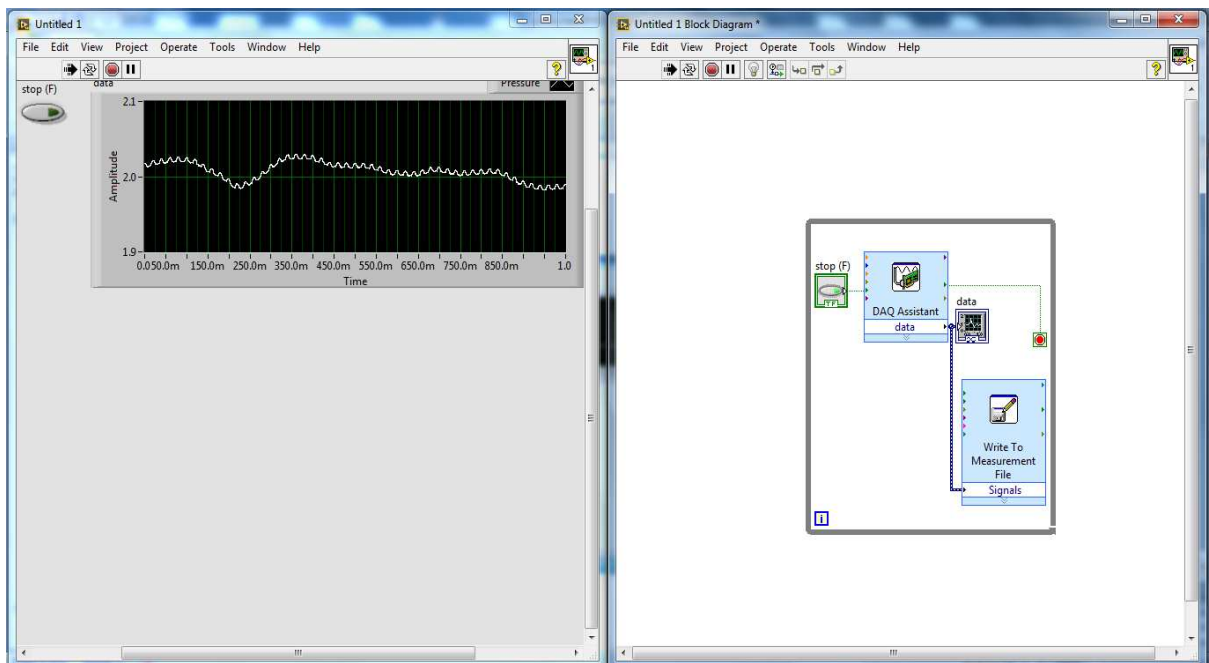


Figure A14. Wiring the Write to Measurement File Express VI from its terminal to the DAQ Assistant



## Appendix B

### Scour Data from Laboratory Experiment

#### Model A

<b>MODEL A Hydraulic condition I</b>									
<b>HU30HD1.5</b>									
<b>X(cm)</b>	<b>Y1(cm)</b>	<b>Y2(cm)</b>	<b>Y3(cm)</b>	<b>D1(cm)</b>	<b>D2(cm)</b>	<b>D3(cm)</b>	<b>Avg Ds</b>	<b>X/Dms</b>	<b>Y/DMS</b>
0	19.97	19.78	19.86	-0.13	-0.32	-0.24	-0.23	0.00	-0.04
1	19.22	19	19.23	-0.88	-1.1	-0.87	-0.95	0.17	-0.16
2	18.99	18.23	18.11	-1.11	-1.87	-1.99	-1.656667	0.34	-0.28
3	17.83	17.78	17.85	-2.27	-2.32	-2.25	-2.28	0.51	-0.39
4	16.9	17.55	17	-3.2	-2.55	-3.1	-2.95	0.68	-0.50
5	16.86	16.91	16.99	-3.24	-3.19	-3.11	-3.18	0.85	-0.54
6	16.03	15.77	15.66	-4.07	-4.33	-4.44	-4.28	1.02	-0.72
7	15.18	15.06	15.09	-4.92	-5.04	-5.01	-4.99	1.18	-0.84
8	14.19	14.55	15	-5.91	-5.55	-5.1	-5.52	1.35	-0.93
9	14.96	14.23	14.43	-5.14	-5.87	-5.67	-5.56	1.52	-0.94
10	14.02	14.22	14.45	-6.08	-5.88	-5.65	-5.87	1.69	-0.99
<b>11</b>	14.13	14.1	14.34	-5.97	-6	-5.76	<b>-5.91</b>	1.86	<b>-1.00</b>
12	14.93	14.77	14.76	-5.17	-5.33	-5.34	-5.28	2.03	-0.89
13	15.93	15.3	14.97	-4.17	-4.8	-5.13	-4.7	2.20	-0.80
14	16.07	15.68	15.59	-4.03	-4.42	-4.51	-4.32	2.37	-0.73
15	16.22	15.4	15.78	-3.88	-4.7	-4.32	-4.3	2.54	-0.73
16	16.39	16.11	16.01	-3.71	-3.99	-4.09	-3.93	2.71	-0.66
17	17.32	17.35	17.65	-2.78	-2.75	-2.45	-2.66	2.88	-0.45
18	18.19	18.45	17.87	-1.91	-1.65	-2.23	-1.93	3.05	-0.33
19	17.25	18.7	18.65	-2.85	-1.4	-1.45	-1.9	3.21	-0.32
20	18.9	18.65	18.67	-1.2	-1.45	-1.43	-1.36	3.38	-0.23
21	19.15	18.99	18.74	-0.95	-1.11	-1.36	-1.14	3.55	-0.19
22	19.56	19.23	19.35	-0.54	-0.87	-0.75	-0.72	3.72	-0.12
23	19.54	19.56	19.28	-0.56	-0.54	-0.82	-0.64	3.89	-0.11
24	19.37	19.77	19.66	-0.73	-0.33	-0.44	-0.5	4.06	-0.08
25	20.05	19.82	19.83	-0.05	-0.28	-0.27	-0.2	4.23	-0.03
26	20.41	19.92	19.97	0.31	-0.18	-0.13	-1.18E-15	4.40	0.00

<b>MODEL A</b>		<b>Hydraulic condition II</b>							
HU30HD3									
<b>X(cm)</b>	<b>Y1(CM)</b>	<b>Y2(CM)</b>	<b>Y3(CM)</b>	<b>D1(CM)</b>	<b>D2(CM)</b>	<b>D3(CM)</b>	<b>Avg Ds</b>	<b>Y/Dms</b>	<b>X/Dms</b>
0	18.67	18.97	18.65	-1.43	-1.13	-1.45	-1.34	-0.25	0.00
1	19.05	18.9	18.75	-1.05	-1.2	-1.35	-1.20	-0.22	0.18
2	17.85	17.95	18.09	-2.25	-2.15	-2.01	-2.14	-0.39	0.37
3	16.95	17.02	17.13	-3.15	-3.08	-2.97	-3.07	-0.57	0.55
4	16.56	16.52	16.84	-3.54	-3.58	-3.26	-3.46	-0.64	0.74
5	15.46	15.48	15.54	-4.64	-4.62	-4.56	-4.61	-0.85	0.92
6	15.11	15	15.13	-4.99	-5.1	-4.97	-5.02	-0.93	1.11
<b>7</b>	14.63	14.68	14.77	-5.47	-5.42	-5.33	<b>-5.41</b>	<b>-1.00</b>	1.29
8	14.7	14.76	14.86	-5.4	-5.34	-5.24	-5.33	-0.98	1.48
9	15.23	15.2	15.37	-4.87	-4.9	-4.73	-4.83	-0.89	1.66
10	15.94	16.01	16.18	-4.16	-4.09	-3.92	-4.06	-0.75	1.85
11	16.59	16.99	16.81	-3.51	-3.11	-3.29	-3.30	-0.61	2.03
12	17.11	17	16.89	-2.99	-3.1	-3.21	-3.10	-0.57	2.22
13	17.45	17.39	17.33	-2.65	-2.71	-2.77	-2.71	-0.50	2.40
14	17.83	17.8	17.79	-2.27	-2.3	-2.31	-2.29	-0.42	2.59
15	18.29	18.4	18.53	-1.81	-1.7	-1.57	-1.69	-0.31	2.77
16	18.82	18.94	19.04	-1.28	-1.16	-1.06	-1.17	-0.22	2.96
17	19.39	19.49	19.59	-0.71	-0.61	-0.51	-0.61	-0.11	3.14
18	19.88	19.85	19.83	-0.22	-0.25	-0.27	-0.25	-0.05	3.33
19	20.14	20	19.88	0.04	-0.1	-0.22	-0.09	-0.02	3.51
20	21.06	21.1	21.08	0.96	1	0.98	0.98	0.18	3.70
21	20.49	20.42	20.31	0.39	0.32	0.21	0.31	0.06	3.88

<b>MODEL A</b>		<b>Hydraulic condition III</b>										
HU30HD5												
<b>X(cm)</b>	<b>Y1(CM)</b>	<b>Y2(CM)</b>	<b>Y3(CM)</b>	<b>D1(CM)</b>	<b>D2(CM)</b>	<b>D3(CM)</b>	<b>Avg Ds</b>	<b>Y/Dms</b>	<b>X/Dms</b>			
0	18.38	18.45	18.73	-1.72	-1.65	-1.37	-1.58	-0.26	0.00			
1	18.03	18.19	18.14	-2.07	-1.91	-1.96	-1.98	-0.33	0.17			
2	17.88	17.9	18.01	-2.22	-2.2	-2.09	-2.17	-0.36	0.34			
3	16.28	16.32	16.42	-3.82	-3.78	-3.68	-3.76	-0.63	0.50			
4	16.09	16.16	16.11	-4.01	-3.94	-3.99	-3.98	-0.67	0.67			
5	15.32	15.41	15.17	-4.78	-4.69	-4.93	-4.8	-0.80	0.84			
6	15.08	15.19	15.09	-5.02	-4.91	-5.01	-4.98	-0.83	1.01			
<b>7</b>	14.22	14.09	14.08	-5.88	-6.01	-6.02	<b>-5.97</b>	<b>-1.00</b>	1.17			
8	14.82	14.76	14.73	-5.28	-5.34	-5.37	-5.33	-0.89	1.34			
9	14.92	14.96	15.24	-5.18	-5.14	-4.86	-5.06	-0.85	1.51			
10	15.76	15.69	15.62	-4.34	-4.41	-4.48	-4.41	-0.74	1.68			
11	16.24	16.28	16.59	-3.86	-3.82	-3.51	-3.73	-0.62	1.84			
12	16.9	16.87	17.05	-3.2	-3.23	-3.05	-3.16	-0.53	2.01			
13	17.24	17.16	17.47	-2.86	-2.94	-2.63	-2.81	-0.47	2.18			
14	17.59	17.55	17.9	-2.51	-2.55	-2.2	-2.42	-0.41	2.35			
15	17.91	17.97	18.24	-2.19	-2.13	-1.86	-2.06	-0.35	2.51			
16	18.55	18.52	18.25	-1.55	-1.58	-1.85	-1.66	-0.28	2.68			
17	18.96	18.93	18.78	-1.14	-1.17	-1.32	-1.21	-0.20	2.85			
18	19.16	19.08	18.91	-0.94	-1.02	-1.19	-1.05	-0.18	3.02			
19	19.28	19.15	19.71	-0.82	-0.95	-0.39	-0.72	-0.12	3.18			
20	19.62	19.58	20.11	-0.48	-0.52	0.01	-0.33	-0.06	3.35			
21	19.88	19.81	20.1	-0.22	-0.29	0	-0.17	-0.03	3.52			

Model B

MODEL B Hydraulic condition I									
HU30HD1.5									
X(cm)	Y1(CM)	Y2(CM)	Y3(CM)	D1(CM)	D2(CM)	D3(CM)	Avg Ds	X/Dms	Y/Dms
0.2	17.75	17.81	17.84	-2.25	-2.19	-2.16	-2.2	0.03	-0.38
1	17.62	17.66	17.88	-2.38	-2.34	-2.12	-2.28	0.17	-0.39
2	17	17.09	17.09	-3	-2.91	-2.91	-2.94	0.34	-0.50
3	16.85	16.67	17.09	-3.15	-3.33	-2.91	-3.13	0.51	-0.54
4	15.91	15.85	16.24	-4.09	-4.15	-3.76	-4	0.68	-0.68
5	15.42	15.56	15.34	-4.58	-4.44	-4.66	-4.56	0.85	-0.78
6	14.78	14.85	15.07	-5.22	-5.15	-4.93	-5.1	1.03	-0.87
7	14.48	14.21	14.96	-5.52	-5.79	-5.04	-5.45	1.20	-0.93
8	14.09	13.94	14.66	-5.91	-6.06	-5.34	-5.77	1.37	-0.99
9	14.09	13.98	14.47	-5.91	-6.02	-5.53	-5.82	1.54	-0.99
10	14.22	14.06	14.17	-5.78	-5.94	-5.83	-5.85	1.71	-1.00
11	14.85	14.68	14.75	-5.15	-5.32	-5.25	-5.24	1.88	-0.90
12	15.16	15.08	15	-4.84	-4.92	-5	-4.92	2.05	-0.84
13	15.29	15.11	15.71	-4.71	-4.89	-4.29	-4.63	2.22	-0.79
14	15.59	15.75	15.7	-4.41	-4.25	-4.3	-4.32	2.39	-0.74
15	16.32	16.44	15.99	-3.68	-3.56	-4.01	-3.75	2.56	-0.64
16	16.82	16.92	16.96	-3.18	-3.08	-3.04	-3.1	2.74	-0.53
17	17.55	17.57	17.8	-2.45	-2.43	-2.2	-2.36	2.91	-0.40
18	18.19	18.26	17.76	-1.81	-1.74	-2.24	-1.93	3.08	-0.33
19	18.29	18.23	18.26	-1.71	-1.77	-1.74	-1.74	3.25	-0.30
20	18.54	18.4	18.38	-1.46	-1.6	-1.62	-1.56	3.42	-0.27
21	18.79	18.69	19.4	-1.21	-1.31	-0.6	-1.04	3.59	-0.18
22	19.05	18.95	19.36	-0.95	-1.05	-0.64	-0.88	3.76	-0.15
23	19.42	19.14	19.55	-0.58	-0.86	-0.45	-0.63	3.93	-0.11
24	19.51	19.49	19.68	-0.49	-0.51	-0.32	-0.44	4.10	-0.08
25	19.62	19.59	19.98	-0.38	-0.41	-0.02	-0.27	4.27	-0.05
26	19.71	19.96	19.73	-0.29	-0.04	-0.27	-0.2	4.44	-0.03
27	20.02	19.89	20.09	0.02	-0.11	0.09	0	4.62	0.00

MODEL B		Hydraulic condition II								
HU30HD3										
X(cm)	Y1(CM)	Y2(CM)	Y3(CM)	D1(CM)	D2(CM)	D3(CM)	Avg Ds	X/Dms	Y/Dms	
0.5	18.71	18.6	18.64	-1.29	-1.4	-1.36	-1.35	0.08	-0.21	
1	18.56	18.49	18.27	-1.44	-1.51	-1.73	-1.56	0.16	-0.25	
2	17.74	17.77	17.95	-2.26	-2.23	-2.05	-2.18	0.32	-0.35	
3	16.91	16.97	17.12	-3.09	-3.03	-2.88	-3	0.48	-0.48	
4	16.43	16.53	16.21	-3.57	-3.47	-3.79	-3.61	0.63	-0.57	
5	15.51	15.59	15.76	-4.49	-4.41	-4.24	-4.38	0.79	-0.70	
6	15.35	15.2	15.26	-4.65	-4.8	-4.74	-4.73	0.95	-0.75	
7	14.61	14.72	14.95	-5.39	-5.28	-5.05	-5.24	1.11	-0.83	
8	14.15	14.21	13.64	-5.85	-5.79	-6.36	-6	1.27	-0.95	
9	13.85	13.68	13.57	-6.15	-6.32	-6.43	-6.3	1.43	-1.00	
10	13.71	13.68	14.01	-6.29	-6.32	-5.99	-6.2	1.59	-0.98	
11	13.89	13.75	13.82	-6.11	-6.25	-6.18	-6.18	1.75	-0.98	
12	14.28	14.41	14.21	-5.72	-5.59	-5.79	-5.7	1.90	-0.90	
13	14.73	14.83	14.78	-5.27	-5.17	-5.22	-5.22	2.06	-0.83	
14	15.28	15.32	14.94	-4.72	-4.68	-5.06	-4.82	2.22	-0.77	
15	15.75	15.86	15.67	-4.25	-4.14	-4.33	-4.24	2.38	-0.67	
16	16.51	16.42	16.48	-3.49	-3.58	-3.52	-3.53	2.54	-0.56	
17	16.87	16.92	17.03	-3.13	-3.08	-2.97	-3.06	2.70	-0.49	
18	17.05	17.15	17.55	-2.95	-2.85	-2.45	-2.75	2.86	-0.44	
19	18.16	18.22	17.71	-1.84	-1.78	-2.29	-1.97	3.02	-0.31	
20	18.32	18.15	18.31	-1.68	-1.85	-1.69	-1.74	3.17	-0.28	
21	18.21	18.27	18.42	-1.79	-1.73	-1.58	-1.7	3.33	-0.27	
22	18.42	18.33	18.45	-1.58	-1.67	-1.55	-1.6	3.49	-0.25	
23	18.78	18.62	18.88	-1.22	-1.38	-1.12	-1.24	3.65	-0.20	
24	18.77	18.86	19.07	-1.23	-1.14	-0.93	-1.1	3.81	-0.17	
25	18.88	19.16	18.99	-1.12	-0.84	-1.01	-0.99	3.97	-0.16	
26	19.18	19.09	19.39	-0.82	-0.91	-0.61	-0.78	4.13	-0.12	
27	19.25	19.18	19.47	-0.75	-0.82	-0.53	-0.7	4.29	-0.11	
28	19.45	19.29	19.4	-0.55	-0.71	-0.6	-0.62	4.44	-0.10	
29	19.78	19.58	19.62	-0.22	-0.42	-0.38	-0.34	4.60	-0.05	
30	19.86	19.98	19.89	-0.14	-0.02	-0.11	-0.09	4.76	-0.01	

MODEL B Hydraulic condition III									
HU30HD5									
X(cm)	Y1(CM)	Y2(CM)	Y3(CM)	D1(CM)	D2(CM)	D3(CM)	Avg Ds	X/Dms	Y/Dms
0.5	19.21	19.14	19.16	-0.79	-0.86	-0.84	-0.83	0.09	-0.15
1	18.91	18.88	18.55	-1.09	-1.12	-1.45	-1.22	0.18	-0.22
2	17.45	17.63	17.63	-2.55	-2.37	-2.37	-2.43	0.37	-0.45
3	16.92	17.15	16.96	-3.08	-2.85	-3.04	-2.99	0.55	-0.55
4	16.11	16.3	16.31	-3.89	-3.7	-3.69	-3.76	0.73	-0.69
5	15.78	15.78	15.96	-4.22	-4.22	-4.04	-4.16	0.92	-0.76
6	15.32	15.24	15.22	-4.68	-4.76	-4.78	-4.74	1.10	-0.87
7	14.76	14.73	14.94	-5.24	-5.27	-5.06	-5.19	1.28	-0.95
8	14.71	14.68	14.5	-5.29	-5.32	-5.5	-5.37	1.47	-0.99
9	14.56	14.47	14.62	-5.44	-5.53	-5.38	-5.45	1.65	-1.00
10	14.76	14.61	14.67	-5.24	-5.39	-5.33	-5.32	1.83	-0.98
11	14.77	14.64	14.72	-5.23	-5.36	-5.28	-5.29	2.02	-0.97
12	15.24	15.34	15.32	-4.76	-4.66	-4.68	-4.7	2.20	-0.86
13	15.59	15.72	15.62	-4.41	-4.28	-4.38	-4.3567	2.39	-0.80
14	16.11	16.04	15.85	-3.89	-3.96	-4.15	-4	2.57	-0.73
15	16.81	16.98	16.91	-3.19	-3.02	-3.09	-3.1	2.75	-0.57
16	17.2	17.14	16.9	-2.8	-2.86	-3.1	-2.92	2.94	-0.54
17	17.69	17.77	17.79	-2.31	-2.23	-2.21	-2.25	3.12	-0.41
18	18.32	18.19	18.3	-1.68	-1.81	-1.7	-1.73	3.30	-0.32
19	19.08	19.21	16.16	-0.92	-0.79	-3.84	-1.85	3.49	-0.34
20	19.58	19.41	19.39	-0.42	-0.59	-0.61	-0.54	3.67	-0.10
21	19.61	19.49	19.49	-0.39	-0.51	-0.51	-0.47	3.85	-0.09
22	19.63	19.87	19.81	-0.37	-0.13	-0.19	-0.23	4.04	-0.04
23	19.73	19.83	20.08	-0.27	-0.17	0.08	-0.12	4.22	-0.02
24	19.93	19.85	19.89	-0.07	-0.15	-0.11	-0.11	4.40	-0.02
25	19.95	19.86	19.95	-0.05	-0.14	-0.05	-0.08	4.59	-0.01

## Model C

MODEL C		Hydraulic condition I									
HU30HD1.5											
X(cm)	Y1(CM)	Y2(CM)	Y3(CM)	D1(CM)	D2(CM)	D3(CM)	Avg Ds	X/Dms	Y/Dms		
0.5	18.41	18.55	18.54	-1.59	-1.45	-1.46	-1.5	0.08	-0.24		
1	18.53	18.44	18.47	-1.47	-1.56	-1.53	-1.52	0.16	-0.24		
2	18.16	18.14	17.88	-1.84	-1.86	-2.12	-1.94	0.32	-0.31		
3	17.77	17.59	17.56	-2.23	-2.41	-2.44	-2.36	0.48	-0.38		
4	17.05	17.25	17.21	-2.95	-2.75	-2.79	-2.83	0.64	-0.45		
5	16.72	16.62	16.7	-3.28	-3.38	-3.3	-3.32	0.80	-0.53		
6	16.35	16.4	16.09	-3.65	-3.6	-3.91	-3.72	0.96	-0.60		
7	15.66	15.82	15.71	-4.34	-4.18	-4.29	-4.27	1.12	-0.68		
8	15.36	15.18	15.24	-4.64	-4.82	-4.76	-4.74	1.28	-0.76		
9	14.76	14.62	14.72	-5.24	-5.38	-5.28	-5.3	1.44	-0.85		
10	14.51	14.41	14.49	-5.49	-5.59	-5.51	-5.53	1.60	-0.89		
11	14.06	14.19	14.26	-5.94	-5.81	-5.74	-5.83	1.76	-0.93		
12	13.85	14.05	14.07	-6.15	-5.95	-5.93	-6.01	1.92	-0.96		
13	13.79	13.68	13.81	-6.21	-6.32	-6.19	-6.24	2.08	-1.00		
14	13.91	13.86	13.69	-6.09	-6.14	-6.31	-6.18	2.24	-0.99		
15	14.11	14.22	14.06	-5.89	-5.78	-5.94	-5.87	2.40	-0.94		
16	14.76	14.72	15.07	-5.24	-5.28	-4.93	-5.15	2.56	-0.83		
17	15.49	15.55	15.58	-4.51	-4.45	-4.42	-4.46	2.72	-0.71		
18	16.23	16.11	16.62	-3.77	-3.89	-3.38	-3.68	2.88	-0.59		
19	16.76	16.91	16.85	-3.24	-3.09	-3.15	-3.16	3.04	-0.51		
20	17.46	17.5	17.63	-2.54	-2.5	-2.37	-2.47	3.21	-0.40		
21	17.98	17.82	17.96	-2.02	-2.18	-2.04	-2.08	3.37	-0.33		
22	18.09	18.01	18.2	-1.91	-1.99	-1.8	-1.9	3.53	-0.30		
23	18.56	18.45	18.4	-1.44	-1.55	-1.6	-1.53	3.69	-0.25		
24	18.48	18.59	18.67	-1.52	-1.41	-1.33	-1.42	3.85	-0.23		
25	18.56	15.58	21.72	-1.44	-4.42	1.72	-1.38	4.01	-0.22		
26	18.94	18.83	19.17	-1.06	-1.17	-0.83	-1.02	4.17	-0.16		
27	19.42	19.36	18.94	-0.58	-0.64	-1.06	-0.76	4.33	-0.12		
28	19.54	19.43	19.56	-0.46	-0.57	-0.44	-0.49	4.49	-0.08		
29	19.76	19.81	19.95	-0.24	-0.19	-0.05	-0.16	4.65	-0.03		

MODEL C		Hydraulic condition II							
HU30HD3									
X(cm)	Y1(CM)	Y2(CM)	Y3(CM)	D1(CM)	D2(CM)	D3(CM)	Avg Ds	X/Dms	Y/Dms
0.5	19.78	19.76	19.92	-0.22	-0.24	-0.08	-0.18	0.10	-0.03
1	14.34	19.36	24.59	-5.66	-0.64	4.59	-0.57	0.19	-0.11
2	19.38	19.32	19.14	-0.62	-0.68	-0.86	-0.72	0.38	-0.14
3	19.26	19.21	19.01	-0.74	-0.79	-0.99	-0.84	0.57	-0.16
4	17.62	17.71	17.35	-2.38	-2.29	-2.65	-2.44	0.77	-0.47
5	17.46	17.51	17.14	-2.54	-2.49	-2.86	-2.63	0.96	-0.50
6	17.23	16.92	17.21	-2.77	-3.08	-2.79	-2.88	1.15	-0.55
7	16.69	16.83	16.58	-3.31	-3.17	-3.42	-3.3	1.34	-0.63
8	16.45	16.34	16.29	-3.55	-3.66	-3.71	-3.64	1.53	-0.70
9	16.25	16.18	15.75	-3.75	-3.82	-4.25	-3.94	1.72	-0.75
10	15.76	15.83	15.6	-4.24	-4.17	-4.4	-4.27	1.92	-0.82
11	15.58	15.55	15.88	-4.42	-4.45	-4.12	-4.33	2.11	-0.83
12	15.37	15.18	15.29	-4.63	-4.82	-4.71	-4.72	2.30	-0.90
13	14.87	14.73	15.22	-5.13	-5.27	-4.78	-5.06	2.49	-0.97
14	14.76	14.76	15.15	-5.24	-5.24	-4.85	-5.11	2.68	-0.98
15	14.63	14.61	15.1	-5.37	-5.39	-4.9	-5.22	2.87	-1.00
16	14.86	14.75	15.15	-5.14	-5.25	-4.85	-5.08	3.07	-0.97
17	15.49	15.53	15.69	-4.51	-4.47	-4.31	-4.43	3.26	-0.85
18	16.08	15.88	16.04	-3.92	-4.12	-3.96	-4	3.45	-0.77
19	16.45	16.61	16.53	-3.55	-3.39	-3.47	-3.47	3.64	-0.66
20	17.61	17.63	17.32	-2.39	-2.37	-2.68	-2.48	3.83	-0.48
21	18.28	18.01	18.73	-1.72	-1.99	-1.27	-1.66	4.02	-0.32
22	18.96	18.87	18.93	-1.04	-1.13	-1.07	-1.08	4.21	-0.21
23	19.42	19.62	19.64	-0.58	-0.38	-0.36	-0.44	4.41	-0.08
24	19.73	19.87	19.83	-0.27	-0.13	-0.17	-0.19	4.60	-0.04
25	19.97	19.99	20.04	-0.03	-0.01	0.04	-1.2E-15	4.79	0.00



MODEL C Hydraulic condition III									
HU30HDS									
X(cm)	Y1(CM)	Y2(CM)	Y3(CM)	D1(CM)	D2(CM)	D3(CM)	Avg Ds	X/Dms	Y/Dms
0.5	19.21	19.04	19.11	-0.79	-0.96	-0.89	-0.88	0.09	-0.15
1	18.83	19.13	19.34	-1.17	-0.87	-0.66	-0.9	0.17	-0.16
2	18.62	18.56	18.53	-1.38	-1.44	-1.47	-1.43	0.35	-0.25
3	17.98	18.15	18.23	-2.02	-1.85	-1.77	-1.88	0.52	-0.33
4	16.91	17.15	17	-3.09	-2.85	-3	-2.98	0.69	-0.52
5	16.49	16.58	16.64	-3.51	-3.42	-3.36	-3.43	0.87	-0.59
6	16.01	15.99	16.48	-3.99	-4.01	-3.52	-3.84	1.04	-0.67
7	15.83	15.79	15.69	-4.17	-4.21	-4.31	-4.23	1.21	-0.73
8	15.56	15.4	15.36	-4.44	-4.6	-4.64	-4.56	1.39	-0.79
9	14.82	14.82	15.12	-5.18	-5.18	-4.88	-5.08	1.56	-0.88
10	14.63	14.58	14.32	-5.37	-5.42	-5.68	-5.49	1.73	-0.95
11	14.09	14.15	14.6	-5.91	-5.85	-5.4	-5.72	1.91	-0.99
12	14.36	14.2	14.13	-5.64	-5.8	-5.87	-5.77	2.08	-1.00
13	14.28	14.23	14.45	-5.72	-5.77	-5.55	-5.68	2.25	-0.98
14	14.59	14.41	14.41	-5.41	-5.59	-5.59	-5.53	2.43	-0.96
15	14.62	14.26	14.8	-5.38	-5.74	-5.2	-5.44	2.60	-0.94
16	15.27	14.91	15.18	-4.73	-5.09	-4.82	-4.88	2.77	-0.85
17	15.29	15.21	15.88	-4.71	-4.79	-4.12	-4.54	2.95	-0.79
18	16.43	16.42	16.65	-3.57	-3.58	-3.35	-3.5	3.12	-0.61
19	17.01	17.05	17.33	-2.99	-2.95	-2.67	-2.87	3.29	-0.50
20	17.75	17.83	17.88	-2.25	-2.17	-2.12	-2.18	3.47	-0.38
21	17.91	18.14	17.95	-2.09	-1.86	-2.05	-2	3.64	-0.35
22	18.52	18.46	18.52	-1.48	-1.54	-1.48	-1.5	3.81	-0.26
23	18.71	18.59	18.68	-1.29	-1.41	-1.32	-1.34	3.99	-0.23
24	18.94	18.93	19.13	-1.06	-1.07	-0.87	-1	4.16	-0.17
25	19.27	19.02	19.37	-0.73	-0.98	-0.63	-0.78	4.33	-0.14
26	19.22	19.35	19.75	-0.78	-0.65	-0.25	-0.56	4.51	-0.10
27	19.63	19.83	19.82	-0.37	-0.17	-0.18	-0.24	4.68	-0.04
28	19.92	19.86	19.92	-0.08	-0.14	-0.08	-0.1	4.85	-0.02

Model D

<b>MODEL D</b>		<b>Hydraulic condition I</b>							
<b>HU30HD1.5</b>									
<b>X(cm)</b>	<b>Y1(CM)</b>	<b>Y2(CM)</b>	<b>Y3(CM)</b>	<b>D1(CM)</b>	<b>D2(CM)</b>	<b>D3(CM)</b>	<b>Avg Ds</b>	<b>X/Dms</b>	<b>Y/Dms</b>
0.5	20	20	20	0	0	0	0	0.09	0.00
1	20	20	20	0	0	0	0	0.18	0.00
2	19.98	20	20.02	-0.02	0	0.02	0	0.35	0.00
3	19.89	19.92	19.77	-0.11	-0.08	-0.23	-0.14	0.53	-0.02
4	19.75	19.66	19.09	-0.25	-0.34	-0.91	-0.5	0.71	-0.09
5	19.36	19.18	19.24	-0.64	-0.82	-0.76	-0.74	0.89	-0.13
6	18.96	18.85	18.98	-1.04	-1.15	-1.02	-1.07	1.06	-0.19
7	18.29	18.42	18.43	-1.71	-1.58	-1.57	-1.62	1.24	-0.29
8	17.86	17.92	17.77	-2.14	-2.08	-2.23	-2.15	1.42	-0.38
9	17.71	17.81	17.34	-2.29	-2.19	-2.66	-2.38	1.60	-0.42
10	17.48	17.44	17.7	-2.52	-2.56	-2.3	-2.46	1.77	-0.44
11	16.85	16.91	17.12	-3.15	-3.09	-2.88	-3.04	1.95	-0.54
12	16.51	16.55	16.77	-3.49	-3.45	-3.23	-3.39	2.13	-0.60
13	16.23	16.29	16.47	-3.77	-3.71	-3.53	-3.67	2.30	-0.65
14	15.96	15.75	15.78	-4.04	-4.25	-4.22	-4.17	2.48	-0.74
15	15.13	15.29	15.33	-4.87	-4.71	-4.67	-4.75	2.66	-0.84
16	14.63	14.82	14.83	-5.37	-5.18	-5.17	-5.24	2.84	-0.93
17	14.53	14.41	14.68	-5.47	-5.59	-5.32	-5.46	3.01	-0.97
18	14.26	14.43	14.39	-5.74	-5.57	-5.61	<b>-5.64</b>	3.19	<b>-1.00</b>
19	14.65	14.48	14.55	-5.35	-5.52	-5.45	-5.44	3.37	-0.96
20	14.51	14.75	14.6	-5.49	-5.25	-5.4	-5.38	3.55	-0.95
21	14.7	14.92	14.81	-5.3	-5.08	-5.19	-5.19	3.72	-0.92
22	14.83	15.18	14.99	-5.17	-4.82	-5.01	-5	3.90	-0.89
23	15.16	15.36	15.26	-4.84	-4.64	-4.74	-4.74	4.08	-0.84
24	15.62	15.48	15.73	-4.38	-4.52	-4.27	-4.39	4.26	-0.78
25	16.09	15.98	16.56	-3.91	-4.02	-3.44	-3.79	4.43	-0.67
26	16.32	16.54	16.46	-3.68	-3.46	-3.54	-3.56	4.61	-0.63
27	16.78	16.95	16.85	-3.22	-3.05	-3.15	-3.14	4.79	-0.56
28	17.18	16.94	17.72	-2.82	-3.06	-2.28	-2.72	4.96	-0.48
29	17.67	17.49	17.55	-2.33	-2.51	-2.45	-2.43	5.14	-0.43
30	17.82	18.05	17.89	-2.18	-1.95	-2.11	-2.08	5.32	-0.37
31	18.53	18.78	18.67	-1.47	-1.22	-1.33	-1.34	5.50	-0.24
32	19.08	18.97	19.34	-0.92	-1.03	-0.66	-0.87	5.67	-0.15
33	19.45	19.61	19.59	-0.55	-0.39	-0.41	-0.45	5.85	-0.08
34	19.86	19.94	19.9	-0.14	-0.06	-0.1	-0.1	6.03	-0.02

<b>MODEL D</b>									
<b>HU30HD3 Hydraulic condition II</b>									
<b>X(cm)</b>	<b>Y1(CM)</b>	<b>Y2(CM)</b>	<b>Y3(CM)</b>	<b>D1(CM)</b>	<b>D2(CM)</b>	<b>D3(CM)</b>	<b>Avg Ds</b>	<b>X/Dms</b>	<b>Y/Dms</b>
0.5	20	20	20	0	0	0	0	0.09	0.00
1	20	20	20	0	0	0	0	0.17	0.00
2	20	20	20	0	0	0	0	0.35	0.00
3	20	19.95	20.05	0	-0.05	0.05	0	0.52	0.00
4	19.96	19.98	20.06	-0.04	-0.02	0.06	0	0.69	0.00
5	19.81	19.81	19.96	-0.19	-0.19	-0.04	-0.14	0.87	-0.02
6	19.85	19.65	19.66	-0.15	-0.35	-0.34	-0.28	1.04	-0.05
7	19.63	19.48	19.54	-0.37	-0.52	-0.46	-0.45	1.21	-0.08
8	19.51	19.36	19.45	-0.49	-0.64	-0.55	-0.56	1.39	-0.10
9	18.98	19.21	19.65	-1.02	-0.79	-0.35	-0.72	1.56	-0.12
10	19.08	18.86	18.85	-0.92	-1.14	-1.15	-1.07	1.73	-0.19
11	18.43	18.18	18.35	-1.57	-1.82	-1.65	-1.68	1.91	-0.29
12	17.91	19.15	16.94	-2.09	-0.85	-3.06	-2	2.08	-0.35
13	17.56	17.38	17.35	-2.44	-2.62	-2.65	-2.57	2.25	-0.45
14	16.58	16.44	16.54	-3.42	-3.56	-3.46	-3.48	2.43	-0.60
15	16.28	16.09	16.17	-3.72	-3.91	-3.83	-3.82	2.60	-0.66
16	15.28	15.03	15.17	-4.72	-4.97	-4.83	-4.84	2.77	-0.84
17	14.68	14.78	14.25	-5.32	-5.22	-5.75	-5.43	2.95	-0.94
18	14.07	14.18	14.44	-5.93	-5.82	-5.56	<b>-5.77</b>	3.12	<b>-1.00</b>
19	14.33	14.53	14.46	-5.67	-5.47	-5.54	-5.56	3.29	-0.96
20	14.81	14.98	14.91	-5.19	-5.02	-5.09	-5.1	3.47	-0.88
21	14.91	15.08	15.19	-5.09	-4.92	-4.81	-4.94	3.64	-0.86
22	15.53	15.38	15.38	-4.47	-4.62	-4.62	-4.57	3.81	-0.79
23	15.86	15.36	16.06	-4.14	-4.64	-3.94	-4.24	3.99	-0.73
24	16.1	16.21	15.66	-3.9	-3.79	-4.34	-4.01	4.16	-0.69
25	16.37	16.56	16.36	-3.63	-3.44	-3.64	-3.57	4.33	-0.62
26	16.5	16.75	17.39	-3.5	-3.25	-2.61	-3.12	4.51	-0.54
27	17.29	17.36	17.76	-2.71	-2.64	-2.24	-2.53	4.68	-0.44
28	18.25	17.96	18.09	-1.75	-2.04	-1.91	-1.9	4.85	-0.33
29	18.76	18.52	18.61	-1.24	-1.48	-1.39	-1.37	5.03	-0.24
30	18.98	18.86	18.62	-1.02	-1.14	-1.38	-1.18	5.20	-0.20
31	19.11	19.26	19.14	-0.89	-0.74	-0.86	-0.83	5.37	-0.14
32	19.62	19.47	19.65	-0.38	-0.53	-0.35	-0.42	5.55	-0.07
33	19.93	19	20.83	-0.07	-1	0.83	-0.08	5.72	-0.01

<b>MODEL D</b>										
<b>HU30HD5</b>		<b>Hydraulic condition III</b>								
<b>X(cm)</b>	<b>Y1(CM)</b>	<b>Y2(CM)</b>	<b>Y3(CM)</b>	<b>D1(CM)</b>	<b>D2(CM)</b>	<b>D3(CM)</b>	<b>Avg Ds</b>	<b>X/Dms</b>	<b>Y/Dms</b>	
0.5	20	20	20	0	0	0	0	0.09	0.00	
1	20	20	20	0	0	0	0	0.19	0.00	
2	20	20	20	0	0	0	0	0.37	0.00	
3	20	20	20	0	0	0	0	0.56	0.00	
4	20	20	20	0	0	0	0	0.74	0.00	
5	20	20	20	0	0	0	0	0.93	0.00	
6	20	20	20	0	0	0	0	1.11	0.00	
7	19.8	19.79	19.87	-0.2	-0.21	-0.13	-0.18	1.30	-0.03	
8	19.75	19.62	19.64	-0.25	-0.38	-0.36	-0.33	1.48	-0.06	
9	19.54	19.41	19.37	-0.46	-0.59	-0.63	-0.56	1.67	-0.10	
10	18.85	18.66	18.74	-1.15	-1.34	-1.26	-1.25	1.85	-0.23	
11	17.85	18.04	18.11	-2.15	-1.96	-1.89	-2	2.04	-0.37	
12	17.08	17.11	17.5	-2.92	-2.89	-2.5	-2.77	2.22	-0.51	
13	16.48	16.38	16.64	-3.52	-3.62	-3.36	-3.5	2.41	-0.65	
14	15.64	15.77	16.02	-4.36	-4.23	-3.98	-4.19	2.59	-0.78	
15	15.28	15.09	15.11	-4.72	-4.91	-4.89	-4.84	2.78	-0.90	
<b>16</b>	14.68	14.51	14.61	-5.32	-5.49	-5.39	<b>-5.4</b>	2.96	<b>-1.00</b>	
17	14.78	14.87	14.33	-5.22	-5.13	-5.67	-5.34	3.15	-0.99	
18	14.73	14.81	15.04	-5.27	-5.19	-4.96	-5.14	3.33	-0.95	
19	14.98	14.87	14.91	-5.02	-5.13	-5.09	-5.08	3.52	-0.94	
20	15.33	15.55	15.5	-4.67	-4.45	-4.5	-4.54	3.70	-0.84	
21	15.84	15.81	16.11	-4.16	-4.19	-3.89	-4.08	3.89	-0.76	
22	16.12	16.07	16.5	-3.88	-3.93	-3.5	-3.77	4.07	-0.70	
23	16.68	16.85	16.72	-3.32	-3.15	-3.28	-3.25	4.26	-0.60	
24	17.08	17.21	17.13	-2.92	-2.79	-2.87	-2.86	4.44	-0.53	
25	17.58	17.62	17.9	-2.42	-2.38	-2.1	-2.3	4.63	-0.43	
26	18.05	18.23	18.26	-1.95	-1.77	-1.74	-1.82	4.81	-0.34	
27	18.75	18.82	19.22	-1.25	-1.18	-0.78	-1.07	5.00	-0.20	
28	19.21	19.17	19.64	-0.79	-0.83	-0.36	-0.66	5.19	-0.12	
29	19.27	19.28	19.86	-0.73	-0.72	-0.14	-0.53	5.37	-0.10	
30	19.32	19.84	19.91	-0.68	-0.16	-0.09	-0.31	5.56	-0.06	
31	19.98	19.58	20.02	-0.02	-0.42	0.02	-0.14	5.74	-0.03	

# Appendix C

## Copyright and Permissions Approval from World Scientific

Copyright and Permissions

0 1 v



Rights <rights@wspc.com>

Tue 09/01, 02:16

Abimbola Adewale <abimbolaadewale44@yahoo.com>; Adewale Olusola ABIMBOLA v

Reply all | v

Dear Abimbola Adewale

Thanks for getting in touch.

We will be pleased to grant you the permission of reproducing the abstract from page 1640017-21 to 16400017-35 of your article entitled 'Failure Mechanisms and Local Scour at Coastal Structures Induced by Tsunami' in your dissertation, provided that full credit been given to the original source in the following format:

Title of the Work, Author (s) and/or Editor(s) Name (s), Title of the Journal, Vol and Issue No., Copyright @ year and name of the publisher

For the electronic version of your thesis, kindly include a link of our journal at <http://www.worldscientific.com/worldscinet/cej> when you upload it onto UEL library and the British Library.

Kind regards,

Tu Ning

\*\*\*



Abimbola Adewale <abimbolaadewale44@yahoo.com>

Tue 02/01, 23:05

Reply | v



Download Save to OneDrive - University of East London

Dear World Scientific and JSCE,

I am completing my PhD thesis at University of East London (UEL) entitled '**Wave Propagation and Scour Failure of Coastal Structures Due to Tsunamis**'.

I seek your permission to reprint, in my thesis an extract from: **Failure Mechanisms and Local Scour at Coastal Structures Induced by Tsunami**. I am one of the authors and the extract to be reproduced is from page 1640017-21 to 16400017-35. These are some of the major experimental works and analyses from my tsunami experimental work.

I would like to include the extract in my electronic thesis which will be added to UEL library and the British Library.

If you are happy to grant me all the permissions requested, please return a signed copy of the attached letter.

**Please find attached the main copy of this letter.**

Kind regards

Abimbola Adewale.

## Appendix D

### Copyright and Permissions approval from Elsevier

#### ELSEVIER LICENSE TERMS AND CONDITIONS

Jan 05, 2018

---

---

This Agreement between Mr. Adewale Abimbola ("You") and Elsevier ("Elsevier") consists of your license details and the terms and conditions provided by Elsevier and Copyright Clearance Center.

License Number	4261031055944
License date	Jan 02, 2018
Licensed Content Publisher	Elsevier
Licensed Content Publication	Journal of Fluids and Structures
Licensed Content Title	Experimental investigation of dynamic pressure loads during dam break
Licensed Content Author	L. Lobovský,E. Botia-Vera,F. Castellana,J. Mas-Soler,A. Souto-Iglesias
Licensed Content Date	Jul 1, 2014
Licensed Content Volume	48
Licensed Content Issue	n/a
Licensed Content Pages	28
Start Page	407
End Page	434
Type of Use	reuse in a thesis/dissertation
Portion	figures/tables/illustrations
Number of figures/tables/illustrations	3
Format	electronic
Are you the author of this Elsevier article?	No
Will you be translating?	No

Original figure numbers	figures 3, 6 and 17.
Title of your thesis/dissertation	Wave Propagation and Scour Failure of Coastal Structures Due to Tsunamis
Expected completion date	Jan 2018
Estimated size (number of pages)	165
Requestor Location	Mr. Adewale Abimbola London, United Kingdom. Attn: Mr. Adewale Abimbola
Publisher Tax ID	GB 494 6272 12
Total	0.00 GBP
Terms and Conditions	

## **INTRODUCTION**

1. The publisher for this copyrighted material is Elsevier. By clicking "accept" in connection with completing this licensing transaction, you agree that the following terms and conditions apply to this transaction (along with the Billing and Payment terms and conditions established by Copyright Clearance Center, Inc. ("CCC"), at the time that you opened your Rightslink account and that are available at any time at <http://myaccount.copyright.com>).

## **GENERAL TERMS**

2. Elsevier hereby grants you permission to reproduce the aforementioned material subject to the terms and conditions indicated.
3. Acknowledgement: If any part of the material to be used (for example, figures) has appeared in our publication with credit or acknowledgement to another source, permission must also be sought from that source. If such permission is not obtained then that material may not be included in your publication/copies. Suitable acknowledgement to the source must be made, either as a footnote or in a reference list at the end of your publication, as follows:  
 "Reprinted from Publication title, Vol /edition number, Author(s), Title of article / title of chapter, Pages No., Copyright (Year), with permission from Elsevier [OR APPLICABLE SOCIETY COPYRIGHT OWNER]." Also Lancet special credit -  
 "Reprinted from The Lancet, Vol. number, Author(s), Title of article, Pages No., Copyright (Year), with permission from Elsevier."

4. Reproduction of this material is confined to the purpose and/or media for which permission is hereby given.

5. Altering/Modifying Material: Not Permitted. However figures and illustrations may be altered/adapted minimally to serve your work. Any other abbreviations, additions, deletions and/or any other alterations shall be made only with prior written authorization of Elsevier Ltd. (Please contact Elsevier at [permissions@elsevier.com](mailto:permissions@elsevier.com)). No modifications can be made to any Lancet figures/tables and they must be reproduced in full.

6. If the permission fee for the requested use of our material is waived in this instance, please be advised that your future requests for Elsevier materials may attract a fee.

7. Reservation of Rights: Publisher reserves all rights not specifically granted in the combination of (i) the license details provided by you and accepted in the course of this licensing transaction, (ii) these terms and conditions and (iii) CCC's Billing and Payment terms and conditions.

8. License Contingent Upon Payment: While you may exercise the rights licensed immediately upon issuance of the license at the end of the licensing process for the transaction, provided that you have disclosed complete and accurate details of your proposed use, no license is finally effective unless and until full payment is received from you (either by publisher or by CCC) as provided in CCC's Billing and Payment terms and conditions. If full payment is not received on a timely basis, then any license preliminarily granted shall be deemed automatically revoked and shall be void as if never granted. Further, in the event that you breach any of these terms and conditions or any of CCC's Billing and Payment terms and conditions, the license is automatically revoked and shall be void as if never granted. Use of materials as described in a revoked license, as well as any use of the materials beyond the scope of an unrevoked license, may constitute copyright infringement and publisher reserves the right to take any and all action to protect its copyright in the materials.

9. Warranties: Publisher makes no representations or warranties with respect to the licensed material.

10. Indemnity: You hereby indemnify and agree to hold harmless publisher and CCC, and their respective officers, directors, employees and agents, from and



against any and all claims arising out of your use of the licensed material other than as specifically authorized pursuant to this license.

11. No Transfer of License: This license is personal to you and may not be sublicensed, assigned, or transferred by you to any other person without publisher's written permission.

12. No Amendment Except in Writing: This license may not be amended except in a writing signed by both parties (or, in the case of publisher, by CCC on publisher's behalf).

13. Objection to Contrary Terms: Publisher hereby objects to any terms contained in any purchase order, acknowledgment, check endorsement or other writing prepared by you, which terms are inconsistent with these terms and conditions or CCC's Billing and Payment terms and conditions. These terms and conditions, together with CCC's Billing and Payment terms and conditions (which are incorporated herein), comprise the entire agreement between you and publisher (and CCC) concerning this licensing transaction. In the event of any conflict between your obligations established by these terms and conditions and those established by CCC's Billing and Payment terms and conditions, these terms and conditions shall control.

14. Revocation: Elsevier or Copyright Clearance Center may deny the permissions described in this License at their sole discretion, for any reason or no reason, with a full refund payable to you. Notice of such denial will be made using the contact information provided by you. Failure to receive such notice will not alter or invalidate the denial. In no event will Elsevier or Copyright Clearance Center be responsible or liable for any costs, expenses or damage incurred by you as a result of a denial of your permission request, other than a refund of the amount(s) paid by you to Elsevier and/or Copyright Clearance Center for denied permissions.

#### **LIMITED LICENSE**

The following terms and conditions apply only to specific license types:

15. **Translation:** This permission is granted for non-exclusive world **English** rights only unless your license was granted for translation rights. If you licensed translation rights you may only translate this content into the

languages you requested. A professional translator must perform all translations and reproduce the content word for word preserving the integrity of the article.

**16. Posting licensed content on any Website:** The following terms and conditions apply as follows: Licensing material from an Elsevier journal: All content posted to the web site must maintain the copyright information line on the bottom of each image; A hyper-text must be included to the Homepage of the journal from which you are licensing

at <http://www.sciencedirect.com/science/journal/xxxxx> or the Elsevier homepage for books at <http://www.elsevier.com>; Central Storage: This license does not include permission for a scanned version of the material to be stored in a central repository such as that provided by Heron/XanEdu.

Licensing material from an Elsevier book: A hyper-text link must be included to the Elsevier homepage at <http://www.elsevier.com> . All content posted to the web site must maintain the copyright information line on the bottom of each image.

**Posting licensed content on Electronic reserve:** In addition to the above the following clauses are applicable: The web site must be password-protected and made available only to bona fide students registered on a relevant course. This permission is granted for 1 year only. You may obtain a new license for future website posting.

**17. For journal authors:** the following clauses are applicable in addition to the above:

**Preprints:**

A preprint is an author's own write-up of research results and analysis, it has not been peer-reviewed, nor has it had any other value added to it by a publisher (such as formatting, copyright, technical enhancement etc.).

Authors can share their preprints anywhere at any time. Preprints should not be added to or enhanced in any way in order to appear more like, or to substitute for, the final versions of articles however authors can update their preprints on arXiv or RePEc with their Accepted Author Manuscript (see below).

If accepted for publication, we encourage authors to link from the preprint to their formal publication via its DOI. Millions of researchers have access to the formal publications on ScienceDirect, and so links will help users to find, access, cite and

use the best available version. Please note that Cell Press, The Lancet and some society-owned have different preprint policies. Information on these policies is available on the journal homepage.

**Accepted Author Manuscripts:** An accepted author manuscript is the manuscript of an article that has been accepted for publication and which typically includes author-incorporated changes suggested during submission, peer review and editor-author communications.

Authors can share their accepted author manuscript:

- immediately
  - via their non-commercial person homepage or blog
  - by updating a preprint in arXiv or RePEc with the accepted manuscript
  - via their research institute or institutional repository for internal institutional uses or as part of an invitation-only research collaboration work-group
  - directly by providing copies to their students or to research collaborators for their personal use
  - for private scholarly sharing as part of an invitation-only work group on commercial sites with which Elsevier has an agreement
- After the embargo period
  - via non-commercial hosting platforms such as their institutional repository
  - via commercial sites with which Elsevier has an agreement

In all cases accepted manuscripts should:

- link to the formal publication via its DOI
- bear a CC-BY-NC-ND license - this is easy to do
- if aggregated with other manuscripts, for example in a repository or other site, be shared in alignment with our hosting policy not be added to or enhanced in any way to appear more like, or to substitute for, the published journal article.

**Published journal article (JPA):** A published journal article (PJA) is the definitive final record of published research that appears or will appear in the journal and embodies all value-adding publishing activities including peer review coordination, copy-editing, formatting, (if relevant) pagination and online enrichment. Policies for sharing publishing journal articles differ for subscription and gold open access articles:

**Subscription Articles:** If you are an author, please share a link to your article rather than the full-text. Millions of researchers have access to the formal publications on ScienceDirect, and so links will help your users to find, access, cite, and use the best available version.

Theses and dissertations which contain embedded PJAs as part of the formal submission can be posted publicly by the awarding institution with DOI links back to the formal publications on ScienceDirect.

If you are affiliated with a library that subscribes to ScienceDirect you have additional private sharing rights for others' research accessed under that agreement. This includes use for classroom teaching and internal training at the institution (including use in course packs and courseware programs), and inclusion of the article for grant funding purposes.

**Gold Open Access Articles:** May be shared according to the author-selected end-user license and should contain a [CrossMark logo](#), the end user license, and a DOI link to the formal publication on ScienceDirect.

Please refer to Elsevier's [posting policy](#) for further information.

18. **For book authors** the following clauses are applicable in addition to the above: Authors are permitted to place a brief summary of their work online only. You are not allowed to download and post the published electronic version of your chapter, nor may you scan the printed edition to create an electronic version. **Posting to a repository:** Authors are permitted to post a summary of their chapter only in their institution's repository.

19. **Thesis/Dissertation:** If your license is for use in a thesis/dissertation your thesis may be submitted to your institution in either print or electronic form. Should your thesis be published commercially, please reapply for permission. These requirements include permission for the Library and Archives of Canada to supply single copies, on demand, of the complete thesis and include permission for Proquest/UMI to supply single copies, on demand, of the complete thesis. Should your thesis be published commercially, please reapply for permission. Theses and dissertations which contain embedded PJAs as part of the formal submission can be posted publicly by the awarding institution with DOI links back to the formal publications on ScienceDirect.

## **Elsevier Open Access Terms and Conditions**

You can publish open access with Elsevier in hundreds of open access journals or in nearly 2000 established subscription journals that support open access publishing. Permitted third party re-use of these open access articles is defined by the author's choice of Creative Commons user license. See our [open access license policy](#) for more information.

### **Terms & Conditions applicable to all Open Access articles published with Elsevier:**

Any reuse of the article must not represent the author as endorsing the adaptation of the article nor should the article be modified in such a way as to damage the author's honour or reputation. If any changes have been made, such changes must be clearly indicated.

The author(s) must be appropriately credited and we ask that you include the end user license and a DOI link to the formal publication on ScienceDirect.

If any part of the material to be used (for example, figures) has appeared in our publication with credit or acknowledgement to another source it is the responsibility of the user to ensure their reuse complies with the terms and conditions determined by the rights holder.

### **Additional Terms & Conditions applicable to each Creative Commons user license:**

**CC BY:** The CC-BY license allows users to copy, to create extracts, abstracts and new works from the Article, to alter and revise the Article and to make commercial use of the Article (including reuse and/or resale of the Article by commercial entities), provided the user gives appropriate credit (with a link to the formal publication through the relevant DOI), provides a link to the license, indicates if changes were made and the licensor is not represented as endorsing the use made of the work. The full details of the license are available at <http://creativecommons.org/licenses/by/4.0>.

**CC BY NC SA:** The CC BY-NC-SA license allows users to copy, to create extracts, abstracts and new works from the Article, to alter and revise the Article, provided this is not done for commercial purposes, and that the user gives appropriate credit (with a link to the formal publication through the relevant DOI), provides a link to the license, indicates if changes were made and the licensor is

not represented as endorsing the use made of the work. Further, any new works must be made available on the same conditions. The full details of the license are available at <http://creativecommons.org/licenses/by-nc-sa/4.0>.

**CC BY NC ND:** The CC BY-NC-ND license allows users to copy and distribute the Article, provided this is not done for commercial purposes and further does not permit distribution of the Article if it is changed or edited in any way, and provided the user gives appropriate credit (with a link to the formal publication through the relevant DOI), provides a link to the license, and that the licensor is not represented as endorsing the use made of the work. The full details of the license are available at <http://creativecommons.org/licenses/by-nc-nd/4.0>. Any commercial reuse of Open Access articles published with a CC BY NC SA or CC BY NC ND license requires permission from Elsevier and will be subject to a fee. Commercial reuse includes:

- Associating advertising with the full text of the Article
- Charging fees for document delivery or access
- Article aggregation
- Systematic distribution via e-mail lists or share buttons

Posting or linking by commercial companies for use by customers of those companies.

## 20. Other Conditions:

v1.9

Questions? [customercare@copyright.com](mailto:customercare@copyright.com) or +1-855-239-3415 (toll free in the US) or +1-978-646-2777.

